Exploring the use of phenocams and satellite data to better inform the pasture phenology and aerobiology of allergenic grass pollen in eastern Australia

by Yuxia Liu

Thesis submitted in fulfilment of the requirements for the degree of

Doctor of Philosophy

under the supervision of

Distinguished Professor Alfredo Huete (principal supervisor)

Doctor Qiaoyun Xie (co-supervisor)

University of Technology Sydney

Faculty of Science

School of Life Science

November 2021

CERTIFICATE OF AUTHORSHIP

I, Yuxia Liu, declare that this thesis is submitted in fulfilment of the requirements for the award of the degree of Doctor of Philosophy, in the Faculty of Science at the University of Technology Sydney.

This thesis is wholly my own work unless otherwise reference or acknowledged. In addition, I certify that all information sources and literature used are indicated in the thesis.

This document has not been submitted for qualifications at any other academic institution.

This research is supported by the International Research Scholarship and President's Scholarship funded by University of Technology Sydney. Also, this research is supported by an Australian Government Research Training Program.

Production Note:
Signature: Signature removed prior to publication.

Date: 15 / 11 / 2021

To my parents.

I love you.

To Professor Alfredo Huete, and Doctor Qiaoyun Xie.

For their endless support and encouragement.

Acknowledgements

I would like to express my sincere thanks to my supervisor panel, Professor Alfredo Huete, and Doctor Qiaoyun Xie. They have taught me the true meaning of scientific research and shown me how to think and do as a real researcher. Although their (he) comments made me doubt myself deeply sometimes, I really would like to say: Thank you. It was those difficult moments that have moulded me into the person I am today. Thank you, Alfredo and Qiaoyun, for everything. They always understood the challenges that I experienced, and they always cheered me up in their own ways. I also would like to say thanks for Qiaoyun (extra), cause of her yummy foods (cheese cake, tiramisu, muffin, steamed bun … and those empty wine bottles …). I feel very lucky to be their student. I am very sure I will miss these four years someday.

Next, I would like to express my thanks to all my groupmates. Especially, Song Leng, Sicong Gao and Ha Nguyen. Thanks for their efforts to set up phenocams that were used in this thesis. I also thank Beth Addison-Smith in the Queensland University of Technology to maintain the Phenocam sites. The use of the Sentinel-2 grass map would not have been possible without the modelling and ongoing assistance of several people: Mr Abolfazl Abdollahi and Professor Biswajeet Pradhan in FEIT of University of Technology Sydney (UTS). I also would like to express my sincere thanks to Ms Shannon Hawkins, the research officer in the Faculty of Science, UTS. My PhD journey would not have been such smooth without her supports in terms of administrative affairs.

Finally, I would like to say thanks to my friends in Sydney and my parents. My life away from home would not have been so smooth and sweet without my friends' support and accompany.

Thank you, mom and dad. Thank you for giving life and endless love to me.

Ponder the path of your feet then all your ways will be sure.

Table of Contents

List of Figures

List of Tables

Abstract

Phenological studies of grassland/ pastures have attracted increased attention for their sensitivity to climate change with associated impacts on allergenic pollen release and public health. Allergenic pollen exposure is expected to increase with global warming following extended grass growing and grass pollen seasons and the prevalence of allergic diseases in Australia is among the highest globally. The primary aims of this thesis were to integrate phenocam and satellite imagery with pollen concentration data, over subtropical to temperate grassland sites in Australia, in order to address critical knowledge gaps in our understanding of the ecological drivers of grass pollen aerobiology.

Phenocams were used to investigate the diurnal and daily greenness variations across solar zenith angles, solar intensity, and direct/ diffuse sky conditions. This information was used to develop an optimised daily compositing methodology. Next, I successfully registered a 3×3 window of Sentinel-2 pixels at 10 m resolution with the phenocam measurement footprint to conduct upscaling analyses. The relationships between Sentinel-2 Enhanced Vegetation Index (EVI) and phenocam green chromatic coordinate (GCC) index were strong and independent of the time of year and grass phenophases. This enabled the more sparse temporal sampling of Sentinel-2 greenness to be converted to daily values.

Relationships between seasonal grass pollen concentrations and phenocam GCC and satellite EVI phenology were also strong with pollen concentration peaks in phase with grass greenness peaks, including multiple sub-seasonal pollen and greenness peaks. The grass greenness amplitudes, a surrogate of biomass, were found to be correlated with total pollen concentrations. Finally, I investigated grass pollen sources at more detailed, 10 m resolution, by generating a neural net grass map, from the Sentinel-2 sensor. This enabled urban, peri-urban and regional grass sources to be quantified based on distance and orientation to the pollen sampler, providing new insights for pollen forecasting. This thesis highlights the ability of near-surface and satellite remote sensing to achieve more accurate grassland/ pasture phenology to improve upon the understanding of ecologically relevant factors for grass pollen aerobiology in Australia.

CHAPTER 1

Chapter 1 Introduction

1.1 Allergenic grass pollen

Allergies are medically and economically important chronic diseases (Weinberg 2011). The first description of the allergenic disease, hay fever, was published in 1819 by John Bostock (Bostock 1819). A half-century later, Charles Harrison Blackley (1873) reported pollen as one of the major clinically important allergen sources. Since then, the relationship between airborne pollen and allergic epidemic has received wide attention from scientists, and the role of pollen in the pathogeny of major allergic diseases, like asthma, rhinitis and conjunctivitis, is now well established. Across Australia, grass pollen is a major aeroallergen source (e.g., for allergic rhinitis and asthma), and recent research has demonstrated that the prevalence and morbidity impact of hay fever and asthma in Australia and New Zealand are among the highest in the world (Asher et al. 2007). Three million Australians (15% of the Australian population) are affected by allergic diseases caused by grass pollen, resulting in an economic burden of A$7.8 billion annually in government health costs (Cook et al. 2007). Allergic diseases can considerably affect patients' quality of life and reduce productivity (Bousquet et al. 2012; Meltzer et al. 2009; Walls et al. 2005). In addition, the relationship between the concentration of grass pollen in the atmosphere and hospital attendance for allergic diseases has been demonstrated (Darrow et al. 2012; Erbas et al. 2007). However, little is known about the timing and levels of human exposure to aeroallergen and spatial distribution of allergenic grass sources across Australia. Providing a thorough and comprehensive understanding of airborne pollen levels and accurately predicting pollen aerobiology patterns would improve health management for both individuals and medical institutions, and consequently reduce the health and economic burden of these diseases.

Pollen is a container that holds the male gametophyte generation for the angiosperms and gymnosperms, and is an evolutionary adaptation to protect the male gametes from the adverse living environment (Moore & Webb 1983). There are two factors wildly used to determine the allergological properties of pollen grains: pollen potency and pollen abundance in the atmosphere. According to these factors, 12 pollen types are highly allergenic: ragweed, alder, mugwort, birch, goosefoots, hazel, yews, olive, plane tree, grass (Poaceae), oak and wall pellitory (Skjøth, Šikoparija & Jäger 2013). In Australia, grass pollen and associated

cytoplasmic fragments have been demonstrated as the major causative allergen in thunderstorm asthma events (Bellomo et al. 1992; Howden, McDonald & Sutherland 2011; Marks et al. 2001; Moore & Webb 1983). The proportion of grass pollens to total pollen in Australia has been reported to range from 6–72% over any given year (Green et al. 2004; Tng et al. 2010). While a wide variety of grasses were observed across most Australia cities, the types of dominant grass vary across the different climate zones, from temperate ryegrass found in Melbourne, Canberra, Hobart and Sydney, to subtropical Bahia grass in Brisbane (Davies et al. 2012).

There are large variations of grass pollen activity across Australia, and grass pollen may be present all year in some cities (e.g., Adelaide, Canberra, Hobart, Melbourne, Perth and Sydney) (Bass & Morgan 1997a; Ong, Singh & Knox 1995; Tng et al. 2010). In a study across six sites (Brisbane, Canberra, Darwin, Hobart, Melbourne and Sydney), Beggs found considerable differences in temporal variations in grass pollen concentration across different sites and different years for the same location. Similarly, the date of peak grass pollen and grass pollen season timing and length display similar variations (see Fig. 1.1) (Beggs et al. 2015a). However, a study in Hobart showed that the pattern in the timing of peak pollen was broadly similar across the research period of October (Tng et al. 2010). Numerous studies have shown that peaks in airborne grass pollen can appear at nearly any stage of the grass pollen season (Beggs et al. 2015a; Davies et al. 2012; Hamid et al. 2015; Ong, Singh & Knox 1995; Stevenson et al. 2007b; Werchan et al. 2017). Apart from the studies of spatial and temporal patterns in grass pollen loads, the relationship between climate change and aerobiology, with rising temperature or atmospheric CO_2 level, may cause increases in allergenic pollen levels (Emberlin 1994; Singer et al. 2005; Ziska & Caulfield 2000).

The grass pollen seasons appear to be distinct in the different climatic zones across Australia. In monsoon-tropical Darwin, the grass pollen seasons follow the dry season (April–May) with prominent pollen loads (Stevenson et al. 2007a). In subtropical Brisbane, the grass pollen peak has been observed from summer to autumn (December–April) (Green et al. 2002). In warm-temperate Sydney, the longest grass pollen season is from spring to autumn (October–May) (Bass, Baldo & Pham 1991; Bass & Morgan 1997b). In temperate Melbourne, the peak of grass pollen only occurs during November to January (spring to early summer) (Ong,

Singh & Knox 1995). Temperate Hobart has the same trend of grass pollen season as Melbourne (Tng et al. 2010). Moreover, there are secondary grass pollen peaks around March in Perth, Adelaide, Sydney and Canberra (Bass & Morgan 1997a; Ong, Singh & Knox 1995; Tng et al. 2010).

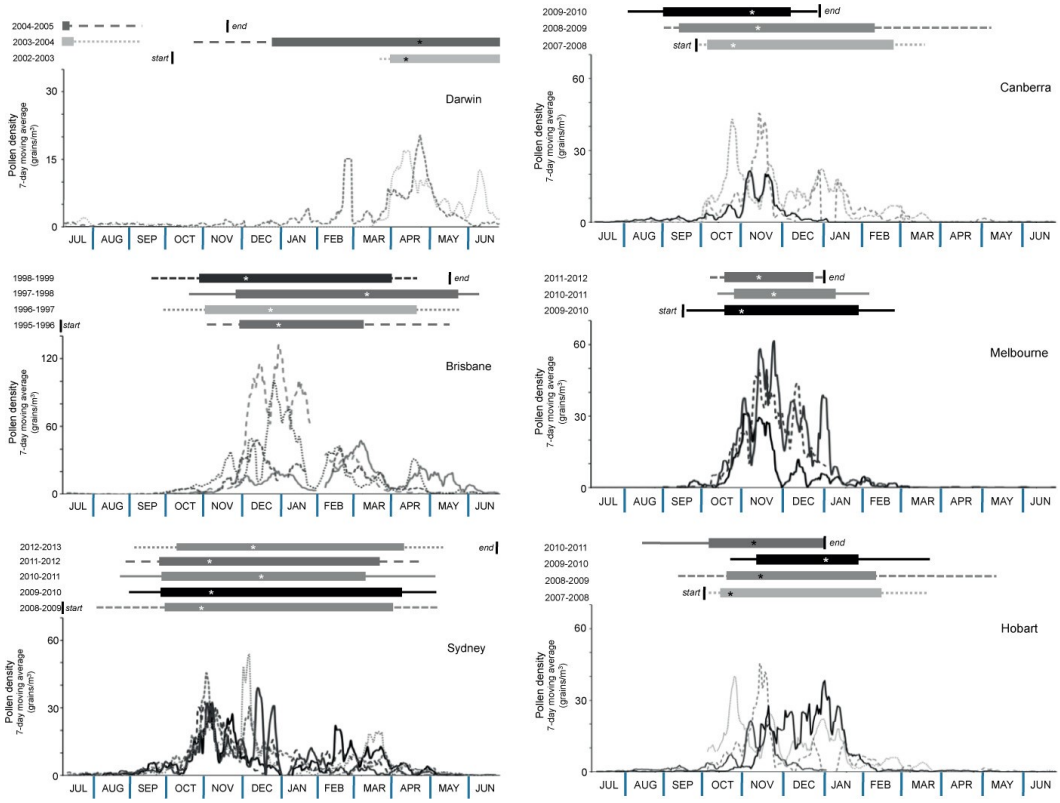

Figure 1.1 Grass pollen density and seasonal pattern for six cities in Australia. The combination of the horizontal line (98% of the annual grass pollen loads in this time) and a horizontal box (98% of the annual grass pollen loads in this range) depict the grass pollen season for each year, with the corresponding curve. The asterisks in the box plots show peak grass pollen date. The vertical bars labelled 'start' and 'end' indicate the start and end of pollen sampling. Source of image: Begges et al., 2015a.

Ryegrass (*Lolium perenne*) is widely accepted as the most important source of grass pollen across most of Australia. In particular, ryegrass is considered a major cause of allergic hay fever and allergenic asthma in Melbourne (Batson 1998; Girgis et al. 2000). On Monday 21 November 2016, a thunderstorm swept through Melbourne, with damaging winds, heavy rainfall and large hail. It triggered sudden asthma epidemics and led to ten deaths, and hospital admissions increased by 681 per cent

as thousands of patients sought asthma-related medical care over a very short period of time. The ryegrass pollen concentration was considered a risk factor 'trifecta' for thunderstorm asthma with clinical allergic rhinitis and acute allergen exposure (Lee et al. 2017). According to the *Pollen calendar* issued by the Australasian Society of Clinical Immunology and Allergy (ASCIA), the pollen season of ryegrass is from August to March (Table 1.1). However, knowledge of ryegrass source and spatial distribution in Australia is incomplete, despite many studies using pollen transport models and land use maps to show grass source and transport under various meteorological factors (Beggs et al. 2015b; Devadas et al. 2018; Girgis et al. 2000; Grundstein et al. 2017; McInnes et al. 2017; Stevenson et al. 2007b).

Table 1.1 Pollen calendar of ryegrass in different states in Australia.

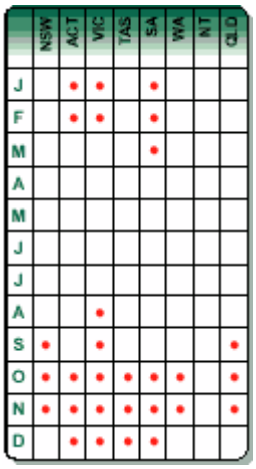

Source: Australasian Society of Clinical Immunology and Allergy (ASCIA), https://www.allergy.org.au/patients/allergic-rhinitis-hay-fever-and-sinusitis/guide-to-common-allergenic-pollen/267-ryegrass.

1.2 'Near-surface' remote sensing - phenocam

1.2.1 Introduction

'Near-surface' remote sensing – Phenocam provides an innovative approach to monitor rapid variations in ecological processes. A better record and understanding of ecological responses to environmental change globally requires an exponential increase in the quantity, diversity and resolution of field-collected data (Brown, Hultine & Steltzer 2016). Unlike conventional remote sensing, phenocams are installed in relatively close proximity to the land surface, provide images with high

temporal frequency and are relatively free of atmospheric aerosols effects. In addition, traditional field-based phenology observation is to record certain growth situations of separate plants, and data quality depends on observers' experience. Further, direct phenological surveys provide observations that lack information on the phenology of a whole community. However, digital camera imagery offers the opportunity to integrally investigate the phenological signal across the whole individual plants canopy when the study object is forest, and also to conduct separate analyses across different species by distinguishing individual vegetation (e.g., single tree crowns). These advantages make up for the deficiency of coarse spatial resolution of satellite remote sensing imagery.

The term 'PhenoCam' was proposed when a collaborative, regional-scale digital camera network in the USA was used to track seasonal variation in the phenology of forest ecosystems (Richardson, Braswell et al. 2009). The general conception of phenocam refers to any repeat digital camera used for repeat or time-lapse photography to research land cover phenology or other ecological changes (Brown, Hultine & Steltzer 2016). Phenocam is an approach that uses imaging sensors, typically installed on permanent structures (e.g., towers or other buildings) to observe and quantify variations in the surface land cover in a manner analogous to remote sensing technology, but at a higher spatial resolution and temporal frequency (Richardson, Klosterman & Toomey 2013).

A considerable number of new camera models are released every year and, therefore, many different types of phenocams are now used globally. Even so, radiometric sensors and imaging sensors are the main two categories for near-surface remote sensing technology (Richardson, Klosterman & Toomey 2013). Radiometric sensors are unable to provide information about spatial variability and cannot distinguish individual objects within the field of view (FOV) (Hilker et al. 2011). Imaging sensors provide an opportunity to conduct spatial variability analysis, because they produce digital pictures of a land cover scene with sufficient temporal and spatial resolutions. Most digital cameras record RGB (red, green, blue) imagery, and then special chromatic coordinate indices (e.g., green chromatic coordinate, GCC) can be derived from these digital values to provide information on vegetation status.

In a typical phenocam system, a camera is installed on a structure taller than the research object (e.g., a forest) to have a view across the landscape. To minimise the lens flare and shadows and obtain ideal imagery, most cameras usually face to the north in the northern hemisphere or to the south in the southern hemisphere, and a reference panel is mounted to provide information about variation in illumination and sensor stability (Fig. 1.2) (Richardson, Klosterman & Toomey 2013).

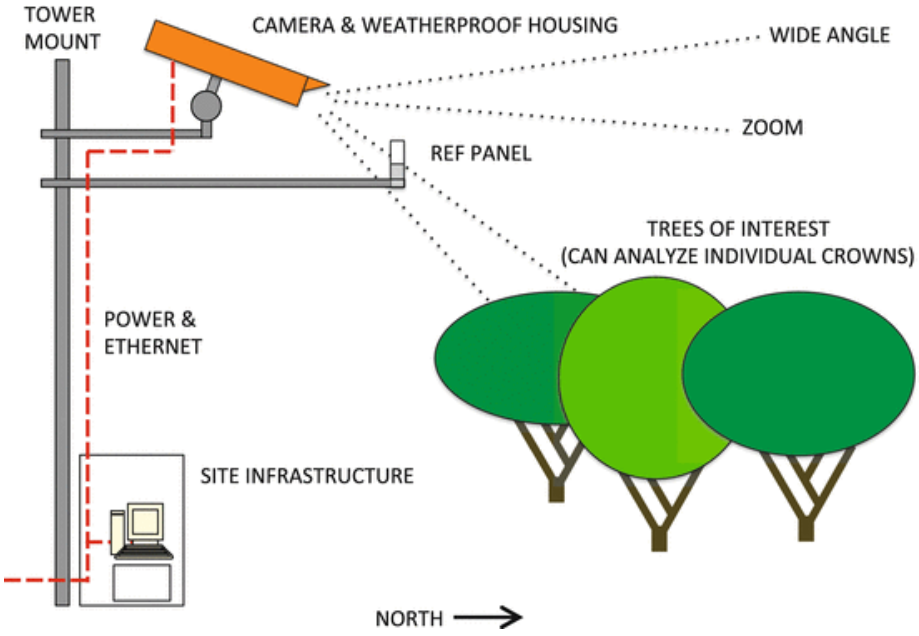

Figure 1.2 Schematic diagram showing phenocam deployment strategy for a forested ecosystem. Source: Richardson, Klosterman & Toomey (2013).

For phenocam image processing, the lens projects the observed object onto a digital chip with light-sensitive structure (see Figure 3 a). Three separate layers (red, green and blue) are used to record colour information of the landscape. A digital number (DN) represents the intensity of each colour layer for each pixel in the image. The quantitative analysis of the image includes (1) selecting a region of interest (ROI) from a scene based on the research objective (e.g., an individual canopy crown, or the entire plant canopy at a certain location) and (2) extracting the DN values for the individual pixels, and then averaging the DN values over all the pixels within the ROI. However, RGB DN values are generally not used to conduct phenological analysis due to both external and internal factors—scene illumination is affected by clouds, aerosols, solar azimuth and so on, and control of exposure and colour balance adjustment could bring uncontrollability in image processing. In contrast to RGB brightness levels, Gillespie et al. (1987) reported a series of RGB chromatic

coordinates by a nonlinear transformation of RGB DNs that could describe the actual three primary colours red, green and blue as perceived by human vison (Gillespie, Kahle & Walker 1987; Sonnentag et al. 2012). To better track seasonal phenology variability, the respective chromatic coordinates of RGB DN values (RCC, GCC, BCC) are widely used (Brown et al. 2016; Klosterman et al. 2014; Liu et al. 2017; Migliavacca, Galvagno & Cremonese 2011; O'Connell & Alber 2016), with the nonlinear transformation shown in Eq. 1.

$$r_{cc} = \frac{R}{(R+G+B)}; \quad g_{cc} = \frac{G}{(R+G+B)}; \quad b_{cc} = \frac{B}{(R+G+B)} \qquad \text{Eq. (1)}$$

Other colour indices have since been construed by nonlinear transformations of RGB DN values, including the VARI (Visible Atmospherically Resistant Index) (Sakamoto et al. 2012), grR (green-red ratio) and rbR (red-blue ratio) (Sonnentag et al. 2011). A widely used method to describe variations in the greenness of vegetation is the excess green (ExG) (Woebbecke et al. 1995), given in Eq. (2).

$$2G - (R+B) \qquad \text{Eq. (2)}$$

Other external factors, like bad weather conditions, dirty lenses and low illumination, can also affect data quality. Therefore, data derived from phenocam images need robust filtering methods to reduce the noise in the time series of the colour indices (Julitta et al. 2014; Migliavacca, Galvagno & Cremonese 2011; Papale et al. 2006; Sonnentag et al. 2011). After filtering, data fitting is conducted to reduce the influence of single observations and better capture the seasonal behaviour (Filippa et al. 2016). Most consumer-grade digital cameras record common JPEG image format. This can reduce file size (allowing for more images to be captured) but also reduces image quality and accuracy. However, Sonnentag et al. (2012) showed that choice of camera and image file formats were of secondary importance for phenological research when they compared 11 digital repeat cameras at Harvard Forest. Fig. 1.3 c shows the various imaging sensors' spectral responses. Typical camera sensors record overlapping bands of RGB wavelengths, with the near-infrared (NIR) and part of the red region beyond about 650 nm often omitted in most economical cameras (dotted line in Fig. 1.3 c). The MODIS sensors have no band overlap and higher sensitivity to specific wavelengths compared to the cameras.

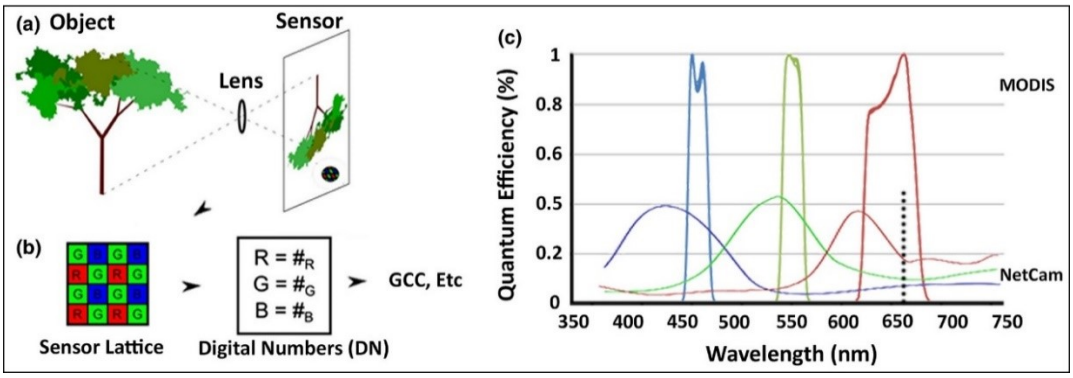

Figure 1.3 How camera sensors work (a and b) and typical spectral response for various imaging sensors (c). Source: Brown et al. (2016).

1.2.2 Phenology research using phenocams

To reduce uncertainties about the role of terrestrial ecosystems in global climate change studies and achieve a better understanding of the temporal and spatial variations of the ecological environment, large-scale phenocam networks have been developed and widely adopted for monitoring ecosystem dynamics over time (Richardson et al. 2018) - for example, the PhenoCam network (phenocam.sr.unh.edu) (Richardson et al. 2007b) and the Phenological Eyes Network (PEN; pen.agbi.tsukuba.ac.jp) (Nasahara & Nagai 2015). The U.S. National Ecological Observatory Network (NEON) and the European Union's Integrated Carbon Observation System (ICOS) have also established phenocam networks. However, crucial issues related to data standardisation, open-access data and expanding phenocam networks are important for the development of phenocam technology, and coverage in under-represented ecosystems is a priority (Richardson et al. 2018).

In recent decades, it has been demonstrated that phenocams can effectively be used to describe vegetation phenological dynamics in deciduous broadleaf forest (Ahrends et al. 2009; Hufkens et al. 2012), evergreen needleleaf forest (Liu et al. 2020), agricultural (Meyer & Neto, 2008; Pérez et al. 2000) and grassland (Browning et al. 2017; Vrieling et al. 2018; Watson et al. 2019). In terms of grassland and rangeland ecological research, heterogeneity is a critical driver and can be used to directly quantify management success across landscapes (McGranahan et al. 2018). Spatial heterogeneity is a concept generally ascribed to a landscape and, sometimes, to a population. It defines the distribution of various

concentrations of each species within a region. Heterogeneous disturbance patterns play a fundamental role in pasture conservation and management by creating patchy vegetation, broadening niche availability and increasing compositional dissimilarity (Limb et al. 2018; McGranahan et al. 2018; Wubs & Bezemer 2018). However, it increases the difficulty of quantitative analysis of grassland phenology, as one phenocam image usually contains several species or patchy vegetation. To reduce the influence of spatial heterogeneity on the phenological study of pasture and obtain more information from limited images, an innovative and robust processing method for phenocam images is necessary.

A single ROI is chosen to analyse and track vegetation phenology in most studies. That ROI is a representation of the mean behaviour of the entire ecosystem (Elmore et al. 2012; Hufkens et al. 2012; Klosterman et al. 2014; Migliavacca, Galvagno & Cremonese 2011). To better understand phenological variations in regions with relatively high heterogeneity, use of more than one ROI is necessary to evaluate phenological differences between plants (Ahrends et al. 2008; Alberton et al. 2014; Henneken et al. 2013).

Phenocams are ideal tools for recording plant phenological variations, animal migrations, and biotic and abiotic disturbance events (Richardson et al. 2007b). Use of phenocam images is promising for phenological studies in various ecosystems, including forests (Archetti et al. 2013; Baumann et al. 2017; Brown et al. 2017; Hufkens, Friedl, Sonnentag et al. 2012; Keenan et al. 2014; Richardson et al. 2012; Richardson, Hollinger et al. 2009; Richardson et al. 2007a; Toomey et al. 2015) and arid grasslands (Kurc & Benton 2010). In agricultural areas, several researchers have highlighted the potential to implement robotic weed control systems based on digital repeat photography with a high level of automation (Slaughter, Giles & Downey 2008). In recent studies, RGB images have been used to derive important information on snowmelt processes (Hinkler et al. 2002; Parajka et al. 2012).

Recent studies have demonstrated that phenocams have great potential to investigate relationships between phenological variations and ecosystem processes (Elmore et al. 2012; Hufkens, Friedl, Keenan et al. 2012; Toomey et al. 2015) and assist in developing new phenology models (Hufkens et al. 2016; Melaas, Friedl & Richardson 2016). Colour indices derived from phenocam images are well

correlated with vegetation indices typically used to detect land-surface phenology via satellites, suggesting that digital repeat photography can provide high-quality ground measurement data for the verification of satellite phenology products (Hufkens, Friedl, Sonnentag et al. 2012; Klosterman et al. 2014; Sakamoto et al. 2012; Shuai et al. 2013a). Phenocam data are usually combined with other ecological observation data, such as meteorology and surface-atmosphere fluxes, to characterise the responses of vegetation productivity to phenological variations (Toomey et al. 2015; Wingate et al. 2015) and thus depict the relationships between seasonal plant dynamics and ecosystem carbon budgets (Hufkens, Friedl, Keenan et al. 2012). Crimmins and Crimmins (2008) report that repeat digital photography provides a reliable, consistent observation of phenophases and changes in the fractional cover of green vegetation in annual or perennial plants.

For the grassland ecosystem, phenocam has been used to analyse the role of plant species composition on phenology in complex subalpine and alpine grasslands (Toomey et al. 2015). Through combined phenocam technology with eddy covariance data at a subalpine grassland, digital camera imagery was demonstrated to have the potential for the development and parameterisation of phenological and radiation use efficiency (RUE) models (Migliavacca, Galvagno & Cremonese 2011). Using the phenocam imagery obtained from the PhenoCam network and satellite data, Yan et al. (2017) evaluated the detection of vegetation phenology in savannas and grasslands. Their results showed that the PhenoCam Normalized Difference Vegetation Index (NDVI) was strongly correlated with the NDVI time series observed from satellites for two grassland ecosystems (Liu et al. 2017).

1.2.3 Phenocams in Australia

As previously stated, phenocams have the potential to greatly improve the current understanding of ecosystem processes. Compared to the promising applications of phenocam technology in North America, Europe and Asia, research progress was slow in Australia, a continent characterised by various ecosystem types with distinct differences in phenological characteristics compared to the temperate and boreal deciduous ecosystems of the northern hemisphere (Chambers et al. 2013).

In Australia, the Australian Phenocam Network (APN) (https://phenocam.org.au/) was established to facilitate the sharing of phenocam data and research using this

novel technology. The APN is a collaboration that archives and distributes digital repeat images collected by phenocams of a wide range of Australian ecosystems. Two Australian National Collaborative Research Infrastructure Strategy (NCRIS) facilities, the Terrestrial Ecosystem Research Network (TERN) and Australian Plant Phenomics Facility (APPF), developed APN. Phenocams are a vital tool for establishing continental-scale ecosystem observation in TERN and can also assist APPF to achieve the goal of developing new and improved agricultural practices.

Phenocam data collected at regional and landscape scales can be used in various ways. In TERN SuperSites (https://supersites.tern.org.au/), digital repeat photography provides a record of vegetation condition at a fine temporal resolution and aids ecosystem carbon and water research combined with TERN OzFlux eddy covariance towers. In addition, phenocam data is used to calibrate and validate observations from satellite platforms at TERN's AusCover facility to effectively conduct upscale research from ground-based sites to the continental scale. Researchers are trying to expand APN to a collaborative network of volunteer sites, at which image data can be downloaded free of charge through an open license, the SuperSites BioImage Data Portal. Fig. 1.4 shows understory phenocams at the Litchfield Savanna SuperSite and photos before and after a fire. Expansion of the current spatial distribution of phenocams in Australia will contribute to enhancing our understanding of the diversity of phenological variations in Australia ecosystems. Further, combined with satellite techniques, phenocams can provide a novel insight for interpreting the function of Australia's ecosystem within our Earth system (Moore et al. 2016).

Figure 1.4 Phenocams at Litchfield Savanna SuperSite (left) and before and after fire photos from July 2013 (middle and right). Source: https://phenocam.org.au/.

1.3 Remote sensing of grasslands and pastures

1.3.1 Remote sensing of grassland

Grasslands are regions dominated by grass species and contain other non-woody plants. They occur naturally in many biomes and are also included in other areas by livestock grazing. As an important terrestrial ecosystem, grasslands play an important role in regulating global carbon cycle and climate (Zhang et al. 2018). Grasslands span much of Earth's latitudes, elevations and climate zones, and are dominated by a single plant family (Poaceae) (Borer et al. 2017). In addition, the grassland biome is highly sensitive to climatic change and human activity (primarily agriculture) (Axelrod 1985; Ellis & Ramankutty 2008; Holling 1992). Various research designs for investigating grassland ecosystems and the environmental conditions of surrounding areas have been reported in recent years (Aldous et al. 2011; Piao et al. 2011; Zhou et al. 2015).

In Australia, temperate grasslands represent areas of species composition, diverse land uses and ecological conditions. Moreover, they historically and currently coexist with pastoral agriculture and urbanisation (McDougall et al. 2005; Ross 1999). The perennial grasses can be classified as C_3 and C_4 plants that use C_3 or C_4 photosynthetic pathway, and all species have the more primitive C_3 pathway. C_3 species are adapted to cooler climates and C_4 species have greater advantages in warmer, dryer conditions (Baldocchi 2011). The responses shown by C_3 and C_4 grasses' phenology to future climate variations, such as increased CO_2, higher temperature and modified rainfall regimes, are important for researching variations in ecological condition and agricultural productivity (Korner 2006; Morgan et al. 2011).

Using satellite-based remote sensing, vegetation characteristics can be consistently assessed at a landscape scale (Huete 2012). Several studies relating to grassland ecosystems have been reported using remote sensing technology. For example, estimating primary productivity (Gu, Wylie & Bliss 2013; Psomas et al. 2011), identifying land cover types and changes (Geerken, Zaitchik & Evans 2005; Henebry 1993; Wylie et al. 2002) and quantifying ecological threats (Zhou et al. 2017). Using remote sensing to evaluate grassland phenological variables that connect flowering and pollen release is an opportunity to provide more accurate information in the development of airborne pollen forecast (Khwarahm et al. 2017).

Vegetation Index (VI) is a spectral transformation of reflectance at two or more bands designed to enhance the contribution of vegetation properties and allow reliable spatial and temporal inter-comparisons of terrestrial photosynthetic activity and canopy structural variations. The NDVI and Enhanced Vegetation Index (EVI) are frequently used in ecological research (Huete et al. 2002; Huete et al. 2006; Tucker 1979). Given the low sensitivity of NDVI when detecting dense canopies, the EVI has a larger dynamic range and is also more resistant to atmospheric and soil background effects (Huete et al. 2002).

The Advanced Very High Resolution Radiometer (AVHRR) and MODIS, which have acquired observations since 1981 and 2000, respectively, have been successfully utilised to monitor diverse land-surface phenology of various ecosystems globally (de Beurs & Henebry 2004; Gray et al. 2014; Liang et al. 2014; Moulin et al. 1997; Myneni et al. 1997; Shuai et al. 2013b; Zhang 2015). To address the issue that land-surface phenology metrics derived from coarse spatial resolution satellite data (e.g., MODIS) and *in-situ* observations of phenology provide different information, increasing researches have focused on moderate spatial resolution imagery from Landsat for monitoring and mapping phenology (Fisher and Mustard, 2007, Baumann et al. 2017, Liu et al. 2017, Bolton et al. 2020). Besides these traditional satellite product datasets, recent data from the Sentinel-2 mission guarantees a more frequent and systematic coverage to sustain the mapping of land use and accurate estimation of biophysical parameters (Immitzer, Vuolo & Atzberger 2016). A new generation of Japanese geostationary meteorological satellite, Himawari 8/9, is supporting plentifully climatic application and monitors landscape dynamics associated with rainfall events, drying/droughts, fires and burnt area mapping. It provides a valuable opportunity for improving analysis of seasonal phenology, because of its 10-min temporal resolution. For vegetation phenological modelling, there are several satellites that can be used to conduct long-term studies with their time series capability (Table 1.2).

Table 1.2 Summary of common satellites used for remote sensing of vegetation phenology.

Satellite	Sensor	Operation	Spatial resolution	Frequency
Landsat	MSS	1973-1985	79 m	18 days
Landsat	TM	1984-present	30 m	16 days
Landsat	ETM+	1999-present	30 m	16 days
SPOT	Vegetation	1999-present	1 km	1-2 days
NOAA	AVHRR	1982-present	8 km	twice monthly
NOAA	AVHRR	1989-present	1 km	biweekly
Terra	MODIS	2000-present	250 m, 500 m, 1 km	1-2 days
Aqua	MODIS	2002-present	250 m, 500 m, 1 km	1-2 days
Envisat	MERIS	2002-present	300 m	1-3 days
Sentinel-2	MSI	2013-present	10 m, 20 m, 60 m	5 days
Himawari-8	AHI	2015-present	500 m, 1 km, 2 km	10 minutes

1.3.2 Pasture in Australia

'Pasture' means an enclosed tract of farmland grazed by domestic stock. The vegetation of pasture consists mainly of legumes and other forbs (non-grass herbaceous plants) (Hughes 1958). Pasture in a wider sense includes rangelands, other unenclosed pastoral systems and land cover types used by wild animals for browsing. In Australia, pasture can be divided into 'native pasture' and 'exotic pasture'. Native pasture refers to natural ecosystems dominated by naturally occurring grasses and other herbaceous species and grazing by livestock or wildlife, whereas exotic pasture means non-native pasture consisting of exotic grasses and other introduced pasture species (Watson 2016).

Pastures have a number of different values in Australian ecological and sociometric aspects, and their importance will vary depending on the goals of the manager. For example, (1) habitat for endangered animals, (2) adapted to the diverse Australian climate, (3) carry stock but require fewer inputs, (4) provide shelter for livestock, or (5) provide drought feed (source: Agriculture in Department of Primary Industries, https://www.dpi.nsw.gov.au/agriculture/pastures-and-rangelands/native-pastures). Currently, the landscape in Australian temperate areas is a mosaic of exotic and native pastures.

To meet the requirement of graziery during British colonisation, most parts of the Australian south-eastern temperate grasslands were stocked with sheep by the mid-1830s (Soeterboek 2011). Shortly thereafter, a large number of exotic species

became common, either through introductions of exotic species to improve pasture productivity or involuntary release (Watson 2016). Currently, exotic pastures are difficult to remove from the landscape for conservation purposes (Zerger et al. 2011) and are still common across Australian graziery. However, native pastures play an increasingly important role in sustainable land management practices (Wong & Dorrough 2015).

Presently, remote sensing technology is mainly used to investigate and estimate pasture growth rate (PGR) across Australian pasture ecosystems. Growth rate and biomass of pastures are reflected by vegetation indices such as the NDVI and Leaf Area Index (LAI). Studies performed in Western Australia (WA) have demonstrated that spatial variations of the NDVI within a paddock are robustly related to the spatial distribution of pasture biomass (Edirisinghe et al. 2002; Edirisinghe et al. 2000; Hill et al. 1998). Hill et al. (2004) used a time series of NDVI derived from the AVHRR combined with coincident climate data in a light use efficiency (LUE) model to generate PGR maps across WA, and the results showed that this approach could readily be applied to improve the basis for feed management in WA (Hill et al. 2004). A feasibility research for measuring Pasture Growth Rate and Feed-on-Offer with satellite imagery in the dairy region of south-west WA has been established with the support and funding by the Commonwealth Scientific and Industrial Research Organisation (CSIRO), WA Department of Agriculture, Landgate and Western Dairy. The focus of this project is to test the effectiveness of the remotely sensed pasture information and commence delivering it directly to end-users (http://www.pasturesfromspace.csiro.au/index.asp).

1.3.3 Mapping grassland and land cover use

Currently available global land cover maps, such as MODIS Land Cover Type 1 (MCD12Q1) - International Geosphere-Biosphere Programme (IGBP) land cover classification data, can be effectively used for monitoring land cover dynamics (Friedl et al. 2002; Friedl et al. 2010; Sidhu, Pebesma & Wang 2017; Yang et al. 2017; Zhang et al. 2017). However, according to the IGBP classification, the Sydney region presently includes no grass vegetation type. This abnormal result indicates that a land cover product with a finer scale is necessary for ecological processing research across Australia. In contrast, national- and regional-scale land cover maps have a higher spatial resolution but fail to resolve grass functional types

and do not have information to distinguish C_3 and C_4 grass species, native or exotic types of grass, or understory grass cover in forests. Given the complexity of grassland dynamics, there is an urgent need to obtain a stronger understanding of grassland compositional variation to provide context to grassland phenology information. Yu et al. (2018) reported that grassland is one of the most common land cover types and also one of the most difficult to classify. They analysed seven maps produced with different approaches but using the same classification system and failed to correctly classify the grasslands (Yu et al. 2018).

Besides global-scale land cover maps, regional-scale datasets have also been used to distinguish and map vegetation spatial distribution. For instance, using the Centre for Ecology and Hydrology (CEH) Land Cover Map 2007 (LCM 2007), a 25 m resolution raster map of Great Britain, Mclnnes et al. (2017) created a grass map and coupled it with health data, such as respiratory hospital admissions, to fill a need for detailed vegetation mapping of allergenic plant species across the UK (McInnes et al. 2017).

Geoscience Australia and the Australian Bureau of Agricultural and Resource Economics and Sciences (ABARES) has developed a Dynamic Land Cover Dataset (DLCD) (Fig. 1.5) for Australia based on analysing a EVI composite collected by MODIS for the period 2000–2008, aiming to provide nationally consistent land cover information to governments and the general public (Tan et al. 2013). It can be used to assess the land cover dynamics of rangelands, woodlands, forests and cropping systems. The Australian Collaborative Land Use and Management Program (ACLUMP) partners have also developed a series of land use maps to manage issues affecting soils, water and vegetation at the catchment scale (*Guidelines for land use mapping in Australia: principles, procedures and definitions - A technical handbook supporting the Australian Collaborative Land Use and Management Program* 2011). Three kinds of maps were developed from this program: (1) the catchment-scale land use maps with optional scales, which vary according to the intensity of land use activities; (2) the most recent catchment-scale land use map created by remapping some jurisdictions based on first type maps and completing the continental coverage; and (3) the national-scale land use map (1:2500000). These maps are of relatively low cost and provide an opportunity for time series mapping.

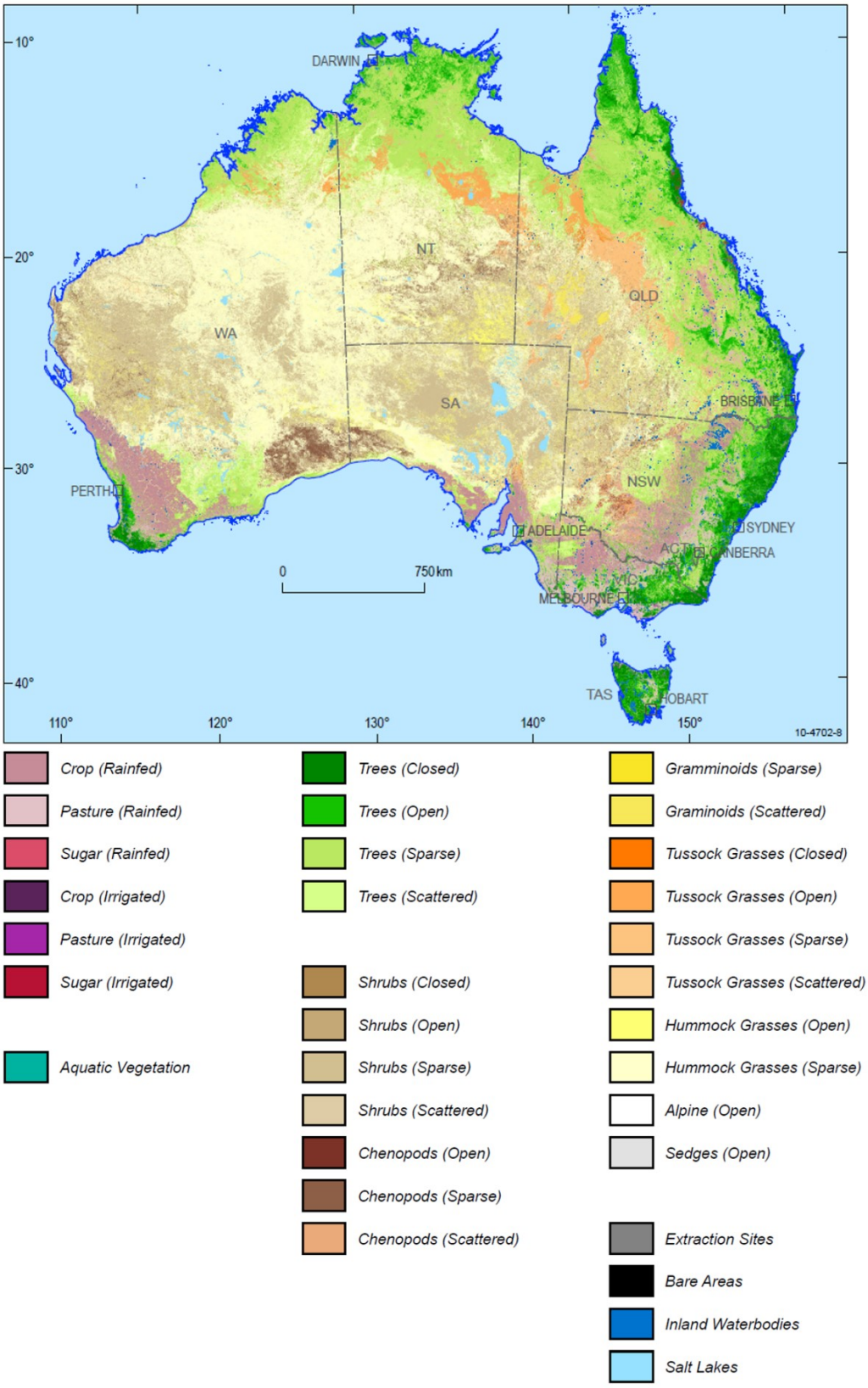

Figure 1.5 Map compiled from the National Dynamic Land Cover Dataset from 2000–2008. Source: http://www.ga.gov.au/scientific-topics/earth-obs/accessing-satellite-imagery/landcover.

1.4 Grassland phenology

1.4.1 Grassland phenology in Australia

Phenology is the study of the seasonal progression of periodic biological occurrences from leaf emergence and flowering to animal migrations and breeding patterns, all of which vary between and within species and are influenced to a certain degree by the climate (Lanza 1976; Moore et al. 2017; Richardson et al. 2013). A better understanding of the phenology of vegetation will contribute to understanding variations in terrestrial ecosystems under a warming climate. Vegetation phenology is directly related to productivity, disturbances and vegetation type, and is thus an important input parameter for climate models (Watson 2016). An earlier occurrence of spring phenology has been observed in the northern hemisphere, which was related to warmer temperatures, either using in-situ measurements (Dai, Wang & Ge 2014; Ma & Zhou 2012; Menzel & Fabian 1999; Menzel et al. 2006) or satellite observations (A. et al. 2009; Cong et al. 2013; Myneni et al. 1997).

To quantify phenological variations, phenological metrics, such as start and end of growing season, peak period of the growing and length of growing season, are used for detecting phenological spatial-temporal patterns across various ecosystems. Many methods have been developed to monitor vegetation phenology using satellite data, including the threshold-based average (Lloyd 1990; White, Thornton & Running 1997), curve fitting and derivative average (Kaduk & Heimann 1996), backward-looking moving average (Reed et al. 1994) and empirical equations (Moulin et al. 1997). However, given that ecosystems comprise multiple growth cycles, these methods have some limitations on their application on a global scale. Zhang et al. (2003) provided a new methodology based on a series of piecewise logistic functions to simulate vegetation growth that was successful in monitoring vegetation phenology. Fig. 16 shows how to define spring phenology using this approach. This method is currently being used to conduct the global phenological project (Collection 5) based on EVI time series derived from MODIS (Frenguelli et al. 2010; Ghitarrini et al. 2017; Zhang, Friedl & Schaaf 2006). For grassland ecosystems, there are some uncertainties in logistic curve fitting when determining GUD from VI time series, due to the fact that the VI profiles from spring to summer do not necessarily follow an ideal sigmoid curve (Cao et al. 2015). This limitation

of Collection 5 might could be solved by upgraded version. Recently, the Collection 6 MODIS Land Cover Dynamics Product was created to map global land surface phenological metrics at 500 resolution using the time series of the 2-band EVI calculated from MODIS nadir BRDF adjusted surface reflectance (NBAR-EVI2). Comparing with Collection 5, Collection 6 product was designed to better capture phenological metrics in ecosystem with multiple vegetation cycles per year, and consequently to increase the reliability of retrieved phenological metrics in arid, semi-arid, and tropical ecosystems (Friedl et al., 2019).

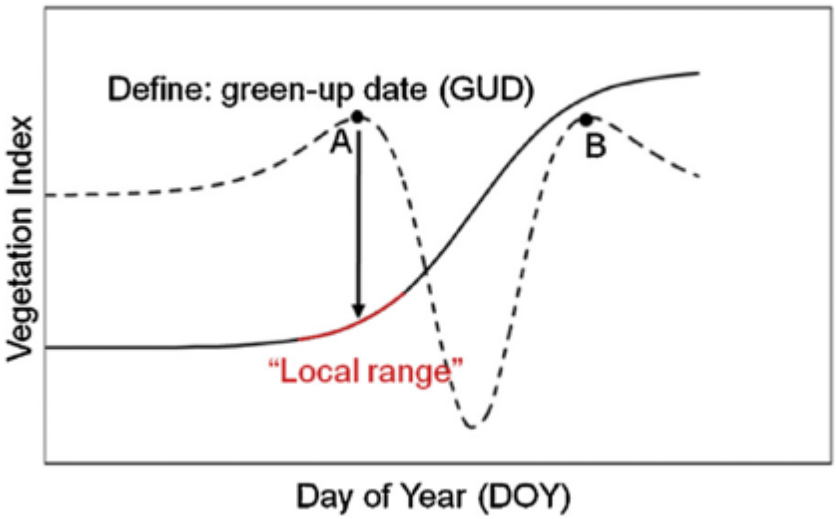

Figure 1.6 A schematic diagram of how to determine the vegetation green-up date (GUD) using the logistic fitting method (Zhang et al. 2003). The fitted logistic curve is shown as a solid line, and the dashed line indicates the rate of change in curvature of the fitted logistic curve. GUD is defined as the first local maximum of the dashed curve, and point B (the second local maximum) is identified as the onset of plant maturity. The 'Local range' means the range where the vegetation index begins to increase rapidly in the time series data. (Cao et al., 2015)

A fundamental part of grass pollen aerobiological investigations is a precise understanding of the spatial and temporal patterns of pollen phenophase, such as flowering (Tng et al. 2010). There is an increasing importance of this knowledge, especially given that climate change has been demonstrated to have significant implications for plant phenology. As touched on in the above review, most studies focus on the development of strategies for long-term phenological monitoring of tree species (Ahrends et al. 2008; Busetto et al. 2010; Fontana et al. 2008; Migliavacca et al. 2008; Moser et al. 2010), while only a few studies on grassland

phenology have been reported (Cernusca et al. 2008; Fonti et al. 2010; Jonas et al. 2008). This is primarily due to the difficulty in developing a protocol for field observation of grassland phenology focused on the whole canopy, instead of on a single species (Migliavacca, Galvagno & Cremonese 2011). In Australia, phenology studies have been limited because of the high climatic variability that produces subtle phenology changes, and there is also a lack of the long-term datasets necessary for trend analysis of vegetation phenology (Gallagher, Hughes & Leishman 2009).

Nevertheless, grassland phenological studies in Australia have a long history. For example, Chan (1980) mapped natural grasslands in the Canberra region using infrared colour and natural colour photography and also listed their flowering times, with the peak flowering occurring in October to November (Chan 1980). Most of these studies have focused on vegetative phenology responses to climate factors. For example, Biddiscombe and Hutchings (1954) investigated species' responses to changes in seasonal climatic conditions and found that moisture and temperature are the principal factors controlling seasonal vegetation dynamics. Recently, a two-year study in southern Tasmania demonstrated that the mean time of commencement of flowering in native grasslands was sensitive to warming temperature but not to elevated CO_2 (Hovenden et al. 2008).

1.4.2 Grassland phenology and environmental drivers

The major climate zones in Australia range from equatorial and tropical in the north to subtropical, desert, and temperate in the south (Stern & Dehani 2013). Long-term mean annual rainfall and temperature distinctly vary across the Australian continent due to this wide-ranging climatic variability. This relative complex climatic conditions causes an irregular phenological pattern in the Southern Hemisphere, especially in Australian grasslands (Ganguly et al. 2010). Same as the temperate deciduous and boreal ecosystems in the Northern Hemisphere, temperature is an important phenological driver in Australian ecosystems (Chambers, Altwegg & Barbraud 2013). However, because deserts and grasslands make up 70% of Australian land, water plays a stronger role in affecting Australia's ecosystem dynamics (Andela et al. 2013; Donohue, McVicar & Roderick 2009; Ellis & Hatton 2008; Specht & Brouwer 1975).

A majority of the research on the relationship between vegetation phenology and climate factors has been conducted in the Northern Hemisphere moist temperate climate zones, and most has focused on deciduous forest or cropland (Ahrends et al. 2008; Chen et al. 2016; Huete ; Moulin et al. 1997; Reed et al. 1994; Richardson et al. 2007a; Wang et al. 2017). However, there are vast areas of the Earth covered by temperate and tropical savannas, grasslands and other dryland habitats in which precipitation plays a much more crucial role in controlling ecological variations (Chambers, Altwegg & Barbraud 2013; Primack & Miller-Rushing 2011). Grassland phenology is evidently sensitive to environmental conditions. For example, frosts can induce widespread senescence in temperate grassland systems, and rainfall following a drought will promote the growth season of grasses and forbs (Watson 2016).

C_3 and C_4 grass species composition, with different phenological characteristics, influence airborne pollen transportation and thus seasonal pollen counts variations. The multiple secondary peaks in grass pollen observed during summer in Sydney are considered to be due to the flowering of C_4 species (Medek et al. 2016). Besides the difference in phenology for C_3 and C_4 grass species, the phenological drivers are also different. C_3 grass species are more productive in cooler regions, whereas C_4 grass species have a greater advantage in warmer regions, due to C_4 grass species generally have higher temperature optima for growth (Baldocchi 2011, Berry & Bjorkman 1980, Watson 2016). Additionally, lower available moisture is expected to favor C_4 grass species because C_4 species generally have higher water use efficiency as compared to C_3 species (Hattersley et al., 1983; Morgan et al., 2011).

As another vegetation phenophase, the seasonal flowering variations are also influenced by diverse meteorological factors. Climate change, warming temperatures and increased CO_2 levels have been demonstrated to be associated with variations in flowering times (Fitter & Fitter 2002). Increasing CO_2 levels have also been reported to cause increasing plant biomass and consequently raise the pollen production of ragweed (Rogers et al. 2006). Temperature and precipitation have dominant roles in controlling flowering conditions of several tree species. In a study comparing the course of flowering and occurrence of pollen grains, Kasprzyk (2003) reported that no rainfall and high temperature caused an intense flowering of

birches over a large area. For other species, flowering was mainly in coincidence with the relatively low temperatures of late winter and early spring (Latorre 1997). A long-term trend analysis of daily weather conditions with daily pollen concentrations showed that an earlier onset of the flowering period for grasses was associated with the rates of change in several meteorological factors such as temperature, radiation, humidity and rainfall (Bruffaerts et al. 2018).

1.4.3 Grassland flowering and airborne pollen

The seasonal progression of periodic biological occurrences in plants, like budburst and senescence, is generally referred to as vegetation phenology. Flowering, pollination and pollen release are important phenology stages of the grass life cycle and grass pollen is a major trigger for aeroallergens. Most phenology studies in Australia have investigated impacts on flowering time. In south-east Australia, the flowering time of native plants shifts earlier or later depending on different species (Keatley & Hudson 2010). Hovenden (2008) showed that the flowering of grassland species responded to warming in Tasmania (higher temperatures resulted an average earlier flowering time). Flowering had the same response to temperature changes in the south-eastern alpine regions (Hovenden et al. 2008).

The presence of pollen in the atmosphere follows a clear seasonal pattern in response to the seasonal flowering of the plant sources (Tormo et al. 2011). Linking grassland phenological information with airborne pollen records has shown that phenology (i.e., flowering season) almost coincides with the occurrence of maximum pollen concentrations (Romero-Morte et al. 2018). Such studies have been performed in Europe; for example, Leon-Ruiz et al. (2011) found that the flowering phenology of most grass species in Spain showed shorter durations in years with warmer springs and longer durations in colder years. The association between grassland flowering and airborne pollen counts for some pollen types has been demonstrated, though there are species, such as Cupressaceae and Poaceae, that do not show the coincidence between flowering and pollen peaks, with up to one week difference in phase (Tormo et al. 2011). Fig. 1.7 shows the pollen concentration of Poaceae species and flowering phenology at Badajoz, Spain, for 2007, 2008 and 2009 (Tormo et al. 2011). Combining MODIS EVI products with grass pollen concentrations, Devadas et al. (2018) found that peak pollen activity lagged behind peak grass cover greenness on average by 2–3 weeks and 4–7 weeks

in temperate sites in France and Australia, respectively. Further, numerous studies have shown that not all the pollen grain records can be explained by flowering of local vegetation; for example, studies for *Betula* pollen in Finland (Ranta et al. 2006), Denmark (Skjoth et al. 2007) and Spain (Jato, Rodriguez-Rajo & Aira 2007), as well as other pollen types in Germany (Estrella et al. 2006).

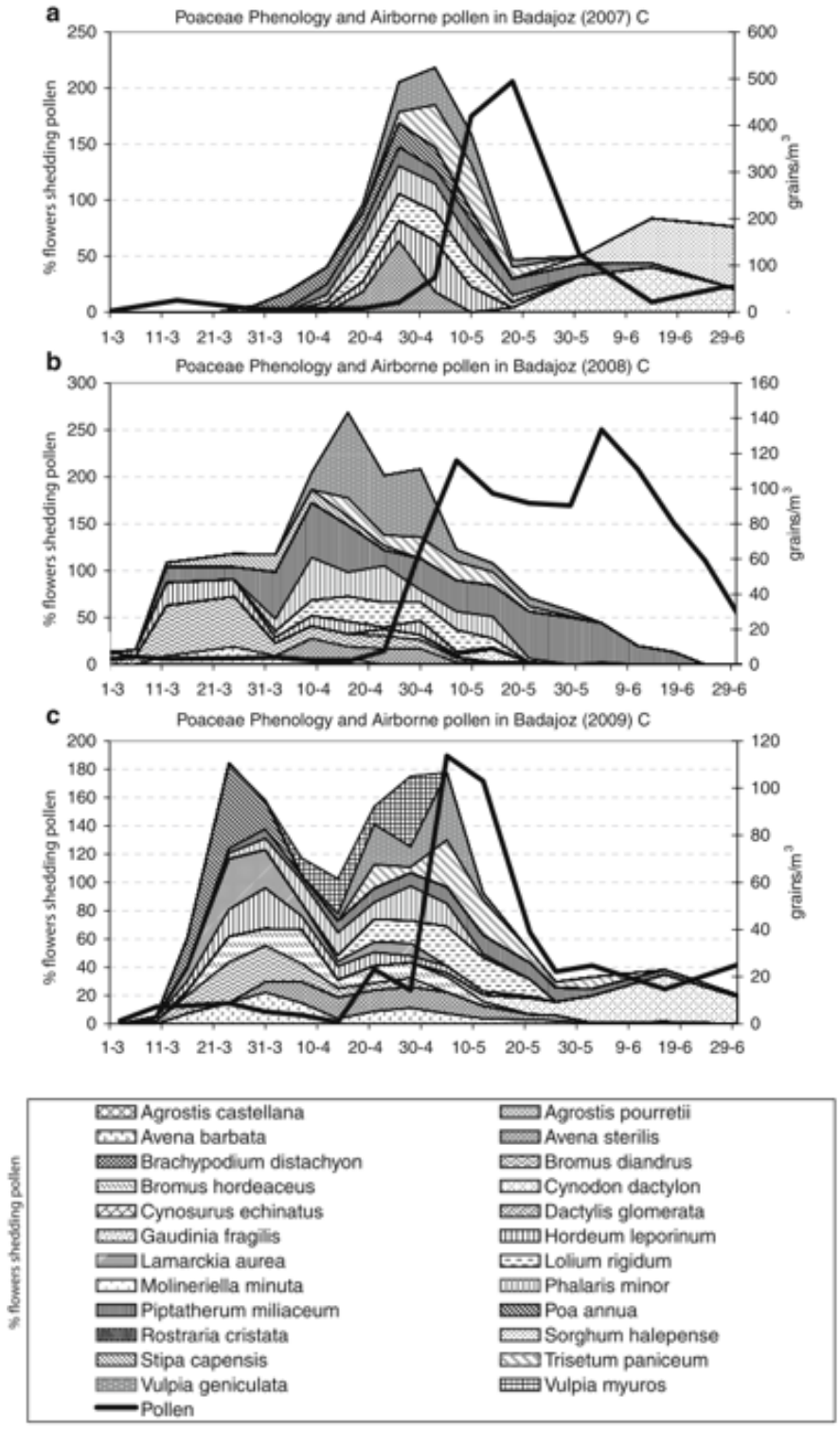

Figure 1.7 Flowering phenology and airborne pollen counts of Poaceae species in Badajoz, Spain, for (a) 2007, (b) 2008 and (c) 2009. Source: Tormo et al. (2011).

1.5 Thesis aim and structure

Grass pollen is the major outdoor aeroallergen source across Australia. Although the prevalence and morbidity impact of outdoor aeroallergen (e.g. hay fever and asthma) in Australia are among the highest in the world, the aerobiology of grass pollen in Australian cities are not well understood. This knowledge gap arises in part because of the lack of grass ecological information with finer temporal and spatial resolutions on complex land cover conditions and very little is known of the spatial distribution of grass pollen sources over time. Yet, such information is vital to understand the ecological drivers of pollen aerobiology and to aid predict pollen future trends in Australia. In other words, fundamental aspects of an accurate grass pollen forecast system are the improved understanding of the spatial and temporal patterns of the grass phenology and their relationships with grass pollen seasons, as well as a land cover map with fine spatial resolutions, which could be used to identify and characterize sources of grass pollen surrounding pollen samplers.

The primary aim of this thesis is to address these critical knowledge gaps in our understanding of the ecological driver of grass pollen aerobiology integrating near-surface and satellite-based satellite imagery with grass pollen concentration data at subtropical to temperate grassland sites in Australia.

Chapter 2 characterizes diurnal patterns of phenocam observed grass greenness (i.e. GCC) as influenced by solar zenith angle-related and weather-related changes in scene illumination in phenocam images archives. And thus, a diurnal-to-daily GCC compositing methodology is proposed to mitigate the influence of changes in solar radiation intensity on phenocam-derived GCC in pastures and grasslands. Phenocam observations can offer grass greenness dynamics with sub-daily frequency and are reliable ground surface validation data for satellite observations. Therefore, the study in this chapter is a foundation for further utilization of phenocam in next chapters.

Chapter 3 examines the ability of multi-resolution satellites (i.e. Sentinel-2, 10 m; MODIS, 250 m; and Himawari-8 AHI, 1000 m) to accurately obtain grass greenness information from heterogeneous landscapes by comparing with phenocam observations. The interrelationships between *in-situ* grass pollen

concentrations and grass greenness as measured by phenocams and satellites were investigated to explore how do differences in spatial and temporal resolution of satellites influence the grass greenness – pollen relationships across sites with different types of land cover. The reason why Landsat data was not applied in this chapter is that though Landsat data provides great temporal resolution for comparison with phenocam observation, I would have had to use 90 m (3x3 pixels) scale of analyses, which is coarser than Sentinel-2 data, instead of 30 m (single pixel). Also, even I had have to use single Landsat pixel, it would most likely not be centered in field of view of phenocam and consequently be hard to co-locate with the phenocam footprint.

Chapter 4 details the differences in filtering grass information from complex landscapes between developed land cover/use maps and a grass map with 10 m resolution, generated by neural net from the Sentinel-2 image. Using this finer resolution grass map, variations in grass phenology and relationships between grass pollen concentrations across different distances and orientations are investigated. Finally, grass pollen sources are mapped with a pixel-wise scale (10 m) using the Sentinel-2 grass map to inform the seasonal variations in spatial distributions of pollen sources.

Chapter 5 provides a summary of the findings of the overall thesis and concludes with a discussion of how multiple remote sensing tools offer an avenue to our understanding of grass pollen aerobiology and contribute to better inform the aerobiology of grass pollen in Australia.

1.5 References

Ahrends, H.E., Brugger, R., Stockli, R., Schenk, J., Michna, P., Jeanneret, F., Wanner, H. & Eugster, W. 2008, 'Quantitative phenological observations of a mixed beech forest in northern Switzerland with digital photography', *Journal of Geophysical Research-Biogeosciences*, vol. 113, no. G4.

Alberton, B., Almeida, J., Helm, R., Torres, R.D., Menzel, A. & Morellato, L.P.C. 2014, 'Using phenological cameras to track the green up in a cerrado savanna and its on-the-ground validation', *Ecological Informatics*, vol. 19, pp. 62-70.

Ahrends, H.E., Etzold, S., Kutsch, W.L., Stoeckli, R., Bruegger, R., Jeanneret, F., Wanner, H., Buchmann, N., Eugster, W., 2009, 'Tree phenology and carbon dioxide fluxes: Use of digital photography for process-based interpretation at the ecosystem scale', *Clim. Res*, vol. 39, pp. 261–274.

Aldous, A., Fitzsimons, J., Richter, B. & Bach, L. 2011, 'Droughts, floods and freshwater ecosystems: evaluating climate change impacts and developing adaptation strategies', *Marine and Freshwater Research*, vol. 62, no. 3, pp. 223-31.

Andela, N., Liu, Y.Y., van Dijk, A., de Jeu, R.A.M. & McVicar, T.R. 2013, 'Global changes in dryland vegetation dynamics (1988-2008) assessed by satellite remote sensing: comparing a new passive microwave vegetation density record with reflective greenness data', *Biogeosciences*, vol. 10, no. 10, pp. 6657-76.

Archetti, M., Richardson, A.D., O'Keefe, J. & Delpierre, N. 2013, 'Predicting climate change impacts on the amount and duration of autumn colors in a New England forest', *PLoS One*, vol. 8, no. 3, p. e57373.

Asher, M.I., Montefort, S., Bjorksten, B. & Grp, I.P.T.S. 2007, 'Worldwide time trends in the prevalence of symptoms of asthma, allergic rhinoconjunctivitis, and eczema in childhood: ISAAC Phases One and Three repeat multicountry cross-sectional surveys (vol 368, pg 733, 2006)', *Lancet*, vol. 370, no. 9593.

Australian Bureau of Agricultural and Resource Economics and Sciences, 2011, Guidelines for land use mapping in Australia: principles, procedures and definitions: A technical handbook supporting the Australian Collaborative

Land Use and Management Program (4th Edition), Report, viewed 27 October 2021, https://www.nintione.com.au/?p=3210.

Axelrod, D.I. 1985, 'Rise of the grassland biome, central North-America', *Botanical Review*, vol. 51, no. 2, pp. 163-201.

Baldocchi, D. 2011, 'The grass response', *Nature*, vol. 476, no. 7359, pp. 160-1.

Bass, D., Baldo, B.A. & Pham, N.H. 1991, 'White cypress pine pollen - an important seasonal allergen source in rural Australia', *Medical Journal of Australia*, vol. 155, no. 8, pp. 572-.

Bass, D. & Morgan, G. 1997a, 'A three year (1993-1995) calendar of pollen and Alternaria mould in the atmosphere of south western Sydney', *Grana*, vol. 36, no. 5, pp. 293-300.

Bass, D. & Morgan, G. 1997b, 'A three year (1993–1995) calendar of pollen and Alternaria mould in the atmosphere of south western Sydney', *Grana*, vol. 36, no. 5, pp. 293-300.

Batson, M.G. 1998, 'Agrostis castellana (Poaceae), dominant Agrostis species, found in bent grass pastures in south-eastern Australia', *Australian Journal of Botany*, vol. 46, no. 5-6, pp. 697-705.

Baumann, M., Ozdogan, M., Richardson, A.D. & Radeloff, V.C. 2017, 'Phenology from Landsat when data is scarce: Using MODIS and Dynamic Time-Warping to combine multi-year Landsat imagery to derive annual phenology curves', *International Journal of Applied Earth Observation and Geoinformation*, vol. 54, pp. 72-83.

Berry, J., Bjrrkman, O. 1980, 'Photosynthetic response and adapta- tion to temperature in higher plants', *Ann Rev Plant Physiol*, vol. 31, pp. 491-543.

Beck, P.S.A., Atzberger, C., Hogda, K.A., Johansen, B. & Skidmore, A.K. 2006, 'Improved monitoring of vegetation dynamics at very high latitudes: A new method using MODIS NDVI', *Remote Sensing of Environment*, vol. 100, no. 3, pp. 321-34.

Beggs, P.J., Katelaris, C.H., Medek, D., Johnston, F.H., Burton, P.K., Campbell, B., Jaggard, A.K., Vicendese, D., Bowman, D., Godwin, I., Huete, A.R., Erbas, B., Green, B.J., Newnham, R.M., Newbigin, E., Haberle, S.G. & Davies, J.M. 2015a, 'Differences in grass pollen allergen exposure across Australia',

Australian and New Zealand Journal of Public Health, vol. 39, no. 1, pp. 51-55.

Beggs, P.J., Katelaris, C.H., Medek, D., Johnston, F.H., Burton, P.K., Campbell, B., Jaggard, A.K., Vicendese, D., Bowman, D.M., Godwin, I., Huete, A.R., Erbas, B., Green, B.J., Newnham, R.M., Newbigin, E., Haberle, S.G. & Davies, J.M. 2015b, 'Differences in grass pollen allergen exposure across Australia', *Aust N Z J Public Health*, vol. 39, no. 1, pp. 51-5.

Bellomo, R., Gigliotti, P., Treloar, A., Holmes, P., Suphioglu, C., Singh, M.B. & Knox, B. 1992, 'Consecutive thunderstorm associated epidemics of asthma in the city of melbourne - the possible role of rye grass-pollen ', *Medical Journal of Australia*, vol. 156, no. 12, pp. 834-7.

Bessho, K., Date, K., Hayashi, M., Ikeda, A., Imai, T., Inoue, H., Kumagai, Y., Miyakawa, T., Murata, H., Ohno, T., Okuyama, A., Oyama, R., Sasaki, Y., Shimazu, Y., Shimoji, K., Sumida, Y., Suzuki, M., Taniguchi, H., Tsuchiyama, H., Uesawa, D., Yokota, H. & Yoshida, R. 2016, 'An Introduction to Himawari-8/9-Japan's New-Generation Geostationary Meteorological Satellites', *Journal of the Meteorological Society of Japan*, vol. 94, no. 2, pp. 151-83.

Biddiscombe, E.F., E.G., C. & Hutchings, R.J. 1954, 'Autecology of some natural pasture species at Trangis, N.S.W.', *Australian Journal of Botany*, vol. 2, no. 1, pp. 69-98.

Borer, E.T., Grace, J.B., Harpole, W.S., MacDougall, A.S. & Seabloom, E.W. 2017, 'A decade of insights into grassland ecosystem responses to global environmental change', *Nature Ecology & Evolution*, vol. 1, no. 5.

Bostock, J. 1819, 'Case of periodic affection of the eyes and chest', *Medico-Chirurgical Transactions*, no. 10, p. 161.

Bousquet, J., Schunemann, H.J., Samolinski, B., Demoly, P. & Baena-Cagnani, C.E. 2012, 'Allergic Rhinitis and its Impact on Asthma (ARIA): Achievements in 10 years and future needs', *Journal of Allergy and Clinical Immunology*, vol. 130, no. 5, pp. 1049-62.

Bolton, D.K., Gray, J.M., Melaas, E.k, Moon, M., Eklundh, L., Friedl, M.A. 2020 ' Continental-scale land surface phenology from harmonized Landsat 8 and

Sentinel-2 imagery', *Remote Sensing of Environment*, vol. 240, 111685, https://doi.org/10.1016/j.rse.2020.111685.

Brown, L.A., Dash, J., Ogutu, B.O. & Richardson, A.D. 2017, 'On the relationship between continuous measures of canopy greenness derived using near-surface remote sensing and satellite-derived vegetation products', *Agricultural and Forest Meteorology*, vol. 247, pp. 280-92.

Brown, T.B., Hultine, K.R. & Steltzer, H. 2016, 'Using phenocams to monitor our changing Earth: toward a global phenocam network', *Frontiers in Ecology and the Environment*, vol. 14, no. 2, pp. 84-93.

Brown, T.B., Hultine, K.R., Steltzer, H., Denny, E.G., Denslow, M.W., Granados, J., Henderson, S., Moore, D., Nagai, S., SanClements, M., Sánchez-Azofeifa, A., Sonnentag, O., Tazik, D. & Richardson, A.D. 2016, 'Using phenocams to monitor our changing Earth: toward a global phenocam network', *Frontiers in Ecology and the Environment*, vol. 14, no. 2, pp. 84-93.

Bruffaerts, N., De Smedt, T., Delcloo, A., Simons, K., Hoebeke, L., Verstraeten, C., Van Nieuwenhuyse, A., Packeu, A. & Hendrickx, M. 2018, 'Comparative long-term trend analysis of daily weather conditions with daily pollen concentrations in Brussels, Belgium', *International Journal of Biometeorology*, vol. 62, no. 3, pp. 483-91.

Busetto, L., Colombo, R., Migliavacca, M., Cremonese, E., Meroni, M., Galvagno, M., Rossini, M., Siniscalco, C., Di Cella, U.M. & Pari, E. 2010, 'Remote sensing of larch phenological cycle and analysis of relationships with climate in the Alpine region', *Global Change Biology*, vol. 16, no. 9, pp. 2504-17.

Cao, R.Y., Chen, J., Shen, M.G. & Tang, Y.H. 2015, 'An improved logistic method for detecting spring vegetation phenology in grasslands from MODIS EVI time-series data', *Agricultural and Forest Meteorology*, vol. 200, pp. 9-20.

Cernusca, A., Bahn, M., Berninger, F., Tappeiner, U. & Wohlfahrt, G. 2008, 'Effects of Land-Use Changes on Sources, Sinks and Fluxes of Carbon in European Mountain Grasslands PREFACE', *Ecosystems*, vol. 11, no. 8, pp. 1335-7.

Chambers, L.E., Altwegg, R. & Barbraud, C. 2013, 'Phenological Changes in the Southern Hemisphere'.

Chambers, L.E., Altwegg, R., Barbraud, C., Barnard, P., Beaumont, L.J., Crawford, R.J.M., Durant, J.M., Hughes, L., Keatley, M.R., Low, M., Morellato, P.C., Poloczanska, E.S., Ruoppolo, V., Vanstreels, R.E.T., Woehler, E.J. & Wolfaardt, A.C. 2013, 'Phenological Changes in the Southern Hemisphere', *Plos One*, vol. 8, no. 10.

Chan, C.W. 1980, 'Natural grasslands in Canberra: their distribution, phenology and effects of mowing', Australian National University.

Chen, M., Melaas, E.K., Gray, J.M., Friedl, M.A. & Richardson, A.D. 2016, 'A new seasonal-deciduous spring phenology submodel in the Community Land Model 4.5: impacts on carbon and water cycling under future climate scenarios', *Glob Chang Biol*, vol. 22, no. 11, pp. 3675-88.

Cong, N., Wang, T., Nan, H.J., Ma, Y.C., Wang, X.H., Myneni, R.B. & Piao, S.L. 2013, 'Changes in satellite-derived spring vegetation green-up date and its linkage to climate in China from 1982 to 2010: a multimethod analysis', *Global Change Biology*, vol. 19, no. 3, pp. 881-91.

Cook, M., Douglass, J., Mallon, D., Mullins, R., Smith, J. & Wong, M. 2007, *The economic impact of allergic disease in Australia: not to be sneezed at*, Access Economics Pty Ltd for Australian Society of Clinical Immunology and Allergy (ASCIA).

Crimmins, M.A. & Crimmins, T.M. 2008, 'Monitoring plant phenology using digital repeat photography', *Environmental Management*, vol. 41, no. 6, pp. 949-58.

Dai, J., Wang, H. & Ge, Q. 2014, 'The spatial pattern of leaf phenology and its response to climate change in China', *International Journal of Biometeorology*, vol. 58, no. 4, pp. 521-8.

Darrow, L.A., Hess, J., Rogers, C.A., Tolbert, P.E., Klein, M. & Sarnat, S.E. 2012, 'Ambient pollen concentrations and emergency department visits for asthma and wheeze', *Journal of Allergy and Clinical Immunology*, vol. 130, no. 3, pp. 630-+.

Davies, J.M., Li, H., Green, M., Towers, M. & Upham, J.W. 2012, 'Subtropical grass pollen allergens are important for allergic respiratory diseases in subtropical regions', *Clinical and Translational Allergy*, vol. 2, no. 1.

de Beurs, K.M. & Henebry, G.M. 2004, 'Land surface phenology, climatic variation, and institutional change: Analyzing agricultural land cover change in Kazakhstan', *Remote Sensing of Environment*, vol. 89, no. 4, pp. 497-509.

Delegido, J., Verrelst, J., Alonso, L. & Moreno, J. 2011, 'Evaluation of Sentinel-2 Red-Edge Bands for Empirical Estimation of Green LAI and Chlorophyll Content', *Sensors*, vol. 11, no. 7, pp. 7063-81.

Devadas, R., Huete, A.R., Vicendese, D., Erbas, B., Beggs, P.J., Medek, D., Haberle, S.G., Newnham, R.M., Johnston, F.H., Jaggard, A.K., Campbell, B., Burton, P.K., Katelaris, C.H., Newbigin, E., Thibaudon, M. & Davies, J.M. 2018, 'Dynamic ecological observations from satellites inform aerobiology of allergenic grass pollen', *Science of the Total Environment*, vol. 633, pp. 441-51.

Donohue, R.J., McVicar, T.R. & Roderick, M.L. 2009, 'Climate-related trends in Australian vegetation cover as inferred from satellite observations, 1981-2006', *Global Change Biology*, vol. 15, no. 4, pp. 1025-39.

Drusch, M., Del Bello, U., Carlier, S., Colin, O., Fernandez, V., Gascon, F., Hoersch, B., Isola, C., Laberinti, P., Martimort, P., Meygret, A., Spoto, F., Sy, O., Marchese, F. & Bargellini, P. 2012, 'Sentinel-2: ESA's Optical High-Resolution Mission for GMES Operational Services', *Remote Sensing of Environment*, vol. 120, pp. 25-36.Edirisinghe, A., Donald, G.E., Hill, M.J. & Henry, D. 2002, 'Precision management of feed supply through timely delivery of biomass and growth rate estimates of Western Australian annual pastures', *Proceedings of the 29th International Symposium on Remote Sensing ofEnvironment*, Buenos Aires, Argentina.

Edirisinghe, A., Hill, M.J., Donald, G.E., Wheaton, G.A., Hyder, M. & Smith, R.C.G. 20000, 'Estimating feed-on-offer and pasture growth rate using remote sensing', paper presented to the *10th Australasian Remote Sensing and Photogrammetry Conference*, Adelaide, Australia.

Ellis, E.C., Ramankutty, N. 2008, 'Putting people in the map: anthropogenic biomes of the world (vol 6, pg 439, 2008)', *Frontiers in Ecology and the Environment*, vol. 6, no. 10, pp. 523-.

Ellis, T.W. & Hatton, T.J. 2008, 'Relating leaf area index of natural eucalypt vegetation to climate variables in southern Australia', *Agricultural Water Management*, vol. 95, no. 6, pp. 743-7.

Elmore, A.J., Guinn, S.M., Minsley, B.J. & Richardson, A.D. 2012, 'Landscape controls on the timing of spring, autumn, and growing season length in mid-Atlantic forests', *Global Change Biology*, vol. 18, no. 2, pp. 656-74.

Emberlin, J. 1994, ' The effects of patterns in climate and pollen abundance on allergy ', *Allergy*, vol. 49, no. 18, pp. 15-20.

Erbas, B., Chang, J.H., Dharmage, S., Ong, E.K., Hyndman, R., Newbigin, E. & Abramson, M. 2007, 'Do levels of airborne grass pollen influence asthma hospital admissions?', *Clinical and Experimental Allergy*, vol. 37, no. 11, pp. 1641-7.

Estrella, N., Menzel, A., Kramer, U. & Behrendt, H. 2006, 'Integration of flowering dates in phenology and pollen counts in aerobiology: analysis of their spatial and temporal coherence in Germany (1992-1999)', *International Journal of Biometeorology*, vol. 51, no. 1, pp. 49-59.

Filippa, G., Cremonese, E., Migliavacca, M., Galvagno, M., Forkel, M., Wingate, L., Tomelleri, E., Morra di Cella, U. & Richardson, A.D. 2016, 'Phenopix: A R package for image-based vegetation phenology', *Agricultural and Forest Meteorology*, vol. 220, pp. 141-50.

Fitter, A.H. & Fitter, R.S.R. 2002, 'Rapid changes in flowering time in British plants', *Science*, vol. 296, no. 5573, pp. 1689-91.

Fontana, F., Rixen, C., Jonas, T., Aberegg, G. & Wunderle, S. 2008, 'Alpine grassland phenology as seen in AVHRR, VEGETATION, and MODIS NDVI time series - a comparison with in situ measurements', *Sensors*, vol. 8, no. 4, pp. 2833-53.

Fonti, P., von Arx, G., Garcia-Gonzalez, I., Eilmann, B., Sass-Klaassen, U., Gartner, H. & Eckstein, D. 2010, 'Studying global change through investigation of the plastic responses of xylem anatomy in tree rings', *New Phytologist*, vol. 185, no. 1, pp. 42-53.

Fornaciari, M., Orlandi, F. & Romano, B. 2000, 'Phenological and aeropalynological survey in an olive orchard in Umbria (Central Italy)', *Grana*, vol. 39, no. 5, pp. 246-51.

Frenguelli, G., Passalacqua, G., Bonini, S., Fiocchi, A., Incorvaia, C., Marcucci, F., Tedeschini, E., Canonica, G.W. & Frati, F. 2010, 'Bridging allergologic and botanical knowledge in seasonal allergy: a role for phenology', *Annals of Allergy Asthma & Immunology*, vol. 105, no. 3, pp. 223-7.

Friedl, M.A., McIver, D.K., Hodges, J.C.F., Zhang, X.Y., Muchoney, D., Strahler, A.H., Woodcock, C.E., Gopal, S., Schneider, A., Cooper, A., Baccini, A., Gao, F. & Schaaf, C. 2002, 'Global land cover mapping from MODIS: algorithms and early results', *Remote Sensing of Environment*, vol. 83, no. 1-2, pp. 287-302.

Friedl, M.A., Sulla-Menashe, D., Tan, B., Schneider, A., Ramankutty, N., Sibley, A. & Huang, X.M. 2010, 'MODIS Collection 5 global land cover: Algorithm refinements and characterization of new datasets', *Remote Sensing of Environment*, vol. 114, no. 1, pp. 168-82.

Friedl, M.A., Gray, J., Sulla-Menashe, D. 2019. 'MCD12Q2 MODIS/Terra+Aqua Land Cover Dynamics Yearly L3 Global 500m SIN Grid V006 [Data set]', NASA EOSDIS Land Processes DAAC. doi: 10.5067/MODIS/MCD12Q2.006

Gallagher, R.V., Hughes, L. & Leishman, M.R. 2009, 'Phenological trends among Australian alpine species: using herbarium records to identify climate-change indicators', *Australian Journal of Botany*, vol. 57, no. 1, pp. 1-9.

Ganguly, S., Friedl, M.A., Tan, B., Zhang, X.Y. & Verma, M. 2010, 'Land surface phenology from MODIS: Characterization of the Collection 5 global land cover dynamics product', *Remote Sensing of Environment*, vol. 114, no. 8, pp. 1805-16.

Geerken, R., Zaitchik, B. & Evans, J.P. 2005, 'Classifying rangeland vegetation type and coverage from NDVI time series using Fourier Filtered Cycle Similarity', *International Journal of Remote Sensing*, vol. 26, no. 24, pp. 5535-54.

Ghitarrini, S., Galan, C., Frenguelli, G. & Tedeschini, E. 2017, 'Phenological analysis of grasses (Poaceae) as a support for the dissection of their pollen season in Perugia (Central Italy)', *Aerobiologia*, vol. 33, no. 3, pp. 339-49.

Gillespie, A.R., Kahle, A.B. & Walker, R.E. 1987, 'COLOR ENHANCEMENT OF HIGHLY CORRELATED IMAGES .2. CHANNEL RATIO AND CHROMATICITY TRANSFORMATION TECHNIQUES', *Remote Sensing of Environment*, vol. 22, no. 3, pp. 343-65.

Girgis, S.T., Marks, G.B., Downs, S.H., Kolbe, A., Car, G.N. & Paton, R. 2000, 'Thunderstorm-associated asthma in an inland town in south-eastern Australia. Who is at risk?', *European Respiratory Journal*, vol. 16, no. 1, pp. 3-8.

Gray, J., Friedl, M., Frolking, S., Ramankutty, N., Nelson, A. & Gumma, M.K. 2014, 'Mapping Asian Cropping Intensity With MODIS', *Ieee Journal of Selected Topics in Applied Earth Observations and Remote Sensing*, vol. 7, no. 8, pp. 3373-9.

Green, B.J., Dettmann, M., Yli-Panula, E., Rutherford, S. & Simpson, R. 2004, 'Atmospheric Poaceae pollen frequencies and associations with meteorological parameters in Brisbane, Australia: a 5-year record, 1994-1999', *International Journal of Biometeorology*, vol. 48, no. 4, pp. 172-8.

Green, B.J., Dettmann, M.E., Rutherford, S. & Simpson, R.W. 2002, 'Airborne pollen of Brisbane, Australia: a five-year record, 1994-1999', *Grana*, vol. 41, no. 4, pp. 242-50.

Grundstein, A., Shepherd, M., Miller, P. & Sarnat, S.E. 2017, 'The Role of Mesoscale-Convective Processes in Explaining the 21 November 2016 Epidemic Thunderstorm Asthma Event in Melbourne, Australia', *Journal of Applied Meteorology and Climatology*, vol. 56, no. 5, pp. 1337-43.

Gu, Y.X., Wylie, B.K. & Bliss, N.B. 2013, 'Mapping grassland productivity with 250-m eMODIS NDVI and SSURGO database over the Greater Platte River Basin, USA', *Ecological Indicators*, vol. 24, pp. 31-6.

Hamid, N., Ali, S.M., Talib, F., Sadiq, I. & Ghufran, M.A. 2015, 'Spatial and temporal variations of pollen concentrations in Islamabad (Pakistan): effect of meteorological parameters and impact on human health', *Grana*, vol. 54, no. 1, pp. 53-67.

Hattersley, P.W. 1983, 'The distribution of C3 and C4 grasses in Australia in relation to climate', *Oecologia*, vol. 57, pp. 113–128.

Henebry, G.M. 1993, 'Detecting change in grasslands using measures of spatial dependence with Landsat TM data', *Remote Sensing of Environment*, vol. 46, no. 2, pp. 223-34.

Henneken, R., Dose, V., Schleip, C. & Menzel, A. 2013, 'Detecting plant seasonality from webcams using Bayesian multiple change point analysis', *Agricultural and Forest Meteorology*, vol. 168, pp. 177-85.

Hidalgo, P.J., Galan, C. & Dominguez, E. 2003, 'Male phenology of three species of Cupressus: correlation with airborne pollen', *Trees-Structure and Function*, vol. 17, no. 4, pp. 336-44.

Hilker, T., Gitelson, A., Coops, N.C., Hall, F.G. & Black, T.A. 2011, 'Tracking plant physiological properties from multi-angular tower-based remote sensing', *Oecologia*, vol. 165, no. 4, pp. 865-76.

Hill, M.J., Donald, G.E., Hyder, M.W. & Smith, R.C.G. 2004, 'Estimation of pasture growth rate in the south west of Western Australia from AVHRR NDVI and climate data', *Remote Sensing of Environment*, vol. 93, no. 4, pp. 528-45.

Hill, M.J., Donald, G.E., Wheaton, G.A., Hyder, M. & Smith, R.C.G. 1998, 'Remote sensing for precision pasture management in South Western Australia', paper presented to the *9th Australasian Remote Sensing and Photogrammetry Conference*, Sydney, Australia.

Hinkler, J., Pedersen, S.B., Rasch, M. & Hansen, B.U. 2002, 'Automatic snow cover monitoring at high temporal and spatial resolution, using images taken by a standard digital camera', *International Journal of Remote Sensing*, vol. 23, no. 21, pp. 4669-82.

Holling, C.S. 1992, 'Cross-scale morphology, geometry, and dynamics of ecosystems', *Ecological Monographs*, vol. 62, no. 4, pp. 447-502.

Hovenden, M.J., Williams, A.L., Pedersen, J.K., Vander Schoor, J.K. & Wills, K.E. 2008, 'Elevated CO2 and warming impacts on flowering phenology in a southern Australian grassland are related to flowering time but not growth form, origin or longevity', *Australian Journal of Botany*, vol. 56, no. 8, pp. 630-43.

Howden, M.L., McDonald, C.F. & Sutherland, M.F. 2011, 'Thunderstorm asthma - a timely reminder', *Medical Journal of Australia*, vol. 195, no. 9, pp. 512-3.

Huete, A., 'Amazon Rainforest Phenology Observed From Space'.

Huete, A. 2012, 'Vegetation Indices, Remote Sensing and Forest Monitoring', *Geography Compass*.

Huete, A., Didan, K., Miura, T., Rodriguez, E.P., Gao, X. & Ferreira, L.G. 2002, 'Overview of the radiometric and biophysical performance of the MODIS vegetation indices', *Remote Sensing of Environment*, vol. 83, no. 1-2, pp. 195-213.

Huete, A.R., Didan, K., Shimabukuro, Y.E., Ratana, P., Saleska, S.R., Hutyra, L.R., Yang, W.Z., Nemani, R.R. & Myneni, R. 2006, 'Amazon rainforests green-up with sunlight in dry season', *Geophysical Research Letters*, vol. 33, no. 6.

Hufkens, K., Friedl, M., Sonnentag, O., Braswell, B.H., Milliman, T. & Richardson, A.D. 2012, 'Linking near-surface and satellite remote sensing measurements of deciduous broadleaf forest phenology', *Remote Sensing of Environment*, vol. 117, pp. 307-21.

Hufkens, K., Friedl, M.A., Keenan, T.F., Sonnentag, O., Bailey, A., O'Keefe, J. & Richardson, A.D. 2012, 'Ecological impacts of a widespread frost event following early spring leaf-out', *Global Change Biology*, vol. 18, no. 7, pp. 2365-77.

Hufkens, K., Keenan, T.F., Flanagan, L.B., Scott, R.L., Bernacchi, C.J., Joo, E., Brunsell, N.A., Verfaillie, J. & Richardson, A.D. 2016, 'Productivity of North American grasslands is increased under future climate scenarios despite rising aridity', *Nature Climate Change*, vol. 6, no. 7, pp. 710-+.

Hughes, R.E. 1958, 'Sheep population and environment in snowdonia (north wales)', *Journal of Ecology*, vol. 46, no. 1, pp. 169-&.Immitzer, M., Vuolo, F. & Atzberger, C. 2016, 'First Experience with Sentinel-2 Data for Crop and Tree Species Classifications in Central Europe', *Remote Sensing*, vol. 8, no. 3.

Jato, V., Rodriguez-Rajo, F.J. & Aira, M.J. 2007, 'Use of phenological and pollen-production data for interpreting atmospheric birch pollen curves', *Annals of Agricultural and Environmental Medicine*, vol. 14, no. 2, pp. 271-80.

Jonas, T., Rixen, C., Sturm, M. & Stoeckli, V. 2008, 'How alpine plant growth is linked to snow cover and climate variability', *Journal of Geophysical Research-Biogeosciences*, vol. 113, no. G3.

Julitta, T., Cremonese, E., Migliavacca, M., Colombo, R., Galvagno, M., Siniscalco, C., Rossini, M., Fava, F., Cogliati, S., di Cella, U.M. & Menzel, A. 2014, 'Using digital camera images to analyse snowmelt and phenology of a subalpine grassland', *Agricultural and Forest Meteorology*, vol. 198, pp. 116-25.

Kaduk, J. & Heimann, M. 1996, 'A prognostic phenology scheme for global terrestrial carbon cycle models', *Climate Research*, vol. 6, no. 1, pp. 1-19.

Kasprzyk, I. 2003, 'Flowering phenology and airborne pollen grains of chosen tree taxa in Rzeszów (SE Poland)', *Aerobiologia*, vol. 19, no. 2, pp. 113-20.

Keatley, M.R. & Hudson, I.L. 2010, *Phenological research: methods for environmental and climate change analysis*, Dordrecht: Springer Netherlands.

Keenan, T.F., Gray, J., Friedl, M.A., Toomey, M., Bohrer, G., Hollinger, D.Y., Munger, J.W., O'Keefe, J., Schmid, H.P., Wing, I.S., Yang, B. & Richardson, A.D. 2014, 'Net carbon uptake has increased through warming-induced changes in temperate forest phenology', *Nature Climate Change*, vol. 4, no. 7, pp. 598-604.

Khwarahm, N.R., Dash, J., Skjoth, C.A., Newnham, R.M., Adams-Groom, B., Head, K., Caulton, E. & Atkinson, P.M. 2017, 'Mapping the birch and grass pollen seasons in the UK using satellite sensor time-series', *Science of the Total Environment*, vol. 578, pp. 586-600.

Klosterman, S.T., Hufkens, K., Gray, J.M., Melaas, E., Sonnentag, O., Lavine, I., Mitchell, L., Norman, R., Friedl, M.A. & Richardson, A.D. 2014, 'Evaluating remote sensing of deciduous forest phenology at multiple spatial scales using PhenoCam imagery', *Biogeosciences*, vol. 11, no. 16, pp. 4305-20.

Korner, C. 2006, 'Plant CO2 responses: an issue of definition, time and resource supply', *New Phytologist*, vol. 172, no. 3, pp. 393-411.

Kurc, S.A. & Benton, L.M. 2010, 'Digital image-derived greenness links deep soil moisture to carbon uptake in a creosotebush-dominated shrubland', *Journal of Arid Environments*, vol. 74, no. 5, pp. 585-94.

Lanza, B. 1976, 'PHENOLOGY AND SEASONALITY MODELING - LIETH,H', *Scientia*, vol. 111, no. 5-8, pp. 518-20.

Latorre, F. 1997, 'Comparison between phenological and aerobiological patterns of some arboreal species of Mar del Plata (Argentina)', *Aerobiologia*, vol. 13, no. 1, p. 49.

Lee, J., Kronborg, C., O'Hehir, R.E. & Hew, M. 2017, 'Who's at risk of thunderstorm asthma? The ryegrass pollen trifecta and lessons learnt from the Melbourne thunderstorm epidemic', *Respiratory Medicine*, vol. 132, pp. 146-8.

Leon-Ruiz, E., Alcazar, P., Dominguez-Vilches, E. & Galan, C. 2011, 'Study of Poaceae phenology in a Mediterranean climate. Which species contribute most to airborne pollen counts?', *Aerobiologia*, vol. 27, no. 1, pp. 37-50.

Liang, L., Schwartz, M.D., Wang, Z.S., Gao, F., Schaaf, C.B., Tan, B., Morisette, J.T. & Zhang, X.Y. 2014, 'A Cross Comparison of Spatiotemporally Enhanced Springtime Phenological Measurements From Satellites and Ground in a Northern U.S. Mixed Forest', *Ieee Transactions on Geoscience and Remote Sensing*, vol. 52, no. 12, pp. 7513-26.

Limb, R.F., Hovick, T.J., Norland, J.E. & Volk, J.M. 2018, 'Grassland plant community spatial patterns driven by herbivory intensity', *Agriculture Ecosystems & Environment*, vol. 257, pp. 113-9.

Liu, Y., Hill, M.J., Zhang, X.Y., Wang, Z.S., Richardson, A.D., Hufkens, K., Filippa, G., Baldocchi, D.D., Ma, S.Y., Verfaillie, J. & Schaaf, C.B. 2017, 'Using data from Landsat, MODIS, VIIRS and PhenoCams to monitor the phenology of California oak/grass savanna and open grassland across spatial scales', *Agricultural and Forest Meteorology*, vol. 237, pp. 311-25.

Liu, Y.X., Wu, C.Y., Peng, D.L., Xu, S.G., Gonsamo, A., Jassal, R.S., Arain, M.A., Lu, L.L., Fang, B. & Chen, J.M. 2016, 'Improved modeling of land surface phenology using MODIS land surface reflectance and temperature at evergreen needleleaf forests of central North America', *Remote Sensing of Environment*, vol. 176, pp. 152-62.

Liu, Y., Wu, C., Sonnentag, O., Desai, A.R., Wang, J., 2020. Using the red chromatic coordinate to characterize the phenology of forest canopy photosynthesis. Agric. For. Meteorol. 285–286, 107910. https://doi.org/10.1016/j.agrformet.2020.107910

Lloyd, D. 1990, 'A phenological classification of terrestrial vegetation cover using shortwave vegetation index imagery', *International Journal of Remote Sensing*, vol. 11, no. 12, pp. 2269-79.

Ma, T. & Zhou, C.G. 2012, 'Climate-associated changes in spring plant phenology in China', *International Journal of Biometeorology*, vol. 56, no. 2, pp. 269-75.

Marks, G.B., Colquhoun, J.R., Girgis, S.T., Koski, M.H., Treloar, A.B.A., Hansen, P., Downs, S.H. & Car, N.G. 2001, 'Thunderstorm outflows preceding epidemics of asthma during spring and summer', *Thorax*, vol. 56, no. 6, pp. 468-71.

McDougall, K.L., Morgan, J.W., Walsh, N.G. & Williams, R.J. 2005, 'Plant invasions in treeless vegetation of the Australian Alps', *Perspectives in Plant Ecology Evolution and Systematics*, vol. 7, no. 3, pp. 159-71.

McGranahan, D.A., Hovick, T.J., Elmore, R.D., Engle, D.M. & Fuhlendorf, S.D. 2018, 'Moderate patchiness optimizes heterogeneity, stability, and beta diversity in mesic grassland', *Ecology and Evolution*, vol. 8, no. 10, pp. 5008-15.

McInnes, R.N., Hernming, D., Burgess, P., Lyndsay, D., Osborne, N.J., Skjoth, C.A., Thomas, S. & Vardoulakis, S. 2017, 'Mapping allergenic pollen vegetation in UK to study environmental exposure and human health', *Science of the Total Environment*, vol. 599, pp. 483-99.

Medek, D.E., Beggs, P.J., Erbas, B., Jaggard, A.K., Campbell, B.C., Vicendese, D., Johnston, F.H., Godwin, I., Huete, A.R., Green, B.J., Burton, P.K., Bowman, D., Newnham, R.M., Katelaris, C.H., Haberle, S.G., Newbigin, E. & Davies, J.M. 2016, 'Regional and seasonal variation in airborne grass pollen levels between cities of Australia and New Zealand', *Aerobiologia*, vol. 32, no. 2, pp. 289-302.

Melaas, E.K., Friedl, M.A. & Richardson, A.D. 2016, 'Multiscale modeling of spring phenology across Deciduous Forests in the Eastern United States', *Global Change Biology*, vol. 22, no. 2, pp. 792-805.

Meltzer, E.O., Blaiss, M.S., Derebery, M.J., Mahr, T.A., Gordon, B.R., Sheth, K.K., Simmons, A.L., Wingertzahn, M.A. & Boyle, J.M. 2009, 'Burden of allergic rhinitis: Results from the Pediatric Allergies in America survey', *Journal of Allergy and Clinical Immunology*, vol. 124, no. 3, pp. S43-S70.

Menzel, A. & Fabian, P. 1999, 'Growing season extended in Europe', *Nature*, vol. 397, no. 6721, pp. 659-.

Menzel, A., Sparks, T.H., Estrella, N., Koch, E., Aasa, A., Ahas, R., Alm-Kubler, K., Bissolli, P., Braslavska, O., Briede, A., Chmielewski, F.M., Crepinsek, Z., Curnel, Y., Dahl, A., Defila, C., Donnelly, A., Filella, Y., Jatcza, K., Mage, F., Mestre, A., Nordli, O., Penuelas, J., Pirinen, P., Remisova, V., Scheifinger, H., Striz, M., Susnik, A., Van Vliet, A.J.H., Wielgolaski, F.E., Zach, S. & Zust, A. 2006, 'European phenological response to climate change matches the warming pattern', *Global Change Biology*, vol. 12, no. 10, pp. 1969-76.

Meyer, G.E., Neto, J.C., 2008, 'Verification of color vegetation indices for automated crop imaging applications', *Comput. Electron. Agric*, vol. 63, pp. 282–293. https://doi.org/10.1016/j.compag.2008.03.009

Migliavacca, M., Cremonese, E., Colombo, R., Busetto, L., Galvagno, M., Ganis, L., Meroni, M., Pari, E., Rossini, M., Siniscalco, C. & di Cella, U.M. 2008, 'European larch phenology in the Alps: can we grasp the role of ecological factors by combining field observations and inverse modelling?', *International Journal of Biometeorology*, vol. 52, no. 7, pp. 587-605.

Migliavacca, M., Galvagno, M. & Cremonese, E. 2011, 'Using digital repeat photography and eddy covariance data to model grassland phenology and photosynthetic CO2 uptake', *Agricultural and Forest Meteorology*, vol. 151, no. 10, pp. 1325-37.

Moore, C.E., Beringer, J., Evans, B., Hutley, L.B. & Tapper, N.J. 2017, 'Tree-grass phenology information improves light use efficiency modelling of gross primary productivity for an Australian tropical savanna', *Biogeosciences*, vol. 14, no. 1, pp. 111-29.

Moore, C.E., Brown, T., Keenan, T.F., Duursma, R.A., van Dijk, A., Beringer, J., Culvenor, D., Evans, B., Huete, A., Hutley, L.B., Maier, S., Restrepo-Coupe, N., Sonnentag, O., Specht, A., Taylor, J.R., van Gorsel, E. & Liddell, M.J. 2016, 'Reviews and syntheses: Australian vegetation phenology: new insights from satellite remote sensing and digital repeat photography', *Biogeosciences*, vol. 13, no. 17, pp. 5085-102.

Moore, P.D. & Webb, J.A. 1983, 'An illustrated guide to pollen analysis ', London: Hodder and Stoughton.

Morgan, J.A., LeCain, D.R., Pendall, E., Blumenthal, D.M., Kimball, B.A., Carrillo, Y., Williams, D.G., Heisler-White, J., Dijkstra, F.A. & West, M. 2011, 'C4 grasses prosper as carbon dioxide eliminates desiccation in warmed semi-arid grassland', *Nature*, vol. 476, no. 7359, pp. 202-U101.

Moser, L., Fonti, P., Buntgen, U., Esper, J., Luterbacher, J., Franzen, J. & Frank, D. 2010, 'Timing and duration of European larch growing season along altitudinal gradients in the Swiss Alps', *Tree Physiology*, vol. 30, no. 2, pp. 225-33.

Moulin, S., Kergoat, L., Viovy, N. & Dedieu, G. 1997, 'Global-scale assessment of vegetation phenology using NOAA/AVHRR satellite measurements', *Journal of Climate*, vol. 10, no. 6, pp. 1154-70.

Myneni, R.B., Keeling, C.D., Tucker, C.J., Asrar, G. & Nemani, R.R. 1997, 'Increased plant growth in the northern high latitudes from 1981 to 1991', *Nature*, vol. 386, no. 6626, pp. 698-702.

Nasahara, K.N. & Nagai, S. 2015, 'Review: Development of an in situ observation network for terrestrial ecological remote sensing: the Phenological Eyes Network (PEN)', *Ecological Research*, vol. 30, no. 2, pp. 211-23.

O'Connell, J.L. & Alber, M. 2016, 'A smart classifier for extracting environmental data from digital image time-series: Applications for PhenoCam data in a tidal salt marsh', *Environmental Modelling & Software*, vol. 84, pp. 134-9.

Ong, E.K., Singh, M.B. & Knox, R.B. 1995, 'GRASS-POLLEN IN THE ATMOSPHERE OF MELBOURNE - SEASONAL DISTRIBUTION OVER 9 YEARS', *Grana*, vol. 34, no. 1, pp. 58-63.

Papale, D., Reichstein, M., Aubinet, M., Canfora, E., Bernhofer, C., Kutsch, W., Longdoz, B., Rambal, S., Valentini, R., Vesala, T. & Yakir, D. 2006,

'Towards a standardized processing of Net Ecosystem Exchange measured with eddy covariance technique: algorithms and uncertainty estimation', *Biogeosciences*, vol. 3, no. 4, pp. 571-83.

Parajka, J., Haas, P., Kirnbauer, R., Jansa, J. & Bloschl, G. 2012, 'Potential of time-lapse photography of snow for hydrological purposes at the small catchment scale', *Hydrological Processes*, vol. 26, no. 22, pp. 3327-37.

Pérez, A.J., López, F., Benlloch, J. V., Christensen, S., 2000. Colour and shape analysis techniques for weed detection in cereal fields. Comput. Electron. Agric. 25, 197–212. https://doi.org/10.1016/S0168-1699(99)00068-X

Piao, S.L., Ciais, P., Lomas, M., Beer, C., Liu, H.Y., Fang, J.Y., Friedlingstein, P., Huang, Y., Muraoka, H., Son, Y.H. & Woodward, I. 2011, 'Contribution of climate change and rising CO2 to terrestrial carbon balance in East Asia: A multi-model analysis', *Global and Planetary Change*, vol. 75, no. 3-4, pp. 133-42.

Primack, R.B. & Miller-Rushing, A.J. 2011, 'Broadening the study of phenology and climate change', *New Phytologist*, vol. 191, no. 2, pp. 307-9.

Psomas, A., Kneubuhler, M., Huber, S., Itten, K. & Zimmermann, N.E. 2011, 'Hyperspectral remote sensing for estimating aboveground biomass and for exploring species richness patterns of grassland habitats', *International Journal of Remote Sensing*, vol. 32, no. 24, pp. 9007-31.

Ranta, H., Kubin, E., Siljamo, P., Sofiev, M., Linkosalo, T., Oksanen, A. & Bondestam, K. 2006, 'Long distance pollen transport cause problems for determining the timing of birch pollen season in Fennoscandia by using phenological observations', *Grana*, vol. 45, no. 4, pp. 297-304.

Reed, B.C., Brown, J.F., Vanderzee, D., Loveland, T.R., Merchant, J.W. & Ohlen, D.O. 1994, 'Measuring phenological variability from satellite imagery', *Journal of Vegetation Science*, vol. 5, no. 5, pp. 703-14.

Reed, B.C., Schwartz, M.D. & Xiao, X. 2009, *Remote sensing phenology: status and the way forward*, New York: Springer-Verlag.

Richardson, A.D., Anderson, R.S., Arain, M.A., Barr, A.G., Bohrer, G., Chen, G., Chen, J.M., Ciais, P., Davis, K.J., Desai, A.R., Dietze, M.C., Dragoni, D., Garrity, S.R., Gough, C.M., Grant, R., Hollinger, D.Y., Margolis, H.A.,

McCaughey, H., Migliavacca, M., Monson, R.K., Munger, J.W., Poulter, B., Raczka, B.M., Ricciuto, D.M., Sahoo, A.K., Schaefer, K., Tian, H., Vargas, R., Verbeeck, H., Xiao, J. & Xue, Y. 2012, 'Terrestrial biosphere models need better representation of vegetation phenology: results from the North American Carbon Program Site Synthesis', *Global Change Biology*, vol. 18, no. 2, pp. 566-84.

Richardson, A.D., Braswell, B.H., Hollinger, D.Y., Jenkins, J.P. & Ollinger, S.V. 2009, 'Near-surface remote sensing of spatial and temporal variation in canopy phenology', *Ecological Applications*, vol. 19, no. 6, pp. 1417-28.

Richardson, A.D., Hollinger, D.Y., Dail, D.B., Lee, J.T., Munger, J.W. & O'Keefe, J. 2009, 'Influence of spring phenology on seasonal and annual carbon balance in two contrasting New England forests', *Tree Physiol*, vol. 29, no. 3, pp. 321-31.

Richardson, A.D., Hufkens, K., Milliman, T., Aubrecht, D.M., Chen, M., Gray, J.M., Johnston, M.R., Keenan, T.F., Klosterman, S.T., Kosmala, M., Melaas, E.K., Friedl, M.A. & Frolking, S. 2018, 'Tracking vegetation phenology across diverse North American biomes using PhenoCam imagery', *Sci Data*, vol. 5, p. 180028.

Richardson, A.D., Jenkins, J.P., Braswell, B.H., Hollinger, D.Y., Ollinger, S.V. & Smith, M.L. 2007a, 'Use of digital webcam images to track spring green-up in a deciduous broadleaf forest', *Oecologia*, vol. 152, no. 2, pp. 323-34.

Richardson, A.D., Jenkins, J.P., Braswell, B.H., Hollinger, D.Y., Ollinger, S.V. & Smith, M.L. 2007b, 'Use of digital webcam images to track spring green-up in a deciduous broadleaf forest', *Oecologia*, vol. 152, no. 2, pp. 323-34.

Richardson, A.D., Keenan, T.F., Migliavacca, M., Ryu, Y., Sonnentag, O. & Toomey, M. 2013, 'Climate change, phenology, and phenological control of vegetation feedbacks to the climate system', *Agricultural and Forest Meteorology*, vol. 169, pp. 156-73.

Richardson, A.D., Klosterman, S. & Toomey, M. 2013, 'Near-Surface Sensor-Derived Phenology', pp. 413-30.

Rogers, C.A., Wayne, P.M., Macklin, E.A., Muilenberg, M.L., Wagner, C.J., Epstein, P.R. & Bazzaz, F.A. 2006, 'Interaction of the onset of spring and

elevated atmospheric CO2 on ragweed (Ambrosia artemisiifolia L.) pollen production', *Environmental Health Perspectives*, vol. 114, no. 6, pp. 865-9.

Romero-Morte, J., Rojo, J., Rivero, R., Fernandez-Gonzalez, F. & Perez-Badia, R. 2018, 'Standardised index for measuring atmospheric grass-pollen emission', *Science of the Total Environment*, vol. 612, pp. 180-91.

Ross, J. 1999, 'Guide to best practice conservation of temperate native grasslands', *Sydney: World Wide Fund for Nature (Australia)*.

Sakamoto, T., Gitelson, A.A., Nguy-Robertson, A.L., Arkebauer, T.J., Wardlow, B.D., Suyker, A.E., Verma, S.B. & Shibayama, M. 2012, 'An alternative method using digital cameras for continuous monitoring of crop status', *Agricultural and Forest Meteorology*, vol. 154, pp. 113-26.

Shuai, Y., Schaaf, C., Zhang, X., Strahler, A., Roy, D., Morisette, J., Wang, Z., Nightingale, J., Nickeson, J., Richardson, A.D., Xie, D., Wang, J., Li, X., Strabala, K. & Davies, J.E. 2013a, 'Daily MODIS 500 m reflectance anisotropy direct broadcast (DB) products for monitoring vegetation phenology dynamics', *International Journal of Remote Sensing*, vol. 34, no. 16, pp. 5997-6016.

Shuai, Y.M., Schaaf, C., Zhang, X.Y., Strahler, A., Roy, D., Morisette, J., Wang, Z.S., Nightingale, J., Nickeson, J., Richardson, A.D., Xie, D.H., Wang, J.D., Li, X.W., Strabala, K. & Davies, J.E. 2013b, 'Daily MODIS 500 m reflectance anisotropy direct broadcast (DB) products for monitoring vegetation phenology dynamics', *International Journal of Remote Sensing*, vol. 34, no. 16, pp. 5997-6016.

Sidhu, N., Pebesma, E. & Wang, Y.C. 2017, 'Usability Study to Assess the IGBP Land Cover Classification for Singapore', *Remote Sensing*, vol. 9, no. 10, p. 15.

Singer, B.D., Ziska, L.H., Frenz, D.A., Gebhard, D.E. & Straka, J.G. 2005, 'Increasing Amb a 1 content in common ragweed (Ambrosia artemisiifolia) pollen as a function of rising atmospheric CO2 concentration', *Functional Plant Biology*, vol. 32, no. 7, pp. 667-70.

Skjøth, C.A., Šikoparija, B. & Jäger, S. 2013, 'Chapter 2: Pollen Sources', in M.S.f. ev & K.-C. Bergmann (eds), *Allergenic Pollen*, Springer Dordrecht Heidelberg New York London.

Skjoth, C.A., Sommer, J., Stach, A., Smith, M. & Brandt, J. 2007, 'The long-range transport of birch (Betula) pollen from Poland and Germany causes significant pre-season concentrations in Denmark', *Clinical and Experimental Allergy*, vol. 37, no. 8, pp. 1204-12.

Slaughter, D.C., Giles, D.K. & Downey, D. 2008, 'Autonomous robotic weed control systems: A review', *Computers and Electronics in Agriculture*, vol. 61, no. 1, pp. 63-78.

Soeterboek, C. 2011, 'Pastoral Australia: Fortunes, Failures & Hard Yakka: A Historical Overview 1788-1967', *Historical Records of Australian Science*, vol. 22, no. 2, pp. 306-7.

Sonnentag, O., Detto, M., Vargas, R., Ryu, Y., Runkle, B.R.K., Kelly, M. & Baldocchi, D.D. 2011, 'Tracking the structural and functional development of a perennial pepperweed (Lepidium latifolium L.) infestation using a multi-year archive of webcam imagery and eddy covariance measurements', *Agricultural and Forest Meteorology*, vol. 151, no. 7, pp. 916-26.

Sonnentag, O., Hufkens, K., Teshera-Sterne, C., Young, A.M., Friedl, M., Braswell, B.H., Milliman, T., O'Keefe, J. & Richardson, A.D. 2012, 'Digital repeat photography for phenological research in forest ecosystems', *Agricultural and Forest Meteorology*, vol. 152, pp. 159-77.

Sonnentag, O., Hufkens, K., Teshera-Sterne, C., Young, A.M., Friedl, M., Braswell, B.H., Milliman, T., O'Keefe, J. & Richardson, A.D. 2012, 'Digital repeat photography for phenological research in forest ecosystems', *Agricultural and Forest Meteorology*, vol. 152, pp. 159-77.

Specht, R.L. & Brouwer, Y.M. 1975, 'Seasonal shoot growth of eucalyptus spp in brisbane area of queensland (with notes on shoot growth and litter fall in other areas of Australia)', *Australian Journal of Botany*, vol. 23, no. 3, pp. 459-74.

Stern, H. & Dehani, R.R. 2013, 'The distribution of climate zones across Australia: identifying and explaining changes during the past century, 25th Conference on Climate Variability and Change, American Meteorological Society, Austin, TX, USA, '.

Stevenson, J., Haberle, S.G., Johnston, F.H. & Bowman, D. 2007a, 'Seasonal distribution of pollen in the atmosphere of Darwin, tropical Australia: Preliminary results', *Grana*, vol. 46, no. 1, pp. 34-42.

Stevenson, J., Haberle, S.G., Johnston, F.H. & Bowman, D.M.J.S. 2007b, 'Seasonal distribution of pollen in the atmosphere of Darwin, tropical Australia: Preliminary results', *Grana*, vol. 46, no. 1, pp. 34-42.

Tan, P., Lymburner, L., Mueller, N., Li, F.Q., Thankappan, M., Lewis, A. & Ieee 2013, 'Applying machine learning methods and time series analysis to create a national dynamic land cover dataset for Australia', *2013 Ieee International Geoscience and Remote Sensing Symposium*, Ieee, New York, pp. 4289-92.

Tng, D.Y.P., Hopf, F., Haberle, S.G. & Bowman, D. 2010, 'Seasonal pollen distribution in the atmosphere of Hobart, Tasmania: preliminary observations and congruence with flowering phenology', *Australian Journal of Botany*, vol. 58, no. 6, pp. 440-52.

Toomey, M., Friedl, M.A., Frolking, S., Hufkens, K., Klosterman, S., Sonnentag, O., Baldocchi, D.D., Bernacchi, C.J., Biraud, S.C., Bohrer, G., Brzostek, E., Burns, S.P., Coursolle, C., Hollinger, D.Y., Margolis, H.A., McCaughey, H., Monson, R.K., Munger, J.W., Pallardy, S., Phillips, R.P., Torn, M.S., Wharton, S., Zeri, M. & Richardson, A.D. 2015, 'Greenness indices from digital cameras predict the timing and seasonal dynamics of canopy-scale photosynthesis', *Ecological Applications*, vol. 25, no. 1, pp. 99-115.

Tormo, R., Silva, I., Gonzalo, A., Moreno, A., Perez, R. & Fernandez, S. 2011, 'Phenological records as a complement to aerobiological data', *International Journal of Biometeorology*, vol. 55, no. 1, pp. 51-65.

Tucker, C.J. 1979, 'Red and photographic infrared linear combinations for monitoring vegetation', *Remote Sensing of Environment*, vol. 8, no. 2, pp. 127-50.

van der Meer, F.D., van der Werff, H.M.A. & van Ruitenbeek, F.J.A. 2014, 'Potential of ESA's Sentinel-2 for geological applications', *Remote Sensing of Environment*, vol. 148, pp. 124-33.Walls, R.S., Heddle, R.J., Tang, M.L.K., Basger, B.J., Solley, G.O. & Yeo, G.T. 2005, 'Optimising the management of allergic rhinitis: an Australian perspective', *Medical Journal of Australia*, vol. 182, no. 1, pp. 28-33.

Wang, C., Li, J., Liu, Q.H., Zhong, B., Wu, S.L. & Xia, C.F. 2017, 'Analysis of Differences in Phenology Extracted from the Enhanced Vegetation Index and the Leaf Area Index', *Sensors*, vol. 17, no. 9, p. 16.

Watson, C.J. 2016, 'Exploring the seasonal dynamics of Australian temperate grasslands through phenocam imagery, remote sensing and field data', University of Technology Sydney.

Weinberg, E.G. 2011, 'The wao white book on allergy 2011-2012', *Current Allergy & Clinical Immunology*, vol. 24, no. 3, pp. 156-7.

Werchan, B., Werchan, M., Mucke, H.G., Gauger, U., Simoleit, A., Zuberbier, T. & Bergmann, K.C. 2017, 'Spatial distribution of allergenic pollen through a large metropolitan area', *Environmental Monitoring and Assessment*, vol. 189, no. 4, p. 19.

White, M.A., Thornton, P.E. & Running, S.W. 1997, 'A continental phenology model for monitoring vegetation responses to interannual climatic variability', *Global Biogeochemical Cycles*, vol. 11, no. 2, pp. 217-34.

Wingate, L., Ogee, J., Cremonese, E., Filippa, G., Mizunuma, T., Migliavacca, M., Moisy, C., Wilkinson, M., Moureaux, C., Wohlfahrt, G., Hammerle, A., Hortnagl, L., Gimeno, C., Porcar-Castell, A., Galvagno, M., Nakaji, T., Morison, J., Kolle, O., Knohl, A., Kutsch, W., Kolari, P., Nikinmaa, E., Ibrom, A., Gielen, B., Eugster, W., Balzarolo, M., Papale, D., Klumpp, K., Kostner, B., Grunwald, T., Joffre, R., Ourcival, J.M., Hellstrom, M., Lindroth, A., George, C., Longdoz, B., Genty, B., Levula, J., Heinesch, B., Sprintsin, M., Yakir, D., Manise, T., Guyon, D., Ahrends, H., Plaza-Aguilar, A., Guan, J.H. & Grace, J. 2015, 'Interpreting canopy development and physiology using a European phenology camera network at flux sites', *Biogeosciences*, vol. 12, no. 20, pp. 5995-6015.

Woebbecke, D.M., Meyer, G.E., Vonbargen, K. & Mortensen, D.A. 1995, 'Color indexes for weed identification under various soil, residue, and lighting conditions ', *Transactions of the Asae*, vol. 38, no. 1, pp. 259-69.

Wong, N. & Dorrough, J.W. 2015, *Integrating grassland conservation into farming practice*, Clayton, Victoria: CSIRO Publishing.

Wubs, E.R.J. & Bezemer, T.M. 2018, 'Plant community evenness responds to spatial plant-soil feedback heterogeneity primarily through the diversity of soil conditioning', *Functional Ecology*, vol. 32, no. 2, pp. 509-21.

Wylie, B.K., Meyer, D.J., Tieszen, L.L. & Mannel, S. 2002, 'Satellite mapping of surface biophysical parameters at the biome scale over the North American grasslands - A case study', *Remote Sensing of Environment*, vol. 79, no. 2-3, pp. 266-78.

Yang, H., Li, S.N.A., Chen, J., Zhang, X.L. & Xu, S.S. 2017, 'The Standardization and Harmonization of Land Cover Classification Systems towards Harmonized Datasets: A Review', *Isprs International Journal of Geo-Information*, vol. 6, no. 5.

Yu, L., Liu, X.X., Zhao, Y.Y., Yu, C.Q. & Gong, P. 2018, 'Difficult to map regions in 30 m global land cover mapping determined with a common validation dataset', *International Journal of Remote Sensing*, vol. 39, no. 12, pp. 4077-87.

Zanotti, A.L. & Puppi, G. 2000, 'Phenological surveys of allergenic species in the neighbourhood of Bologna (Italy)', *Aerobiologia*, vol. 16, no. 2, pp. 199-206.

Zerger, A., McIntyre, S., Gobbett, D. & Stol, J. 2011, 'Remote detection of grassland nutrient status for assessing ground layer vegetation condition and restoration potential of eucalypt grassy woodlands', *Landscape and Urban Planning*, vol. 102, no. 4, pp. 226-33.

Zhang, M., Ma, M.G., De Maeyer, P. & Kurban, A. 2017, 'Uncertainties in Classification System Conversion and an Analysis of Inconsistencies in Global Land Cover Products', *Isprs International Journal of Geo-Information*, vol. 6, no. 4.

Zhang, R.P., Liang, T.G., Guo, J., Xie, H.J., Feng, Q.S. & Aimaiti, Y. 2018, 'Grassland dynamics in response to climate change and human activities in Xinjiang from 2000 to 2014', *Scientific Reports*, vol. 8.

Zhang, X.Y. 2015, 'Reconstruction of a complete global time series of daily vegetation index trajectory from long-term AVHRR data', *Remote Sensing of Environment*, vol. 156, pp. 457-72.

Zhang, X.Y., Friedl, M.A. & Schaaf, C.B. 2006, 'Global vegetation phenology from Moderate Resolution Imaging Spectroradiometer (MODIS): Evaluation of global patterns and comparison with in situ measurements', *Journal of Geophysical Research-Biogeosciences*, vol. 111, no. G4.

Zhang, X.Y., Friedl, M.A., Schaaf, C.B., Strahler, A.H., Hodges, J.C.F., Gao, F., Reed, B.C. & Huete, A. 2003, 'Monitoring vegetation phenology using MODIS', *Remote Sensing of Environment*, vol. 84, no. 3, pp. 471-5.

Zhou, W., Gang, C.C., Zhou, F.C., Li, J.L., Dong, X.G. & Zhao, C.Z. 2015, 'Quantitative assessment of the individual contribution of climate and human factors to desertification in northwest China using net primary productivity as an indicator', *Ecological Indicators*, vol. 48, pp. 560-9.

Zhou, W., Yang, H., Huang, L., Chen, C., Lin, X.S., Hu, Z.J. & Li, J.L. 2017, 'Grassland degradation remote sensing monitoring and driving factors quantitative assessment in China from 1982 to 2010', *Ecological Indicators*, vol. 83, pp. 303-13.

Ziska, L.H. & Caulfield, F.A. 2000, 'Rising CO2 and pollen production of common ragweed (Ambrosia artemisiifolia), a known allergy-inducing species: implications for public health', *Australian Journal of Plant Physiology*, vol. 27, no. 10, pp. 893-8.

CHAPTER 2

Chapter 2 Diurnal and seasonal phenocam greenness variations in eastern Australian pastures and grasslands

2.1 INTRODUCTION

Near-surface remote sensing based on time-lapse digital cameras – phenocams – has been commonly adopted in ecological observatory networks around the world (Moore et al., 2016; Nagai et al., 2016a; Richardson et al., 2018a; Templ et al., 2018). It has been demonstrated that phenocams can effectively describe vegetation phenological dynamics in a variety of ecosystems (Ahrends et al., 2009; Ide and Oguma, 2010; Julitta et al., 2014; Luo et al., 2018; Seyednasrollah et al., 2019).

The traditional method of field observations for phenology states is based on human observers (Rutishauser et al., 2007; Sparks and Menzel, 2002; Templ et al., 2018). However, inherent subjectivity, the lack of consistent monitoring with the high temporal resolution, and insufficient spatial representativeness of the larger landscape (Richardson et al., 2018b) restrict the observer records to characterize vegetation phenology at the regional scale. In contrast, satellite remote sensing provides historical time-series images to track the vegetation seasonality and assist in revealing the ecosystem responses to climate change at the global scale (Morisette et al., 2009; Zhang et al., 2003). Nevertheless, the description of the subtle ecological activities for landscapes with high spatial heterogeneity and brief phenological transition using satellite data is limited by the coarse temporal and spatial resolution (Fisher and Mustard, 2007; Zeng et al., 2020). As the technology develops, long-term phenology observations with cost-effective phenocam sensors can potentially overcome these limitations and bridge the gap between vegetation monitoring at the scale of individual organisms and satellite regional observations (Liu et al., 2017; Richardson et al., 2018b; Watson et al., 2019).

Furthermore, large-scale phenocam networks have been developed within the last decade. In North America and Japan, the PhenoCam network (Richardson et al., 2009) and the Phenological Eyes Network (PEN) (Nagai et al., 2016b) have been developed, respectively. The US National Ecological Observatory Network (NEON) and the European Union's Integrated Carbon Observation System (ICOS) also established a phenocam network. In Australia, to facilitate the sharing of phenocam data and research using this novel technology, researchers established Australian Phenocam Network (APN) (Moore et al., 2016). As a result, there has

been an increased interest in effectively utilizing digital repeat camera data for purpose of monitoring vegetation activity at the in-situ scale.

Technologically, visible-light phenocam sensors store color information into three primary colour layers, i.e. red, green and blue (RGB). Thus, each image pixel possesses an RGB digital number (DN) triple, i.e. pixel value (Richardson et al., 2018a). By altering the intensity of RGB DN triples, any given color could be represented in any individual pixel. Due to camera sensors usually feature a variable aperture lens that responded to ambient light levels (Richardson et al., 2007), the red-green-blue brightness of each pixel are subjected to scene illumination changes caused by weather conditions, daily rotation of the earth, and sun-camera geometry (Sonnentag et al., 2012).

To suppress high correlation among the three color space components (Cheng et al., 2001) and to conduct further quantitative analysis, color indices were transformed from RGB DN values. These indices were designed for minimizing the effects of illumination by normalising the RGB DNs to RGB chromatic coordinates, e.g. green chromatic coordinate (GCC) (Gillespie et al., 1987), or for enhancing the green signal from vegetation canopies, e.g. excess green index (ExG) (Woebbecke et al., 1995). As a widely used phenocam color index, GCC has been extensively used to describe canopy greenness and extract phenological information in agricultural (Meyer and Neto, 2008; Pérez et al., 2000), deciduous broadleaf forest (Ahrends et al., 2009; Hufkens et al., 2012; Liu et al., 2020), and grassland (Browning et al., 2017a; Vrieling et al., 2018; Watson et al., 2019). Despite the extensive use of these phenocam indices, scene illumination variations related to solar illumination geometry and weather (i.e. sky condition) cause day-to-day fluctuations in the diurnal profile of these colour indices (Ahrends et al., 2009; Brown et al., 2017; Ide and Oguma, 2010; Sonnentag et al., 2012; Toomey et al., 2015), consequently, creating outliers in the seasonal trajectories and hampering the derivation of phenological metrics from these colour indices time series (Richardson et al. 2009, 2018a, Wingate et al. 2015). Given this, better understanding of the roles of scene illumination changes, which is controlled by solar radiation intensity, on diurnal phenocam greenness measurements is critical

for mitigating their influences on the monitoring of diurnal and seasonal pasture/ grassland dynamics.

The variations of scene illumination conditions are attributed to many external factors, including diurnal variations in solar geometry. Previous studies focused on forested canopies reported diurnal course of GCC values increased and then decreased over a day with the maximum value were reached around solar noon time (Ahrends et al., 2008; Sonnentag et al., 2012). By contrast, the diurnal GCC profiles of winter wheat experienced a concave trend with minimum values appeared about 12:00 pm (local time) (Li et al., 2019). Also, the diurnal scene illumination is subjected to diffuse/direct solar radiation due to changes in weather conditions, i.e. sunny or overcast. For example, studies at deciduous forest sites showed GCC and ExG values were higher in sunny days dominated by direct solar radiation than in overcast conditions when diffuse solar radiation turned to be dominated (Ahrends et al., 2008; Mizunuma et al., 2013; Sonnentag et al., 2012). Another phenocam study conducted on evergreen conifer canopies, however, showed GCC values under sunny days generally decreased comparing with days under sub-optimal illumination conditions (Richardson et al., 2009). To suppress these illumination-related impacts on tracking seasonal vegetation phenology, previous studies often use images from mid-day (Ahrends et al., 2009; Kurc and Benton, 2010; Richardson et al., 2009; Richardson et al., 2007) or mid-morning time (Sonnentag et al., 2011) as the daily value. Also, in phenocam networks around the world, there is a widely used approach for compositing daily values, i.e. *per90* (Sonnentag et al., 2012).

Compared with forests, the impact of solar radiation intensity in pasture/ grassland phenocam images is less understood. A study focused on grazed peatland showed RGB DNs exhibited convex patterns with an asymmetrical manner over the course of the day (Sonnentag et al., 2011). However, the metrics extracted from imagery were absolute channel brightness, rather than colour chromatic coordinates. As for impacts of weather conditions, O'Connell and Alber (2016) demonstrated GCC values under cloudy scenes higher than sunlit illumination images at the salt marsh ecosystem, but the canopy character of salt marsh is different with grassland/ pasture. Since there is no phenocam GCC compositing method, which proposed by

analyses on grassland ecosystem, grassland/ pasture phenology studies using phenocam image have to adopt diurnal-to-daily compositing method, which proposed by the forested canopy, to mitigate the impact of scene illumination changes on diurnal greenness values (Browning et al., 2017b; Cui et al., 2019; Julitta et al., 2014; Yan et al., 2019). As a result, two pressing questions needed to be answered in grassland/ pasture phenocam research. Are there differences between forest and grassland/ pasture in the responses of diurnal GCC values to solar intensity changes? And consequently, whether these differences should be taken into account for diurnal data compositing?

In this study, we focused on the pasture/ grassland ecosystems across eastern Australia to explore the effects of solar radiation intensity related to diurnal solar zenith angle (SZA) variations and weather-related changes in direct/ diffuse radiation to phenocam-derived GCC values. The objectives of this study are to:

(1) characterize how the diurnal GCC changes with the variations in SZA within one day at different phenophases stages;
(2) assess the diurnal differences between pasture GCC values under sunny and overcast weather conditions (i.e. the sky conditions dominated by direct and diffuse solar irradiation, respectively) at different phenophases stages; and
(3) propose a diurnal-to-daily GCC compositing methodology to mitigate the influence of changes in solar radiation intensity on phenocam-derived GCC in pastures and grasslands.

2.2 METHOD

2.2.1 Study areas and site description

The study was conducted at four phenocam sites, located at the state of Victoria (VIC), New South Wales (NSW) and Queensland (QLD) across the southeast Australian pasture/ grassland ecosystem (Fig. 2.1). The climate types in the study area are mainly Temperate with warm summer (i.e. VIC site and NSW site) and Subtropical with no dry season (i.e. two QLD sites), according to climate classification maps released from Bureau of Meteorology (http://www.bom.gov.au). These four sites encompass a wide range of climate and grassland types, i.e. temperate grasses in NSW and VIC sites, and subtropical grasses in QLD sites.

Detailed descriptions of these sites are given in Table 2.1 including their land cover type from Dynamic Land Cover Dataset product (DLCD) and dominant pasture species in phenocam field of view.

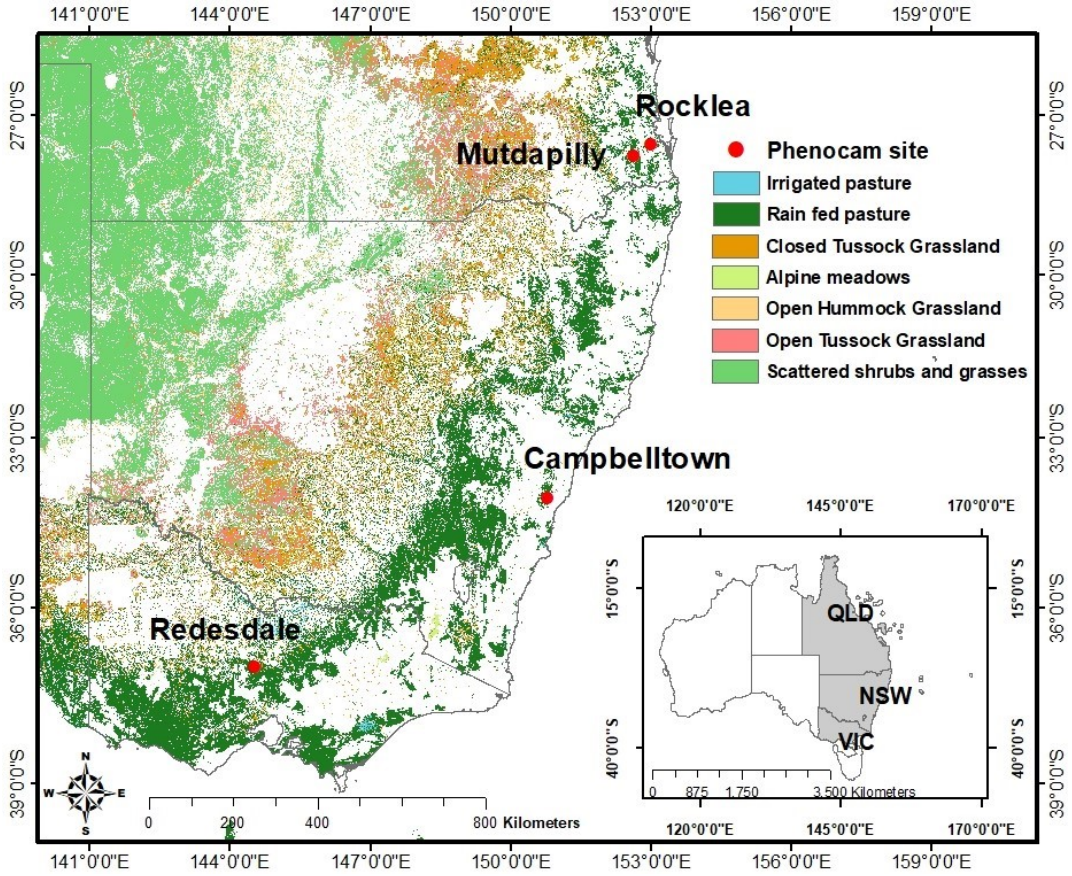

Figure 2.1 Spatial distribution of phenocam sites used in this study. Land cover types were according to Dynamic Land Cover Dataset (DLCD, https://data.gov.au/dataset/1556b944-731c4b7f-a03e-14577c7e68db)

Table 2.1 Descriptions of research sites in this study.

State	Sites Name	Latitude; Longitude (°)	Elevation (m)	Land Cover Type [1]	Dominant pasture species
VIC	*Redesdale*	-37.0194; 144.5203	290	Rain fed pasture	Canary grass
NSW	*Campbelltown*	-34.067; 150.796	112	Rain fed pasture	Oat grass
QLD	*Rocklea*	-27.536; 152.993	7	Rain fed pasture	Rhodes grass
	Mutdapilly	-27.750; 152.644	21	Rain fed pasture	Panicoideae genera

[1] The all of land cover types of study sites referred to DLCD (Dynamic Land Cover Dataset) product (https://data.gov.au/dataset/1556b944-731c-4b7f-a03e-14577c7e68db).

Table 2.2 Overview of time-laps digital cameras used in this study.

Sites	Manufacturer: model	Resolution	Max aperture	Temporal coverage (h AEST); interval	Observation period	View direction: depression angle
Redesdale	Bushnell, Aggressor No Glow HD trophy Cam; 119776C	4416 x 3312	2.8	8:00 – 17:00; 30 min	2018.12 – 2020.2	~NE; ~10°
Campbelltown	Ltl Acorn; Ltl-6310WMC	4000 x 3000	3.2	8:00 – 17:00; 15 min	2018.10 – 2019.6	190° due North; ~5°
Rocklea	Bushnell, Aggressor No Glow HD trophy Cam; 119776C	4416 x 3312	2.8	9:00 – 17:00; 15 min	2018.7 – 2019.7	140° due North; ~10°
Mutdapilly	Bushnell, Aggressor No Glow HD trophy Cam; 119776C	4416 x 3312	2.8	9:00 – 17:00; 15 min	2018.7 – 2019.7	54° due North; ~10°

2.2.2 Digital time-lapse camera data

A set of phenocams was deployed at four study sites (Fig. 2.1) with different observation periods, and time intervals (15 or 30 min). Two brands of time-lapse digital camera, i.e. Ltl Acorn Scouting Camera (model: Ltl-6310WMC) and Bushnell Aggressor No Glow HD trophy Cam (model: 119776C), were used in this study. The cameras all used automatic white balance and exposure setting. The differences between the two camera types are mainly in resolution and maximum aperture. Phenocams faced mostly south with an oblique view angle. The reason why cameras were deployed with different azimuthal orientations is to ensure the camera's FOV would capture the most pasture area, without obstruction from trees or other non-target objects. Detailed descriptions of these phenocams are given in Table 2.2.

To describe the pasture greenness dynamics, the green chromatic coordinate (GCC) was derived from phenocam imagery as following steps. Firstly, the region of interest (ROI) was selected at each site to sample the most representative pasture area in the FOV of the camera (Fig. 2.2); secondly, RGB DNs for each pixels within the ROI were extracted and converted to GCC by Eq. (2.1); and then the GCC value for each pixel was averaged across ROI.

$$GCC = \frac{G}{R+G+B} \tag{2.1}$$

Where R, G and B are the red, green and blue pixel digital numbers.

Figure 2.2 Phenocam example RGB images at each site. The red polygons denoted the regions of interest (ROIs) selected for green chromatic coordinate (GCC) calculation.

2.2.3 Solar zenith angle data

Though the diurnal changes in solar elevation and azimuth caused the variations in GCC (and overall brightness) over the course of a day (Richardson et al., 2009),

there is a lack of quantitative analyses for their specific relationships. Therefore, we obtained the solar zenith angle (SZA) for each image, according to the time when that image was taken, as the quantified value of solar elevation to assist the understanding for variations in diurnal GCC profiles related to solar geometry. The SZA values were calculated by "oce" R package (https://cran.r-project.org/web/packages/oce/oce.pdf).

2.2.4 Hourly solar irradiation data

The Australian hourly solar radiation dataset provided by the Bureau of Meteorology Australia (BOM) (http://www.bom.gov.au/climate/how/newproducts/IDCJAD0111.shtml) was used in this study to quantify the diurnal variations in solar radiation caused by SZA changes and assist distinguish sunny and cloudy days for all phenocam observation periods. The product includes two gridded hourly solar irradiance fractions - solar global horizontal irradiance (GHI) and solar direct normal irradiance (DNI). They were estimated by hourly visible images from geostationary meteorological satellites using the Australian Bureau of Meteorology's computer radiation model (Gautier et al., 1980).

We extracted the hourly GHI and DNI from this product for each phenocam site. And then, the hourly solar diffuse horizontal irradiance (DHI) was calculated followed Eq. (2.2).

$$\text{Global Horizontal irradiance (GHI)} = \text{Direct Normal irradiance (DNI)} \times \cos(\text{SZA}) + \text{Diffuse Horizontal irradiance (DHI)} \quad (2.2)$$

Where SZA is the solar zenith angle at the specific time, which corresponding to the timing of hourly solar irradiations for each phenocam location.

The GHI values are usually the highest in the middle of the day and vary with atmospheric condition changes, e.g. cloudiness. Compared with DNI values, which are usually the highest in cloud-free conditions, DHI values are usually the dominant solar irradiation fraction under cloudy sky condition (Nann and Riordan, 1991). According to this characteristic, we plotted the hourly solar radiation for each day to recognize sunny and cloudy days across the entire growing season for each phenocam site. Fig. 2.3 illustrates the schematic example of hourly GHI, DNI

x cos (SZA), and DHI under cloudy (Fig. 2.3 a) and sunny (Fig. 2.3 b) sky conditions at Rocklea site. For example, the DHI dominated the overall solar radiation on May-4-2019 with extremely low DNI x cos (SZA) values through a day (Fig. 2.3 a). Therefore, we classified this day as a cloudy (or overcast) day. Inversely, a specific day was be recognized as a sunny day when the DHI values are dramatically low and DNI x cos (SZA) become the dominant fraction over this day, such as May-5-2019 (Fig. 2.3 b). Considering the coarse resolution of the hourly solar radiation product, we did the visual inspection for phenocam imagery to make sure the sky conditions are 100% cloud-free or overcast.

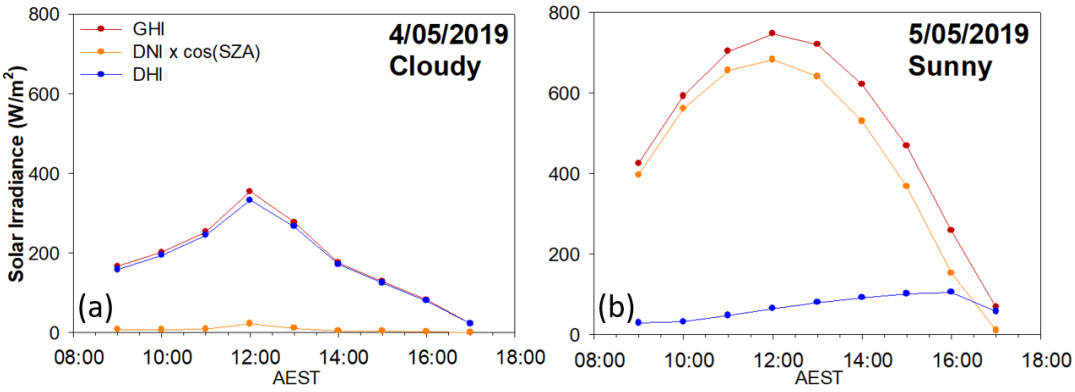

Figure 2.3 The schematic representation for recognizing sunny and cloudy days based on diurnal profiles of solar direct normal irradiance (DNI) x cos (SZA) and diffuse horizontal irradiance (DHI) at Rocklea.

2.2.5 Analysis strategy

2.2.5.1 Solar radiation effects on diurnal phenocam GCC values

To understand how diurnal variations in solar irradiation due to diurnal SZA changes impact the GCC values, we plotted diurnal GCC alongside SZA and DNI x cos(SZA) values on the same day at Campbelltown site. Considering cloudy sky condition can introduce uncertainties in phenocam imagery scene illumination, we performed this study on four sunny days. They are located at different phenophases, i.e. “peak greenness”, “green-up”, “brown-down” and “dry pasture”.

Also, we compared diurnal GCC values under sunny and overcast days at different phenophases at Campbelltown site to examine the effects of diffuse/direct solar radiation-related changes in scene illumination on diurnal GCC values. Note that the criterion for selecting example days, in which analyses were conducted, is to

ensure selected sunny and overcast days are adjacent as much as possible so that the growing stages of pasture on these days are similar.

2.2.5.2 Compositing methodology

We applied a moving-window approach based on minimum SZA time with three-day step-size to composite diurnal GCC values into daily values. Firstly, a four-hour window was selected centred at minimum SZA time. And then we calculated the 10^{th} percentile of all four-hour window GCC values for three days so that to pick the bottom of diurnal GCC profile. Finally, in this four-hour window across three days, we averaged all GCC values that were smaller than the 10^{th} percentile and assigned this average as the daily value of the window centre day. Also, we composited diurnal GCC values to daily scale using *per90* method by assigning the 90^{th} percentile of all daytime GCC values within a three-day window to the centre day as its daily values. More details are described in Sonnentag et al. (2012).

According to previous studies (Ma et al., 2015; Wang and Liang, 2008), the SSA-Pheno (singular spectrum analysis for phenology) algorithm was used to fit time-series of daily GCC profiles derived from *per90* and min SZA method, as well as retrieve phenological metrics, including the start of growing season (SGS), peak of growing season (PGS), end of growing season (EGS), and length of growing season (LGS) from fitted GCC time series. The timing was defined as PGS when GCC reaches its seasonal maximum; the SGS and EGS were then detected when smoothed curves of daily GCC first and last reached 10% of the seasonal amplitude, respectively; and then the difference between SGS and EGS is the LGS (Ma et al., 2020).

To compare the differences between two compositing methods, we used least-squares linear regression to calculate coefficients of determination (R^2) and p-value for all-sites GCC values. Meanwhile, the root mean square error (RMSE) was calculated to assess the differences of two methods in retrieving phenological metrics from GCC time series.

2.3 RESULTS

2.3.1 Diurnal GCC, green channel, and overall brightness variations with incident direct solar radiation in relation to solar zenith angle

We explored the temporal variations in diurnal GCC values with changed SZA and solar irradiation at Campbelltown under clear sky conditions for four phenophases (Fig. 2.4). The diurnal SZA profiles were characterized as concave shapes with minimum values that occurred around 12:00 pm (local time). Consequently, the incident direct solar radiation (i.e. cos (SZA) x DNI) increased and reached the highest value around noon and then decreased alongside the increased SZA after noon time. The diurnal GCC profiles varied synchronously with diurnal SZA and showed a characteristic concave shape as well, with higher values occurring in the morning and late afternoon and the minimum values appeared around noon at all phenophases. However, influences of diurnal SZA on diurnal GCC values are phenological dependent with near-flat temporal GCC profiles under 'dry pasture' (Fig. 2.4 d). Diurnal GCC profiles at 'Green-up' and 'Dry pasture' possessed the largest and least amplitudes, respectively (Fig. 2.4 a and d).

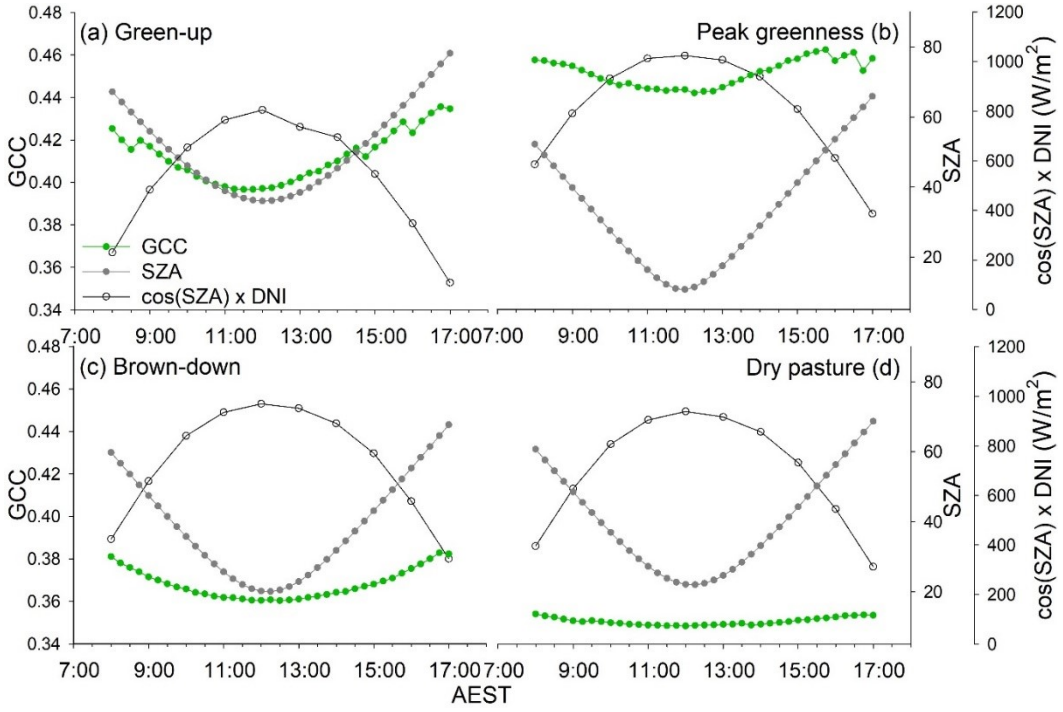

Figure 2.4 Diurnal profiles of green chromatic coordinate (GCC), solar zenith angle (SZA) and direct horizontal irradiance (cos (SZA) x DNI) under different four phenophases at example days with clear-sky condition, Campbelltown. The specific

dates for ‘Peak greenness’ is 25-Dec-2018, for ‘Green-up’ is 26-Mar-2019, for ‘Dry-down’ is 11-Feb-2019, and for ‘Dry pasture’ is 17-Feb-2019.

2.3.2 Differences in diurnal GCC under direct and diffuse solar radiation conditions

Diurnal patterns in GCC and solar radiation components for sunny and overcast days were significantly different in all phenophases at Campbelltown, especially during mid-day hours (Fig. 2.5).

The incident direct irradiance (cos (SZA) x DNI, red solid points and lines) were dramatically higher than diffuse horizontal irradiance (DHI, red hollow points and lines) under sunny days, with highest values around noon time. However, cos (SZA) x DNI values closely reached zero and DHI values were higher than them under overcast days (blue points and lines in Fig. 2.5 e - h). As expected, it indicates that direct and diffuse solar radiation were dominant solar radiation components under sunny (clear-sky) and overcast weather conditions, respectively.

The GCC values in overcast days (i.e. under diffuse solar radiation) were generally higher than sunny days (i.e. under direct solar radiation) at all phenophases with the differences were smaller in the morning and late afternoon (Fig. 2.5 a - d). As compared with direct solar condition, GCC values extracted from images under diffuse solar condition experienced a more complicated diurnal variation. Moreover, the temporal structure of diurnal GCC was flipped from concave to convex (Fig. 2.5 c and d) or varied more flatted (Fig 2.5 a and b), besides overall GCC values increased under diffuse solar condition. The difference in GCC values between direct and diffuse conditions was the smallest at ‘dry pasture’ among four phenophases.

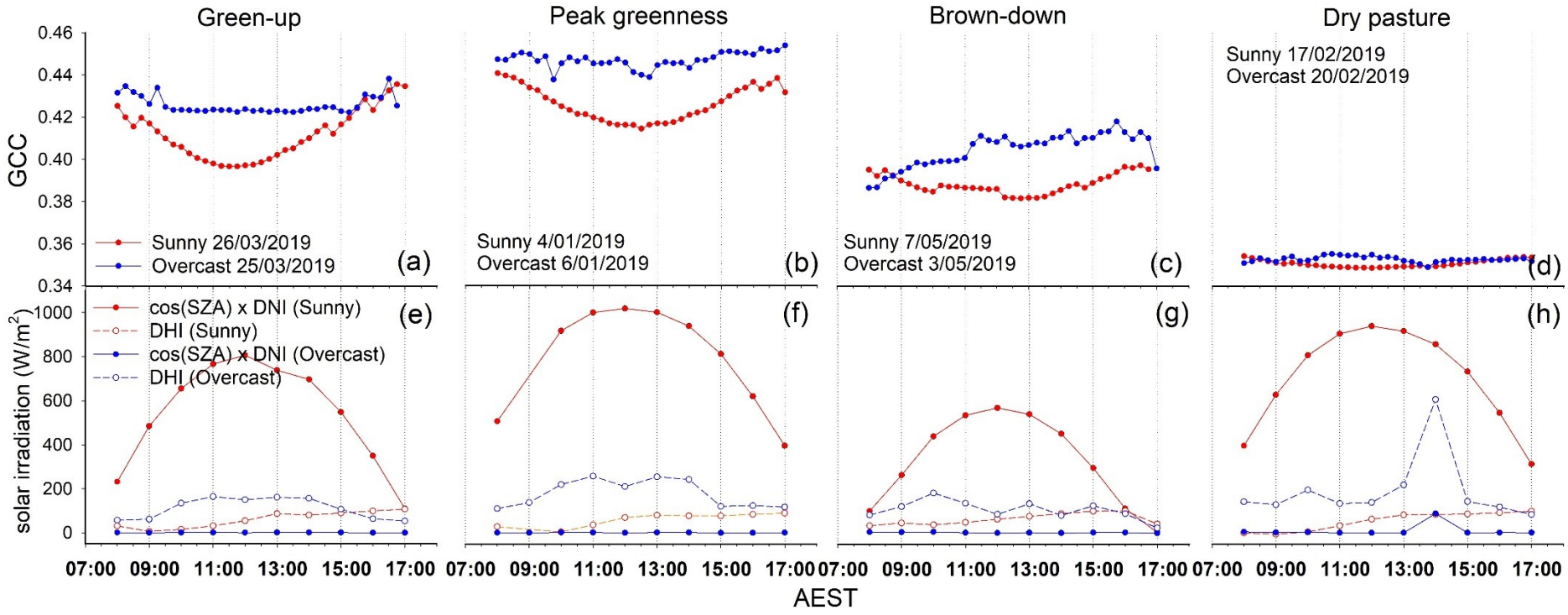

Figure 2.5 Diurnal GCC profiles (a - d) and solar radiance components (DHI and cos (SZA) x DNI) (e - h) under sunny and cloudy weather conditions for different phenophases at Campbelltown. Red and blue points and lines denote GCC values and solar radiance components under sunny days and overcast days, respectively. The temporal locations of these example days at the seasonal GCC profile throughout the entire study period were shown in Fig 2.A1.

2.3.3 Diurnal GCC compositing using min SZA method and per90

To reduce the influence of diurnal and weather-related variations in scene illumination on GCC values for seasonal GCC dynamic analyses, we needed to design a method to composite diurnal GCC values from optimal and stable illumination images for daily representation of pasture greenness. According to the results shown in Figs. 2.4 to 2.5, the images taken under optimal illumination conditions (e.g. noon-time or sunny days) always had lower GCC values as compared with sub-optimal illumination (e.g. early morning and afternoon, or overcast days). Therefore, we proposed a three-day moving window method based on the timing of minimum SZA, i.e. min SZA method. It assigns the average GCC values, which less than the 10^{th} percentile of GCC values within a four-hour window centered at the minimum SZA time, to the center day.

We compared compositing results of min SZA method and *per90* at four sites (Fig. 2.6). Comparisons with *per90*-GCC values (black points in Fig. 2.6) that followed the upper envelope of diurnal GCC profiles, daily GCC values obtained by the min SZA method tracked the bottom envelope of the seasonal GCC trajectory (green point in Fig. 2.6). Moreover, differences between two methods are more obvious during greenness transition periods compared with other phenophases (see red dotted lines in Fig. 2.6). For example, the differences in two methods sharply increased before the grass dried down at Rocklea and Campbelltown (Fig. 2.6 a and b), as well as before the grass reached the peak greenness at Redesdale and Mutdapilly (Fig.2.6 c and d). Though the shape of GCC profiles composited by two methods was similar, the variations in the amplitude of *per90*-GCC profiles were more obvious than min SZA method-GCC and their differences in magnitude greater during the greenness-transition periods. Even so, both two methods could efficiently filter outliers caused by non-phenological reasons, for example, abnormal GCC values caused by the worse illumination at dusk or lens problems around July 2019 at Campbelltown site and April o August 2019 at Redesdale site. (Fig. 2.6 b and c).

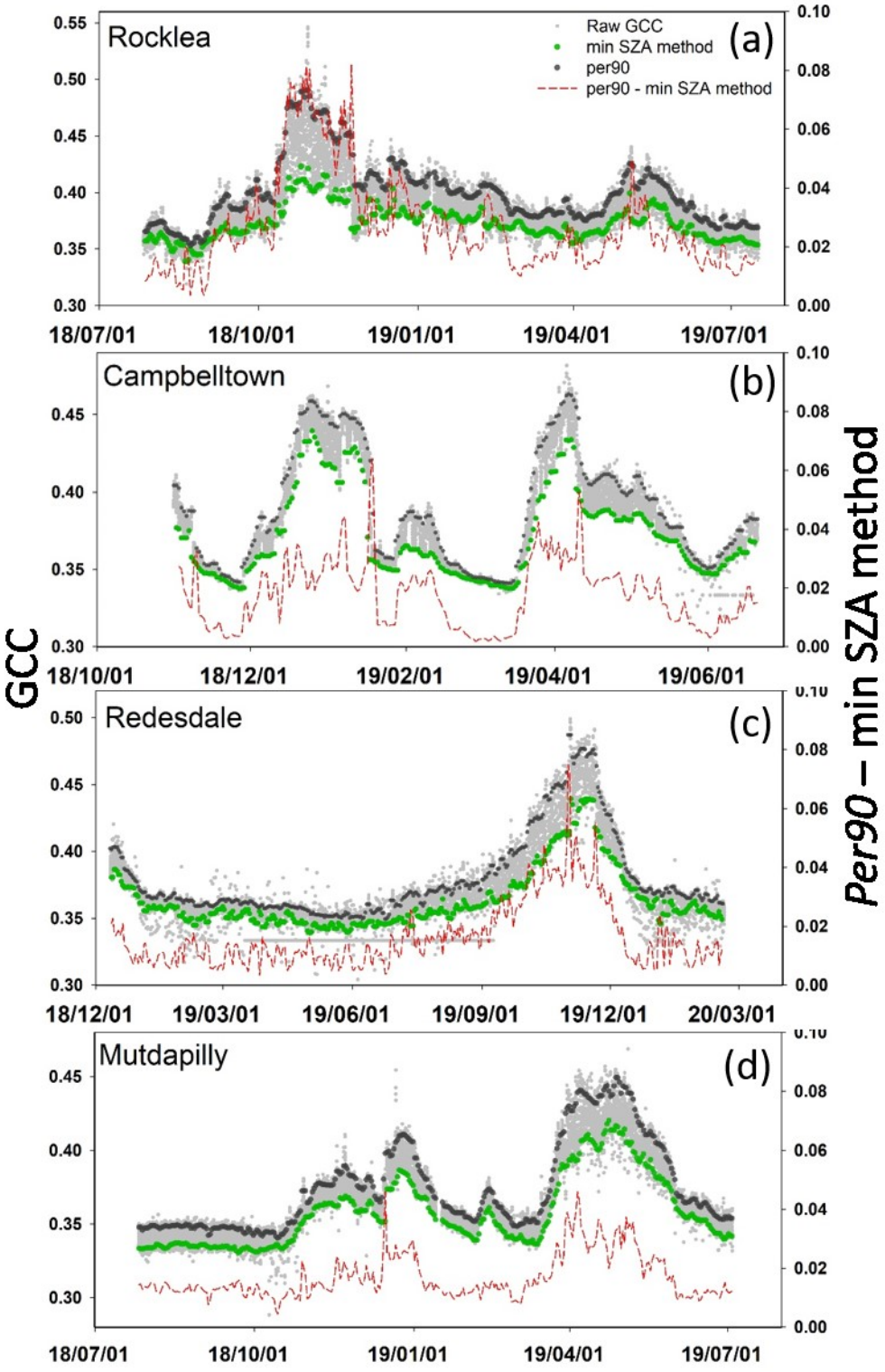

Figure 2.6 Compositing diurnal GCC as daily values by per90 and min SZA method at research sites. Grey small points represent diurnal GCC with 15 or 30 min time intervals; black and green points denote composting values by per90 and min SZA method, respectively. The red dotted lines represent the 'per90 – min SZA method' difference.

2.3.4 Differences in phenological metrics between min SZA method and per90

The specific phenological transition dates (i.e. SGS, PGS, and EGS) at each site were labelled in Fig. 2.7 and listed in Table 2.3. Across all four sites, we obtained 10 growing seasons and consequently 29 phenological transition dates (3 phenophases x 10 seasons, but no EGS at the last season for Campbelltown due to the lowest GCC values were at the end of the season and couldn't be assessed). There were five SGS and PGS, respectively, extracted from *per90*-GCC that occurred before those extracted from min SZA method-GCC time series. However, seven PGS from min SZA method-GCC were ahead of those from *per90*-GCC among all 10 seasons. This indicates that our compositing method based on min SZA tracked earlier PGS as compared with *per90* method. Also, for SGS and EGS, their differences between two methods were site dependent.

Fig. 2.8 presents the cross-site relationships and uncertainties (RMSE) between phenological transitional dates retrieved from SSA-reconstructed *per90*-GCC and min SZA method-GCC time series. We set our min SZA method as the x-axis to use it as a reference. Though all phenophases showed significant correlations between two methods with R^2= 0.99 across all sites, the response of GCC values on poor solar intensity introduced non-negligible uncertainties on phenological transitional dates retrieved from two methods. The uncertainties (RMSE) of using *per90*-GCC time series for retrieving SGS, EGS, PGS and LGS, as compared to the use of min SZA method-GCC, were 5.18, 4.07, 3.79, and 3.27 days respectively (Fig. 2.8).

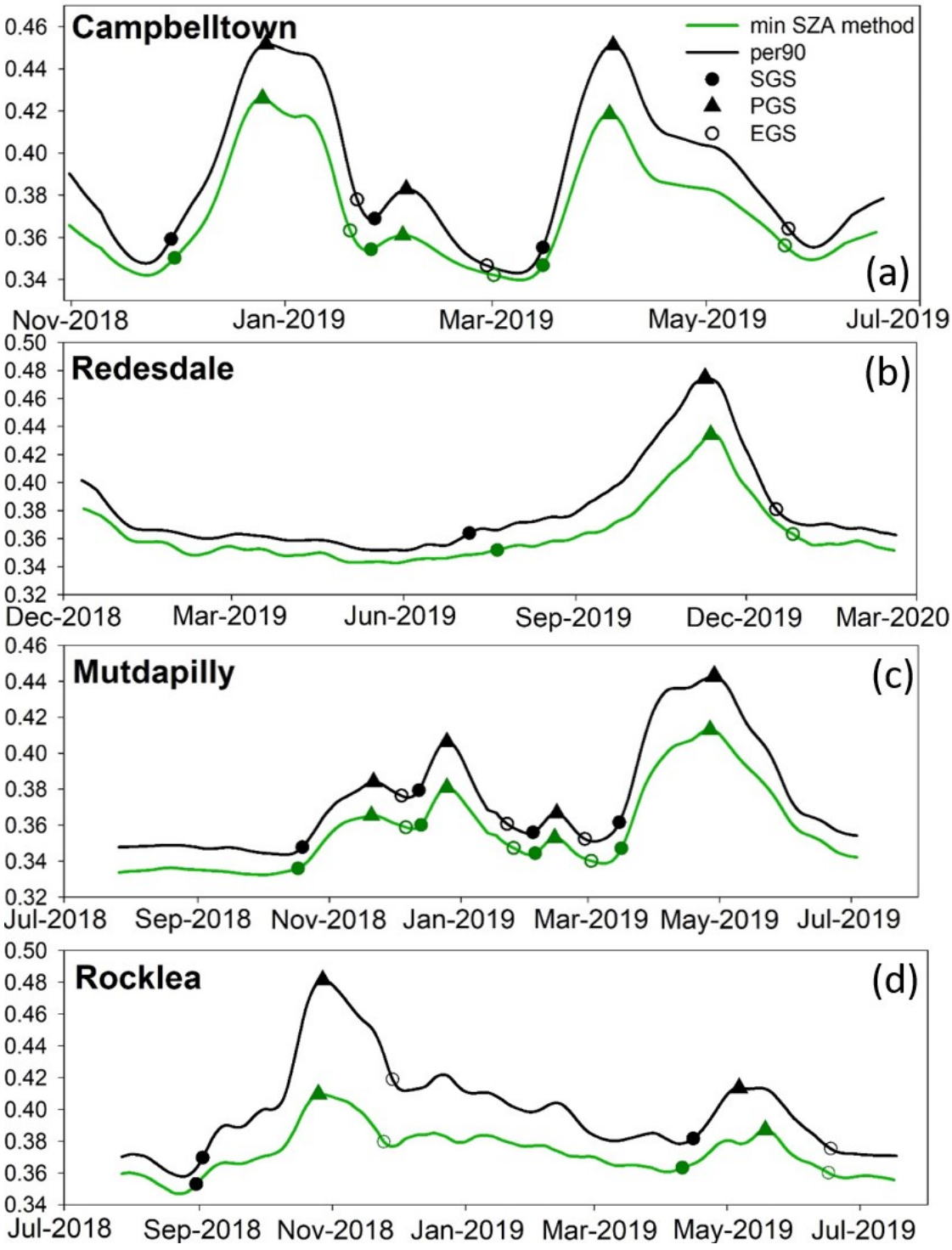

Figure 2.7 Seasonal GCC trajectories, which composited by min SZA method (green color) and per90 (black color) and then fitted by SSA method, at all sites. Phenological transition dates are labelled on each time series, including the start of growing season (SGS, solid circles), the peak of growing season (PGS, solid triangles), and the end of growing season (EGS, hollow circles).

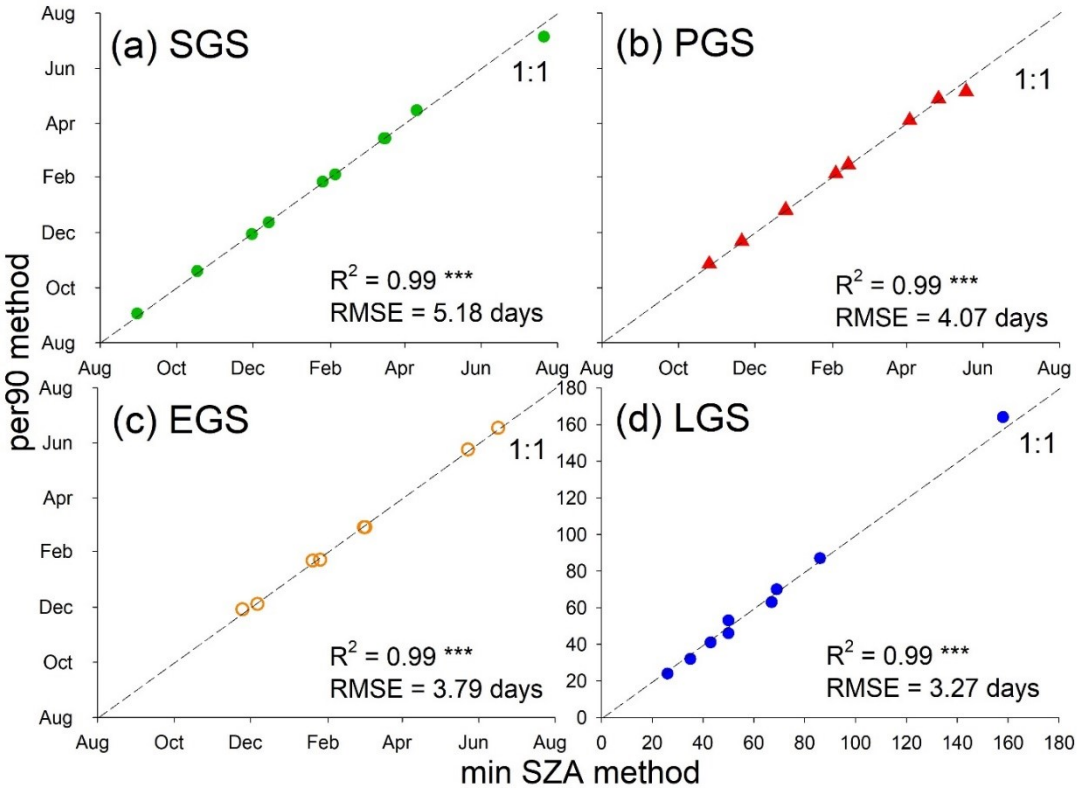

Figure 2.8 Cross-site comparison between the phenological transitional dates extracted from seasonal GCC trajectories obtained by min SZA method and per90 at four sites. SGS: Start of Growing Season; PGS: Peak of Growing Season; EGS: End of Growing Season; LGS: Length of Growing Season. *** denotes correlation significant at the 0.0001 p-value level.

Table 2.3 Comparison of differences in each phenological transition dates between min SZA method and *per90* at all sites. Bold font shows the earliest date for SGS, PGS, and EGS among two methods, as well as the longest LGS extracted from time series of daily GCC composited by min SZA method and *per90*, respectively. SGS: Start of Growing Season; PGS: Peak of Growing Season; EGS: End of Growing Season; LGS: Length of Growing Season. Phenological transition dates are corresponding to Fig. 2.8.

		Campbelltown		*Mutdapilly*		*Rocklea*		*Redesdale*	
		Min SZA method	*per 90*	*Min SZA method*	*per 90*	*Min SZA method*	*per 90*	*Min SZA method*	*per 90*
Season 1	*SGS*	334, 2018	**333, 2018**	**290, 2018**	292, 2018	**242, 2018**	245, 2018	202, 2019	**187, 2019**
	PGS	**359, 2018**	360, 2018	**324, 2018**	325, 2018	**298, 2018**	300, 2018	316, 2019	**313, 2019**
	EGS	**19, 2019**	21, 2019	340, 2018	**338, 2018**	**328, 2018**	332, 2018	360, 2019	**351, 2019**
	LGS	50 days	**53 days**	**50 days**	46 days	86 days	**87 days**	158 days	**164 days**
Season 2	*SGS*	**25, 2019**	26, 2019	347, 2018	**346, 2018**	**100, 2019**	105, 2019		
	PGS	**34, 2019**	35, 2019	359, 2018	359, 2018	138, 2019	**126, 2019**		
	EGS	60, 2019	**58, 2019**	25, 2019	**22, 2019**	**167, 2019**	168, 2019		
	LGS	**35 days**	32 days	**43 days**	41 days	**67 days**	63 days		
Season 3	*SGS*	74, 2019	74, 2019	35, 2019	**34, 2019**				
	PGS	**93, 2019**	94, 2019	**44, 2019**	45, 2019				
	EGS	**143, 2019**	144, 2019	61, 2019	**58, 2019**				
	LGS	69 days	**70 days**	**26 days**	24 days				
Season 4	*SGS*			75, 2019	**74, 2019**				
	PGS			**116, 2019**	118, 2019				

2.4 DISCUSSION

In this study, we investigated the influence of scene illumination changes, related to diurnal solar zenith angle changes and direct/diffuse solar radiation under different weather conditions, on the diurnal GCC values (Figs. 2.4 and 2.5). Our results showed scene illumination changes had pronounced effects on GCC values, despite this widely used index being designed for suppressing the effects of illumination. As such, we proposed a diurnal-to-daily compositing method to further suppress the illumination-effects on GCC calculated from pasture/ grassland phenocam images. By comparing with the prevalent approach, *per90*, our method has the ability to composite diurnal GCC values obtained from more optimal scene illumination conditions (Fig. 2.6). Although the difference between the two methods is small in the numerical value, there is still significant uncertainties in retrieving phenological transitional dates using *per90* when min SZA method was used as a reference (Fig. 2.7 and 2.8).

2.4.1 Effects of solar radiation intensity changes on diurnal pasture GCC

An interesting finding in this study is that the diurnal pattern of pasture GCC is concave (Fig. 2.4) and it is opposite to results from previous studies conducted in forest canopies. For example, Using digital camera images collected from deciduous and coniferous-dominated forests, a study showed GCC values started to increase around 6:00 am (local time) followed by stable values, and then decreased around 6:00 pm (local time) (Sonnentag et al., 2012). Similarly, diurnal GCC profiles were convex shaped from morning to afternoon, influenced by illumination changes and self-shading within forest canopies (Ahrends et al., 2008). Though the change in sun geometries caused by the earth's daily rotation was considered as a critical factor to influence phenocam scene illumination (Richardson et al., 2009; Sonnentag et al., 2012), there are fewer efforts to quantify the response of diurnal GCC profiles to scene illumination changes, especially in grassland/ pasture ecosystem. The solar zenith angle (SZA) corresponding to each image is included in the North America PhenoCam dataset. However, it was only used as an image quality-control filter (Richardson et al., 2018b). In this study, choosing SZA and cos (SZA) x DNI corresponding to each GCC value as quantitative metrics of diurnal sun angle and solar intensity changes, the comparison of diurnal GCC with

SZA and cos (SZA) x DNI profiles at an example site (Fig. 2.4) showed a clear pattern of the noontime images with smaller SZA and larger solar intensity had lower GCC values over a day than morning and afternoon images, which were under sub-optimal illumination due to larger SZA and lower solar intensity. Our result is consistent with responses of diurnal vegetation indices derived from 10-min Himawari-8 AHI sensor to diurnal range of solar zenith angles (Tran et al., 2020). In other words, our results demonstrated the diurnal pasture/ grassland GCC observed by phenocam also experienced significant BRDF (bidirectional reflectance distribution function) influences throughout the day, which was widely exhibited among geostationary (GEO) satellite derived vegetation indices (Ma et al., 2020; Proud et al., 2014).

In terms of weather-related illumination changes, we found lower illuminated images under diffuse illumination conditions led to higher GCC values compared to brighter images taken from direct illumination condition (Fig. 2.5). This finding is independent on grass phenophase stages. It is opposite to the conclusion drawn by previous studies conducted at forest ecosystems, where GCC values under sub-optimal illumination conditions (cloudiness and precipitation), were smaller than those under sunny sky condition (Sonnentag et al., 2012). Also, compared with sunlit conditions, GCC values generally decrease under shadowy conditions in forested canopies (Ide and Oguma, 2013). As for non-forested canopies, however, the situation was more consistent with our results. The diurnal GCC of the winter wheat under the case of diffuse atmospheric scattering was higher than those of the direct illumination condition (Li et al., 2019). Moreover, images collected from cloudy days had slightly greater GCC values than optimal illumination images at salt marsh canopy (O'Connell and Alber, 2016). This indicates the response of diurnal phenocam GCC on weather-related illumination changes varied among different types of vegetation. Also, the diurnal GCC patterns were less pronounced in overcast days, when diffuse solar radiation is more dominant. This is due to overcast conditions with weak and relatively stable solar intensity during the whole day, so the sun-angle effect has less impact on diurnal GCC pattern.

The physical reasons that near solar noon and clear-sky observations, related to greater solar radiation intensities, resulted in lower GCC values, while the larger

SZA conditions and overcast sky yielded higher GCC values are not fully clear at present, but here we provided some clues for our results. The changes in the proportion of sunlit grass and background materials, e.g., bare soil and standing litters, in phenocam imagery might be one of the potential causes. In forest canopies, larger SZA tends to cause lots of inter-crown shadows and consequently lower GCC, while smaller SZA around solar noon causes the maximum sunlit leaves and thus higher GCC values. In grass canopies, however, there is more sunlit background and less unlit grass at noontime with smaller SZA, hence lowering GCC values. In contrast, sunlit grasses dominate the images with soil background materials covered by shadows in early morning and late afternoon with larger SZA, so GCC values are higher. For example, a previous study showed the Normalized Difference Vegetation Index (NDVI) observed from an incomplete cotton canopy using multimodular radiometer also has the same response to diurnal SZA changes like our phenocam GCC did (Huete, 1987). That is a higher proportion of sunlit soil caused by small SZA tended to lower NDVI values. Considering the functional differences between NDVI and GCC, however, there needs to be more research carried out to determine if these explanations are accurate or plausible to interpret diurnal GCC patterns in pasture/ grasslands.

2.4.2 Statistical methodology of compositing GCC over pastures

Current temporal compositing schemes for phenocam greenness observations are designed to minimize the influence of variations in scene illumination on diurnal greenness indices. A prevalent GCC compositing method used by most phenocam researchers (Luo et al., 2018; Peter et al., 2018; Richardson et al., 2018b; Seyednasrollah et al., 2019; Vrieling et al., 2018) is the *per90* technique, proposed from extensive analyses at many forest canopy sites (Sonnentag et al., 2012). It assigns the 90^{th} percentile of all daytime GCC values within a three-day window to the centre day as its daily value. As with most of the maximum value compositing (MVC) methods, the logic behind this method is to restrict the sun-angle effect by selecting observations near solar noon where they maintain moderate variations. The results in this study presented, however, show lower GCC values found at smaller SZA and stronger solar intensities encountered at local solar noon and clear sky conditions, with the higher GCC values occurring at the beginning/ end of a day

and overcast days (Figs. 2.4 and 2.5). These findings motivated us to propose an alternative approach that only considered images collected around the time of minimum SZA when compositing diurnal GCC to daily value at grassland/ pasture ecosystem, in which images were taken under optimal illumination and moderate sun angle variations.

An ideal diurnal-daily compositing method should select GCC values from images taken under optimal illumination condition to represent the vegetation greenness on that day. According to Fig. 2.6, composited GCC values by *per90* kept firmly tracked the upper envelope of diurnal GCC trajectories, or opposite to the min SZA method. This indicates the *per90* method tends to choose GCC values from early morning or late afternoon images, in which the scene illumination is more susceptible to uncertain factors (i.e. the shadows caused by surrounding objectives due to large SZA and camera geometry). Also, considering GCC values under diffuse radiation (i.e. cloudy scene) tend to be higher than under direct radiation (i.e. sunlit scene) (Fig. 2.5), the *per90* approach selected GCC values from cloudy scenes instead of sunny images. However, our method based on minimum SZA timing can avoid these impacts. First, GCC from morning and afternoon images can be excluded by opening a 4-hour window centred at minimum SZA timing. And then, by averaging GCC less than the 10^{th} percentile of all GCC values within this 4-hour window, GCC extracted from images under diffuse radiation condition could be excluded further. Additionally, it is the difference between our method and widely used *mean* mid-day (*mmd*, e.g. mean GCC values between 10:00 and 14:00 h local time), that is we didn't consider all GCC values around minimum SZA timing (i.e. around noon-time) but only values less than the 10^{th} percentile among these values. In the other words, though phenocam images under high SZA (i.e., early morning and late afternoon) could be excluded by opening time window centred on minimum SZA (i.e., solar noon), sub-optimal illumination images remain mixed with optimal illumination images (e.g., cloudy vs. clear-sky) within the minimum SZA-window, especially at cloudy days. Therefore, using the 10^{th} percentile as an empirical threshold could further select as small as possible GCC values, with optimal illumination conditions, as the daily extraction of grass greenness. The result from a phenocam study conducted at a salt marsh site is

consistent with our finding. They also found the *per90* approach introduced considerable noise to GCC time series profiles by selecting data from cloudy scenes and substituting these for data with optimal scene illuminations (O'Connell and Alber, 2016). Moreover, the *per90* method demonstrated that it is more susceptible to outliers than to ideal values because it closely tracks the extreme upper values in the data (Richardson et al., 2018a). Furthermore, the *per90* method caused around 3-5 days uncertainty in retrieving pasture phenological metrics (using our method as reference), especially for SGS (quantitatively, with the highest RMSE = 5.18 days) and PGS (qualitatively, with 70% *per90*-PGS lagged behind min SZA method - PGS) (Fig. 2.8 and Table 2.3). These uncertainties are non-negligible for pasture/ grassland ecosystems, which generally experienced subtle phenological transition during a short-term period.

2.5 CONCLUSION

An important finding in this study is the structure of diurnal pasture GCC profiles, characterized as a concave pattern over the course of a day, with smaller SZA and greater solar intensities resulting in lower GCC values; while larger SZA and weaker solar intensities of early morning and afternoon yielded higher GCC values. This was opposite with diurnal greenness indices derived from forested canopies. Additionally, the comparison of GCC under various weather conditions and variable diffuse and direct illumination conditions showed a clear pattern of diffuse illumination providing larger GCC values than direct illumination condition. Considering the unique diurnal GCC temporal pattern at pasture canopy as compared with forest, the maximum value compositing (MVC) method would no longer be applicable since the highest GCC value may occur at the largest SZA near sunrise and sunset periods with sub-optimal illumination conditions. Given this, we proposed a compositing approach based on minimum SZA to suppress the effects of scene illumination changes on diurnal GCC and highly recommend using this method as a diurnal-to-daily compositing approach for phenocam observations in grassland/ pasture canopy. As the applications of the digital camera for monitoring the phenological status of grassland and agriculture have increased in recent decades, in future studies, the technical analyses about the response of camera

observations to external non-biotic impact factors at canopies dominated by non-forest vegetation types should receive much more attention.

2.6 REFERENCES

Ahrends, H.E., Bräugger, R., Stöckli, R., Schenk, J., Michna, P., Jeanneret, F., Wanner, H., Eugster, W., 2008, 'Quantitative phenological observations of a mixed beech forest in northern Switzerland with digital photography', J. Geophys. Res. Biogeosciences 113, 1–11. https://doi.org/10.1029/2007JG000650

Ahrends, H.E., Etzold, S., Kutsch, W.L., Stoeckli, R., Bruegger, R., Jeanneret, F., Wanner, H., Buchmann, N., Eugster, W., 2009, 'Tree phenology and carbon dioxide fluxes: Use of digital photography for process-based interpretation at the ecosystem scale', Clim. Res. 39, 261–274. https://doi.org/10.3354/cr00811

Brown, L.A., Dash, J., Ogutu, B.O., Richardson, A.D., 2017, 'On the relationship between continuous measures of canopy greenness derived using near-surface remote sensing and satellite-derived vegetation products', Agric. For. Meteorol. https://doi.org/10.1016/j.agrformet.2017.08.012

Browning, D.M., Karl, J.W., Morin, D., Richardson, A.D., Tweedie, C.E., 2017a, 'Phenocams bridge the gap between field and satellite observations in an arid grassland ecosystem', Remote Sens. 9. https://doi.org/10.3390/rs9101071

Browning, D.M., Karl, J.W., Morin, D., Richardson, A.D., Tweedie, C.E., 2017b, 'Phenocams bridge the gap between field and satellite observations in an arid grassland ecosystem', Remote Sens. https://doi.org/10.3390/rs9101071

Cheng, H.D., Jiang, X.H., Sun, Y., Wang, J., 2001, 'Color image segmentation: Advances and prospects', Pattern Recognit. 34, 2259–2281. https://doi.org/10.1016/S0031-3203(00)00149-7

Cui, T., Martz, L., Lamb, E.G., Zhao, L., Guo, X., 2019, 'Comparison of Grassland Phenology Derived from MODIS Satellite and PhenoCam Near-Surface Remote Sensing in North America', Can. J. Remote Sens. 45, 707–722. https://doi.org/10.1080/07038992.2019.1674643

Fisher, J.I., Mustard, J.F., 2007, 'Cross-scalar satellite phenology from ground, Landsat, and MODIS data', Remote Sens. Environ. 109, 261–273. https://doi.org/10.1016/j.rse.2007.01.004

Gautier, C., Diak, G., Masse, S., 1980, 'A simple physical model to estimate incident

solar-radiation at the surface from GOES satellite data', J. Appl. Meteorol. 19, 1005–1012. https://doi.org/10.1175/15200450(1980)019<1005:ASPMTE>2.0.CO;2

Gillespie, A.R., Kahle, A.B., Walker, R.E., 1987, 'Color enhancement of highly correlated images. II. Channel ratio and “chromaticity” transformation techniques', Remote Sens. Environ. 22, 343–365. https://doi.org/10.1016/0034-4257(87)90088-5

Huete, A.R., 1987, 'Soil and sun angle interactions on partial canopy spectra', Int. J. Remote Sens. 8, 1307–1317. https://doi.org/10.1080/01431168708954776

Hufkens, K., Friedl, M., Sonnentag, O., Braswell, B.H., Milliman, T., Richardson, A.D., 2012, 'Linking near-surface and satellite remote sensing measurements of deciduous broadleaf forest phenology', Remote Sens. Environ. https://doi.org/10.1016/j.rse.2011.10.006

Ide, R., Oguma, H., 2013, 'Ecological Informatics A cost-effective monitoring method using digital time-lapse cameras for detecting temporal and spatial variations of snowmelt and vegetation phenology in alpine ecosystems', Ecol. Inform. 16, 25–34. https://doi.org/10.1016/j.ecoinf.2013.04.003

Ide, R., Oguma, H., 2010, 'Use of digital cameras for phenological observations', Ecol. Inform. 5, 339–347. https://doi.org/10.1016/j.ecoinf.2010.07.002

Julitta, T., Cremonese, E., Migliavacca, M., Colombo, R., Galvagno, M., Siniscalco, C., Rossini, M., Fava, F., Cogliati, S., Morra di Cella, U., Menzel, A., 2014, 'Using digital camera images to analyse snowmelt and phenology of a subalpine grassland', Agric. For. Meteorol. 198–199, 116–125. https://doi.org/10.1016/j.agrformet.2014.08.007

Kurc, S.A., Benton, L.M., 2010, 'Digital image-derived greenness links deep soil moisture to carbon uptake in a creosotebush-dominated shrubland', J. Arid Environ. 74, 585–594. https://doi.org/10.1016/j.jaridenv.2009.10.003

Li, Q., Chen, X., Chen, J., 2019, 'A Method to Improve the GCC Series of Phenology Cameras Based on Histogram Features Using Multiple Linear Regression', Int. Geosci. Remote Sens. Symp. 6606–6609.

https://doi.org/10.1109/IGARSS.2019.8898529

Liu, Y., Wu, C., Sonnentag, O., Desai, A.R., Wang, J., 2020, 'Using the red chromatic coordinate to characterize the phenology of forest canopy photosynthesis', Agric. For. Meteorol. 285–286, 107910. https://doi.org/10.1016/j.agrformet.2020.107910

Luo, Y., El-Madany, T.S., Filippa, G., Ma, X., Ahrens, B., Carrara, A., Gonzalez-Cascon, R., Cremonese, E., Galvagno, M., Hammer, T.W., Pacheco-Labrador, J., Martín, M.P., Moreno, G., Perez-Priego, O., Reichstein, M., Richardson, A.D., Römermann, C., Migliavacca, M., 2018, 'Using near-infrared-enabled digital repeat photography to track structural and physiological phenology in Mediterranean tree-grass ecosystems', Remote Sens. https://doi.org/10.3390/rs10081293

Ma, X., Huete, A., Moran, S., Ponce-Campos, G., Eamus, D., 2015, 'Abrupt shifts in phenology and vegetation productivity under climate extremes', J. Geophys. Res. Biogeosciences 120, 2036–2052. https://doi.org/10.1002/2015JG003144

Ma, X., Huete, A., Tran, N.N., Bi, J., Gao, S., Zeng, Y., 2020, 'Sun-angle effects on remote-sensing phenology observed and modelled using himawari-8', Remote Sens. 12. https://doi.org/10.3390/RS12081339

Meyer, G.E., Neto, J.C., 2008, 'Verification of color vegetation indices for automated crop imaging applications', Comput. Electron. Agric. 63, 282–293. https://doi.org/10.1016/j.compag.2008.03.009

Mizunuma, T., Wilkinson, M., L. Eaton, E., Mencuccini, M., I. L. Morison, J., Grace, J., 2013, 'The relationship between carbon dioxide uptake and canopy colour from two camera systems in a deciduous forest in southern England', Funct. Ecol. 27, 196–207. https://doi.org/10.1111/1365-2435.12026

Moore, C.E., Brown, T., Keenan, T.F., Duursma, R.A., Van Dijk, A.I.J.M., Beringer, J., Culvenor, D., Evans, B., Huete, A., Hutley, L.B., Maier, S., Restrepo-Coupe, N., Sonnentag, O., Specht, A., Taylor, J.R., Van Gorsel, E., Liddell, M.J., 2016, 'Reviews and syntheses: Australian vegetation phenology: New insights from satellite remote sensing and digital repeat photography', Biogeosciences.

https://doi.org/10.5194/bg-13-5085-2016

Morisette, J.T., Richardson, A.D., Knapp, A.K., Fisher, J.I., Graham, E.A., Abatzoglou, J., Wilson, B.E., Breshears, D.D., Henebry, G.M., Hanes, J.M., Liang, L., 2009, 'Tracking the rhythm of the seasons in the face of global change: phenological research in the 21st century', Front. Ecol. Environ. 7, 253–260. https://doi.org/10.1890/070217

Nagai, S., Ichie, T., Yoneyama, A., Kobayashi, H., Inoue, T., Ishii, R., 2016a, 'Ecological Informatics Usability of time-lapse digital camera images to detect characteristics of tree phenology in a tropical rainforest', Ecol. Inform. 32, 91–106. https://doi.org/10.1016/j.ecoinf.2016.01.006

Nagai, S., Nasahara, K.N., Inoue, T., Saitoh, T.M., Suzuki, R., 2016b, 'Review: advances in in situ and satellite phenological observations in Japan. Int. J. Biometeorol', 60, 615–627. https://doi.org/10.1007/s00484-015-1053-3

Nann, S., Riordan, C., 1991, 'Solar spectral irradiance under clear and cloudy skies: measurements and a semiempirical model', J. Appl. Meteorol. 30, 447–462. https://doi.org/10.1175/1520-0450(1991)030<0447:SSIUCA>2.0.CO;2

O'Connell, J.L., Alber, M., 2016, 'A smart classifier for extracting environmental data from digital image time-series: Applications for PhenoCam data in a tidal salt marsh', Environ. Model. Softw. 84, 134–139. https://doi.org/10.1016/j.envsoft.2016.06.025

Pérez, A.J., López, F., Benlloch, J. V., Christensen, S., 2000, 'Colour and shape analysis techniques for weed detection in cereal fields', Comput. Electron. Agric. 25, 197–212. https://doi.org/10.1016/S0168-1699(99)00068-X

Peter, J.S., Hogland, J., Hebblewhite, M., Hurley, M.A., Hupp, N., Proffitt, K., 2018, 'Linking phenological indices from digital cameras in Idaho and Montana to MODIS NDVI', Remote Sens. 10, 1–15. https://doi.org/10.3390/rs10101612

Proud, S.R., Zhang, Q., Schaaf, C., Fensholt, R., Rasmussen, M.O., Shisanya, C., Mutero, W., Mbow, C., Anyamba, A., Pak, E., Sandholt, I., 2014, 'The normalization of surface anisotropy effects present in SEVIRI reflectances by using the MODIS BRDF method', IEEE Trans. Geosci. Remote Sens. 52, 6026–

6039. https://doi.org/10.1109/TGRS.2013.2294602

Richardson, A.D., Hollinger, D.Y., Dail, D.B., Lee, J.T., Munger, J.W., O'Keefe, J., 2009, 'Influence of spring phenology on seasonal and annual carbon balance in two contrasting New England forests', Tree Physiol. 29, 321–331. https://doi.org/10.1093/treephys/tpn040

Richardson, A.D., Hufkens, K., Milliman, T., Aubrecht, D.M., Chen, M., Gray, J.M., Johnston, M.R., Keenan, T.F., Klosterman, S.T., Kosmala, M., Melaas, E.K., Friedl, M.A., Frolking, S., 2018a, 'Tracking vegetation phenology across diverse North American biomes using PhenoCam imagery', Sci. Data 5, 1–24. https://doi.org/10.1038/sdata.2018.28

Richardson, A.D., Hufkens, K., Milliman, T., Frolking, S., 2018b, 'Intercomparison of phenological transition dates derived from the PhenoCam Dataset V1.0 and MODIS satellite remote sensing', Sci. Rep. 8. https://doi.org/10.1038/s41598-018-23804-6

Richardson, A.D., Jenkins, J.P., Braswell, B.H., Hollinger, D.Y., Ollinger, S. V., Smith, M.L., 2007, 'Use of digital webcam images to track spring green-up in a deciduous broadleaf forest', Oecologia. https://doi.org/10.1007/s00442-006-0657-z

Richardson, A.D., Raswell, B.O.H.B., Ollinger, D.A.Y.H., Enkins, J.U.P.J., 2009, 'Near-surface remote sensing of spatial and temporal variation in canopy phenology', 19, 1417–1428.

Rutishauser, T., Luterbacher, J., Jeanneret, F., Pfister, C., Wanner, H., 2007, 'A phenology-based reconstruction of interannual changes in past spring seasons', J. Geophys. Res. Biogeosciences 112. https://doi.org/10.1029/2006JG000382

Seyednasrollah, B., Young, A.M., Hufkens, K., Milliman, T., Friedl, M.A., Frolking, S., Richardson, A.D., 2019, 'Tracking vegetation phenology across diverse biomes using PhenoCam imagery: The PhenoCam Dataset v2.0', Sci. Data 1–11. https://doi.org/10.1038/s41597-019-0229-9

Sonnentag, O., Detto, M., Vargas, R., Ryu, Y., Runkle, B.R.K., Kelly, M., Baldocchi, D.D., 2011, 'Tracking the structural and functional development of a perennial

pepperweed (Lepidium latifolium L.) infestation using a multi-year archive of webcam imagery and eddy covariance measurements', Agric. For. Meteorol. 151, 916–926. https://doi.org/10.1016/j.agrformet.2011.02.011

Sonnentag, O., Hufkens, K., Teshera-Sterne, C., Young, A.M., Friedl, M., Braswell, B.H., Milliman, T., O'keefe, J., Richardson, A.D., 2012, 'Digital repeat photography for phenological research in forest ecosystems', Agric. For. Meteorol. 152, 159–177. https://doi.org/10.1016/j.agrformet.2011.09.009

Sparks, T.H., Menzel, A., 2002, 'Observed changes in seasons: An overview', Int. J. Climatol. 22, 1715–1725. https://doi.org/10.1002/joc.821

Templ, B., Koch, E., Bolmgren, K., Ungersböck, M., Paul, A., Scheifinger, H., Rutishauser, T., Busto, M., Chmielewski, F.M., Hájková, L., Hodzić, S., Kaspar, F., Pietragalla, B., Romero-Fresneda, R., Tolvanen, A., Vučetič, V., Zimmermann, K., Zust, A., 2018, 'Pan European Phenological database (PEP725): a single point of access for European data', Int. J. Biometeorol. 62, 1109–1113. https://doi.org/10.1007/s00484-018-1512-8

Toomey, M., Friedl, M.A., Frolking, S., Hufkens, K., Klosterman, S., Sonnentag, O., Baldocchi, D.D., Bernacchi, C.J., Biraud, S.C., Bohrer, G., Brzostek, E., Burns, S.P., Coursolle, C., Hollinger, D.Y., Margolis, H.A., McCaughey, H., Monson, R.K., Munger, J.W., Pallardy, S., Phillips, R.P., Torn, M.S., Wharton, S., Zeri, M., Richardson, A.D., 2015, 'Greenness indices from digital cameras predict the timing and seasonal dynamics of canopy-scale photosynthesis', Ecol. Appl. https://doi.org/10.1890/14-0005.1

Tran, N.N., Huete, A., Nguyen, H., Grant, I., Miura, T., Ma, X., Lyapustin, A., Wang, Y., Ebert, E., 2020, 'Seasonal Comparisons of Himawari-8 AHI and MODIS Vegetation Indices over Latitudinal Australian Grassland Sites', Remote Sens. 12, 2494. https://doi.org/10.3390/rs12152494

Vrieling, A., Meroni, M., Darvishzadeh, R., Skidmore, A.K., Wang, T., Zurita-Milla, R., Oosterbeek, K., O'Connor, B., Paganini, M., 2018, 'Vegetation phenology from Sentinel-2 and field cameras for a Dutch barrier island', Remote Sens. Environ. 215, 517–529. https://doi.org/10.1016/j.rse.2018.03.014

Wang, D., Liang, S., 2008, 'Singular spectrum analysis for filling gaps and reducing uncertainties of modis land products', Int. Geosci. Remote Sens. Symp. 5, 558–561. https://doi.org/10.1109/IGARSS.2008.4780153

Watson, C.J., 2016, 'Exploring the seasonal dynamics of Australian temperate grasslands through phenocam imagery, remote sensing and field data'.

Watson, C.J., Restrepo-Coupe, N., Huete, A.R., 2019, 'Multi-Scale Phenology of Temperate Grasslands: Improving Monitoring and Management With Near-Surface Phenocams', Front. Environ. Sci. 7, 14. https://doi.org/10.3389/fenvs.2019.00014

Wingate, L., Ogeé, J., Cremonese, E., Filippa, G., Mizunuma, T., Migliavacca, M., Moisy, C., Wilkinson, M., Moureaux, C., Wohlfahrt, G., Hammerle, A., Hörtnagl, L., Gimeno, C., Porcar-Castell, A., Galvagno, M., Nakaji, T., Morison, J., Kolle, O., Knohl, A., Kutsch, W., Kolari, P., Nikinmaa, E., Ibrom, A., Gielen, B., Eugster, W., Balzarolo, M., Papale, D., Klumpp, K., Köstner, B., Grünwald, T., Joffre, R., Ourcival, J.M., Hellstrom, M., Lindroth, A., George, C., Longdoz, B., Genty, B., Levula, J., Heinesch, B., Sprintsin, M., Yakir, D., Manise, T., Guyon, D., Ahrends, H., Plaza-Aguilar, A., Guan, J.H., Grace, J., 2015, 'Interpreting canopy development and physiology using a European phenology camera network at flux sites', Biogeosciences 12, 5995–6015. https://doi.org/10.5194/bg-12-5995-2015

Woebbecke, D.M., Meyer, G.E., Von Bargen, K., Mortensen, D.A., 1995, 'Color indices for weed identification under various soil, residue, and lighting conditions', Trans. Am. Soc. Agric. Eng. https://doi.org/10.13031/2013.27838

Yan, D., Scott, R.L., Moore, D.J.P., Biederman, J.A., Smith, W.K., 2019, 'Understanding the relationship between vegetation greenness and productivity across dryland ecosystems through the integration of PhenoCam, satellite, and eddy covariance data', Remote Sens. Environ. 223, 50–62. https://doi.org/10.1016/j.rse.2018.12.029

Zeng, L., Wardlow, B.D., Xiang, D., Hu, S., Li, D., 2020, 'A review of vegetation phenological metrics extraction using time-series, multispectral satellite data',

Remote Sens. Environ. 237, 111511. https://doi.org/10.1016/j.rse.2019.111511

Zhang, X., Friedl, M.A., Schaaf, C.B., Strahler, A.H., Hodges, J.C.F., Gao, F., Reed, B.C., Huete, A., 2003, 'Monitoring vegetation phenology using MODIS', Remote Sens. Environ. 84, 471–475. https://doi.org/10.1016/S0034-4257(02)00135-9

2.7 APPENDIX

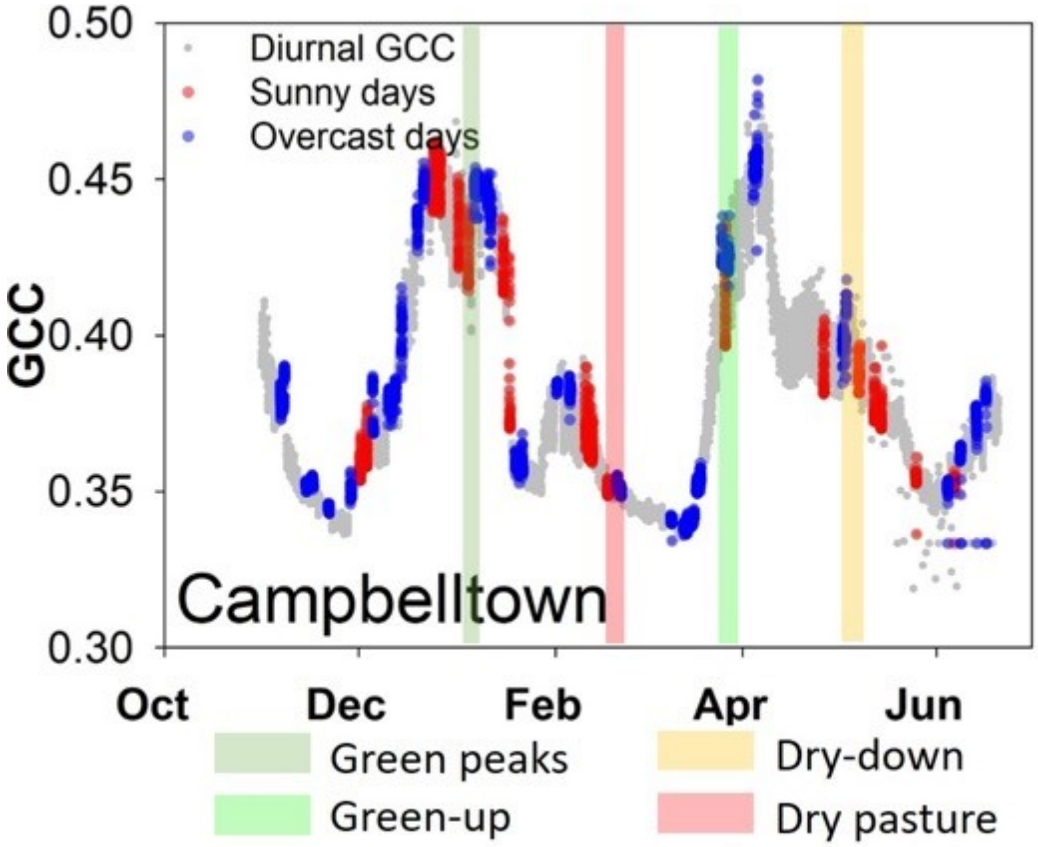

Figure 2.A 1 Seasonal time series of GCC with 15 min interval at Campbelltown. The sunny and cloudy days are highlighted by red and blue colours, respectively. The four pairs of adjacent days with clear and cloudy sky conditions were selected to compare their diurnal GCC values at different phenophases.

CHAPTER 3

Chapter 3 Multi-scales seasonal pasture grassland greenness observations from phenocam to satellites and relationships with grass pollen concentrations

3.1 INTRODUCTION

Grass pollen is the primary outdoor aeroallergen source, one which triggers allergic rhinitis and asthma across Australia (Davies et al., 2015). The prevalence of allergic rhinitis in Australia was the highest in a study conducted in adults aged between 20 and 44 across 15 countries. Meanwhile, Australia also has the highest prevalence of asthma around the world (Beggs et al., 2015). In terms of respiratory health, the impact of grass pollens on our next generation, a correlation between allergic rhinitis and asthma in children exhibiting sensitisation to grass pollen in late summer was observed in northern New South Wales (Bass et al., 2000). Therefore, increasingly studies have paid attention to the management of pollen allergen exposure to reduce the health and socioeconomic burden caused by these allergic diseases in Australia (Beggs et al., 2015; Devadas et al., 2018; Tng et al., 2010).

A valuable indicator for both current and future trends in allergenic grass pollen exposure, long-term grass pollen concentration records, measured using volumetric spore collection traps at sites, are suffering limitations pertaining to a sparsity of within-site pollen trap sampling and the requirement for intensive labour (Devadas et al., 2018). To further assist in the management of symptoms and disease, pollen forecast models have been developed to predict local pollen aerobiology using empirical or process-based approaches. Empirical forecast models, such as statistical approaches, aim to understand the effect of relevant factors such as temperature, precipitation, and relative humidity in influencing the patterns of pollen release based on their empirical interrelationships pollen concentrations (Laaidi 2001; Smith & Emberlin, 2006; Stach et al., 2008). Process-based models predict pollen release through modelling the processes of plant pollen phenology as influenced by changing weather conditions (Li et al., 2019; Zhang et al., 2015). However, both empirical and process-based models are focused on explanatory factors (e.g., metrological conditions) that impact the pattern and concentrations of pollen, rarely considering the available ecological information or phenological status (i.e., the timing of key plant phenophases) of allergenic plants. Actually, such information is vital to understanding the ecological and climate drivers of pollen aerobiology and to further predict its future trends (Devadas et al., 2018). On the other hand, the spatial representation of these forecast models is low due to the fact

that grass pollen concentrations are usually obtained from a fixed and relatively small number of pollen sampling stations (Khwarahm et al., 2017). Ecological information on the phenology of allergenic plants with finer spatial resolution over larger areas would therefore be deemed essential and useful.

Over the last half-century, the development of new satellite sensors and the increased availability of satellite remote sensing data of ecologically relevant landscape variables has provided a unique opportunity to estimate the phenological dynamics of vegetation on both a regional and a global scale (Crowley & Cardille, 2020; Lloyd, 1990; Ma et al., 2013; Reed et al., 1994; Watson, Restrepo-Coupe & Huete, 2019). This, therefore, would augment the coverage currently restricted to extant *in-situ* pollen trap networks. Increasingly studies have used satellite-driven vegetation indices to characterise important phenological variables related to pollen release. For example, the Normalised Difference Vegetation Index (NDVI) has been shown to be closely associated with the onset of birch flowering in Norway (Karlsen et al., 2009). A standard phenology product that used the Enhanced Vegetation Index (EVI) captured strong seasonal Juniperus greenness activity which is useful in the analysis of the preconditions for the timing and magnitudes of pollen release (Jeffrey et al., 2011). Similarly, there has been a strong correspondence of EVI greenness correlating with observations of grass pollen aerobiology data over sites in eastern Australia and northern France (Devadas et al., 2018). Moreover, the start of birch and grass pollen release was defined using the Medium Resolution Imaging Spectrometer (MERIS) Terrestrial Chlorophyll Index (MTCI) and showed large positive correlations with *in-situ* ground reference data across the UK (Khwarahm et al., 2017). This indicates that the greenness dynamics of allergenic plant species could be used to determine the timing of pollen release.

It is well known that satellite remote sensing has the advantage of examining vegetation changes consistently at both regional and global levels, but its ability in phenological studies is constrained by spatial resolution (i.e. pixel size) and temporal limitations (i.e. time intervals of satellite revisits) (Riihimäki, Luoto & Heiskanen, 2019; Watson, Restrepo-Coupe & Huete, 2019). Most of the vegetation phenology-pollen studies are thus based on coarse resolution satellite data such as Advanced Very-High Resolution Radiometer (AVHRR; 8 km, sub-daily) (Hogda et

al., 2002a); or MERIS; ~1 km, ≥ 3 days) (Khwarahm et al., 2017); Moderate Resolution Imaging Spectrometer (MODIS; ≥ 250 m, ≥ 8 days) (Devadas et al. 2018); or Medium Resolution Satellite (e.g. Landsat; 30 m, 16 days) (Li et al., 2019). However, some allergenic plant species, such as subtropical grass species in Australia, typify spatially heterogeneous and dramatically variable landscapes as their phenological dynamics are strongly driven by rainfall (Ma et al., 2013). The heterogeneity of the land surface (can potentially) influence the accuracy of allergenic grass phenology indicators derived from coarse spatial resolution satellite data (Devadas et al., 2018). For example, the grass may not be the dominant species in a 1x1 km pixel grid or even in a 250 m grid, especially for those urban domains in which pollen traps are often situated. Higher spatial resolution satellite data, such as Landsat, might be appropriate to describe such heterogeneous regions (Lugonja et al., 2019; Rapinel et al., 2019; Vrieling et al., 2018). However, finer resolution satellite acquisitions usually come at the cost of longer revisiting intervals (Vrieling et al., 2018). Such images generally result in relatively low temporal resolution and these sensors may only capture a small number of cloud-free images over the entire growing season (Liu et al., 2017). Some important phenological transition records in allergenic plant species might be lost due to the big data gap within or between growing seasons and, consequently, it is difficult to reconcile this incomplete phenological information with daily pollen concentration data. Thus, finer spatial and temporal resolution satellite data, as well as novel methods, are needed to bridge the gaps arising between scales.

In terms of the drawback of finite spatial resolution, the utility of Multi-Spectral Instrument (MSI) of Sentinel-2 mission with 10 m resolution (in four spectral bands) for retrieving vegetation phenology is good news, particularly for those scattered and relative tiny distributions of allergenic grass located in backyards or urban green spaces. Recent studies indicate the great advantages of Sentinel-2 data in retrieving phenology from semi-arid shrublands (Peng et al., 2021) and mapping tree and grass species (Rapinel et al., 2019). Vrieling et al. (2018) reported, as compared with commonly used medium resolution sensors, that Sentinel-2 data allows the retrieval of vegetation phenology with higher accuracy in those areas with intensive spatial heterogeneity (e.g., grasslands in Dutch barrier islands). As

for the limitations in effective temporal resolutions of moderate resolution and polar-orbiting satellite sensors, the hyper-temporal data (with 10 min intervals) from the Advanced Himawari Imager (AHI) aboard the Himawari-8 satellite has demonstrated great potential in improving the characterisation of vegetation phenology (Miura et al., 2019; Yan et al., 2019). Meanwhile, the improved spectral and spatial resolution (1000 m), as compared with previous geostationary satellite data, means that the Himawari-8 AHI attains comparable results to the commonly used and developed MODIS product, but with the added advantage of much finer temporal resolution (Tran et al., 2020). However, the utility of Sentinel-2 and Himawari-8 AHI data to characterise the relationships arising between grass phenology and grass pollen dynamics remains poorly investigated.

Compared with traditional satellite-based remote sensing, near-surface remote sensing using a consumer-grade visual camera (phenocam) can provide a continuous record of vegetation phenology with a high frequency (sub-daily; Fig. 3.1). One of the advantages that cannot be ignored is that the vegetation of interest can be directly monitored via phenocam. Therefore, a growing body of research has used phenocam images as a reference for surface vegetation dynamics to evaluate remote sensing phenology products and model simulations (Chen, Jin & Brown, 2019; Liu et al., 2017; Moore et al., 2016; Richardson et al., 2007; Zhang et al., 2020). In the northern hemisphere, phenocams have shown great promise in capturing phenological information about vegetation in a deciduous broadleaf forest (Hufkens et al., 2012a; Klosterman et al., 2014; Nagai et al., 2011), equatorial mangroves (Songsom et al., 2021), Brazilian cerrado (Alberton et al., 2014), and a regularly-flooded salt marsh (O'Connell & Alber, 2016). In Australia, phenocam data was demonstrated to be useful for monitoring temperate grassland dynamics and showed strong correlations with biomass estimates and satellite-based phenology (Watson, Restrepo-Coupe & Huete, 2019). In general, phenocam data provides a unique opportunity to bridge the gap between field observations and those from multiple resolution satellites, thereby improving our ability to quantify and predict the vegetation ecological dynamics across a range of biomes.

In this study, we use greenness observations from a set of phenocams in eastern Australian grasslands/pasture ecosystems as a surface grassland dynamics

reference, together with multiple sources of satellite data including Sentinel-2, MODIS, and Himawari-8 AHI (Fig. 3.1), as well as the grass pollen concentrations collected by pollen traps co-located with phenocam sites to investigate the following questions:

(1) To what extent does multi-resolution satellite data, at a pixel scale, obtain grass greenness information in heterogeneous landscapes?
(2) Whether Sentinel-2 data of finer resolution can obtain more accurate grass greenness information from heterogeneous landscapes than satellite data with coarse resolution, and whether such an advantage can be maintained at increased scales?
(3) What are the interrelationships between *in-situ* grass pollen concentrations and grass greenness as measured by phenocams and satellites across sites with different types of land cover?
(4) How do the spatial resolutions of satellites influence the relationship between grass pollen seasonality and satellite-observed grass greenness dynamics?
(5) How do temporal resolutions of satellite data influence the above relationships?

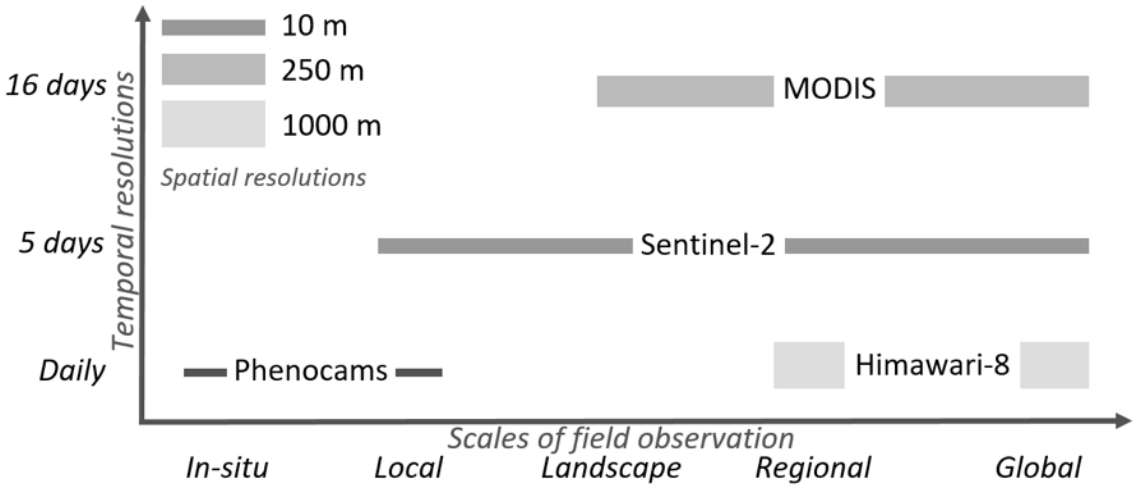

Figure 3.1 Scales of field observation, spatial and temporal resolution for remote sensing multi-sensors as used in this study.

3.2 Materials and Methods

3.2.1 Research sites and land cover types

We conducted this study at three phenocam sites, specifically Campbelltown, Mutdapilly, and Rocklea. Their locations and other related information are

described in greater detail in Chapter 2, Fig. 2.1 and Table 2.1. These sites were chosen for their relatively long-term phenocam observations. Also, these sites are characterised as having urban and rural types of land cover. Therefore, we could explore our research questions at different sites with both long-term and *in-situ* grassland greenness information as well as varied spatial heterogeneity.

The Dynamic Land Cover Dataset Version 2 (DLCDv2.1) (http://www.ga.gov.au/scientific-topics/earth-obs/accessing-satellite-imagery/landcover) with 250 m spatial resolution was used to assess the land cover type surrounding each site. We defined five composite classes based on the original land cover type of Dynamic Land Cover Dataset (DLCD) to perform a more direct comparison for vegetation dynamic variation at different spatial scales. These are:

[Grassland & Pasture]: Rain-fed pasture, closed tussock grassland, open tussock grassland, open hummock grassland, scattered shrubs and grasses and irrigated pasture.

[Urban & Built-up]: Mines and quarries and urban areas

[Cropland & Shrubland]: Rain-fed cropping, irrigated cropping, irrigated sugar, rain-fed sugar, and dense shrubland.

[Forest]: Open forest, closed forest, open woodland and woodland.

[Water body & wetland]: Lakes and dams, salt lakes and wetland.

The land cover distributions and percentage of the five composite classifications surrounding a research site within a 10 square kilometre area are shown in Fig. 3.2. Significant differences in the proportion of grass cover, considered a potential source of grass pollen, was proven to exist among these sites. The surroundings of the Mutdapilly site principally consisted of grassland and pasture cover, with the percentage of [Grassland & Pasture] being 73.11%; while the [Urban & Built-up] class is primarily present around the Rocklea site, with the percentage of grass being only 20.81%. Unlike the extreme situations presented in Mutdapilly and Rocklea, the [Grassland & Pasture] and [Urban & Built-up] classes are relatively evenly distributed around Campbelltown, with the percentage of grass cover at 30.21%.

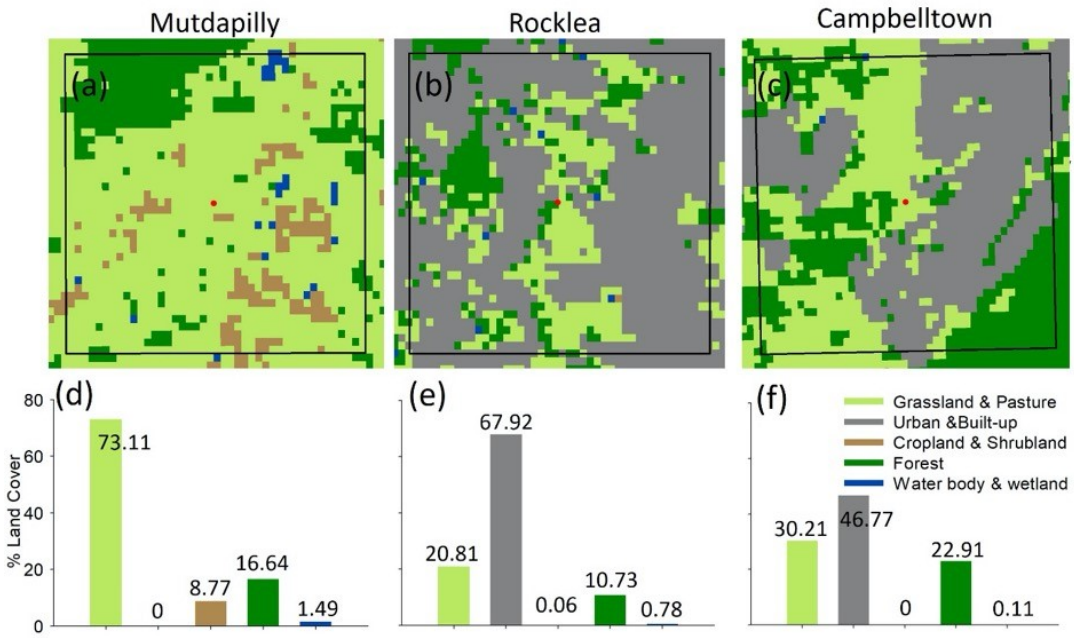

Figure 3.2 An overview of the heterogeneity of composite classes derived from DLCD within a 10 km × 10 km square area as demarcated by black lines surrounding the phenocam sites for Mutdapilly (a), Rocklea (b), and Campbelltown (c). The percentage land cover (%) is plotted as a colour-coded bar chart beneath every panel.

3.2.2 Phenocam greenness data

The phenocam imagery data used for this study has previously been described in detail in Chapter 2, including camera setup and imagery data processing. As for Chapter 2, we used the green chromatic coordinate (GCC) as the metric to represent pasture/grassland greenness at the *in-situ* scale. Using the minimum SZA method proposed in Chapter 2, we composited diurnal phenocam GCC to daily values to track the seasonal dynamics of pasture greenness. Furthermore, seasonally fitted GCC curves were obtained using the SSA (Singular Spectrum Analysis) method (Golyandina & Korobeynikov, 2014).

3.2.3 Multi-scale satellite data

Satellite data was used in this study, which was obtained from three sensors, namely the Sentinel-2 MSI aboard the Sentinel-2 satellite; the MODIS sensor aboard the Terra satellite; and the AHI aboard the Himawari-8 satellite. The satellite sensor spectral bands, wavelengths, temporal and spatial resolution used in this study are shown in Table 3.1.

3.2.3.1 Sentinel-2 data

The Sentinel-2 mission includes two satellites and frequent revisits of every single Sentinel-2 satellite occurs with a periodicity of every 10 days and thus the combined constellation revisiting interval is 5 days. The MSI has 13 spectral bands spanning from the visible to short wave infrared, and its spatial resolution varies from 10m to 60m depending on the particular spectral band viewed (Drusch et al., 2012).

We downloaded all available (partially) cloud-free acquisitions of Sentinel-2A data over specified research areas from 2018 to 2020 (https://scihub.copernicus.eu/dhus/#/home). A Sen2Cor processor (Louis et al., 2016) was used to perform atmospheric corrections to Top-Of-Atmosphere (TOA) Level-1C product and then the Level-2A (L2A) surface reflectance product was obtained which includes 10m, 20m and 60m spatial resolution bands. After this, for each image, L2A outputs were resampled at 10m spatial resolution for all bands also using Sen2Cor. Then the EVI was calculated from the 10m resolution spectral bands as follows:

$$EVI = 2.5 \times \frac{(NIR - RED)}{(NIR + 6 \times RED - 7.5 \times Blue + 1)} \tag{3.1}$$

where *NIR*, *RED* and *Blue* represent near-infrared, red and blue bands in terms of the L2A surface reflectance product. The EVI is thus a spectral surrogate of the vegetation greenness seasonal dynamic and is characterised by an improved sensitivity in high biomass regions and enhanced vegetation monitoring ability (Huete et al., 2002).

3.2.3.2 MODIS data

Another satellite data source was the 16-Day Terra MODIS Vegetation Indices product (MOD13Q1, 250m) which was acquired from the Oak Ridge National Laboratory Distributed Archive Center (DAAC) website (https://modis.ornl.gov/globalsubset/). The data were filtered based on the quality assurance (QA) flags provided in the quality control (QC) layers of the product. This product is processed for both atmospheric effects and BRDF (Bidirectional Reflectance Distribution Function) to standardise differences arising due to

variations in viewing and illumination angles. The 16-day composite data reduces the impact of clouds on long-term datasets. The EVI is derived from atmospherically corrected reflectance within the red, near-infrared, and blue wavebands. The MODIS EVI has been demonstrated to have a good dynamic range and sensitivity for monitoring spatial and temporal variations in vegetation, including grassy areas (Huete et al., 2002).

3.2.3.3 Himawari-8 AHI data

The AHI onboard the Himawari-8 geostationary (GEO) satellite offers observation data every 10 minutes for Full Disk (across the Asia-Pacific region) with spatial resolutions of 500m for the red spectral band, 1000m for visible and near-infrared bands, and 2000m for infrared bands, respectively (Bessho et al., 2016).

The gridded TOA reflectance data product was collected and processed by the NASA GeoNEX project (https://www.nasa.gov/geonex/about). The Multi-Angle Implementation of Atmospheric Correction (MAIAC) algorithm was used to derive the top-of-canopy directional surface reflectance with 10-min intervals (Lyapustin et al. 2012). The 500 m red band data was aggregated to match the 1000 m spatial resolution of the NIR and blue bands, and then, the EVI was calculated using equation 3. To further capture the clearly seasonal dynamics for H-8 AHI EVI from noisy daily values we employed the SSA method to obtain a fitted curve.

Table 3.1 Satellite sensor spectral bands, wavelength, temporal resolution, and spatial resolution used for the calculation of EVI within the established data period for this study.

Sensors	Band	Wavelength Band (µm)	Temporal Resolution	Spatial Resolution	Data period
Sentinel-2 MSI	4 (Red)	0.634 – 0.696	5 days	10 m	2018 – 2020
	8 (NIR)	0.727 – 0.939		10 m	
	2 (Blue)	0.426 – 0.558		10 m	
MODIS	1 (Red)	0.620 – 0.670	16 days	250 m	2018 – 2020
	2 (NIR)	0.841 – 0.876		250 m	
	3 (Blue)	0.459 – 0.479		250 m	
H-8 AHI	3 (Red)	0.63 – 0.66	10 min	500 m	2018
	4 (NIR)	0.85 – 0.87		1000 m	
	1 (Blue)	0.43 – 0.48		1000 m	

3.2.4 Grass pollen concentrations

Grass pollen traps are co-located with phenocams at Mutdapilly and Rocklea. The daily (24-hour period) atmospheric grass pollen concentrations (grains/m^3) recorded during observations for the period 2018 to 2020 were collected from the Mutdapilly and Rocklea sites following the most common method in Australia with Hirst-type volumetric pollen and spore trappers (Burkard Scientific Ltd, Uxbridge, UK), an approach that is described in detail in previous research (Haberle et al. 2014). We used the SSA method with window length $L = 10$ to smooth daily values so as to obtain the season90al trajectory of grass pollen concentrations for each site. Following this, the grass pollen peaks were extracted from these reconstructed seasonal profiles to conduct the analyses for time intervals arising between grass pollen peaks and grass greenness peaks as derived from the phenocam GCC and satellite EVI time series.

3.2.5 Analysis strategy

In this study, using spatial and temporal multi-scale remote sensing data in addition to grass pollen concentrations data, we explore the capacity of multi-scale satellite data to capture the seasonal grass greenness dynamics as compared with traditional *in-situ* phenocam grass cover observations and also the relationships arising between grass pollen seasons and these greenness observations across different remote sensing sensors (using the same scales for different sensors) and scales (same sensors for different scales).

To identify the phenocam view footprint in Sentinel-2 image, we first created a 'fishnet' with a 10m×10m grid-scale based on a Sentinel-2 image so that this fishnet can maintain the same geographic coordinate system with each subsequent Sentinel-2 image. Each grid in this fishnet corresponded to each pixel of a Sentinel-2 image. Then, we input this fishnet into Google Earth Pro to locate Sentinel-2 pixels surrounding the phenocam site. Combining hyper-resolution Google map and phenocam images we were able to identify a set of 3×3 Sentinel-2 pixels that were co-localised with the field of view of the phenocam. Finally, we used these 3×3 pixels to calculate grass EVI as a grass greenness value as measured by the Sentinel-2 at a phenocam footprint scale for subsequent comparisons with a phenocam GCC.

We also calculated EVI values from the MODIS and H-8 AHI images at their respective pixel scale to explore their performance in terms of recording grass greenness dynamics at their smallest scales (i.e., 250m and 1000m, respectively) by correlating their EVI to *in-situ* phenocam GCC. However, the one-pixel data obtained for MODIS and H-8 AHI could be impacted by non-ecological factors such as data QC or the existence of clouds within any given pixel. Therefore, we compared the agreements arising between phenocam GCC and satellite EVI at extensive scales. For Sentinel-2 and MODIS, research scales were extended to 10 km at all three sites (i.e., 1km, 3km, 5km, and 10km). Sentinel-2 and MODIS EVI values were calculated by averaging all pixels for each research scale. However, for Himawari-8 AHI, the research scale only extended to 3km (i.e., 1km and 3km) at Mutdapilly and Rocklea due to the issue of data availability at the Campbelltown site.

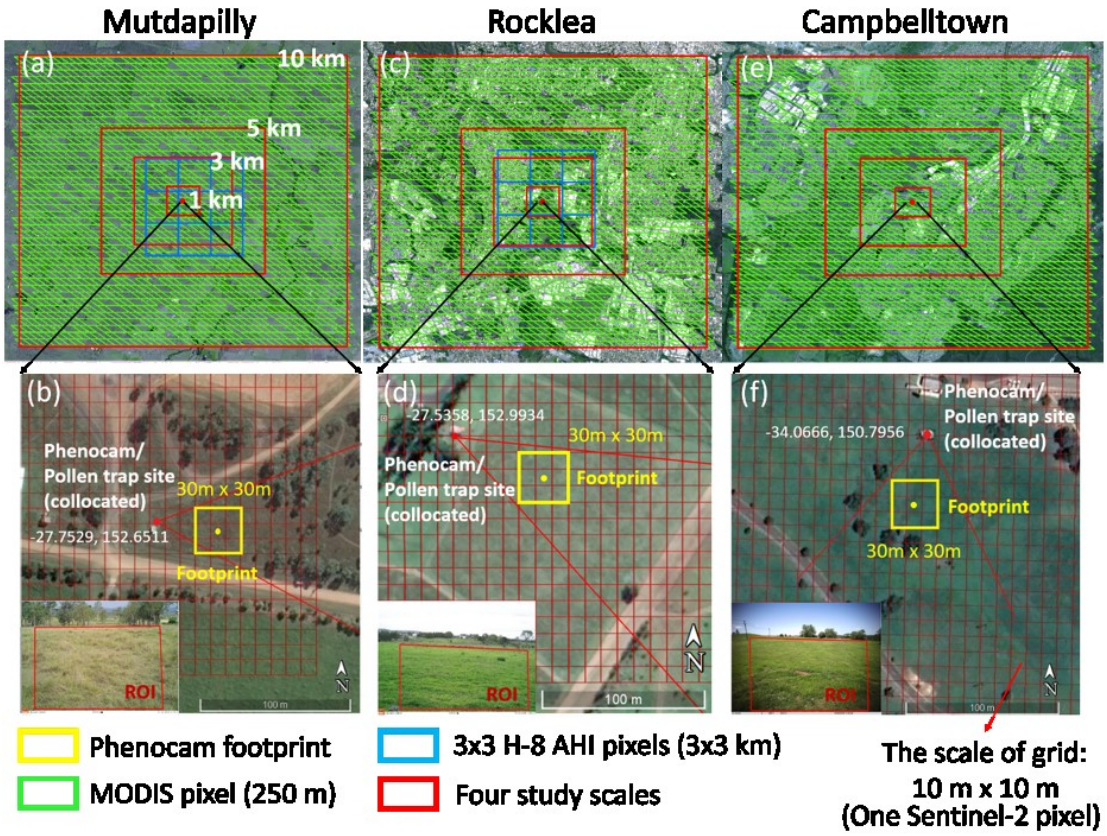

Figure 3.3 The research scales and overlap of MODIS pixels (green grids) and H-8 AHI pixels (blue grids) within study scales for Rocklea, Mutdapilly and Campbelltown (a, b, and c). The 3x3 Sentinel-2 pixels co-located with the

phenocam footprint (i.e., field of view depicted by yellow squares) at each site (b, d, and f). The small red grid for each site is the Sentinel-2 pixel fishnet with 10m spatial resolution. The red and yellow points represent the coordinates of phenocams and centres of footprint pixels, respectively. The phenocam sample image is depicted at the bottom-left corner for each site. The red square is the Region of Interest (ROI) from which the phenocam GCC is calculated.

We plotted the time series of Sentinel-2, MODIS, and Himawari-8 AHI EVI values with phenocam GCC across different research scales and compared the day of year (DOY) of greenness peaks derived from each greenness profile. It is worth noting that the DOY of greenness peaks from non-daily satellites observations is not the accurate peak DOY as the phenocam GCC tracked, but the reason why we compared non-daily satellite EVI with the daily phenocam GCC profile is that satellite images with big data gaps are unsuitable for reconstructing seasonal curves within the short timeframe of this research (~ 1 year) or some phenological transition information would be lost. To compare the relationships arising between *in-situ* phenocam GCC and EVI derived from multi-resolution satellites across various research scales we used a least-squares linear regression to calculate the coefficients of determination (R^2) and p-values.

In addition, to evaluate the relationships arising between grass pollen concentrations and grass greenness dynamics derived from multi-resolution near-surface and satellite-based remote sensing, we compared their respective time series and correlations by conducting least-squares quadratic polynomial regression analyses to calculate coefficients of determination (R^2) and p-values. The reason why we adopted polynomial regression is that the simple linear regression model is not suitable to fit the curvilinear shape between grass pollen concentrations and grass greenness. In my pilot study at pasture sites, mature flowers associated with grass seed maturity and pollination were observed after grass greenness peaks by half month (The specific contents and figures of this pilot study are shown in Section 3.7 Appendix). Furthermore, previous studies reported that airborne grass pollen concentrations usually appeared after grass flowering time (Estrella et al., 2006; Tormo et al., 2011). In the other words, grass pollen tended to be released after grass reached the greenness peak. Similarly, a study adopted a polynomial

regression model to describe the relationships between pollen concentrations and asthma hospital admissions because admissions increased following increasing pollen concentrations (Gowrie et al. 2016). As in our study, grass greenness peaks generally triggered grass pollen concentrations increase. Additionally, although polynomial regression fits a nonlinear model to the data, as a statistical estimation problem it is linear. For this reason, R^2 is a robust statistic for polynomial regression (Fan et al., 1996) and is widely used in previous studies adopted polynomial regression (Oteros et al., 2015; Sadeh et al., 2021). Further, we extracted grass greenness peaks from original EVI and reconstructed GCC time series and grass pollen peaks from reconstructed grass pollen concentration trajectories. By comparing grass pollen-greenness correlations and intervals arising between peaks across remote sensing sensors, we evaluated the spatial and temporal scale effects on grass phenology-pollen relationships. The study framework of this study is shown in Fig. 3.4.

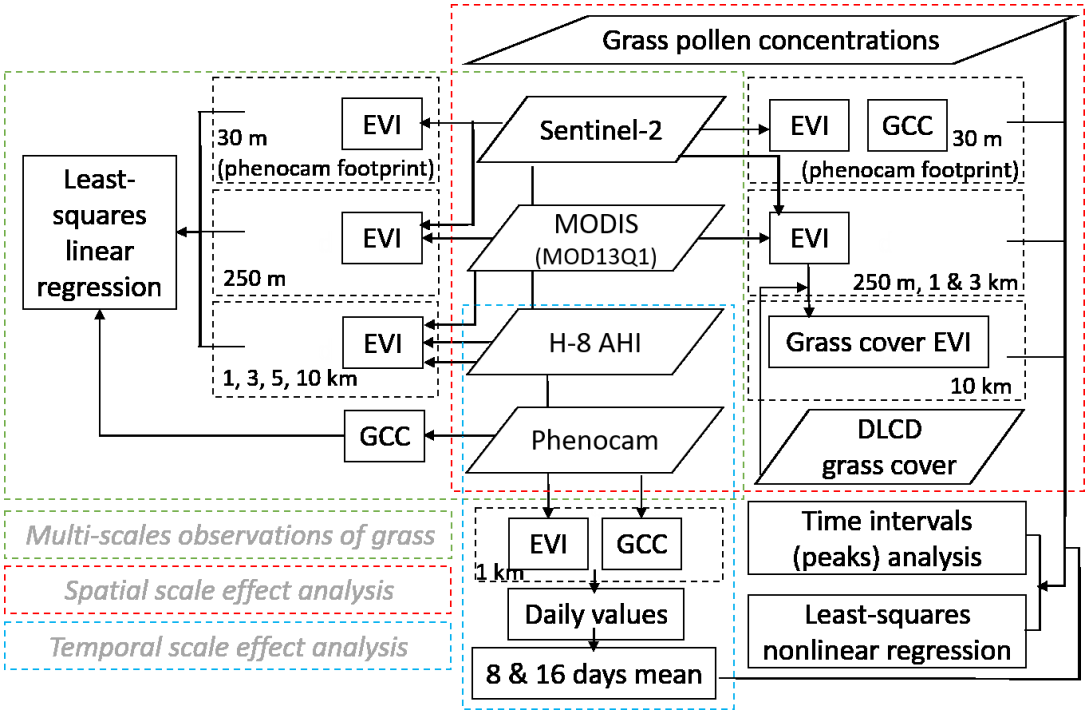

Figure 3.4 The study framework of this study.

3.3 RESULTS

3.3.1 Matching in-situ phenocam GCC with satellite-derived EVI across pixel scales

3.3.1.1 Matching in-situ phenocam GCC with Sentinel-2 EVI at phenocam footprint scale

Figure 3.5 shows the temporal trajectories and correlations arising between phenocam GCC and Sentinel-2 EVI at the Mutdapilly, Rocklea and Campbelltown sites. Phenocam GCC was compared with Sentinel-2 EVI from 3x3 pixels, which was co-located with the phenocam footprint. There is a notable seasonality in pasture greenness observations from both phenocam GCC and Sentinel-2 EVI at phenocam footprint scales for all three sites. The pasture greenness observations at all sites exhibit two major peaks. Though the specific dates varied among sites, their first major peak appeared from November to January and the second around May (Fig. 3.5 a, c, and e). The detailed dates of two major greenness peaks for all three sites is presented in Table 3.2.

The daily GCC values obtained varied from 0.33 to 0.42, 0.34 to 0.42, and 0.34 to 0.44 at Mutdapilly, Rocklea and Campbelltown, respectively. Sentinel-2 EVI values, however, obviously exhibited a degree of variance between sites (i.e. 0.10 to 0.38 at Mutdapilly; 0.17 to 0.67 at Rocklea; and 0.21 to 0.77 at Campbelltown). Even so, the Sentinel-2 EVI data at a phenocam footprint scale maintained highly synchronised temporal variations with the *in-situ* phenocam GCC. We found significant correlations between phenocam GCC and Sentinel-2 EVI at Mutdapilly (Fig. 3.5 b) and Campbelltown (Fig. 3.5 f) with an R^2 of 0.95 and 0.96, respectively. The correlation coefficient between the two metrics at Rocklea was lower ($R^2 = 0.75$) than for the other two sites, although still statistically significant (Fig. 3.5 d).

The differences of major peak dates arising between phenocam GCC and Sentinel-2 EVI varied among peaks and sites. For the first peak, Rocklea has a 7 day gap between phenocam and Sentinel-2 greenness observations, although they took place on the same day at Campbelltown. Comparing the first peak at all three sites, phenocam GCC and Sentinel-2 EVI recorded larger gaps for the second peak of 12 days at Mutdapilly and Rocklea and 6 days at Campbelltown. Phenocam GCC

peaks arose before Sentinel-2 EVI peaks at Mutdapilly and Campbelltown, but occurred behind at Rocklea (Table 3.2).

Also, the Sentinel-2 EVI at the phenocam footprint did not catch other minor GCC peaks due to a lack of data. For example, there is a minor grass greenness peak around the end of February at Mutdapilly and this was characterised by phenocam GCC, yet we could not find it within the Sentinel-2 EVI profile as there is only one available Sentinel-2 image during the period from January to the middle of March (Fig 3.5. a). Similarly, phenocam GCC values decreased despite a series of fluctuations from December to April at Rocklea, yet Sentinel-2 EVI could not catch the subtle greenness observations owing to insufficient data around that period (Fig 3.5. c). Also, the phenocam data at the Rocklea site is very noisy, while that obtained from Sentinel-2 is not. It might be because cloud-related illumination changes impact the amplitude of sub-daily GCC values.

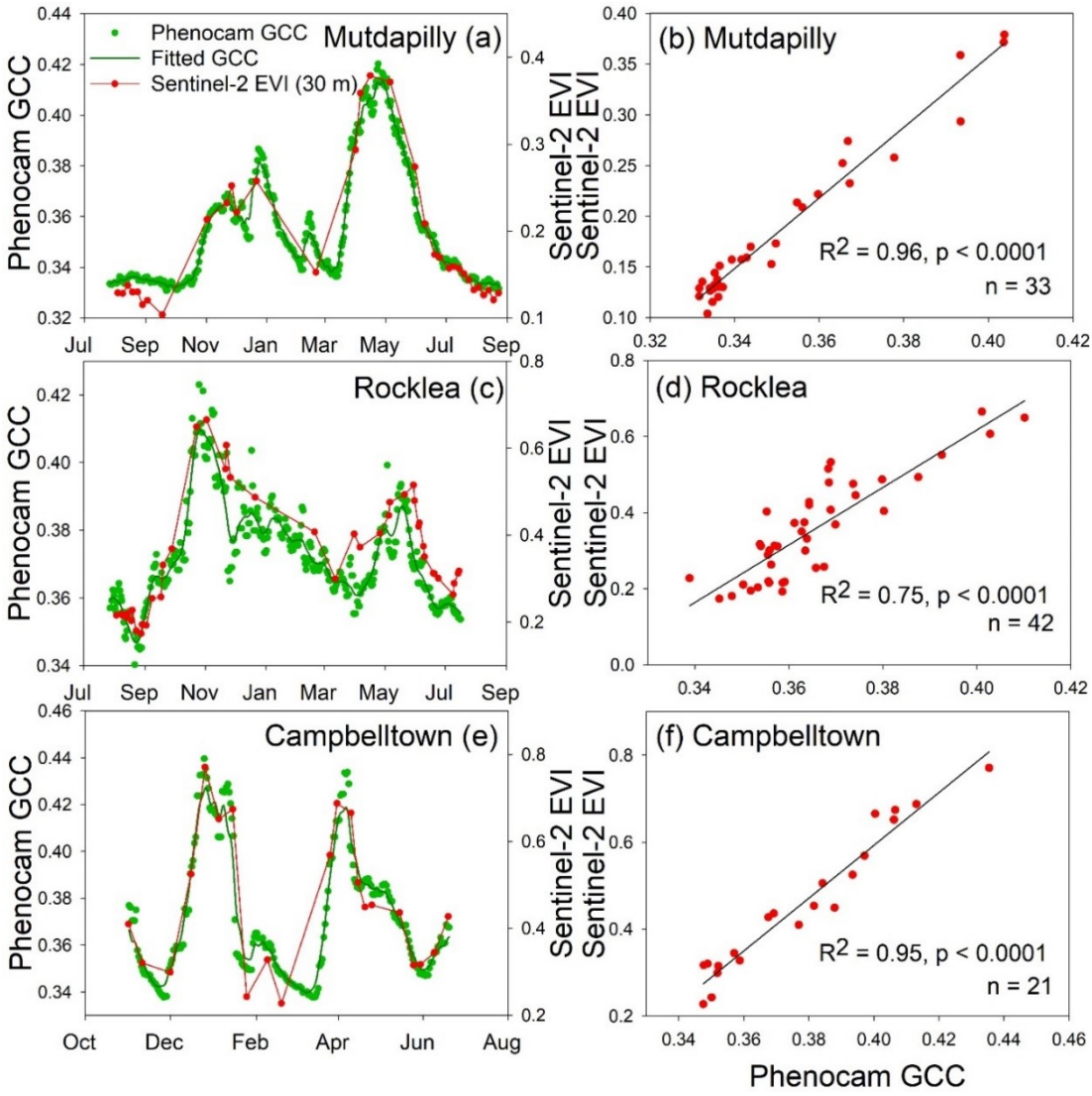

Figure 3.5 The relationships arising between phenocam GCC and Sentinel-2 EVI data at the phenocam footprint scale (3x3 pixels) for Mutdapilly (a and b); Rocklea (c and d); and Campbelltown (e and f), respectively.

Table 3.2 The DOY of grass greenness peaks derived from phenocam GCC and Sentinel-2 EVI at a phenocam footprint scale for Mutdapilly, Rocklea and Campbelltown sites. Δ days = (GCC peak date – EVI peak date)

		Mutdapilly	*Rocklea*	*Campbelltown*
Peak1	Phenocam GCC	358	299	360
	Sentinel-2 EVI	355	306	360
	Δ *days*	***3***	***-7***	***0***
Peak 2	Phenocam GCC	117	138	96
	Sentinel-2 EVI	105	150	90
	Δ *days*	***12***	***-12***	***6***

3.3.1.2 Matching in-situ phenocam GCC with MODIS EVI at its pixel scale (250m). Figure 3.6 shows the temporal trajectories and correlations arising between phenocam GCC and one-pixel MODIS EVI at the Mutdapilly, Rocklea and Campbelltown sites. We found significant correlations arising between phenocam GCC and MODIS EVI at Mutdapilly (Fig. 3.6 a) with an R^2 of 0.72. The correlation coefficient between these two values at Rocklea and Campbelltown are lower (R^2 = 0.50 and 0.57, respectively) than for Mutdapilly (although still statistically significant, Fig. 3.6 d and f).

Though the notable seasonality in grass greenness dynamics is also captured by MODIS EVI, peaks of grass greenness observations inevitably vary between phenocam and MODIS data. At Mutdapilly, the MODIS EVI peaks lagged with advanced phenocam GCC by 16 and 12 days for the first and second greenness peaks, respectively (Fig. 3.6 a and Table 3.3). The MODIS EVI peaks also lagged behind the phenocam GCC at the first peak for the other two sites, yet the Δ days (i.e., phenocam peak dates – MODIS peak dates) at Campbelltown were smaller than for Rocklea at this peak (Table 3.3). For the second peak, however, the MODIS EVI peak significantly lagged behind the phenocam GCC peak, with differences of over one month (41 days) observed in Campbelltown (Fig 3.6 e, Table 3.3). Also, the MODIS EVI experienced a sudden drop around January and then increased from January to March at Rocklea. This trend is diametrically opposite to the phenocam GCC trajectory over the same period (Fig. 3.6 c). All of these non-conformities in seasonal trajectories arising between phenocam GCC and MODIS EVI can be attributed to the mixed pixel effect arising in coarse MODIS data. One MODIS pixel is viewing an area almost 70 times that of the phenocam. As revealed in Fig. 3.2, when compared with Mutdapilly (the rural site), the Rocklea and Campbelltown sites (which are situated in urban areas with more complicated land cover types) inevitably lead to a more evident mixed pixel effect.

Table 3.3 The DOY of grass greenness peaks as derived from phenocam GCC and one-pixel MODIS EVI at Mutdapilly, Rocklea and Campbelltown sites. Δ days = (GCC peak date – EVI peak date).

		Mutdapilly	*Rocklea*	*Campbelltown*
Peak1	Phenocam GCC	358 (2018)	299	299
	MODIS EVI	9 (2019)	313	300
	Δ *days*	***-16***	***-14***	***-1***
Peak 2	Phenocam GCC	117	138	96
	MODIS EVI	105	121	137
	Δ *days*	***12***	***17***	***-41***

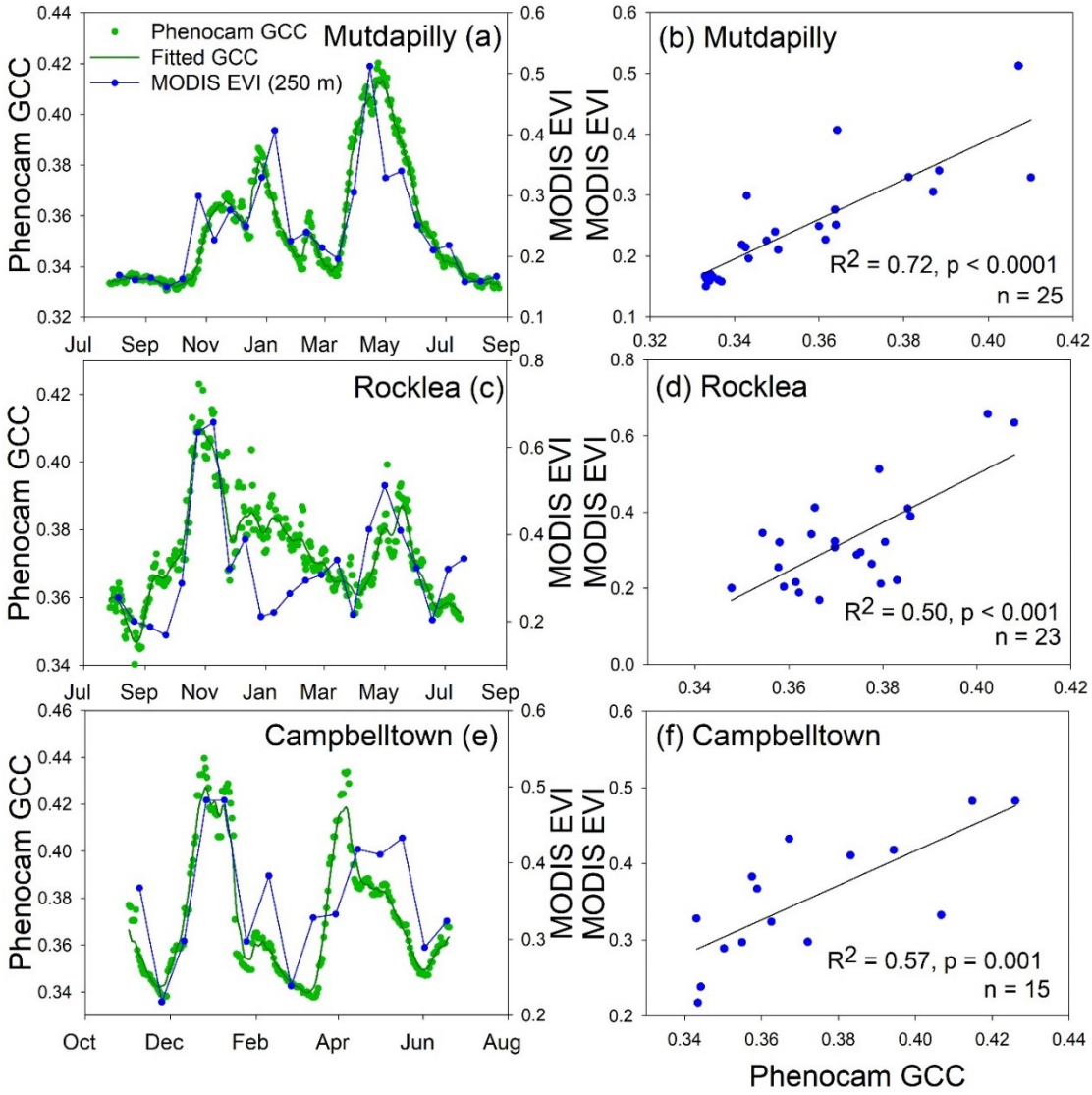

Figure 3.6 The temporal trajectories and correlations arising between phenocam GCC and MODIS EVI at the MODIS pixel scale (250m) for Mutdapilly (a and b), Rocklea (c and d) and Campbelltown (e and f) from 2018 to 2019.

3.3.1.3 Matching in-situ phenocam GCC with Himawari-8 AHI EVI at its respective pixel scale (1000m).

Figure 3.7 shows the temporal trajectories and correlations between phenocam GCC and one-pixel H-8 AHI EVI at the Mutdapilly and Rocklea sites from August to December 2018 (note that this period spans only 5 months and not 12 months as per the Sentinel-2 and MODIS analyses). We found significant correlations between phenocam GCC and H-8 AHI EVI at both sites with an R^2 of 0.86 and 0.63 (Fig. 3.7 b and d). As with the Sentinel-2 and MODIS EVI, H-8 AHI EVI also maintained highly synchronised temporal variations with *in-situ* phenocam GCC seasonal dynamics at both sites.

As compared with non-daily Sentinel-2 and MODIS EVI peaks, the peak of the daily H-8 AHI EVI time series at both sites also exhibited large time intervals relative to phenocam GCC peaks. The H-8 AHI EVI peak was 15 days in advance of the phenocam GCC peak at Mutdapilly yet lagged behind it by 6 days at Rocklea (Fig. 3.7 a and d, Table 3.4). This arises because the coarse spatial resolution inherent in H-8 AHI data offsets its advantage in terms of temporal resolution. For example, the grass cover proportion is 43.75% within 1km around the Rocklea site according to DLCD. Even if the grass cover proportion were 87.50% within 1km of the Mutdapilly phenocam site, according to DLCD, we still cannot exclude the possibility that grasses within this 1 km radius have a different phenology. Therefore, one-pixel H-8 AHI EVI values cannot accurately represent the grass greenness dynamics as recorded by phenocam at an *in-situ* scale.

Table 3.4 The DOY of grass greenness peaks derived from phenocam GCC and one-pixel Himawari-8 AHI EVI at the Mutdapilly, Rocklea and Campbelltown sites from August to December 2018. Δ days = (GCC peak date – EVI peak date).

		Mutdapilly	*Rocklea*
Peak 1	Phenocam GCC	324	299
	Himawari-8 AHI EVI	309	305
	Δ *days*	***15***	***-6***

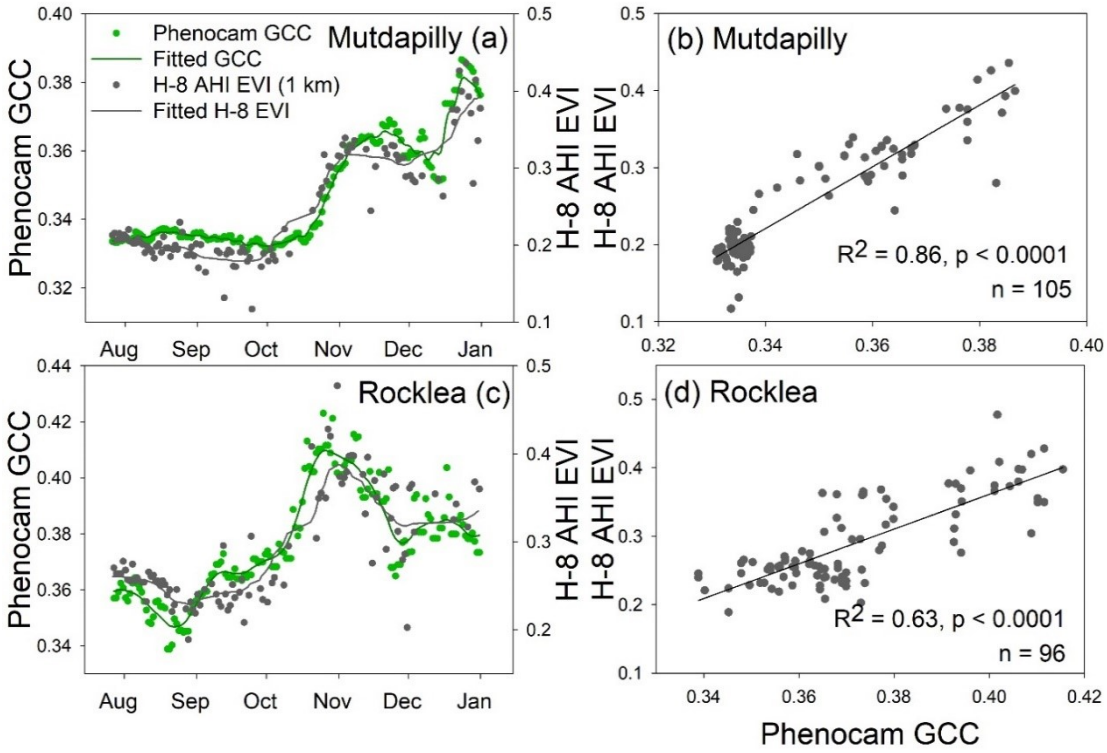

Figure 3.7 The temporal trajectories and correlations arising between phenocam GCC and Himawari-8 AHI EVI at its pixel scale (1km) for Mutdapilly (a and b) and Rocklea (c and d) for the period from August to December 2018.

3.3.2 Changes in phenocam GCC-satellite EVI relationships across research scales at sites with varied spatial heterogeneity

The correlations between *in-situ* phenocam GCC and multi-sensor satellites EVI with increasing scales were analysed for each site. At all three sites, we compared the correlations between phenocam GCC and EVI derived from the Sentinel-2 and MODIS satellites between August 2018 and August 2019 at Mutdapilly and Rocklea. Also, H-8 AHI EVI was analysed at these two sites during the period spanning from August to December 2018. For the Campbelltown site we performed the same analyses between phenocam and satellites (i.e., Sentinel-2 and MODIS) from November 2018 to July 2019, although there were no H-8 AHI analyses due to restricted data access (Fig. 3.8 and Table 3.5).

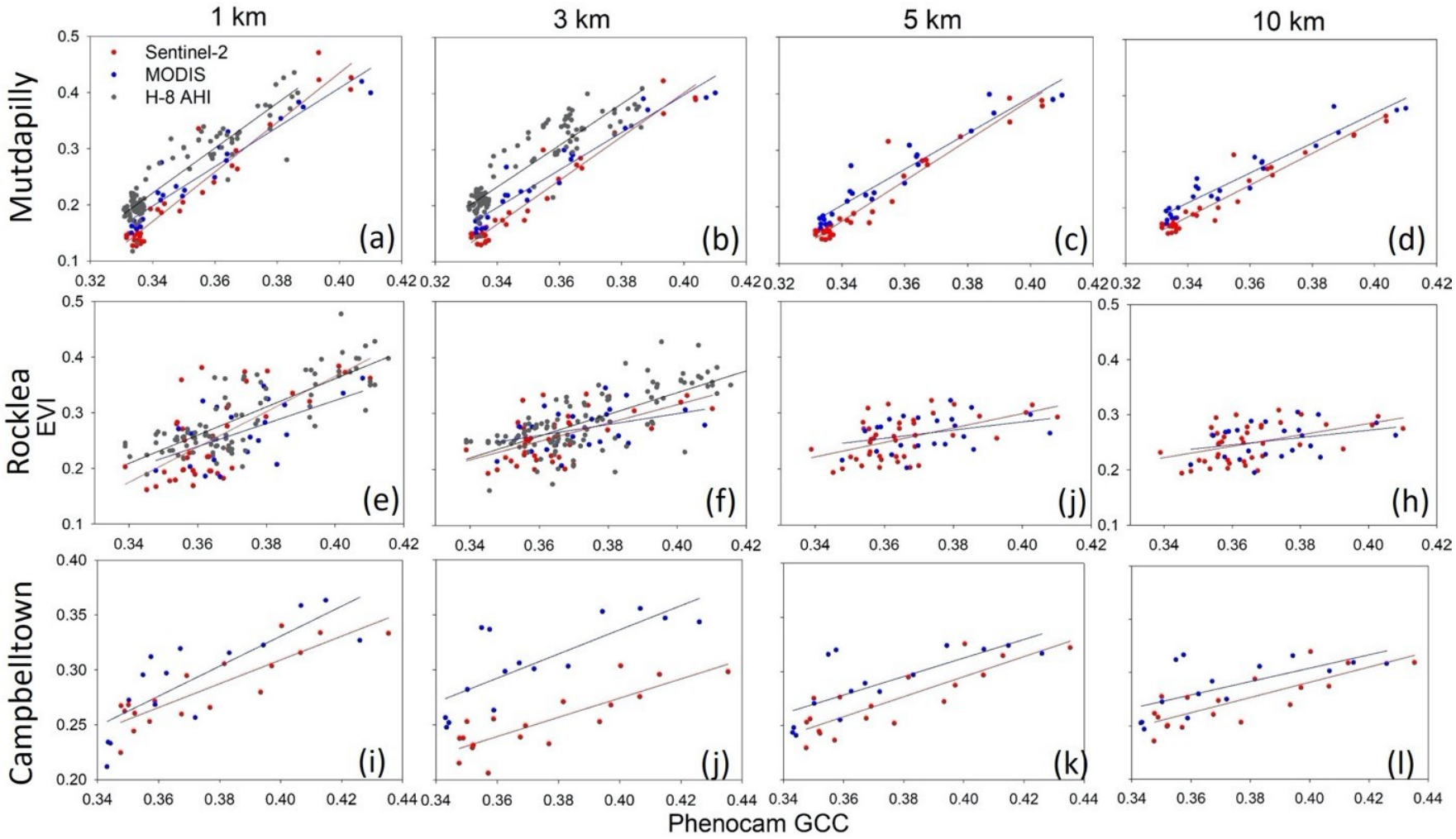

Figure 3.8 Correlations between phenocam GCC and satellites EVI across sensors (i.e., Sentinel-2, MODIS, Himawari-8 AHI) and spatial scales (i.e. 1, 3, 5, and 10km). The R^2 (coefficient of determination) and grass cover proportion within each research scale are summarised in Table 3.5.

Table 3.5 The coefficient of determination (in terms of R^2) derived between phenocam GCC and multi-sensor satellite EVI at increased study scales for Mutdapilly, Rocklea, and Campbelltown. Note that H-8 AHI EVI did not participate in the comparison due to it only having five months of data.

	Scales	*Grass%*	*Sentinel-2*	*MODIS*	*Himawari-8 AHI*
Mutdapilly	1 km	87.50	**0.93** ***	0.92 ***	0.86 ***
	3 km	92.31	**0.95** ***	0.93 ***	0.83 ***
	5 km	85.89	**0.93** ***	0.92 ***	
	10 km	73.11	**0.94** **	0.92 ***	
Rocklea	1 km	43.75	**0.46** ***	0.32	0.63 ***
	3 km	37.06	**0.34**	0.15	0.52 ***
	5 km	30.86	**0.28**	0.12	
	10 km	20.81	**0.23**	0.10	
Campbelltown	1 km	93.75	**0.76** ***	0.66 **	
	3 km	54.55	**0.70** ***	0.59 **	
	5 km	36.84	**0.72** ***	0.55 *	
	10 km	30.21	**0.64** ***	0.44 *	

Note: Grass % is defined as the percentage of [grassland + pasture] composite classes at each study scale. The asterisks *, **, and *** denote correlations significant at the 0.01, 0.001, and 0.0001 p-value levels, respectively. Underline highlights the highest grass % among all study scales and the highest correlations arising among all study scales for the same satellite sensor (the same sensor was used for different scales). Bold font indicates the highest correlation arising between Sentinel-2 and MODIS data within the same study scale (again the same scale was used for different sensors).

All Sentinel-2 and MODIS data showed significant correlations with *in-situ* phenocam GCC measurements at increased study scales besides Rocklea (Table 3.5). For Sentinel-2 EVI, the data significantly correlated with that of phenocam GCC at both Mutdapilly and Campbelltown, with R^2 values ranging from 0.64 to 0.95 (Fig 3.8, a to d and i to l). Phenocam GCC-satellite EVI correlations at Rocklea, however, were weaker than for either Mutdapilly or Rocklea, with the smallest R^2 values recorded among the three sites. For MODIS data, the relationships between its regional mean EVI determined with the *in-situ* phenocam GCC had the same trend as for Sentinel-2 data (i.e., the highest R^2 values were recorded at Mutdapilly, and the lowest values at Rocklea). For the H-8 AHI sensor, only five months of EVI data were analysed with *in-situ* phenocam GCC. However,

we still found significant correlations, with R^2 values ranging from 0.52 to 0.86, although there were weaker correlations at Rocklea as compared with Mutdapilly.

As for the correlations of greenness metrics between phenocam and certain sensors among increased study scales (i.e., 1, 3, 5 and 10km), the highest R^2 value was usually found at the study scale revealing the highest percentage of grass cover (i.e., grass %). For example, the grass % at Campbelltown was 93.75% within 1km and this was the highest percentage of grass coverage among all study scales. On the other hand, both Sentinel-2 and MODIS EVIs showed the strongest correlations, with *in situ* phenocam GCC (R^2 = 0.76 and 0.66, respectively) recorded at the 1km scale (Table 3.5). This indicates the spatial heterogeneity observed around phenocam sites which affected the performance of satellites with various spatial resolutions in observing grass greenness dynamics.

3.3.3 Characterising relationships arising between grass pollen concentrations and grass/landscape greenness observations from phenocam and multi-resolution satellites

Grass pollen concentrations are plotted alongside the time series data recorded by phenocam GCC and satellites EVI for the two growing seasons at the Mutdapilly, Rocklea and Campbelltown sites. Also, we cross-plotted them for each site to reveal how grass pollen concentrations varied with data depicting grass greenness seasonal dynamics as derived from multi-scale remote sensing (Fig. 3.9 to Fig. 3.10).

The grass pollen concentrations at these three sites exhibited different seasonal dynamics within the growing seasons studied. At the Mutdapilly site, grass pollen concentration peaks occurred during the late spring month (November in Australia) and late autumn months (April to May). The second autumn peak is higher than the first (Fig. 3.9 a). In contrast, Rocklea exhibited more complicated grass pollen concentration peak patterns over the two grass growing seasons studied. There are three major peaks at Rocklea within a short period and they occurred during the summer and early autumn months (i.e., January to March) and middle autumn months (April). At Campbelltown, a similar grass pollen pattern was observed as Mutdapilly, where grass pollen peaks occurred from November to January and in May. However, at this site, the November peak was the major one rather than the

May peak. It was the opposite for Mutdapilly. In terms of the magnitude of grass pollen concentrations for each site, Rocklea and Campbelltown have the highest and lowest magnitudes among the three sites, respectively. The major January peak at Rocklea was 13.5-fold higher than the one that occurred in November in Campbelltown (459.68 *vs.* 34.03, respectively).

3.3.3.1 Relationships between grass pollen concentrations as measured with phenocam GCC and Sentinel-2 EVI at the phenocam footprint scale

The temporal profiles and cross plots between grass pollen concentrations and grass greenness values observed at *in-situ* scale using phenocam and Sentinel-2 sensor at Mutdapilly, Rocklea, (from August 2018 to August 2019) and Campbelltown (from October 2018 to August 2019) are shown in Fig. 3.9.

At the Mutdapilly site, seasonal grass pollen concentrations corresponded well with phenocam GCC and grass Sentinel-2 EVI at the phenocam footprint scale, with peak grass activity (greenness) arising in November, January, March, and May. The highest grass pollen peak corresponded to the highest grass greenness peak which occurred in May. Among these four grass greenness peaks, no grass pollen activity corresponded with the March greenness peak. Although the GCC and EVI values at the November peak were higher than that of the January peak, the grass pollen concentrations at these two peaks were similar to each other (i.e., 18.96 and 16.93 grains/m^3, respectively; Fig. 3.9 a).

In contrast, major grass greenness peaks did not correspond well with grass pollen activities at Rocklea (Fig. 3.9 b). The first grass greenness peak was 69 days earlier than the first grass pollen peak and, although the second grass greenness peak corresponded well with a slight grass pollen peak around June, this was 62 days later than the third grass pollen peak. A notable observation is that grass pollen reached its second peak on 16/02/2019 and its third on 29/03/2019, even though grass greenness values continuously declined over the same period. A possible reason for this is that the grass pollens recorded in these two pollen peaks came from grass situated beyond the phenocam footprint scale.

Grass GCC and EVI peaks did not correspond well with the grass pollen peaks observed at Campbelltown, with the greenness peak lagging behind the major grass

pollen peak by almost a month (Fig. 3.9 c). However, an obvious increase in the pollen concentration profile coincided with the grass greenness trajectories reaching their first peak in November. In contrast, the second greenness peak in April did not trigger a steep increase in grass pollen as it did in November. Note that, although phenocam GCC values at each of the two sites were similar (the mean GCC at Mutdapilly was 0.36 while the mean GCCs at Rocklea and Campbelltown were 0.37), the Sentinel-2 EVI value at Campbelltown was the highest, followed by Rocklea and Mutdapilly (0.46, 0.36, and 0.18, respectively).

We found that grass pollen concentrations showed significant non-linear correlations with Sentinel-2 EVI data at Mutdapilly and Rocklea (R^2 = 0.92 and 0.2, respectively; Fig. 3.9 d and e). The grass pollen concentration only showed a significant correlation with phenocam GCC (R^2 = 0.63) at the Mutdapilly site (Fig. 3.9 d), yet there were no significant correlations arising between them for the other two sites (Fig. 3.9 e and f). In general, Sentinel-2 EVI data at a phenocam footprint scale and *in-situ* phenocam GCC data correlated well with grass pollen activity at Mutdapilly, although this pattern was not established for the other two sites, and the non-linear correlations indicate that significant time intervals arose between grass pollen and greenness dynamics.

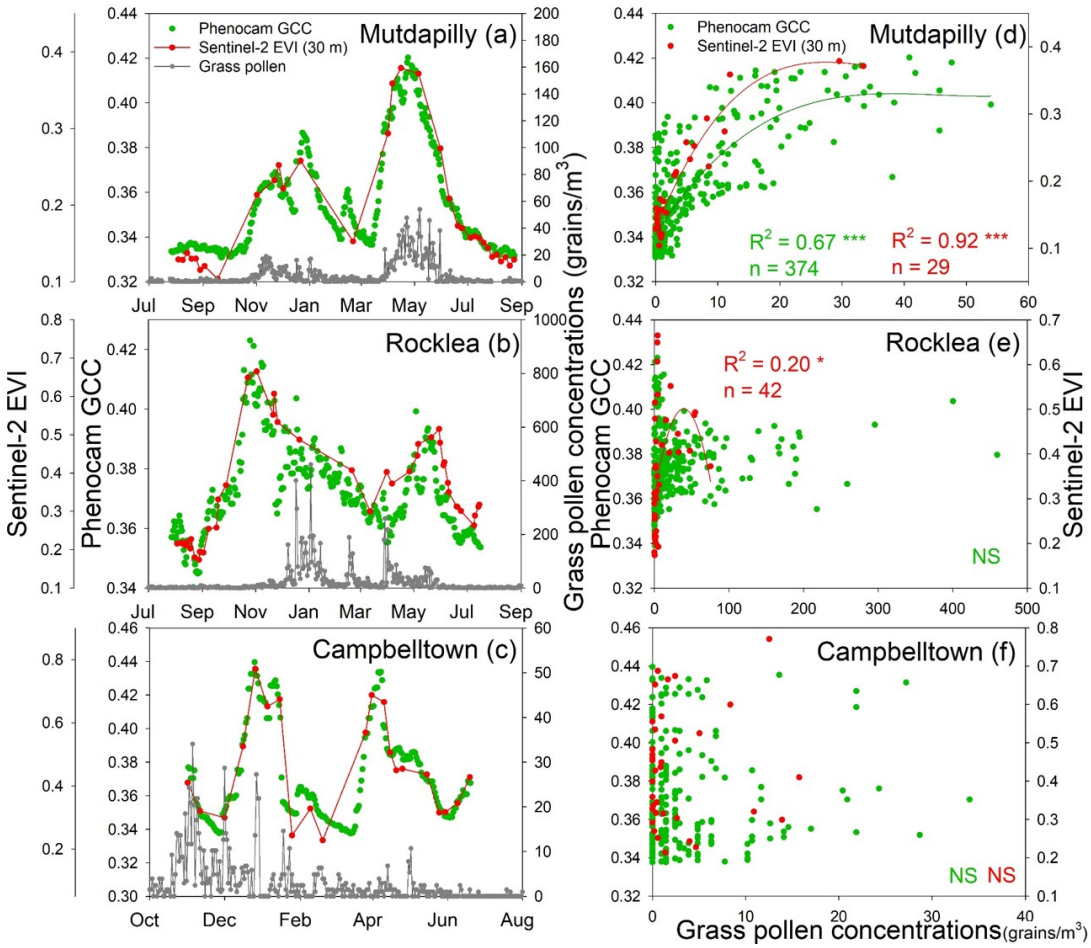

Figure 3.9 Time series plots (a - c) and polynomial relationships (d - f) of grass pollen concentrations and phenocam GCC and Sentinel-2 EVI at a phenocam footprint scale (3x3 pixels) for Mutdapilly, Rocklea and Campbelltown (from August 2018 to August 2019). The asterisks ***, **, and * denote significance at p-values of 0.0001, 0.001, and 0.01, respectively. NS denotes 'no significant relationship'.

3.3.3.2 Relationships arising between grass pollen concentrations with grass EVI derived from Sentinel-2 and MODIS satellites at the 250m scale

Fig. 3.10 shows the time series and cross plots of MODIS EVI (at a 1 pixel scale) and grass pollen concentrations at Mutdapilly, Rocklea, and Campbelltown. To compare capacities in observing landscape greenness between Sentinel-2 and MODIS satellites at the same study scale, we averaged all Sentinel-2 EVI data within 250m and also correlated these mean Sentinel-2 EVI data with grass pollen concentrations at each of the three sites. Seasonal grass pollen concentrations corresponded well with the one-pixel MODIS EVI time series at Mutdapilly, with

peak grass activity (greenness) occurring at the end of October, in January, and the end of April (Fig. 3.10 a). Comparing these findings with Sentinel-2 EVI data, the first and second MODIS EVI peaks occurred before and after the corresponding grass pollen peaks, respectively. Further, the highest grass pollen peak corresponded to the highest grass greenness peak (Fig. 3.10 a). Similar to the phenocam GCC and Sentinel-2 data at both *in-situ* and 250m scales, major MODIS EVI peaks were characterised by clear asynchronicity with grass pollen peaks at Rocklea (Fig. 3.10 b). The time interval between the highest grass pollen peak and the MODIS EVI peak was 55 days. However, the MODIS EVI values decreased around the month of January and then increased from January to March. Sentinel-2 EVI did not capture the same pattern due to the big data gap arising during this period. At the Campbelltown site (Fig. 3.10 c), both MODIS and Sentinel-2 EVI values reached their first peak concomitantly yet lagged behind the major grass pollen peak. In contrast, MODIS EVI data exhibited a later second peak as compared with Sentinel-2 EVI of one and half months. We found significantly non-linear correlations between grass pollen and EVI at Mutdapilly (Fig. 3.10 d). As for the other two sites, only Sentinel-2 EVI data significantly correlated with grass pollen peaks at Rocklea (Fig.3.10 e).

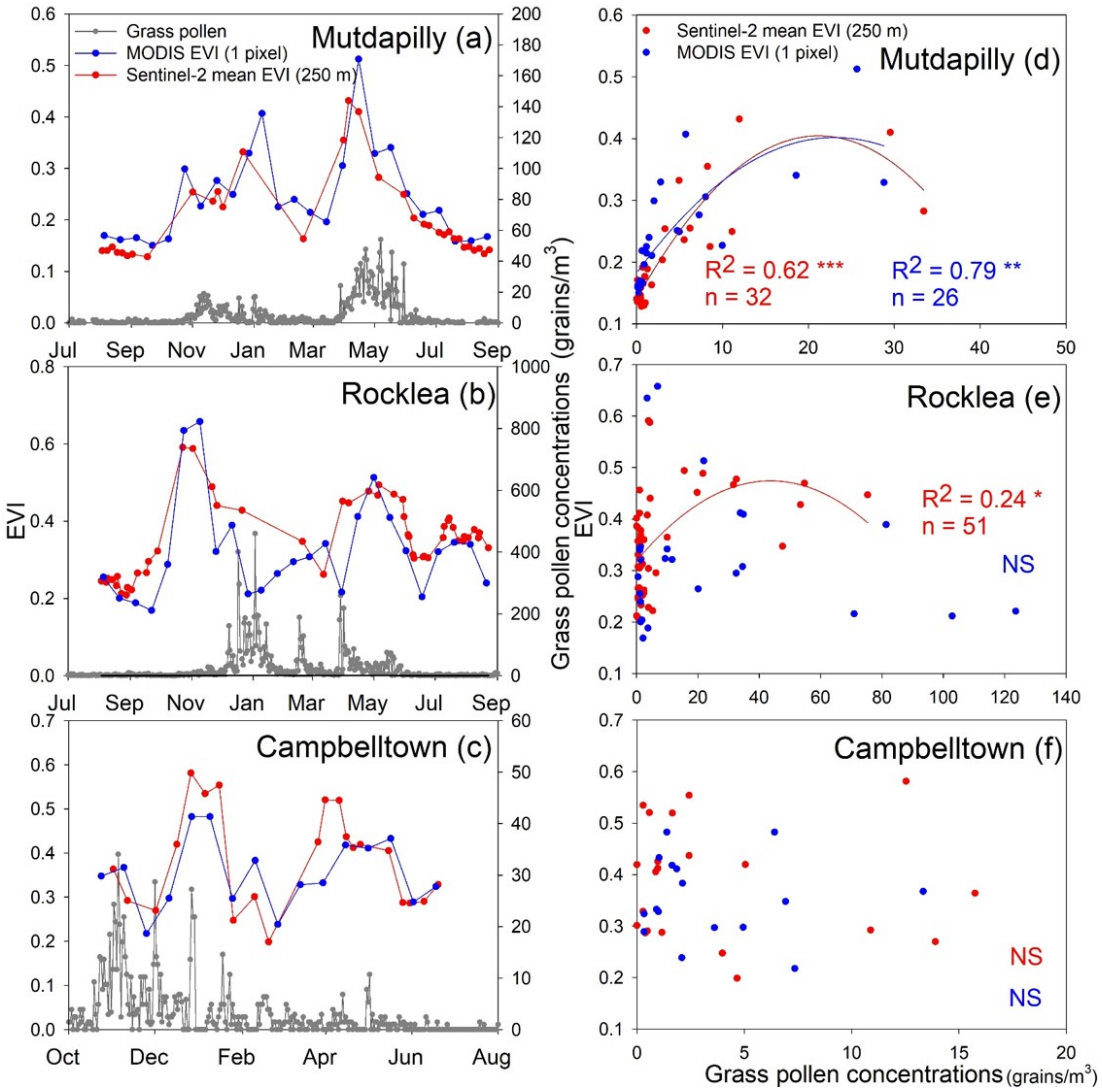

Figure 3.10 Time series plots (a - c) and polynomial relationships (d - f) of grass pollen concentrations and Sentinel-2, MODIS EVI data at MODIS pixel scale (250m) for Mutdapilly, Rocklea and Campbelltown (period from August 2018 to August 2019). The asterisks ***, **, and * denote significant correlations at p-values of 0.0001, 0.001, and 0.01, respectively. NS denotes 'no significant relationship'.

3.3.3.3 Relationships arising between grass pollen time series with landscape greenness observations from Himawari-8 AHI data at a 1000m scale

The Himawari-8 AHI EVI time series are plotted alongside grass pollen concentrations at the Mutdapilly and Rocklea sites for the entirety of 2018 (Fig. 3.11 a and c). Their respective correlations were also analysed (see Fig. 3.11 b and

d) to reveal how grass pollen concentrations trapped by *in-situ* sites varied with Himawari-8 AHI EVI at a 1km spatial resolution.

There was a major grass pollen peak around April and a secondary peak that occurred around December during the annual cycle at Mutdapilly. Meanwhile, the one-pixel resolution H-8 AHI EVI time series reached its first peak on the 7th of January (Australian summertime), while the second peak occurred around the middle of March (early autumn). H-8 AHI EVI data decreased continuously from March to September and thereafter increased from October, reaching its third peak around November (Fig. 3.11 a). For the H-8 AHI EVI January peak, it is not altogether clear whether it corresponded to the grass pollen peak due to the limited grass pollen data availability. For the other two EVI peaks, they arose 5 and 10 days in advance of grass pollen peaks, respectively. The significant correlation arising between grass pollen and H-8 AHI EVI data ($R^2 = 0.34$) also confirmed our findings from the time series analyses.

The grass pollen concentration profile had two obvious peaks in March and at the end of December at the Rocklea site. For the first grass pollen peak at Rocklea, it appeared earlier than for Mutdapilly, by around a month, yet its EVI peak came 19 days later than Mutdapilly (Fig. 3.11 a and c). This means that the EVI peak happened after the first grass pollen peak at Rocklea. Even so, this EVI peak indeed occurred within the active grass pollen period (i.e., January to May). It is risky to say that no EVI peak caused this grass pollen peak around March, as we only plotted data from January. For another peak period, the EVI peak preceded the grass pollen peak by one and a half months (Fig. 3.11 c). In contrast with Mutdapilly, there was no significant correlation (R^2=0.13), between H-8 AHI EVI data at one-pixel resolution and the grass pollen concentrations. The pattern of the cross-plot revealed, even though the H-8 AHI EVI values were very low, that the grass pollen still reached high values (Fig. 3.11 d).

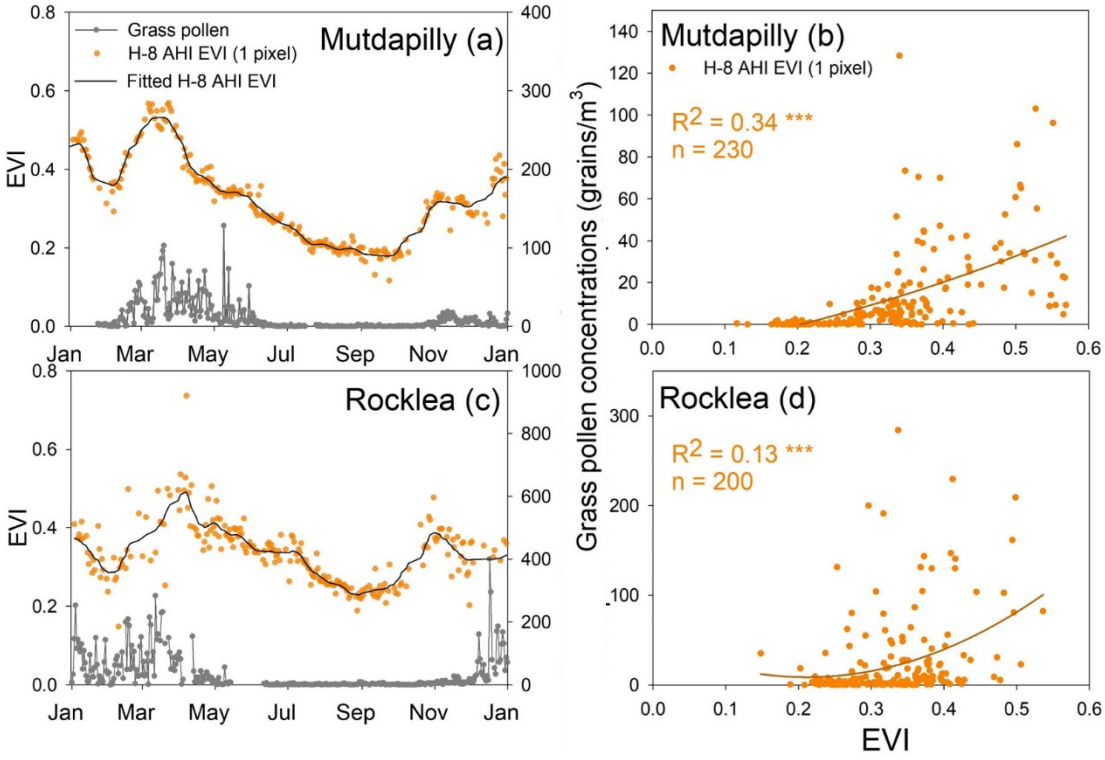

Figure 3.11 Temporal trajectories (a and c) and polynomial relationships (b and d) of grass pollen concentrations and H-8 AHI EVI data at a 1000m scale for Mutdapilly (a and b) and Rocklea (c and d). Asterisks *** denote statistical significance in p-values of 0.0001.

3.3.4 Changes in relationships arising between grass pollen concentrations and grass/landscape greenness observations across sensors and study scales.

To determine whether the differences arising in grass greenness, as observed by phenocam and satellite sensors across a range of study scales, and, by extension, if the relationships arising between grass pollen and greenness values were impacted by sensors, we plotted phenocam GCC and satellite EVI alongside the grass pollen concentrations over the equivalent period (from August to December 2018) for Mutdapilly and Rocklea (Fig. 3.12). Four study scales (i.e., 30m, 250m, 1km, and 3km) were adopted to conduct this analysis. The first three scales corresponded to the phenocam footprint scale, MODIS, and H-8 AHI pixel scales, respectively.

For the time series of grass greenness values and grass pollen levels, their temporal dynamic patterns, and interrelationships varied across sensors and research scales. In general, grass pollen concentration peaks corresponded to grass greenness values

peaks at Mutdapilly (Fig 3.12 a- d), yet significantly lagged behind grass greenness observations at the Rocklea site (Fig 3.12 e-h).

At the 30m study scale (Fig. 3.12 a and e), we could only obtain accurate grass greenness information from *in-situ* phenocam and fine-resolution Sentinel-2 data. The 3x3 pixel Sentinel-2 EVI trajectories closely tracked phenocam GCC values at both sites. Their peak dates, however, exhibited an interval of almost one week. Sentinel-2 EVI peaks occurred 6 and 8 days later than the GCC peaks at Mutdapilly and Rocklea, respectively. Grass pollen concentrations at Mutdapilly conformed consistently with grass greenness values, as the GCC and EVI peaks lagged the grass pollen peak by only 7 and 13 days, respectively. However, the peaks for GCC and EVI fell in advance of the grass pollen peak by more than two months (i.e., 70 and 62 days, respectively) at Rocklea. Note that there is an obvious secondary GCC peak at Rocklea around the middle of December, one that corresponded with grass pollen peaks, yet the 3x3 pixel Sentinel-2 EVI data did not exhibit a peak during the same period (Fig 3.12, e).

At the MODIS pixel scale, we compared EVI derived from one-pixel MODIS data and mean Sentinel-2 EVI data within 250m scales as centred on study sites (Fig. 3.12 b and f). The EVI values and seasonal patterns varied among sensors at this study scale, notably at Mutdapilly. MODIS EVI peaks advanced and lagged behind Sentinel-2 EVI peaks at Mutdapilly and Rocklea, respectively, and therefore impact upon their temporal relationships between grass pollen peaks. At Mutdapilly, MODIS EVI reached its first major peak on the 16th October and then its secondary peak on the 17th November. Sentinel-2 EVI data at this site appeared as two peaks on the 1st November (secondary peak) and the 26th November (major peak). Both peaks in the MODIS EVI profile arose 15 and 9 days in advance of the Sentinel-2 EVI time series, respectively. As compared with grass greenness trajectories at the 30m scale, only the Sentinel-2 EVI peak maintained synchronicity with the grass pollen peak at 250m for Mutdapilly, with the first MODIS EVI peak appearing 28 days before the grass pollen peak at the 250m scale (Fig. 3.12 b). For the Rocklea site, the intervals between the two sensors' EVI peaks was only 9 days. The MODIS EVI peak happened before the grass pollen peak by 63 days, and the time interval for Sentinel-2 EVI was 72 days (Fig. 3.12 f).

At the H-8 AHI 1km pixel scale (Fig. 3.12 c and g), we compared seasonal EVI patterns derived from both Sentinel-2 and MODIS data that centred on the study sites, as well as one H-8 AHI EVI pixel at each site. At the Mutdapilly site, Sentinel-2 and MODIS EVI values reached their peaks at the same time (1st November), 4 days ahead of the H-8 AHI EVI. All EVI peaks from all three sensors occurred before the grass pollen concentration peak recorded at Mutdapilly, with intervals of 12 and 8 days, respectively (Fig. 3.12 c). MODIS EVI did not keep a consistent seasonal dynamic with the Sentinel-2 and H-8 AHI EVI data at Rocklea. Its peak was almost half a month ahead of the EVI peaks derived from the other two sensors (Fig. 3.12 g).

EVI values and seasonal patterns obtained from Sentinel-2, MODIS, and H-8 AHI sensors at the 3km scale were similar to those observed at the 1km scale at both sites (Fig. 3.12 d and h). At the Mutdapilly site, Sentinel-2 and MODIS EVI peaks appeared on the same day, although the H-8 AHI EVI peak lagged by 5 days. Meanwhile, all EVI peaks occurred before the grass pollen peak by around 10 days (Fig. 3.12 d). In contrast, the MODIS EVI peak lagged behind the Sentinel-2 EVI peak by 15 days at the Rocklea site, and peak date for the H-8 AHI EVI was the same as that of Sentinel-2 EVI (Fig. 12 h).

We cross-plotted the grass pollen concentrations with grass/landscape greenness values at Mutdapilly and Rocklea (Fig. 3.13), with the regression functions and R^2 values derived summarised in Table 3.6. As for the correlations in temporal patterns arising between grass pollen and grass greenness metrics, these varied across sensors and scales. Phenocam GCC and multi-sensors EVI exhibited significant correlations between grass pollen concentrations at all study scales for Mutdapilly (Fig 3.13 a – d, Table 6). In contrast, only EVI derived from Sentinel-2 and H-8 AHI satellites showed significant correlations, although the R^2 values were lower for Mutdapilly than for grass pollen at Rocklea (Fig 3.13 e to h, Table 3.6).

Phenocam GCC showed significant non-linear relationships with grass pollen at Mutdapilly (R^2=0.54), yet there was no significant correlation at Rocklea (Table 3.6). Compared with the other two satellites with coarser resolutions, the relationships arising between grass pollen and Sentinel-2 EVI had the highest R^2 values, ranging from 0.64 to 0.76 at Mutdapilly and from 0.32 to 0.38 at Rocklea.

The seasonal MODIS EVI dynamics across various scales were more closely correlated to grass pollen dynamics than H-8 AHI EVI at Mutdapilly, but did not show significant correlations with grass pollen levels at Rocklea (Table 3.6). For H-8 AHI EVI at different scales, all were significantly correlated with grass pollen at two sites, but with the lowest R^2 values (0.36 and 0.38) observed at Mutdapilly (in contrast to 0.1 and 0.31 at Rocklea) among the various sensors. We also found that the grass pollen concentrations usually had the highest R^2 values, with EVI values derived from large research scales at both sites (see bold font in Table 6).

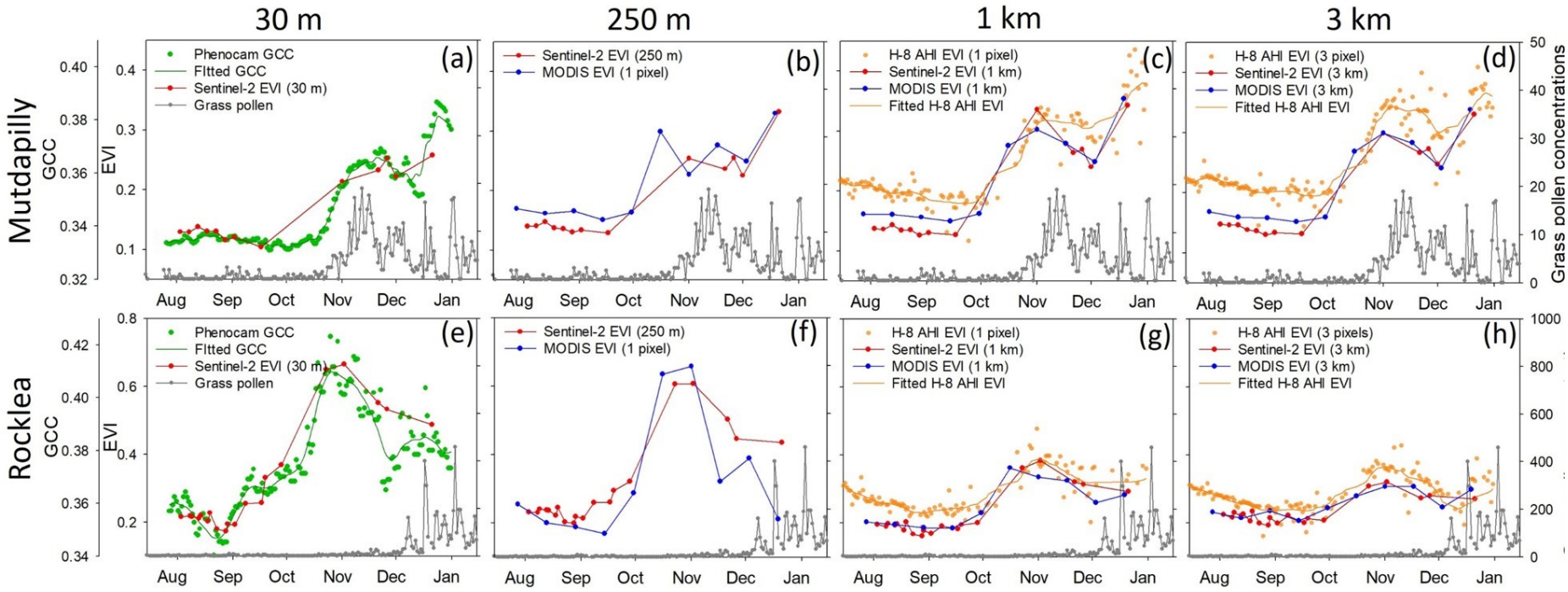

Figure 3.12 Time series plots of grass pollen concentrations and grass/landscape greenness values observed by phenocam, Sentinel-2, MODIS, and H-8 AHI at increased study scales (i.e., 30m, 250m, 1km and 3km) for Mutdapilly (a to d) and Rocklea (e to h) (data shown from August to December 2018).

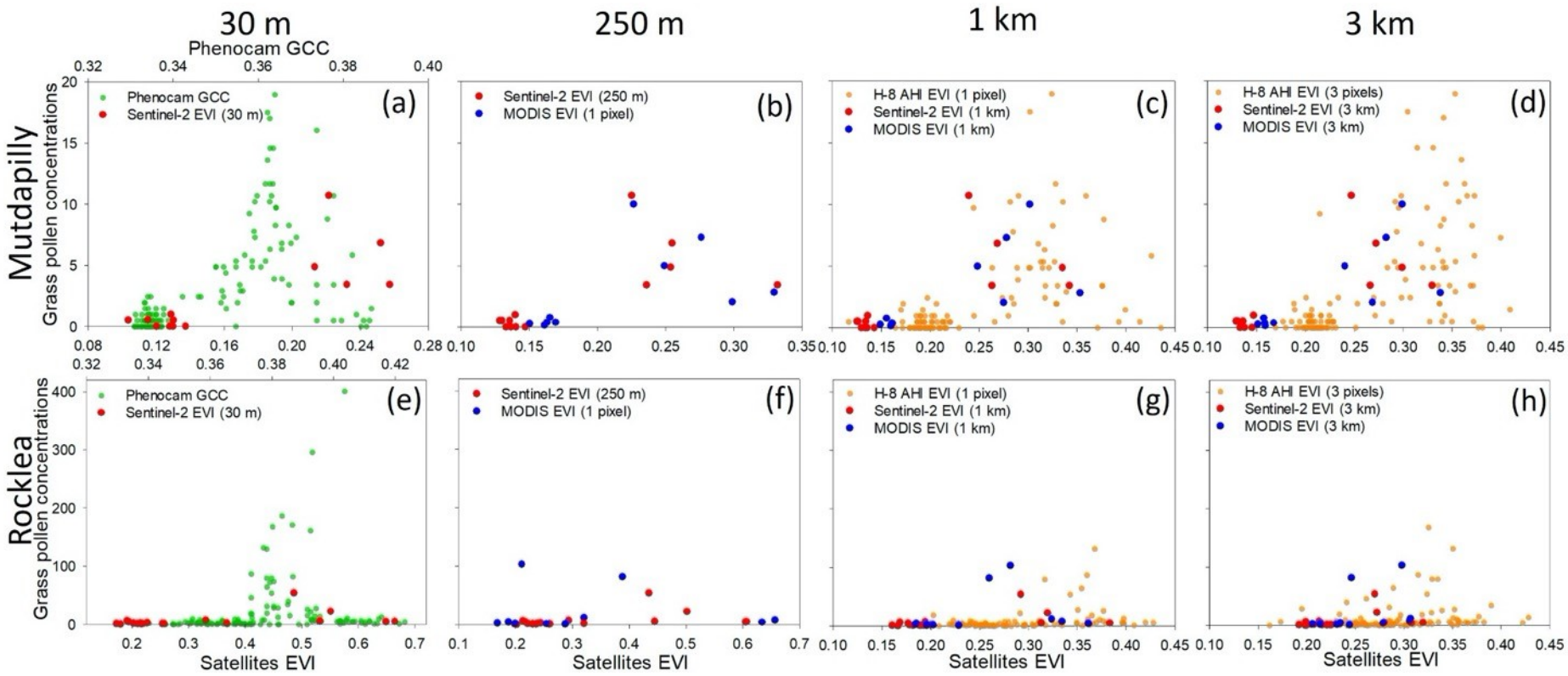

Figure 3.13 Cross plots between grass pollen concentrations and grass/landscape greenness values as observed by phenocam, Sentinel-2, MODIS, and H-8 AHI at increasing study scales (i.e., 30m, 250m, 1km and 3km) for Mutdapilly (a to d) and Rocklea (e to h) (data shown from August to December 2018).

Table 3.6 The statistics of polynomial relationships arising between grass pollen concentrations and grass/landscape greenness as observed by phenocam, Sentinel-2, MODIS, and Himawari-8 AHI across various study scales (30m, 250m, 1km and 3km) for Mutdapilly and Rocklea over the period from August to December 2018.

	Scales	Phenocam	Sentinel-2	MODIS	Himawari-8 AHI
Mutdapilly	*30 m*	$y = 6587.11x - 9101.23x^2 - 1184.6732$ $R^2 = 0.54$*** (n = 159)	$y = 178.18x - 366.95x^2 - 15.96$ $R^2 = 0.64$* (n = 13)		
	250 m		$y = 232.62x - 465.84x^2 - 22.66$ $R^2 = 0.72$* (n = 13)	$y = 411.91x - 828.03x^2 - 44.34$ ***$R^2 = 0.71$*** (n = 10, p = 0.01)	
	1 km		$y = 224.99x - 439.96x^2 - 21.79$ ***$R^2 = 0.76$*** (n = 13)	$y = 204.97x - 363.51x^2 - 22.94$ $R^2 = 0.65$ (n = 10, p = 0.02)	$y = 145.40x - 216.75x^2 - 19.24$ $R^2 = 0.36$*** (n = 107)
	3 km		$y = 273.99x - 556.21x^2 - 26.86$ ***$R^2 = 0.76$*** (n = 13)	$y = 209.31x - 372.92x^2 - 23.51$ $R^2 = 0.63$ (n = 10, p = 0.03)	$y = 128.23x - 161.00x^2 - 18.84$ ***$R^2 = 0.38$***** (n = 124)
Rocklea	*30 m*	NS	$y = 240.38x - 259.28x^2 - 37.73$ $R^2 = 0.32$ (n = 20, p = 0.04)		
	250 m		$y = 380.89x - 437.36x^2 - 63.03$ $R^2 = 0.37$ (n = 20, p = 0.02)	NS	
	1 km		$y = 1028.89x - 1800.93x^2 - 126.04$ ***$R^2 = 0.38$*** (n = 20, p = 0.02)	NS	$y = 416.97x - 515.89x^2 - 68.12$ $R^2 = 0.10$* (n = 105)
	3 km		NS	NS	$y = 2963.58x - 1704.25x^2 - 248.89$ ***$R^2 = 0.31$***** (n = 126)

Note: NS indicated that the correlation is not significant. Asterisks *, **, and *** denote significant correlation at p-values of 0.01, 0.001, and 0.0001, respectively. The bold font shows the highest correlation arising across scales for a certain sensor. The red font shows the highest correlation among sensors for a certain scale.

3.3.5 Comparing temporal relationships arising between grass pollen concentrations and satellite grass EVI across sensors and study scales.

3.3.5.1 Temporal profiles and relationships arising between grass pollen concentrations and Sentinel-2 and MODIS grass EVI at a regional scale.

Multiple-year grass pollen concentrations were plotted alongside the grass cover EVI cover time series at 10km study scales for Mutdapilly, Rocklea and Campbelltown (Fig. 3.14). Both grass pollen concentrations and grass cover EVI time series exhibited strong interannual variability across sites.

At the Mutdapilly site, seasonal grass pollen concentrations corresponded well with satellite EVI profiles, with peaks in grass pollen concentrations and landscape greenness occurring during the Australian late summer to early winter period (February to June) and dormant grass (with minimal greenness values) associated with no grass pollen during the July to January cycle (Fig. 3.14 a, S1 and S3). Upon comparing grass pollen seasons in 2020 and 2018, however, bimodal peaks in satellite EVI were observed from November 2018 to June 2019, which corresponded with bimodal grass pollen peaks (Fig. 3.14 a, S2). Although we were unable to establish whether slight grass pollen peaks occurred around the season from November to January between 2020 and 2021, owing to missing data, we can clearly observe that no grass pollen activity was observed during September 2020 even though the satellite EVI recorded a secondary peak. This indicates that this slight grass EVI within the study scale increased around September 2020, yet did not trigger any substantial grass pollen activity.

The satellite EVI and grass pollen phenology profiles exhibited much stronger interannual variability at Rocklea as compared to Mutdapilly (Fig. 3.14 b). The Rocklea site had a strong pollen release period from the end of December to June (Australian summer to late autumn), yet this was associated with complicated temporally variability in grass pollen concentration values across the years. For the 2018-2019 grass pollen season (Fig. 3.14 b, S2), grass pollen concentration increases were preceded by a sustained increase in satellite EVI, with peak EVI values observed 57 days, on average, before grass pollen peaks. Satellite EVI profiles then reached another peak around the Australian autumn (usually May), corresponding to a grass pollen peak. The interesting finding is that, unlike for other

seasons, the major grass pollen concentration peak did not correlate with major satellite EVI peaks, occurring during a decreasing period of EVI (Fig. 3.14 b, S2). For the 2019-2020 grass pollen season (Fig. 3.15 b, S3), however, increases in satellite EVI values and grass pollen concentrations showed a strong synchronicity. Also, no secondary satellite EVI peaks occurred when the grass pollen concentrations increased around May.

At the Campbelltown site, the grass pollen concentrations exhibited their lowest values across season one (from January to May) as compared with the other two seasons (Fig. 3.14 c, S1). For the 2018-2019 grass pollen season (Fig. 3.14 c, S2), grass pollen concentrations increased sharply with EVI, increasing around November, and then decreasing. There were other two EVI peaks within this season, although these did not trigger grass pollen peaks as the November EVI peak had done. Moving on to the 2019-2020 season (Fig. 3.14 c S3), the two grass pollen peaks correlated closely with grass EVI peaks, which occurred around November and April, respectively. However, although EVI values during the April peak were much higher than for the November peak, the magnitude of grass pollen concentrations was apparently inverted.

Both Sentinel-2 and MODIS grass EVI display significantly positive correlations with grass pollen concentrations at all sites (although R^2 values varied; Fig. 3.14 d, e, and f). We found the strongest correlations between grass EVI and grass pollen concentrations at Mutdapilly (R^2=0.86 and 0.56 for MODIS and Sentinel-2, respectively). This finding was in line with temporal patterns of seasonal dynamics arising between EVI and grass pollen at Mutdapilly (Fig. 3.14 a). However, the correlations were significant, though weak at Rocklea and Campbelltown. As compared with Sentinel-2 EVI, MODIS grass EVI showed a much better predictive ability for grass pollen exposures, with higher R^2 values obtained for all three sites.

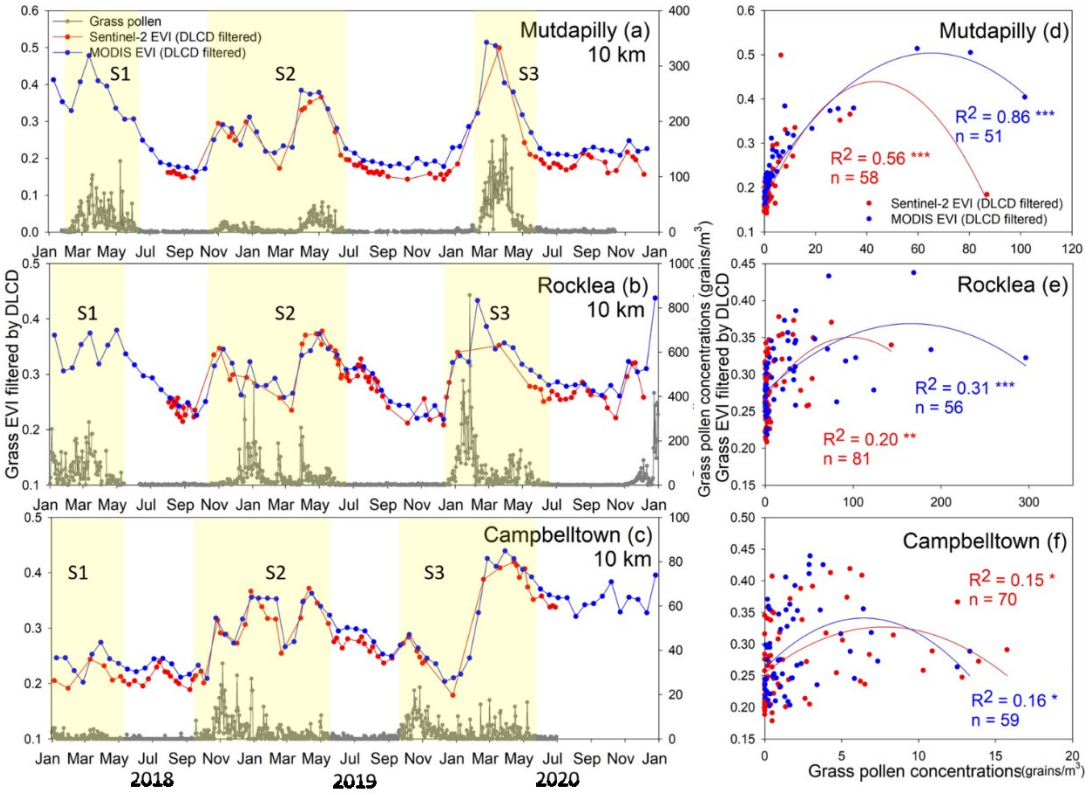

Figure 3.14 Temporal trajectories of grass pollen concentrations and grass EVI from Sentinel-2 and MODIS satellites (as filtered by DLCD grass mask) and relationships between grass pollen concentrations and grass EVI at the 10km scale for Mutdapilly (a and d), Rocklea (b and e), and Campbelltown (c and f) for the period 2018 to 2020. Three grass pollen seasons are highlighted by light yellow rectangles. 'S1' means 'grass pollen season 1', and so forth. The specific dates for each of the grass pollen seasons are shown in Table 7. The polynomial relationships between grass EVI and grass pollen concentrations, as shown in panels (d), (e), and (f), were conducted during periods where both satellite EVI values were available.

Although the increase in grass pollen was closely associated with the increase of EVI values, the value of grass pollen concentrations and the length of time varied over years and between sites. For example, S2 (grass pollen season 2) at Mutdapilly lasted longer than others, yet it had the lowest sum and average values of grass pollen concentrations (sum=1,978.92 grains/m^3; mean = 8.39 grains/m^3 as presented in Table 3.7 and Fig. 3.14 a) among all grass pollen seasons recorded. In contrast, S3 at Rocklea was over shorter duration than S2, but grass pollen concentrations during the pollen activity period were dramatically higher than those at S2 (Table 3.7 and Fig. 3.14 b). It is however interesting to note that the

percentages of grass cover at Mutdapilly and Campbelltown were higher than at Rocklea (Fig. 3.2, Table 3.2), and the sum of grass pollen concentrations trapped from Rocklea were 2.5, 4.6 and 2.6-fold higher than from Mutdapilly for S1 to S3; and 94.3, 10.6, and 15.4 times higher than Rocklea for S1 to S3, respectively (Table 3.7). These findings are consistent with the grass pollen collected at Rocklea deriving from areas beyond the 10×10 km grid and hence the Sentinel-2 and MODIS grass EVI may not correlate well with grass pollen activities.

Table 3.7 The sum and mean values of grass pollen concentrations and corresponding mean EVI derived from satellites for each grass pollen season. S1 represents grass pollen season 1, and so on. They correspond to the light yellow areas marked in Fig. 14. The term g% represents the percentage of grass cover within 10 km for each site. The bold font denotes the highest values for each column.

	Grass pollen seasons	*Grass pollen con. (grains/m^3)*		*Sentinel-2 grass EVI*	*MODIS grass EVI*
		SUM	*AVE*		
Mutdapilly	S1 (1/01/2018 – 15/06/2018)	3128.61	25.03		0.36
g% = 73.11%	S2 (23/10/2018 – 15/06/2019)	1978.92	8.39	0.28	0.28
	S3 (1/02/2020 – 31/05/2020)	**4823.31**	**40.53**	**0.32**	**0.37**
Rocklea	S1 (1/01/2018 – 14/05/2018)	7836.40	65.30		**0.34**
g% = 20.81%	S2 (23/10/2018 – 15/06/2019)	9145.66	39.25	**0.32**	0.31
	S3 (14/12/2019 – 6/06/2020)	**12542.18**	**76.95**	0.29	**0.34**
Campbelltown	S1 (1/01/2018 – 14/05/2018)	83.13	0.62	0.21	0.24
g% = 30.21%	S2 (23/10/2018 – 15/06/2019)	**864.31**	**7.97**	0.31	**0.32**
	S3 (23/09/2019 – 9/05/2020)	813.75	7.28	**0.32**	0.31

3.3.5.2 Summary of time intervals for peaks between grass greenness profiles and grass pollen concentrations across sensors and study scales

We compared time intervals between grass pollen concentration peaks and the nearest grass greenness peaks across all sensors (phenocam, Sentinel-2, and MODIS) and study scales (30m, 250m, and 10km) at Mutdapilly (Fig. 3.15), Rocklea (Fig. 3.16), and Campbelltown (Fig. 3.17). The black and red dashed lines in Fig. 3.15 -17 denote the grass pollen concentration peaks derived from fitted curves of grass pollen time series for each location. The difference between the solid and dashed lines is that there were greenness peaks that either occurred before or after grass pollen peaks denoted by the black lines, yet no greenness peak

corresponded to grass pollen peaks which are denoted by the dashed red lines. For each of the grass pollen peaks, we used coloured bars to denote different sensors so as to represent the time intervals arising between pollen peak and the grass greenness peaks across our study scales. When the bar is located to the left of the grass pollen peak line, it indicates that the greenness peak preceded the grass pollen peak, and vice versa. We highlighted 30m and 10km scales using a green colour due to the EVI values at these two scales being averaged from grass pixels (as filtered by the DLCD land cover map with 250m resolution at 10km and so there is an inevitable mixed pixel effect), whereas the EVI were mean values from all pixels at the 250m scale. Tables 3.8, 3.9 and 3.10 summarise the DOY for each peak at the three sites. Also, the time intervals of peaks (in days) between grass greenness and grass pollen are shown in brackets.

In general, most of the greenness peaks occurred before grass pollen peaks at all sites. However, the durations of time intervals for all seasons at Rocklea were dramatically longer than for those at the other two sites, especially grass pollen peak 2 which occurred on 3 DOY, 2019 (Table 3.9), where the mean days of time intervals were 12.14, 44.75, and 12.59 days at Mutdapilly, Rocklea, and Campbelltown, respectively. Meanwhile, Rocklea had the lowest greenness peaks and these appeared before the grass pollen peaks across the three sites, and the percentage of 'before' greenness peaks (red font in Table 3.8 to 3.10) were 76.19%, 50.00% and 85.00% among all greenness peaks at Mutdapilly, Rocklea and Campbelltown, respectively.

There were obvious variations in the time intervals recorded across sensors and study scales at Mutdapilly (Fig. 3.15 and Table 3.8). At the *in-situ* scale, the time interval between peaks as recorded by Sentinel-2 EVI and the grass pollen were consistent with phenocam GCC at two peaks yet were opposite at another major grass pollen peak (Fig. 3.15 a). At the 250m scale, the patterns between EVI peaks and pollen peak 2 were contradictory between Sentinel-2 and MODIS (the MODIS EVI peak is over a month ahead of the peak of Sentinel-2 EVI) yet was consistent at peaks 3 and 4 (Fig. 3.15 b). However, inverse patterns arose between the two sensors at grass pollen peak 4 when the study scale increased to 10km (Fig. 3.15 c). As for the same sensor at increased scales, MODIS EVI peaks kept a consistent

interval pattern with pollen peaks at the 250m and 10km scales, but Sentinel-2 EVI peaks shifted across scales (e.g., peaks 2 and 4).

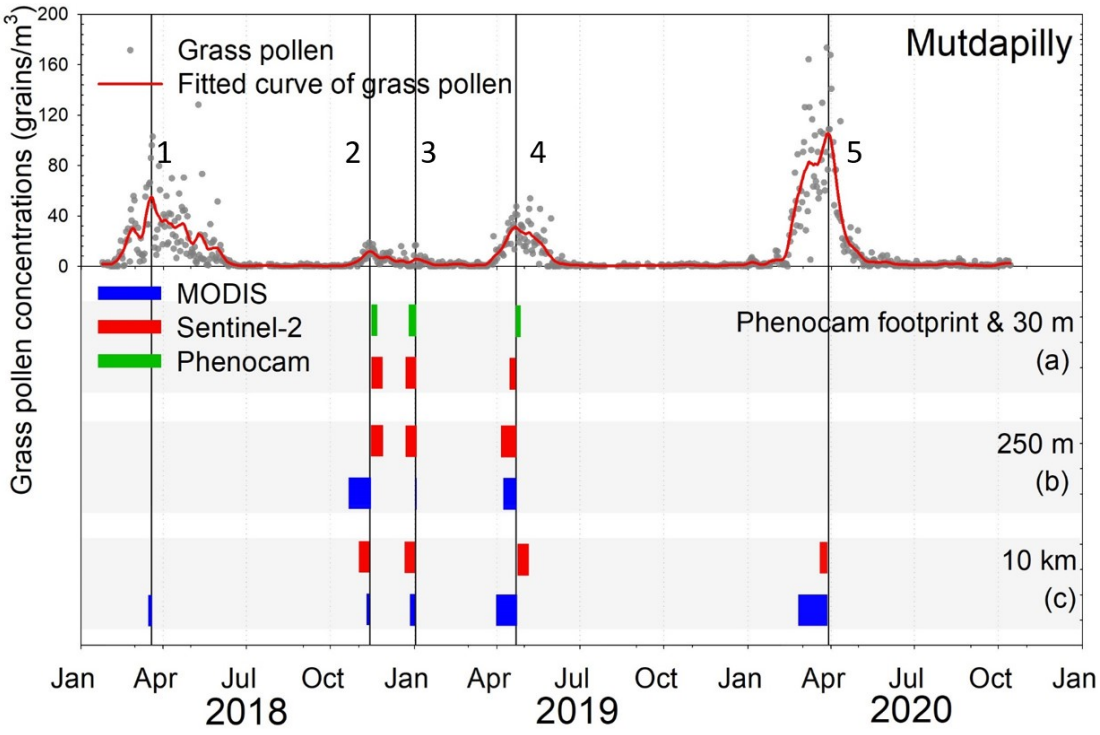

Figure 3.15 Changes in time intervals arising between grass pollen concentration and grass greenness peaks derived from multi-sensors (phenocam, Sentinel-2, and MODIS) across various study scales at Mutdapilly. The black lines denote the dates of grass pollen concentration peaks occurring from 2018 to 2020. The coloured bars denote time intervals in days between peaks in greenness profiles and grass pollen concentrations.

The pattern of time intervals arising in Rocklea is more complicated than that observed for Mutdapilly. This is not only because some greenness peaks lagged significantly behind grass pollen peaks, but also because some grass peaks did not correspond to greenness peaks (e.g., grass peaks 3, 5 and 7; Fig. 3.16 and Table 3.9). At the *in-situ* scale (Fig. 3.16 a), Sentinel-2 EVI recorded consistent intervals between grass pollen peaks in relation to phenocam GCC, and the differences arising between them were around 10 days. At the 250m and 10 km scales (Fig. 3.16 b and c), Sentinel-2 EVI peaks exhibited longer time intervals with respect to grass pollen peaks as compared with the MODIS EVI time series, yet they kept consistent interval patterns. For the grass pollen peaks 1, 4 and 6, all greenness

peaks lagged behind the respective pollen peaks. In contrast, all greenness peaks preceded grass pollen peak 2 by 55 to 72 days. Though the satellite EVI peaks were also in advance of pollen peak 8, the time intervals were shorter than for pollen peak 4. As for the same sensor at increased scales, Sentinel-2 EVI peaks tended to occur in close temporal proximity to grass pollen peak 4 (almost 1 month) at 30m to 10km scales, yet maintained similar intervals across scales at pollen peak 2. As compared with Sentinel-2, MODIS EVI peaks shifted to a lesser extent around pollen peak 2 but to a greater degree around pollen peak 4.

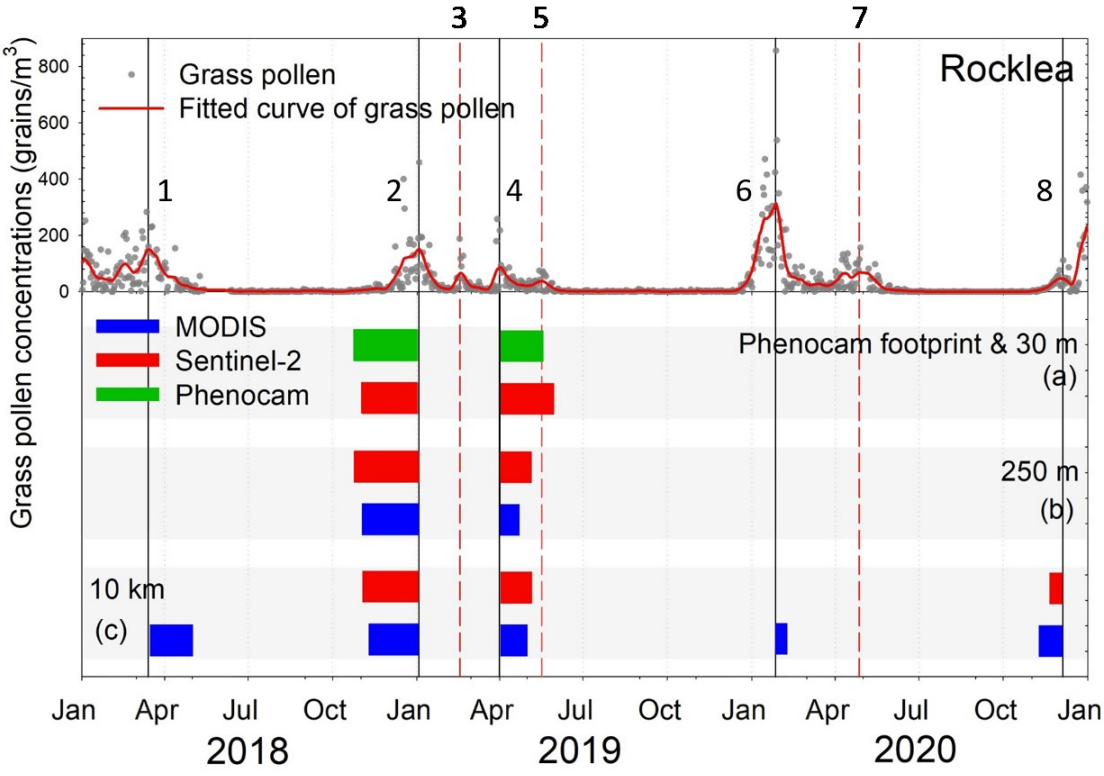

Figure 3.16 Changes in time intervals arising between grass pollen concentration peaks and grass greenness peaks derived from multiple sensors (phenocam, Sentinel-2, and MODIS) across varied study scales at Rocklea. The black and red (dashed) lines denote the dates of grass pollen concentration peaks during the seasons spanning from 2018 to 2020. The coloured bars denote the time intervals in days between peaks in greenness profiles and grass pollen concentrations.

At the Campbelltown site, six grass greenness peaks correlated with grass pollen concentration peaks and most of them preceded pollen peaks with time intervals varying from 1 to 32 days (Fig. 3.17 and Table 3.10). Among all the pollen peaks

recorded, peak 4 (361 DOY, 2018) and peak 7 (112 DOY, 2019) had the shortest and longest intervals between grass greenness metrics and pollen peaks, respectively. Meanwhile, Sentinel-2 EVI maintained the same interval patterns across scales at peak 4, showing a slight difference in patterns at peak 7. In contrast, MODIS EVI exhibited opposite patterns pollen peaks at 250m and 10km for peak 7. At the largest study scale (10 km), all satellite EVI peaks preceded pollen peaks at Campbelltown (Fig. 3.17 c) although this was not the case at the other two sites.

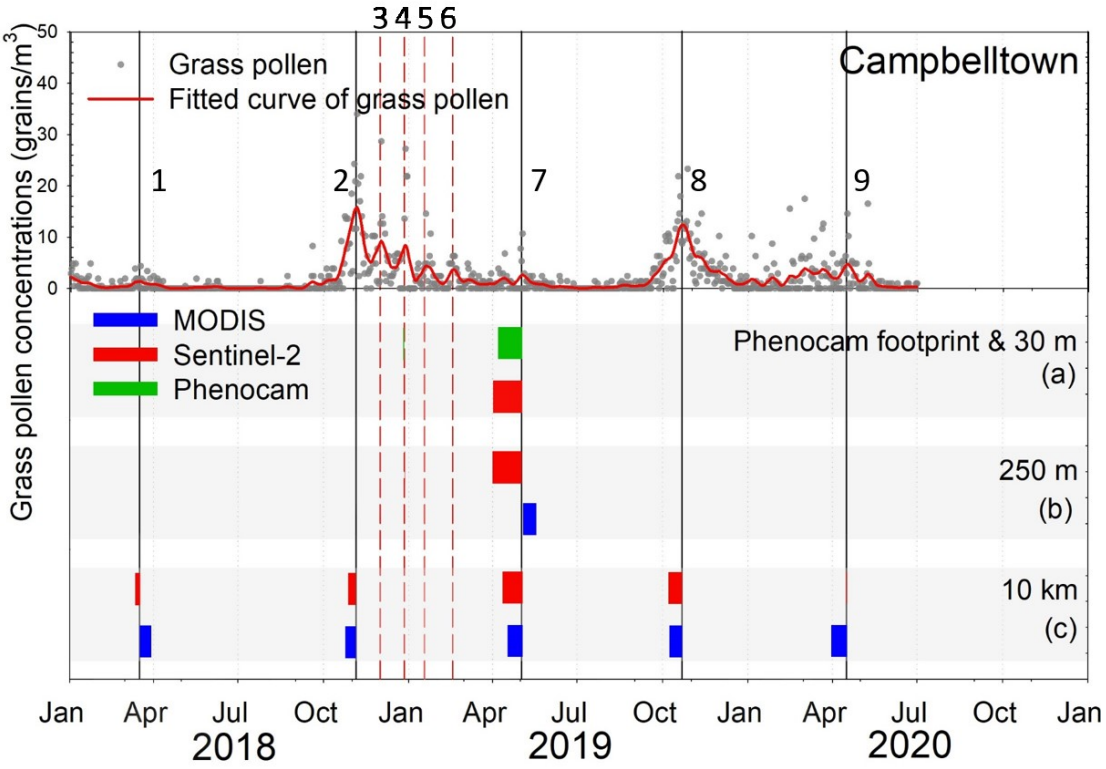

Figure 3.17 Changes in time intervals arising between grass pollen concentration and grass greenness peaks as derived from multiple sensors (phenocam, Sentinel-2, and MODIS) across various study scales at Campbelltown. The black and red (dashed) lines denote the dates of grass pollen concentration peaks during the seasons spanning from 2018 to 2020. The coloured bars denote time intervals in days between peaks of greenness profiles and grass pollen concentrations.

Table 3.8 The DOY of grass pollen peaks and greenness observation peaks from multi-sensors remote sensing across study scales at Mutdapilly from 2018 to 2020.

Sensors	**Scales**	***Grass pollen peak 1*** *88 (2018)*	***Grass pollen peak 2*** *317 (2018)*	***Grass pollen peak 3*** *2 (2019)*	***Grass pollen peak 4*** *112 (2019)*	***Grass pollen peak 5*** *89 (2020)*
Phenocam	*30 m*		324 (7)*	358 (2018) (-9)	117 (5)	
Sentinel-2	*30 m*		326 (13)	355 (2018) (-12)	105 (-7)	
	250 m		326 (13)	355 (2018) (-12)	95 (-17)	
	10 km		305 (-12)	355 (2018) (-12)	125 (13)	80 (-9)
MODIS	*250 m*		289 (-28)	1 (-1)	97 (-15)	
	10 km	73 (-5)	313 (-4)	361 (-6)	89 (-23)	57 (-32)

*: (days) = (*DOY of grass pollen peak*) – (DOY of greenness peak)

Table 3.9 The DOY of grass pollen peaks and greenness observation peaks from multi-sensors remote sensing across study scales at Rocklea from 2018 to 2020.

Sensors	**Scales**	***Grass pollen peak 1*** *73 (2018)*	***Grass pollen peak 2*** *3 (2019)*	***Grass pollen peak 4*** *91 (2019)*	***Grass pollen peak 6*** *27 (2020)*	***Grass pollen peak 8*** *340 (2020)*
Phenocam	*30 m*		298 (-70)*	138 (47)		
Sentinel-2	*30 m*		306 (-62)	150 (59)		
	250 m		296 (-72)	126 (35)		
	10 km		306 (-62)	126 (35)		325 (-15)
MODIS	*250 m*		305 (-63)	113 (22)		
	10 km	121 (48)	313 (-55)	121 (30)	41 (14)	313 (-27)

*: (days) = (*DOY of grass pollen peak*) – (DOY of greenness peak)

3.3.6 Changes in relationships arising between grass pollen concentrations and phenocam GCC and Himawari-8 AHI EVI across temporal scales (temporal scale effects)

Using daily phenocam GCC and Himawari-8 AHI (H-8 AHI) EVI data, we compared those relationships arising between grass greenness observations and grass pollen concentrations across varied temporal scales (i.e., daily, 8 days, and 16 days) at the Mutdapilly site to explore how the temporal scale effect impacts their interrelationships, asking whether the hyper-temporal scale is best suited for grass pollen forecasting via satellite. These analyses were conducted at the *in-situ* scale using phenocam GCC data from August 2018 to August 2019, and also at the 1km scale using Himawari-8 AHI EVI data in 2018 at Mutdapilly. These two datasets overlapped from August to December 2018 (Fig. 3.18). The reason why we conducted analyses at Mutdapilly is that the proportion of grass cover at 1km at Mutdapilly is 87.50% (Table 3.5), and thus the confounding mixed pixel effect in observing grass greenness using H-8 AHI data could be reduced.

We averaged daily phenocam GCC and H-8 AHI EVI data to 8-day and 16-day mean values. The daily, 8-day and 16-day mean phenocam GCC and H-8 AHI EVI values are plotted alongside the grass pollen concentration time series in Fig. 18. Seasonal phenocam GCC and H-8 AHI EVI data corresponded well with grass pollen concentration profiles from 2018 to 2019 at all temporal scales, with peak grass activities (greenness) and pollen concentrations occurring during the autumn (March-May) and late spring to summer (November-January) seasons. The coloured lines at the bottom of the figures show the peak grass pollen concentrations and grass greenness metrics. Firstly, all peaks move forward as the temporal scale decreases (i.e., from daily to 16 days). Further, the time intervals arising between grass pollen and grass greenness peaks narrow as the temporal scale decreases. For example, the H-8 AHI EVI and phenocam GCC peaks even occur at the same time as pollen concentration peaks during the 'April-May' season when presented at the 16-day temporal scale (Fig. 3.18 c). As for the other two temporal scales, the pollen-greenness intervals for both phenocam GCC and H-8 AHI EVI were longer at the 8-day scale than those at the daily scale (Fig. 3.18 a and b). Another factor that should not be ignored is the secondary or moderate grass

pollen peak triggered by an increase in grass greenness which duly disappeared in terms of its pollen trajectory with a temporal scale decrease. According to the red circle shown in Fig. 3.18, there was moderate grass pollen activity around January 2019. However, it was 'wiped' from pollen profile when temporal scale was decreased from daily to a 16-day periodicity. If further research were to be conducted using the 16-day temporal scale, we would draw the incorrect conclusion that the January grass greenness peak did not correspond to an increase in grass pollen.

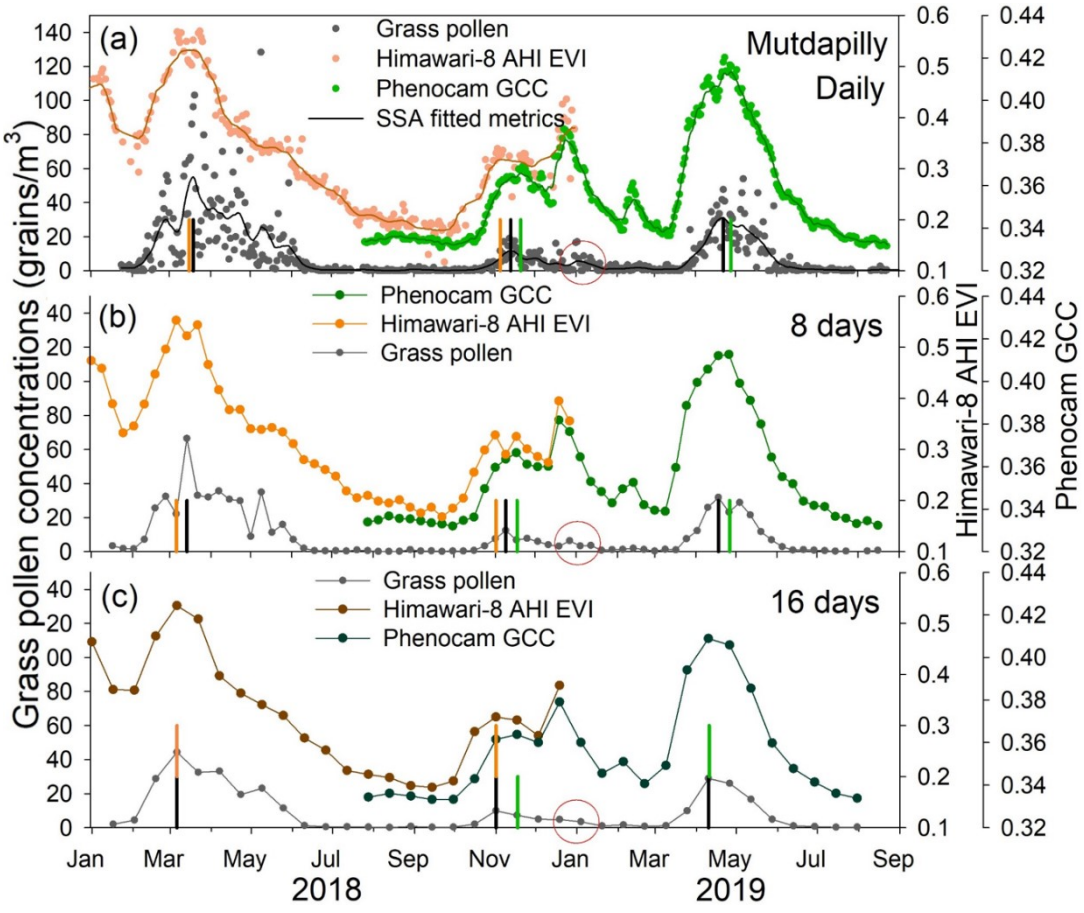

Figure 3.18 Seasonal trajectories of daily (a) and average phenocam GCC and Himawari-8 AHI EVI (1km) at 8 day (b) and 16 day (c) temporal scales at Mutdapilly. The coloured lines at the foot of the figures denote peaks of grass greenness and grass pollen concentrations. The black, yellow and green colours represent pollen concentrations, H-8 AHI EVI, and phenocam GCC data, respectively.

Fig. 3.19 shows the interrelationships arising between grass pollen concentrations and grass greenness metrics across a range of temporal scales. In general, both phenocam GCC and H-8 AHI EVI data significantly correlate with grass pollen concentrations across all temporal scales. As the temporal scale decreases, correlations between grass greenness values and grass pollen concentrations increase, with values of R^2 varying from 0.5 to 0.73 for H-8 AHI EVI (Fig. 3.19 a) and from 0.67 to 0.89 for phenocam GCC (Fig. 3.19 b). During the period of overlap (Fig. 3.20), phenocam GCC exhibits a stronger correlation with grass pollen concentrations than H-8 AHI EVI across all temporal scales. Similarly, the relationships varied across temporal scales (i.e., stronger correlations were observed at shorter temporal scales).

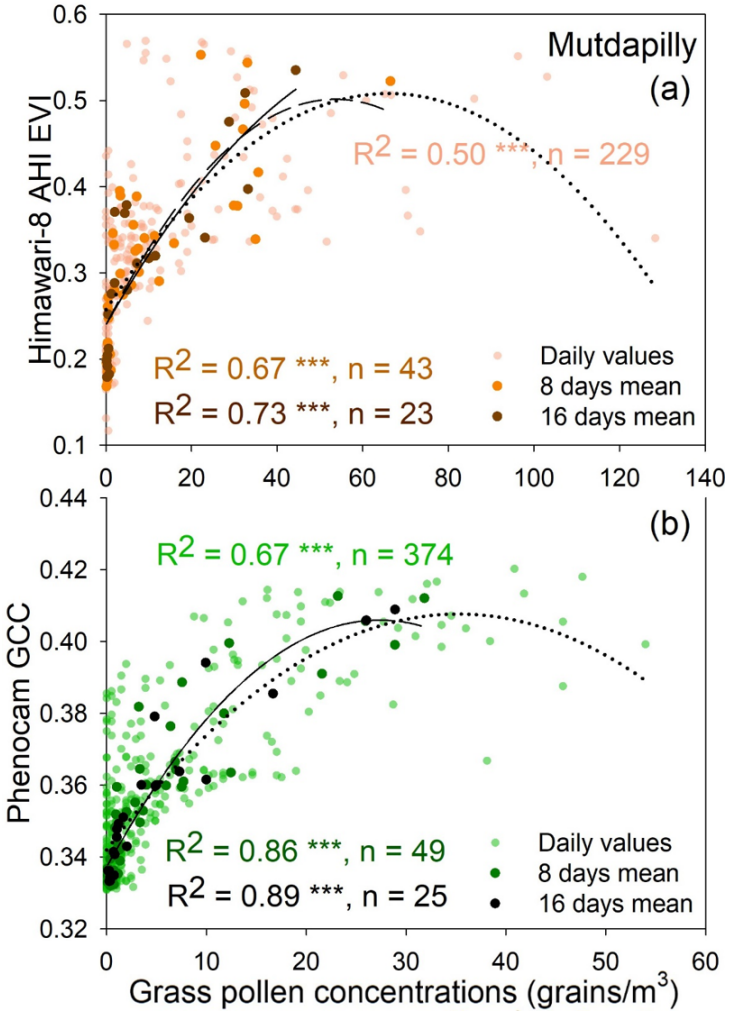

Figure 3.19 Polynomial relationships between daily, 8-day, and 16 day average grass pollen concentrations and Himawari-8 AHI EVI data (1km) through the

entirety of 2018 (a), and phenocam GCC data from August 2018 to August 2019 (b) at Mutdapilly.

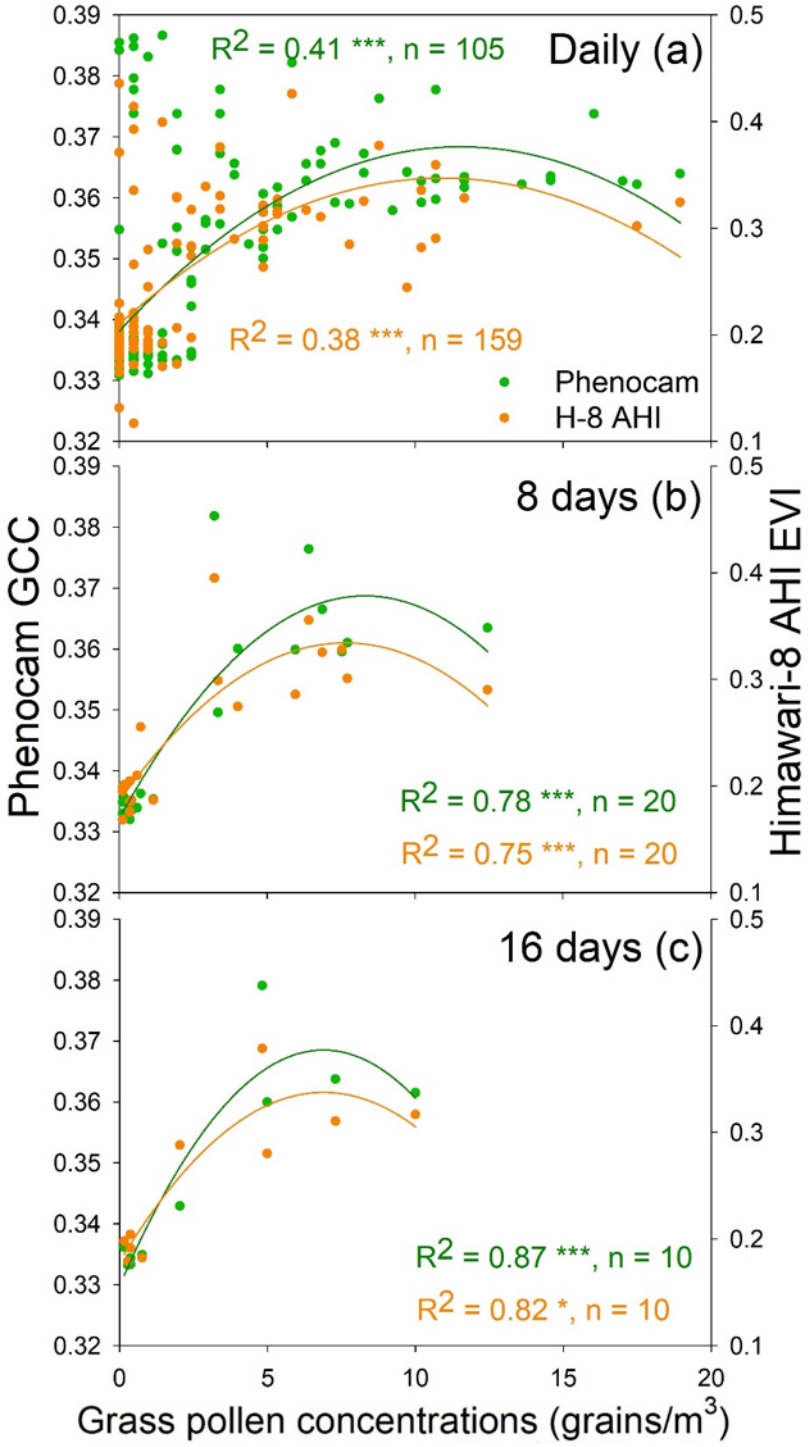

Figure 3.20 Polynomial relationships between daily, 8-day, and 16 day average Himawari-8 AHI EVI (1km) (a) and phenocam GCC (b) and grass pollen concentrations with corresponding temporal scales during the period of study (August to December 2018) for Mutdapilly.

3.4 DISCUSSION

This study exemplifies the potential for multiple scales in remote sensing imagery to detect grass cover phenology and their capacity to assist in our understanding of the relationships arising between grass cover phenology and grass pollen concentrations at three sites which characterise different types of land cover in terms of vegetation.

In recent decades, various models and approaches have been introduced to explore the relationships arising between satellite observations of vegetation phenology and *in-situ* pollen data (Devadas et al., 2018; Hogda et al., 2002b; Karlsen et al., 2009; Khwarahm et al., 2017; Li et al., 2019). Despite these promising applications of satellite-based vegetation phenology in the study of pollen aerobiology, developing confident grass phenology-pollen relationships remains difficult owing to the limitations of the spatial and temporal resolutions of satellite imagery, especially when we consider complex land coverage in terms of the spatial heterogeneity of vegetation surrounding pollen traps. Therefore, in sections 3.3.1 and 3.3.2, our study assessed the performance in detecting grass greenness information across different land cover types from space based upon widely used satellite data with *in-situ* phenocam observations serving as a land surface reference.

To understand the grass pollen-greenness interrelationships and their observed differences across various sites and sensors, we conducted our analyses from two perspectives. The first was conducting quantitative correlations between grass greenness metrics (i.e., phenocam GCC and satellite EVI) and grass pollen concentrations. A second perspective was comparing grass pollen concentration peaks and grass greenness peaks following the methods adopted by previous studies (Devadas et al., 2018; Li et al., 2019). These analyses were included in sections 3.3.3 to 3.3.5.

To explore how differences in spatial resolution between each satellite impact grass pollen-greenness relationships, we compared the time series and correlations arising between satellite measures of grass/landscape and grass pollen concentrations over the same period for two sites (Figs. 3.13 and 3.14; Table 3.6). Given that grass cover proportions changed across research scales, a series of spatial windows were

opened that were centred on pollen traps to explore whether the grass pollen-greenness relationships varied with changes in research scale. Finally, besides the spatial scale effect, the temporal resolution of satellite measures of grass cover is also an important factor in generating more accurate pollen forecast models. We began by exploring which temporal resolution in terms of grass greenness time series showed better performance in helping us to understand the dynamics of grass pollen concentrations (section 3.3.6).

3.4.1 Grass phenology monitoring using multi-scale satellites

Our results confirm that multi-scale satellite observations of grass/landscape greenness can be effectively linked to phenocam observations at the single-pixel level. However, their performance in detecting real land surface grass greenness information became weaker as research scales increased, especially at more heterogeneous sites.

The Sentinel-2 EVI time series extracted from the phenocam footprint (i.e., 3x3 pixels) correlated well with ground-based phenocam GCC, with the R^2 values ranging from 0.75 to 0.96 across the three sites (Fig. 3.5). Thus, there is a good correlation between phenocam observations and fine-resolution Sentinel-2 data, in agreement with previous studies. For example, Gómez-Giráldez et al. (2020) found significant correlations between Sentinel-2 EVI time series data and phenocam GCC data ($r > 0.7$) in a savannah ecosystem. In the forested canopy, phenocam GCC and Sentinel-2 EVI were reported as following similar seasonal patterns and also showed good agreement as reflected in their high correlation coefficients ($r = 0.92$; Thapa, Garcia Millan & Eklundh, 2021). On the other hand, the phenological transition dates derived from phenocam and Sentinel-2 were in close agreement in grassland ecosystems (Burke & Rundquist, 2021; Vrieling et al., 2018; Zhou et al., 2019), shrubland ecosystems (Peng et al., 2021), and forest ecosystems (Lange et al., 2017; Zhang et al., 2020).

Despite the Sentinel-2 EVI data showing statistically significant relationships (i.e., high values of coefficient of determination, presented as R^2) with phenocam GCC, this was nonetheless limited by the revisit frequency and the capacity to acquire clear images when tracking subtle variations in grass greenness. According to Fig. 3.5 a, there was only one available Sentinel-2 image within three months (from the

end of December 2018 to April 2019). Therefore, this sensor failed to capture the grass greenness activity around February as recorded by phenocam images with a daily temporal resolution. Similarly, the big data gap arising between January and March at Rocklea (Fig. 3.5 c) also caused the paucity of information in relation to grass greenness dynamics from Sentinel-2 EVI profiles, whereas phenocam GCC recorded a series of grass greenness fluctuations. This finding also could be used to partially explain why the statistical correlation between EVI and phenocam GCC data was the lowest among the three sites studied. Another obvious phenomenon is that Sentinel-2 images are usually clustered around 'dry-grass' growing seasons. For example, in Fig. 3.5 a and c, a cluster of Sentinel-2 EVI points was gathered from July to September, a period when grass greenness metrics were at their lowest levels within the growing season. We can attribute this phenomenon to the wet-cloudy season as this hindered the acquisition of cloud-free images. These two sites (Mutdapilly and Rocklea) were located close to Brisbane where the climate is characterised as humid subtropical (Carver, Mikkelsen & Woodward, 2002), a region in which there is less precipitation from April to September and more intensive precipitation from October to March (sources: *Climate statistics for Australian locations*. Bureau of Meteorology). The chances of obtaining cloud-free Sentinel-2 images dramatically decreases during the wet-cloudy season, even though it is a critical period for grassland greenness shifts because previous studies have proved that Australia's arid and semi-arid grassland dynamics are primarily derived from rainfall patterns (Ma et al., 2013; Petus, Lewis & White, 2013). As technology develops further, fusion of Visible Infrared Imaging Radiometer Suite (VIIRS) and the NASA Harmonized Landsat and Sentinel-2 (HLS) product (Zhang et al., 2020), which now routinely produce near real-time image feeds by combining Landsat-8 and Sentinel-2A/B observations at a 30m resolution, might provide us with an opportunity to solve this restriction for land surface phenology observations caused by irregular temporal sampling of data (Bolton et al., 2020; Peng et al., 2021).

When compared with Sentinel-2 EVI, the performance of MODIS EVI in detecting grass greenness dynamics at its single-pixel level (250m) decreased substantially, with lower R^2 values being recorded, although still significant (Fig. 3.6). Also,

although MODIS EVI and phenocam GCC recorded similar seasonal patterns, they obviously differed in terms of the peaks of greenness reported. Meanwhile, their correlations of seasonal patterns att the heterogeneous site (Rocklea) were lower than at the homogeneous site (Mutdapilly). Similarly, despite H-8 AHI EVI possessing hyper-temporal resolution, it still only weakly correlated with phenocam GCC data at Rocklea, with a slightly higher R^2 than MODIS EVI (Fig. 3.7). These poor correlations could be due to the mixed pixel effect introduced by coarser resolutions at the heterogeneous site. A pixel in MODIS and H-8 AHI may contain non-grassy vegetation in terms of land cover types or else mixed grass species were included in the pixel which differed from the grass species observed by phenocam. A number of researchers reported the mixed pixel effect affecting the interrelationships arising between MODIS VIs and *in-situ* phenocam GCC (Browning et al., 2017; Hufkens et al., 2012b; Liu et al., 2017; Peter et al., 2018). For example, a study conducted on grassland reported a highly heterogeneous landscape of the MODIS pixel in which research site resided, thereby affecting the relationship between MODIS EVI and phenocam GCC (Cui et al., 2019). A more comprehensive study seeking agreement between phenocam and MODIS greenness metrics across various vegetation types also stated that landscape heterogeneity and a mismatch between the phenocam footprint and the associated MODIS pixel are recurring themes when interpreting the poor agreements between them (Richardson et al., 2018). The distinct differences arising in terms of the original time series between Himawari-8 AHI data and *in-situ* phenocam GCC data also was attributed to heterogeneous landscapes (Yan et al., 2019).

Section 3.3.2 explores the research question as to whether the advantages of Sentinel-2 data can be maintained over extended research scales. According to our results (Fig. 3.8 and Table 3.5), Sentinel-2 EVI consistently provided stronger agreements with phenocam GCC across increased research scales as compared to MODIS EVI at the same study period. Also, more homogeneous research scales were associated with stronger correlations at both sites (i.e., 3km scale for Mutdapilly and 1km scale for Rocklea; Table 3.5). Because the study period for H-8 AHI EVI was only a segment of that for MODIS and Sentinel-2 EVI, we cannot truly compare its performance with MODIS and Sentinel-2 directly. Even so, higher

R^2 values between H-8 AHI EVI and phenocam GCC were obtained than for Sentinel-2 EVI at Rocklea (a heterogeneous site), which could lead us to think that the performance of H-8 AHI data could benefit from hyper-temporal resolution at such locations with a heterogeneous landscape (as opposed to a finer spatial resolution data with lower temporal resolution). In general, Sentinel-2 data of finer spatial resolution maintained its advantage in observing grass greenness across larger research scales.

3.4.2 Relationships between grass pollen concentrations and grass/landscape phenology

In general, the grass pollen concentrations showed considerable interannual and inter-site variability. Throughout the period from 2018 to 2020, although grass pollen seasons lengths and magnitudes of pollen concentrations varied across sites and years, three major grass pollen seasons were exhibited at each of these three sites. At the Mutdapilly and Rocklea sites (both located in Queensland), two autumnal pollen seasons occurred in 2018 and 2020 (S1 and S3 in Fig. 3.14 a and b), plus another long pollen season run from November 2018 to June 2019 (Australian late spring to autumn; S2 in Fig. 3.14 a and b), exhibiting bimodal and trimodal patterns at Mutdapilly and Rocklea, respectively. At Campbelltown (New South Wales), two long grass pollen seasons lasted from October to May of the next year, yet it had the lowest concentrations among three sites. This variation is likely related to differences in grass species or other factors such as meteorological conditions including rainfall, temperature, and wind, which impacted grass growth (Chuine & Belmonte, 2011; Li et al., 2019; Rojo et al., 2015).

In general, the time series of phenocam and satellite measurements of grass cover and landscape (for Himiawari-8 AHI) can interpret the seasonal dynamics of grass pollen concentrations at all sites. However, the correlations between the two metrics varied across sites, with coefficients of determination that were quite variable (Figs. 3.9 – 3.14). For example, at the 10km scale, Sentinel-2 and MODIS data accounted for 56% and 86%, respectively, of the seasonal variation in grass pollen concentrations at Mutdapilly. In contrast, satellite data only accounted for 15% to 31% of the pollen concentration dynamics at Rocklea and Campbelltown (Fig. 3.14). These poor correlations can partly be correlated to asynchronous patterns

arising between satellite EVI peaks and pollen peaks during S2 at both sites (Fig. 3.14 b and c). At Rocklea, the grass pollen peak around January 2019 significantly lagged behind the Sentinel-2 and MODIS EVI data by 62 and 55 days, respectively (Table 3.9). However, the major grass pollen peak at S2 arose in advance of the satellite EVI peaks and the increased grass greenness observed at Campbelltown (Fig. 3.14 c). Besides, time intervals between grass pollen and grass greenness peaks vary distinctly among sites, by 12.14 days (on average across peaks and sensors), 44.75 days, and 11.40 days at Mutdapilly, Rocklea, and Campbelltown, respectively (Figs. 3.15-17, Table 3.8-10).

The contrasting results observed among sites may at least partly be attributed to land cover conditions, grass species diversity, and pollen source distributions. Land cover types and grass cover at the Mutdapilly site were otherwise relatively homogeneous and uniformly distributed (Fig. 3.2), resulting in good correlations and relatively short intervals in peaks between grass pollen and multi-sensor measures of grass greenness. Land cover conditions were more heterogeneous at Rocklea and Campbelltown with a number of buildings and roads surrounding pollen trap sites (Fig. 3.2). Therefore, the grass phenological profiles at these two sites included some non-grass information as a coarse grass map was adopted. Even the coarse grass map though accurately filtered grass components, although these grass classes might comprise diverse grass species, especially in regions around Sydney. According to previous studies, grassy areas in the Sydney region are comprised of mixed temperate cool season grasses (C_3 grass) and subtropical or summer-flowering grasses (C_4 grass; Davies et al., 2015; Medek et al., 2016), as well as native and exotic species that exhibit different phenology patterns (Watson, Restrepo-Coupe & Huete, 2019). It partly explains the broader grass phenology profiles and corresponding long pollination periods found at the Campbelltown site (located in the greater Sydney region). Another potential reason which cannot be overlooked is the long range transport of pollen (Hogda et al., 2002b; Holben, 1986; Sauliene et al., 2013). This means that these grass pollens collected by *in-situ* traps likely come from grass sources which lie beyond the 10km study areas. Therefore, the time series of grass cover greenness observed nearby pollen traps are strongly asynchronous with actual pollen profiles (e.g., S2 in Rocklea; Fig. 3.14 b).

Even interannual climate condition variability can introduce unexpectedly sharp increases in grass greenness and, consequently, impact the seasonal dynamics of grass pollen (Haberle et al., 2014; Ramón & Peter, 2020). For example, these unexpectedly greener grasses might not be within their normal pollination period or else only release a small quantity of grass pollen (e.g., the grass greenness peaks observed around April for S2 and S3 at Campbelltown; Fig. 3.14 c).

Additionally, our result that most grass greenness peaks occurred before grass pollen peaks at all sites (Fig. 3.15 - 3.17) keeps in line with the previous study. Combining MODIS EVI product with grass pollen concentrations, Devadas et al. (2018) found that peak pollen activity lagged behind peak grass cover greenness on average by 2–3 weeks and 4–7 weeks in temperate sites in France and Australia, respectively. To further interpret the temporal gap between grass greenness and airborne grass pollen concentrations, a fundamental question is related to the temporal gap between grass growth phenology (i.e., greenness changes) and reproductive phenology (i.e., flowering time and pollination period) should not be omitted. According to previous studies, the grass flowering to be the same green color as the grass stems at the start of reproduction life phase (Melissa et al., 2016, Fiona et al., 2010). Therefore, the onset of flowering is hard to identify with phenocam, let alone satellites. Until the emergence of the seed head from the sheath of the flag leaf and the seed gradually reaches maturity with yellow color, flowers cannot be observed from phenocam. Therefore, the “flowering” observed by phenocam with lower GCC (3.7 Appendix, Fig. 3.A3 and 4) is related to the late flowering stage in ecology perspective, in which grass seeds tend to mature and are ready for pollination (Sheila et al., 1968). The ecological “flowering time” occurred at the same time with the end of the vegetative growth phase that is corresponding to the greenness peak in phenocam and satellite observations. Furthermore, there are plenty of studies that reported the grass flowering phase (i.e., near grass greenness peak) is prior to airborne grass pollen concentrations. For example, Ickovic et al. (1989) studies 18 grass species over 2 years within Paris suburban area, and found noticeable grass pollen concentration usually appeared after most of grass flowered for 2-3 weeks. Estrella et al. (2006) studied *Poaceae* species at 51 stations over 5 years in Germany, and found though grass pollen season started

almost on the same day (0.6 days later) as local flowering phenology, the peak of grass pollen lagged 22.6 days after local flowering. Similarly, Tormo et al. (2011) demonstrated that the asynchronism between grass flowering peak and airborne pollen concentration peak in Spain with up to one week difference in phase, i.e. airborne pollen appeared after grass flowering. In review of the above, our hypothesis is the hysteresis of remote sensing observations and airborne grass pollen concentrations for grass flowering time caused the temporal sequences between the peaks of GCC/EVI and grass pollen concentrations in our results.

3.4.3 Scale effect related to spatial and temporal resolutions and research scales on relationships between grass pollen concentrations and grass/landscape phenology

According to the results presented in Figs. 3.13, 3.14, and Table 3.6, Sentinel-2 grass cover EVI at 10m resolution showed stronger correlations with pollen concentrations relative to MODIS and H-8 AHI EVI with coarser spatial resolutions for certain grass pollen seasons. When compared with phenocam GCC, the Sentinel-2 EVI data at the phenocam footprint scale also exhibited better correlations with pollen concentrations at both urban (Rocklea) and rural (Mutdapilly) sites (e.g., Fig. 3.9). As for other coarse resolution satellites, their EVI time series only correlated well with grass pollen dynamics at the homogeneous site and not at the heterogeneous sites. These findings are in agreement with a previous study which showed that the phenology dynamics of grass cover derived from finer resolution satellite data (i.e. Landsat, 30m) show a better correlation with pollen concentrations than MODIS data and, consequently, offer a new avenue for the use of finer resolution satellite data in mapping pollen seasons and their dynamics at scale (Li et al., 2019). Further, a finer resolution Sentinel-2 sensor, comparable to Landsat, has the potential to map the grass distribution in urban domains featuring heterogeneous land cover types and can therefore more accurately assess the risk of respiratory allergies in urban neighbourhoods.

As for the variations in grass pollen-greenness correlations across research scales for the same satellite sensor, stronger correlations were found at larger research scales (Table 3.6). This might be related to the differences in grass cover proportions (grass %) at different scales. For example, the grass % within 3km was higher than for 1km at Mutdapilly (Table 3.5) and thus EVI profiles calculated from

3km included more grasses than 1km resolution, thereby improving the correlation with grass pollen dynamics. However, the variation in time intervals observed between grass pollen and grass greenness peaks were complicated as the research scales increased (Figs. 3.15 – 17; Table 8 – 10). This could also be attributed to the spatial heterogeneity of land cover types and the spatial resolution of satellite data. As research scales increase, the possibilities of measuring different grass species and even recording non-grass information objectively via satellite sensors also increased and thus the peaks of EVI time series shifted accordingly. In general, satellite data maintained relatively consistent peaks at the homogeneous site (Mutdapilly; Fig. 3.15) but showed obvious variations in peaks across research scales at the more heterogeneous site (Rocklea; Fig. 3.16).

Our results pertaining to the temporal scale effect on grass pollen-greenness relationships indicate that the daily GCC and EVI time series did not show strong correlations between daily pollen concentrations except at the very coarsest temporal resolution (16 days) which showed the best correlations with 16-day mean pollen concentrations (Fig. 3.19). However, it is dangerous to state that coarse temporal resolutions are more suitable for informing pollen dynamics as compared to a daily scale. According to the time series recorded via GCC, EVI and pollen concentrations presented in Fig. 3.18, greenness metrics at a daily scale effectively recorded subtle changes in grass pollen profiles, for instance the slight grass pollen peak arising around January 2019. However, these details were lost when the temporal scale was reduced to 16 days. The weaker correlations arising between grass greenness metrics and grass pollen concentrations on a daily scale might be attributed to the details that were erased from time series when we downscaled from 8-day to 16-day reporting windows. Therefore, the choice of temporal resolution scales depends on the application scenarios. It is thus ambiguous to conclude which temporal scale is the best for understanding grass pollen concentration dynamics using satellite data.

3.5 CONCLUSION

In this study, we evaluated satellite-based grass/ pasture phenology using phenocam observations and explored the relationships between satellite-based and near-surface remote sensing observations of grass/ pasture greenness and *in-situ* grass pollen concentrations at varied spatial and temporal scales. The results and discussions have identified five key conclusions:

(1) All satellites with multiple spatial resolutions can measure grass/ pasture phenology at their single pixel scale. Especially, Sentinel-2 data with 10 m resolution can effectively obtain pasture greenness information from phenocam footprint.

(2) As research scales increased, the performances in observing grass phenology from MODIS (250 m) and Himawari-8 AHI (1 km) decreased in heterogeneous landscapes. Though the relationships between Sentinel-2 EVI and phenocam GCC tended to be poor at the same time, the ability of Sentinel-2 data remains better than coarse satellites (with higher coefficients of determination).

(3) We identified good interrelationships between *in-situ* grass pollen concentrations and grass greenness as measured by phenocams and satellites at the homogeneous site (i.e. Mutdapilly), but poor relationships at heterogeneous sites due to some grass pollen seasons have asynchronous trends with phenological dynamics of local grass (within 10 km).

(4) Sentinel-2 observations of grass greenness indeed explained more dynamics of grass pollen concentrations than MODIS and Himawari-8 AHI at the same pollen season. However, its advantage tended to be weak with increasing study periods (from several months to multiple years).

(5) Though daily phenocam and Himawari-8 AHI observations recorded a lot of details of grass greenness changes, phenocam and Himawari-8 AHI observations also introduced noises into time series and then decreased relationships between grass pollen – greenness correlations. Observations of grass greenness with a 16-day temporal scale had the strongest relationships with grass pollen, but it came at the cost of accurately detecting subtle temporal differences between grass greenness and pollen.

3.6 REFERENCES

Alberton, B., Almeida, J., Helm, R., Torres, S., Menzel, A., Patricia, L. & Morellato, C. 2014, 'Ecological Informatics Using phenological cameras to track the green up in a cerrado savanna and its on-the-ground validation', *Ecological Informatics*, vol. 19, pp. 62–70.

Bass, D.J., Delpech, V., Beard, J., Bass, P. & Walls, R.S. 2000, 'Late summer and fall (March-May) pollen allergy and respiratory disease in Northern New South Wales, Australia', *Annals of Allergy, Asthma and Immunology*, vol. 85, no. 5, pp. 374–81, viewed 9 June 2021, <https://pubmed.ncbi.nlm.nih.gov/11101179/>.

Beggs, P.J., Katelaris, C.H., Medek, D., Johnston, F.H., Burton, P.K., Campbell, B., Jaggard, A.K., Vicendese, D., Bowman, D.M.J.S., Godwin, I., Huete, A.R., Erbas, B., Green, B.J., Newnham, R.M., Newbigin, E., Haberle, S.G. & Davies, J.M. 2015, 'Differences in grass pollen allergen exposure across Australia', *Australian and New Zealand Journal of Public Health*, vol. 39, no. 1, pp. 51–5.

Bessho, K., Date, K., Hayashi, M., Ikeda, A., Imai, T., Inoue, H., Kumagai, Y., Miyakawa, T., Murata, H., Ohno, T., Okuyama, A., Oyama, R., Sasaki, Y., Shimazu, Y., Shimoji, K., Sumida, Y., Suzuki, M., Taniguchi, H., Tsuchiyama, H., Uesawa, D., Yokota, H. & Yoshida, R. 2016, 'An introduction to Himawari-8/9 — Japan's new-generation geostationary meteorological satellites', *Journal of the Meteorological Society of Japan*, vol. 94, no. 2, pp. 151–83.

Bolton, D.K., Gray, J.M., Melaas, E.K., Moon, M., Eklundh, L. & Friedl, M.A. 2020, 'Continental-scale land surface phenology from harmonized Landsat 8 and Sentinel-2 imagery', *Remote Sensing of Environment*, vol. 240, p. 111685.

Browning, D.M., Karl, J.W., Morin, D., Richardson, A.D. & Tweedie, C.E. 2017, 'Phenocams bridge the gap between field and satellite observations in an arid grassland ecosystem', *Remote Sensing*.

Burke, M.W.V. & Rundquist, B.C. 2021, 'Scaling Phenocam GCC, NDVI, and EVI2 with Harmonized Landsat-Sentinel using Gaussian Processes', *Agricultural and Forest Meteorology*, vol. 300, no. December 2020, p. 108316.

Carver, S., Mikkelsen, N. & Woodward, J. 2002, 'Long-term rates of mass wasting in Mesters Vig, northeast Greenland: Notes on a re-survey', *Permafrost and Periglacial Processes*, vol. 13, no. 3, pp. 243–9.

Chen, B., Jin, Y. & Brown, P. 2019, 'An enhanced bloom index for quantifying floral phenology using multi-scale remote sensing observations', *ISPRS Journal of Photogrammetry and Remote Sensing*, vol. 156, no. August, pp. 108–20.

Chuine, I. & Belmonte, J. 2011, 'Improving prophylaxis for pollen allergies: Predicting the time course of the pollen load of the atmosphere of major allergenic plants in France and Spain', *http://dx.doi.org.ezproxy.lib.uts.edu.au/10.1080/00173130410019163*, vol. 43, no. 2, pp. 65–80, viewed 8 July 2021, <https://www-tandfonline-com.ezproxy.lib.uts.edu.au/doi/abs/10.1080/00173130410019163>.

Crowley, M.A. & Cardille, J.A. 2020, 'Remote Sensing's Recent and Future Contributions to Landscape Ecology', *Current Landscape Ecology Reports*, vol. 5, no. 3, pp. 45–57.

Cui, T., Martz, L., Lamb, E.G., Zhao, L. & Guo, X. 2019, 'Comparison of Grassland Phenology Derived from MODIS Satellite and PhenoCam Near-Surface Remote Sensing in North America', *Canadian Journal of Remote Sensing*, vol. 45, no. 5, pp. 707–22.

Davies, J.M., Beggs, P.J., Medek, D.E., Newnham, R.M., Erbas, B., Thibaudon, M., Katelaris, C.H., Haberle, S.G., Newbigin, E.J. & Huete, A.R. 2015, 'Trans-disciplinary research in synthesis of grass pollen aerobiology and its importance for respiratory health in Australasia', *Science of the Total Environment*, vol. 534, pp. 85–96, viewed 15 May 2019, <http://dx.doi.org/10.1016/j.scitotenv.2015.04.001>.

Devadas, R., Huete, A.R., Vicendese, D., Erbas, B., Beggs, P.J., Medek, D., Haberle, S.G., Newnham, R.M., Johnston, F.H., Jaggard, A.K., Campbell, B., Burton, P.K., Katelaris, C.H., Newbigin, E., Thibaudon, M. & Davies, J.M. 2018, 'Dynamic ecological observations from satellites inform aerobiology of allergenic grass pollen', *Science of the Total Environment*, vol. 633, pp. 441–51, viewed 15 May 2019, <https://doi.org/10.1016/j.scitotenv.2018.03.191>.

Drusch, M., Del Bello, U., Carlier, S., Colin, O., Fernandez, V., Gascon, F., Hoersch, B., Isola, C., Laberinti, P., Martimort, P., Meygret, A., Spoto, F., Sy, O., Marchese, F. & Bargellini, P. 2012, 'Sentinel-2: ESA's Optical High-Resolution Mission for GMES Operational Services', *Remote Sensing of Environment*, vol. 120, pp. 25–36.

Estrella, N., Menzel, A., Kramer, U. & Behrendt, H. 2006, 'Integration of flowering dates in phenology and pollen counts in aerobiology: analysis of their spatial and temporal coherence in Germany (1992-1999)', *International Journal of Biometeorology*, vol. 51, no. 1, pp. 49-59.

Fan, Jianqing (1996). Local Polynomial Modelling and Its Applications: *From linear regression to nonlinear regression*. Monographs on Statistics and Applied Probability. Chapman & Hall/CRC. ISBN 978-0-412-98321-4.

Fiona Tooke, Nicholas H. Battey, Temperate flowering phenology, *Journal of Experimental Botany*, Volume 61, Issue 11, June 2010, Pages 2853–2862, <https://doi.org/10.1093/jxb/erq165>

Gómez-Giráldez, P.J., Pérez-Palazón, M.J., Polo, M.J. & González-Dugo, M.P. 2020, 'Monitoring grass phenology and hydrological dynamics of an oak-grass savanna ecosystem using sentinel-2 and terrestrial photography', *Remote Sensing*, vol. 12, no. 4.

Golyandina, N., Korobeynikov, A. 2014, ' Basic Singular Spectrum Analysis and forecasting with R', *Computational Statistics and Data Analysis*, vol. 71, pp. 934-354, < http://dx.doi.org/10.1016/j.csda.2013.04.009 >.

Gowrie, M. , Agard, J. , Barclay, G. and Mohammed, A. 2016, 'Forecasting Emergency Paediatric Asthma Hospital Admissions in Trinidad and Tobago:

Development of a Local Model Incorporating the Interactions of Airborne Dust and Pollen Concentrations with Meteorological Parameters and a Time-Lag Factor', *Open Journal of Air Pollution*, vol. 5, pp. 109-126, <doi: 10.4236/ojap.2016.54009>.

Haberle, S.G., Bowman, D.M.J.S., Newnham, R.M., Johnston, F.H., Beggs, P.J., Buters, J., Campbell, B., Erbas, B., Godwin, I., Green, B.J., Huete, A., Jaggard, A.K., Medek, D., Murray, F., Newbigin, E., Thibaudon, M., Vicendese, D., Williamson, G.J. & Davies, J.M. 2014, 'The macroecology of airborne pollen in Australian and New Zealand urban areas', *PLoS ONE*, vol. 9, no. 5.

Hogda, K.A., Karlsen, S.R., Solheim, I., Tommervik, H. & Ramfjord, H. 2002a, 'The start dates of birch pollen seasons in Fennoscandia studied by NOAA AVHRR NDVI data', *International Geoscience and Remote Sensing Symposium (IGARSS)*, vol. 6, pp. 3299–301.

Hogda, K.A., Karlsen, S.R., Solheim, I., Tommervik, H. & Ramfjord, H. 2002b, 'The start dates of birch pollen seasons in Fennoscandia studied by NOAA AVHRR NDVI data', *International Geoscience and Remote Sensing Symposium (IGARSS)*, vol. 6, no. May 2014, pp. 3299–301.

Holben, B.N. 1986, 'Characteristics of maximum-value composite images from temporal AVHRR data', *http://dx.doi.org.ezproxy.lib.uts.edu.au/10.1080/01431168608948945*, vol. 7, no. 11, pp. 1417–34, viewed 9 July 2021, <https://www-tandfonline-com.ezproxy.lib.uts.edu.au/doi/abs/10.1080/01431168608948945>.

Huete, A., Didan, K., Miura, T., Rodriguez, E.P., Gao, X. & Ferreira, L.G. 2002, 'Overview of the radiometric and biophysical performance of the MODIS vegetation indices', *Remote Sensing of Environment*, vol. 83, no. 1–2, pp. 195–213.

Hufkens, K., Friedl, M., Sonnentag, O., Braswell, B.H., Milliman, T. & Richardson, A.D. 2012a, 'Linking near-surface and satellite remote sensing measurements of deciduous broadleaf forest phenology', *Remote Sensing of Environment*.

Hufkens, K., Friedl, M., Sonnentag, O., Braswell, B.H., Milliman, T. & Richardson, A.D. 2012b, 'Linking near-surface and satellite remote sensing measurements of deciduous broadleaf forest phenology', *Remote Sensing of Environment*.

Ickovic M.R., Boussioud-Corbieres F., Sutra J.P., Thibaudon M., 1989, 'Hay fever symptoms compared to atmospheric pollen counts and floral phenology within Paris suburban area in 1987 and 1988', *Aerobiologia*, vol. 5, no. 1, pp. 30-36.

Jeffrey, L., William, S., Estelle, L., Alfredo, H., Slobodan, N., Goran, P., WATER Peter, V. DE, Orrin, M., Amy, B. & Theresa, C. n.d., *Use of MODIS Satellite Images and an Atmospheric Dust Transport Model To Evaluate Juniperus Spp. Pollen Phenology and Dispersal*, viewed 10 May 2019, <https://ntrs.nasa.gov/search.jsp?R=20110014813>.

Karlsen, S.R., Ramfjord, H., Høgda, K.A., Johansen, B., Danks, F.S. & Brobakk, T.E. 2009, 'A satellite-based map of onset of birch (Betula) flowering in Norway', *Aerobiologia*, vol. 25, no. 1, pp. 15–25, viewed 9 June 2021, <https://link.springer.com/article/10.1007/s10453-008-9105-3>.

Khwarahm, N.R., Dash, J., Skjï¿½th, C.A., Newnham, R.M., Adams-Groom, B., Head, K., Caulton, E. & Atkinson, P.M. 2017, 'Mapping the birch and grass pollen seasons in the UK using satellite sensor time-series', *Science of the Total Environment*, vol. 578.

Klosterman, S.T., Hufkens, K., Gray, J.M., Melaas, E., Sonnentag, O., Lavine, I., Mitchell, L., Norman, R., Friedl, M.A. & Richardson, A.D. 2014, 'Evaluating remote sensing of deciduous forest phenology at multiple spatial scales using PhenoCam imagery', *Biogeosciences*.

Laaidi, M. 2001, 'Forecasting the start of the pollen season of Poaceæ: Evaluation of some methods based on meteorological factors', *International Journal of Biometeorology*, vol. 45, no. 1, pp. 1–7.

Lange, M., Dechant, B., Rebmann, C., Vohland, M., Cuntz, M. & Doktor, D. 2017, 'Validating MODIS and sentinel-2 NDVI products at a temperate deciduous forest site using two independent ground-based sensors', *Sensors*

(Switzerland), vol. 17, no. 8, p. 1855, viewed 28 June 2021, <www.mdpi.com/journal/sensors>.

Li, X., Zhou, Y., Meng, L., Asrar, G., Sapkota, A. & Coates, F. 2019, 'Characterizing the relationship between satellite phenology and pollen season: A case study of birch', *Remote Sensing of Environment*, vol. 222, no. January, pp. 267–74.

Liu, Y., Hill, M.J., Zhang, X., Wang, Z., Richardson, A.D., Hufkens, K., Filippa, G., Baldocchi, D.D., Ma, S., Verfaillie, J. & Schaaf, C.B. 2017, 'Using data from Landsat, MODIS, VIIRS and PhenoCams to monitor the phenology of California oak/grass savanna and open grassland across spatial scales', *Agricultural and Forest Meteorology*, pp. 311–25, viewed 30 May 2019, <http://dx.doi.org/10.1016/j.agrformet.2017.02.026>.

Lloyd, D. 1990, 'A phenological classification of terrestrial vegetation cover using shortwave vegetation index imagery', *International Journal of Remote Sensing*, vol. 11, no. 12, pp. 2269–79, viewed 9 June 2021, <https://www.tandfonline.com/action/journalInformation?journalCode=tres20>.

Louis, J., Debaecker, V., Pflug, B., Main-Knorn, M., Bieniarz, J., Mueller-Wilm, U., Cadau, E. & Gascon, F. 2016, 'Sentinel-2 SEN2COR: L2A processor for users', *European Space Agency, (Special Publication) ESA SP*, vol. SP-740, no. May, pp. 9–13.

Lugonja, P., Brdar, S., Simović, I., Mimić, G., Palamarchuk, Y., Sofiev, M. & Šikoparija, B. 2019, 'Integration of in situ and satellite data for top-down mapping of Ambrosia infection level', *Remote Sensing of Environment*, vol. 235, no. September, p. 111455.

Lyapustin, A.I., Wang, Y., Laszlo, I., Hilker, T., G.Hall, F., Sellers, P.J., Tucker, C.J. & Korkin, S. V. 2012, 'Multi-angle implementation of atmospheric correction for MODIS (MAIAC): 3. Atmospheric correction', *Remote Sensing of Environment*, vol. 127, pp. 385–93.

Ma, X., Huete, A., Yu, Q., Coupe, N.R., Davies, K., Broich, M., Ratana, P., Beringer, J., Hutley, L.B., Cleverly, J., Boulain, N. & Eamus, D. 2013, 'Spatial patterns and temporal dynamics in savanna vegetation phenology across the north australian tropical transect', *Remote Sensing of Environment*, vol. 139, pp. 97–115.

Medek, D.E., Beggs, P.J., Erbas, B., Jaggard, A.K., Campbell, B.C., Vicendese, D., Johnston, F.H., Godwin, I., Huete, A.R., Green, B.J., Burton, P.K., Bowman, D.M.J.S., Newnham, R.M., Katelaris, C.H., Haberle, S.G., Newbigin, E. & Davies, J.M. 2016, 'Regional and seasonal variation in airborne grass pollen levels between cities of Australia and New Zealand', *Aerobiologia*, vol. 32, no. 2, pp. 289–302.

Miura, T., Nagai, S., Takeuchi, M., Ichii, K. & Yoshioka, H. 2019, 'Improved Characterisation of Vegetation and Land Surface Seasonal Dynamics in Central Japan with Himawari-8 Hypertemporal Data', *Scientific Reports*, pp. 1–12.

Moore, C.E., Brown, T., Keenan, T.F., Duursma, R.A., Van Dijk, A.I.J.M., Beringer, J., Culvenor, D., Evans, B., Huete, A., Hutley, L.B., Maier, S., Restrepo-Coupe, N., Sonnentag, O., Specht, A., Taylor, J.R., Van Gorsel, E. & Liddell, M.J. 2016, 'Reviews and syntheses: Australian vegetation phenology: New insights from satellite remote sensing and digital repeat photography', *Biogeosciences*.

Nagai, S., Maeda, T., Gamo, M., Muraoka, H., Suzuki, R. & Nasahara, K.N. 2011, 'Using digital camera images to detect canopy condition of deciduous broad-leaved trees', *Plant Ecology and Diversity*, vol. 4, no. 1, pp. 79–89.

O'Connell, J.L. & Alber, M. 2016, 'A smart classifier for extracting environmental data from digital image time-series: Applications for PhenoCam data in a tidal salt marsh', *Environmental Modelling and Software*, vol. 84, pp. 134–139.

Oteros, J., García-Mozo, H., Alcázar, P., Belmonte, J., Bermejo, D., Boi, M., Cariñanos, P., Díaz de la Guardia, C., Fernández-González, D., González-Minero, F., Gutiérrez-Bustillo, A. M., Moreno-Grau, S., Pérez-Badía, R.,

Rodríguez-Rajo, F. J., Ruíz-Valenzuela, L., Suárez, Pérez, J., Trigo, M. M., Domínguez-Vilches, E., Galán, C. 2015, 'A new method for determining the sources of airborne particles', *Journal of Environmental Management*, vol. 155, pp. 212-218.

Peng, D., Wang, Y., Xian, G., Huete, A.R., Huang, W., Shen, M., Wang, F., Yu, L., Liu, Liangyun, Xie, Q., Liu, Lingling & Zhang, X. 2021, 'Investigation of land surface phenology detections in shrublands using multiple scale satellite data', *Remote Sensing of Environment*, vol. 252, no. October 2020.

Peter, J.S., Hogland, J., Hebblewhite, M., Hurley, M.A., Hupp, N. & Proffitt, K. 2018, 'Linking phenological indices from digital cameras in Idaho and Montana to MODIS NDVI', *Remote Sensing*, vol. 10, no. 10, pp. 1–15.

Petus, C., Lewis, M. & White, D. 2013, 'Monitoring temporal dynamics of Great Artesian Basin wetland vegetation, Australia, using MODIS NDVI', *Ecological Indicators*, vol. 34, pp. 41–52.

Ramón, G.D. & Peter, J. 2020, Global Climate Change and Pollen Aero allergens A Southern Hemisphere Perspective Aeroallergens Carbon dioxide Climate change Biodiversity.

Rapinel, S., Mony, C., Lecoq, L., Clément, B., Thomas, A. & Hubert-Moy, L. 2019, *Evaluation of Sentinel-2 time-series for mapping floodplain grassland plant communities*, viewed 30 May 2019, <https://doi.org/10.1016/j.rse.2019.01.018>.

Reed, B.C., Brown, J.F., VanderZee, D., Loveland, T.R., Merchant, J.W. & Ohlen, D.O. 1994, 'Measuring phenological variability from satellite imagery', *Journal of Vegetation Science*, vol. 5, no. 5, pp. 703–14, viewed 9 June 2021, <https://onlinelibrary.wiley.com/doi/full/10.2307/3235884>.

Reyes-Fox, Melissa, Steltzer, Heidi, LeCain, Daniel R., McMaster, Gregory S, 2016, 'Five years of phenology observations from a mixed-grass prairie exposed to warming and elevated CO_2', *Sci Data,* vol. 3, pp. 1-8, <https://doi.org/10.1038/sdata.2016.88>.

Richardson, A.D., Hufkens, K., Milliman, T. & Frolking, S. 2018, 'Intercomparison of phenological transition dates derived from the PhenoCam Dataset V1.0 and MODIS satellite remote sensing', *Scientific Reports*.

Richardson, A.D., Jenkins, J.P., Braswell, B.H., Hollinger, D.Y., Ollinger, S. V. & Smith, M.L. 2007, 'Use of digital webcam images to track spring green-up in a deciduous broadleaf forest', *Oecologia*.

Riihimäki, H., Luoto, M. & Heiskanen, J. 2019, 'Estimating fractional cover of tundra vegetation at multiple scales using unmanned aerial systems and optical satellite data', *Remote Sensing of Environment*, vol. 224, no. February, pp. 119–32.

Rojo, J., Rapp, A., Lara, B., Fernández-González, F. & Pérez-Badia, R. 2015, 'Effect of land uses and wind direction on the contribution of local sources to airborne pollen', *Science of The Total Environment*, vol. 538, pp. 672–82.

Sauliene, I., Belmonte, J., Niemelä, S., Magyar, D., Rodinkova, V., Bullock, J.M., Rantio-Lehtimäki, A., Sofiev, M., Dahl, A., Severova, E., Berger, U., Chapman, D.S., Kovtunenko, I., Sikoparija, B., Jäger, S. & Prank, M. 2013, 'An operational model for forecasting ragweed pollen release and dispersion in Europe', *Agricultural and Forest Meteorology*.

Sheila A. G., R.F. Hunter 1968, 'Variation in yield, maturity type, winter greenness and sensitivity to gutting of hill grass species', *Grass and Forage Science*, vol. 23, pp. 149-155.

Smith, M. & Emberlin, J. 2006, 'A 30-day-ahead forecast model for grass pollen in north London, United Kingdom', *International Journal of Biometeorology*, vol. 50, no. 4, pp. 233–42.

Songsom, V., Koedsin, W., Ritchie, R.J.. & Huete, A. 2021, 'Mangrove Phenology and Water Influences Measured with Digital Repeat Photography', *Remote Sens.*, vol. 13, no. 307, pp. 1–18.

Stach, A., Smith, M., Prieto Baena, J.C. & Emberlin, J. 2008, 'Long-term and short-term forecast models for Poaceae (grass) pollen in Poznań, Poland, constructed

using regression analysis', *Environmental and Experimental Botany*, vol. 62, no. 3, pp. 323–32.

Sadeh, Yuval, Zhu, Xuan, Dunkerley, David, Walker, Jeffrey P., Zhang, Yuxi, Rozenstein, Offer, Manivasagam, V.S., Chenu, Karine, 2021, ' Fusion of Sentinel-2 and PlanetScope time-series data into daily 3 m surface reflectance and wheat LAI monitoring', *International Journal of Applied Earth Observation and Geoinformation*, vol. 92, pp. 102260.

Tormo, R., Silva, I., Gonzalo, A., Moreno, A., Perez, R. & Fernandez, S. 2011, 'Phenological records as a complement to aerobiological data', *International Journal of Biometeorology*, vol. 55, no. 1, pp. 51-65.

Thapa, S., Garcia Millan, V.E. & Eklundh, L. 2021, 'Assessing forest phenology: A multi-scale comparison of near-surface (UAV, spectral reflectance sensor, phenocam) and satellite (MODIS, sentinel-2) remote sensing', *Remote Sensing*, vol. 13, no. 8.

Tng, D.Y.P., Hopf, F., Haberle, S.G., Bowman, D.M.J.S., Hopf B, F., Haberle, S.G. & Bowman, D.M.J.S. 2010, 'Seasonal pollen distribution in the atmosphere of Hobart, Tasmania: preliminary observations and congruence with flowering phenology', *Australian Journal of Botany*, vol. 58, no. 6, p. 440, viewed 15 May 2019, <www.publish.csiro.au/journals/ajb>.

Tran, N.N., Huete, A., Nguyen, H., Grant, I., Miura, T., Ma, X., Lyapustin, A., Wang, Y. & Ebert, E. 2020, 'Seasonal Comparisons of Himawari-8 AHI and MODIS Vegetation Indices over Latitudinal Australian Grassland Sites', *Remote Sensing*, vol. 12, no. 15, p. 2494.

Vrieling, A., Meroni, M., Darvishzadeh, R., Skidmore, A.K., Wang, T., Zurita-Milla, R., Oosterbeek, K., O'Connor, B. & Paganini, M. 2018, 'Vegetation phenology from Sentinel-2 and field cameras for a Dutch barrier island', *Remote Sensing of Environment*, vol. 215, pp. 517–29.

Watson, C.J., Restrepo-Coupe, N. & Huete, A.R. 2019, 'Multi-Scale Phenology of Temperate Grasslands: Improving Monitoring and Management With Near-Surface Phenocams', *Frontiers in Environmental Science*, vol. 7, p. 14, viewed

13 May 2019, <https://www.frontiersin.org/article/10.3389/fenvs.2019.00014/full>.

Yan, D., Zhang, X., Nagai, S., Yu, Y., Akitsu, T., Nasahara, K.N., Ide, R. & Maeda, T. 2019, 'Evaluating land surface phenology from the Advanced Himawari Imager using observations from MODIS and the Phenological Eyes Network', *International Journal of Applied Earth Observation and Geoinformation*, vol. 79, pp. 71–83, viewed 13 May 2019, <https://www.sciencedirect.com/science/article/pii/S0303243418304136>.

Zhang, X., Wang, J., Henebry, G.M. & Gao, F. 2020, 'Development and evaluation of a new algorithm for detecting 30 m land surface phenology from VIIRS and HLS time series', *ISPRS Journal of Photogrammetry and Remote Sensing*, vol. 161, no. August 2019, pp. 37–51.

Zhang, Y., Bielory, L., Cai, T., Mi, Z. & Georgopoulos, P. 2015, 'Predicting onset and duration of airborne allergenic pollen season in the United States', *Atmospheric Environment*, vol. 103, pp. 297–306.

Zhou, Q., Rover, J., Brown, J., Worstell, B., Howard, D., Wu, Z., Gallant, A.L., Rundquist, B. & Burke, M. 2019, 'Monitoring landscape dynamics in central U.S. grasslands with harmonized Landsat-8 and Sentinel-2 time series data', *Remote Sensing*, vol. 11, no. 3.

3.7 APPENDIX

3.7.1 Research sites and phenocam data

This pilot study was conducted at two pasture sites located in the north and west of Melbourne in the state of Victoria, Australia. A set of time-lapse digital RGB phenocams were installed at these two sites. The land cover type is *Rain fed pasture* for all research sites according to DLCD (Dynamic Land Cover Dataset) product.

To quantify phenological variations of the pasture over time, green chromatic coordinate (GCC) was calculated and processed using an R package "Phenopix" as following steps:

(1). Select regions of interest (ROIs). An ROI, which contained most of pasture in the file of view (FOV), was chosen for each phenocam. Fig. 3.A1 shows the sample images of each site and its ROIs.

(2). Extract vegetation indices. GCC is computed as below:

$$GCC = \frac{G_{DN}}{R_{DN} + G_{DN} + B_{DN}} \tag{1}$$

Where R_{DN}, G_{DN} and B_{DN} are the red, green and blue pixel digital numbers. GCC was computed and averaged through all pixels within ROI at each site.

(3). Filter daily GCC values. To reduce noise caused by low illumination or weather conditions, on time series of GCC, we applied a three-day moving window method named *per90*.

(4). Fit the GCC seasonal curve. After filtering GCC, to better analyze greenness seasonal behaviour of pasture, filtered time-series of GCC was fitted using a double logistic equation, written as

$$VI(\mathrm{t}) = a_0 + a_1 \frac{\tanh[(t - a_2) * a_3] + 1}{2} + a_4 \frac{\tanh[(t - a_5) * a_6] + 1}{2} - a_4 \tag{2}$$

where t is time; a_0 is the minimum GCC value, a_1 and a_4 mean amplitude of green-up and senescence phases; a_2 and a_5 are the inflection point (midpoint) for the growth and decay phases along with the time series; a_3 and a_6 control the slope of both phases.

Figure 3.A1. Phenocam field of views and regions of interest (ROIs) at each site.

In addition, the flowering information was also obtained from phenocam images by visual assessments. We selected images around 1 pm for every day since they have ideal exposure and scene illumination to conduct visual assessment of flowering existences. The tiny and light yellow flower heads could be seen on a certain day, which would be labelled as “flowering” by comparing the images with the same shooting time. It is worth noting that phenocam is not able to detect a specific onset date of flowering time, because flowers generally are green color as the grass stem at the beginning (Melissa et al. 2016). The start of flowering observed by phenocam is closer to maturity of flowering, associated with mature grass seed and pollination (Fiona et al. 2010), instead of the onset of flowering phase. Fig. 3.A2 shows the sample images for near onset of flowering and near maturity of flowering at Redesdale.

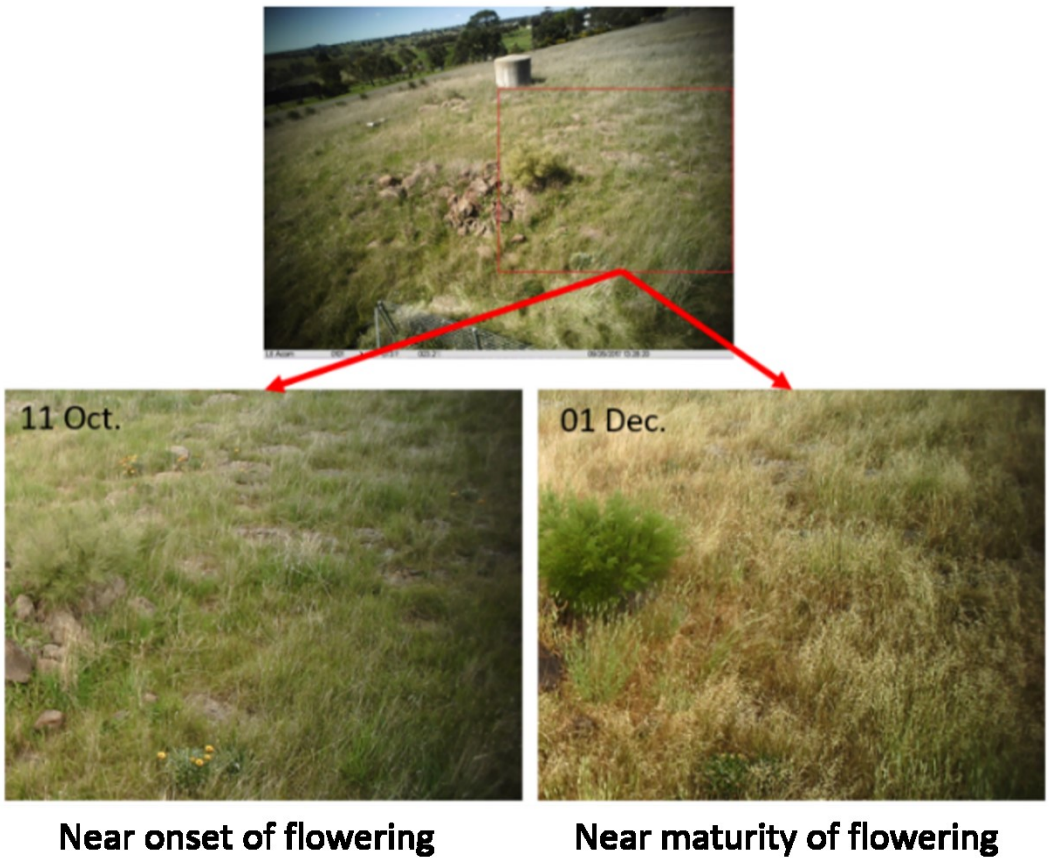

Figure 3.A2. The sample phenocam images indicate near onset of flowering and near maturity of flowering situations at Redesdale.

3.7.2 Temporal lags between pasture greenness and maturity of flowering

We found maturity of flowering lagged GCC peaks by 13 and 15 days at Casterton and Redesdale sites, respectively (Table 3.A1). The mature flowers nearly could be observed at the same time at Casterton and Redesdale might be contributed to they had adjacent GCC peak dates. Fig. 3.A3 and 3.A4 showed the phenocam images corresponding to GCC peak, maturity of flowering and other DOYs along with variations in pasture greenness.

Table 3.A1. The day of year for maximum GCC, maturity of flowering, and their differences at two research sites. (Note: Flowering in table means the DOY of detectable mature flowers, instead of onset of flowering time.)

Sites Name	Max GCC (DOY)	Flowering (DOY)	Max GCC – Flowering (days)
Casterton	295	308	13
Redesdale	291	306	15

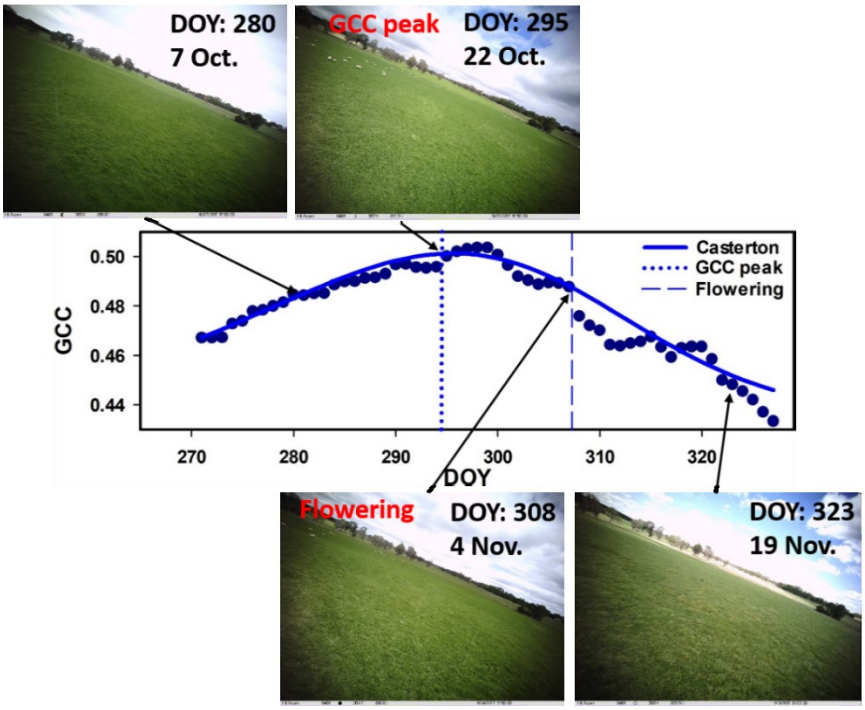

Figure 3.A3. GCC profile, DOYs of GCC peak and flowering, as well as phenocam images corresponding to specific dates at Casterton. (Note: Flowering in figure means the DOY of detectable mature flowers, instead of onset of flowering time.)

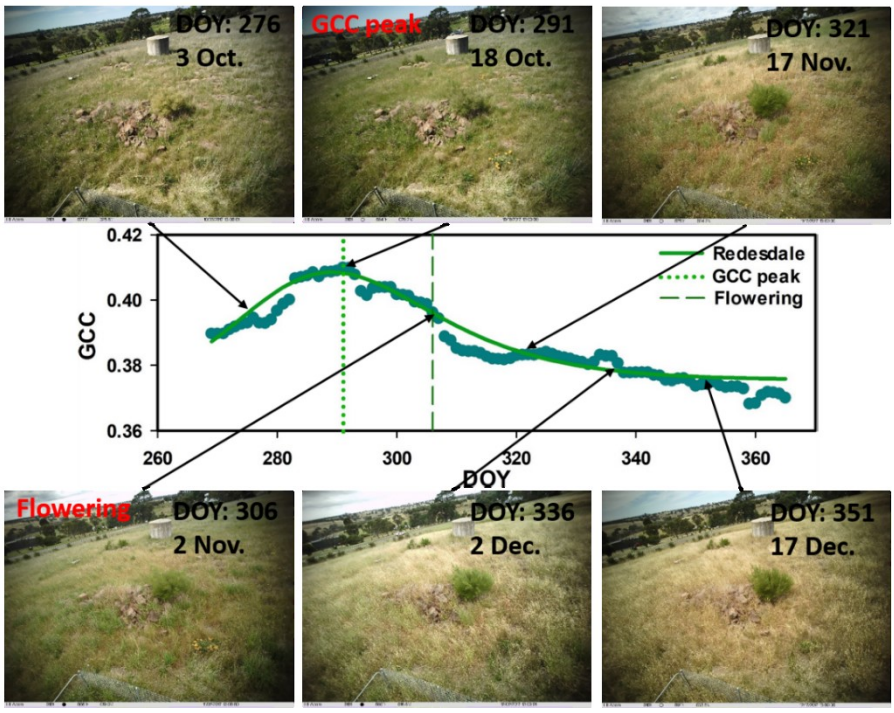

Figure 3.A4. GCC profile, DOYs of GCC peak and flowering, as well as phenocam images corresponding to specific dates at Redesdale. (Note: Flowering in figure means the DOY of detectable mature flowers, instead of onset of flowering time.)

CHAPTER 4

Chapter 4 Using 10 m grass map from Sentinel-2 to filter grass phenology and map grass pollen sources from complex landscapes

4.1 INTRODUCTION

Remote sensing imagery has been shown to be useful for gaining insights into grass phenological information (Descals et al. 2020; Gómez-Giráldez et al. 2020; Vrieling et al. 2018) and mapping grass spatial distributions (Khwarahm et al. 2016; McInnes et al. 2017; Rapinel et al. 2019; Verstraeten et al. 2021). Maps showing the locations of allergenic vegetation taxa have many applications, including improved pollen forecasting in combination with weather data (Zink et al. 2011); combining with health data to inform exposure of aeroallergens (Newson et al. 2014); improving pollen emission models (Zink et al. 2013); and individuals' self-management of allergy or asthma (McInnes et al. 2017).

Vegetation mapping of plants with allergenic pollen requires land cover maps as a reference (i.e., base maps). For example, adopting the Corine Land Cover 2000 (CLC2000) (100 m) as a base map, Khwarahm et al. (2016) mapped the birch and grass pollen seasons in the UK with 1 km resolution using a time series of MERIS Terrestrial Chlorophyll Index (MTCI) data. Similarly, researchers used finer resolution satellite data combined with the CLC2000 land cover map to derive grass pollen source inventories across the city of Aarhus, Denmark (Skjøth et al. 2013). Another land cover map with finer resolution (The Centre for Ecology and Hydrology (CEH) Land Cover Map 2007, 25 m) was used to generate a grass map at a continental scale in the UK (McInnes et al. 2017). In contrast to northern hemisphere (especially European) studies with finer resolution land cover maps, studies of allergenic grass pollen sources in Australia use coarse spatial resolution land cover maps, such as the MODerate-resolution Imaging Spectroradiometer (MODIS) Land Cover Type 1-International Geosphere-Biosphere Programme land cover classification (IGBP, 500 m) (Devadas et al. 2018) or Australian Land Use and Management (ALUM, 50 m) classification (Emmerson et al. 2019). The Dynamic Land Cover Dataset (DLCD, 250 m) is also used to provide nationally consistent land cover information for Australia; however, its spatial resolutions cannot meet the requirement of mapping precise grass pollen sources, especially considering the intensive spatial heterogeneity around capital cities and the existence of urban 'green spaces', which play a significant role in grass pollen exposure (Skjøth et al. 2013).

Recently, Sentinel-2 satellite data at 10 m resolution has shown the potential for generating more precise and updated land cover maps (Chen et al. 2015). The Sentinel-2 satellite was launched when many advanced classification methods based on machine learning approaches were already developed (Phiri et al. 2020). Advanced machine learning techniques such as random forests (RF) (Clark 2017; Fragoso-Campón et al. 2018), support vector machines (SVM) (Denize et al. 2018; Nguyen et al. 2020) and convolutional neural network (CNN) (Längkvist et al. 2016; Qiu et al. 2020) have been applied for land cover classification—including crop (Mazzia, Khaliq & Chiaberge 2020), forest (Miranda et al. 2019) and grassland (Pelletier et al. 2019; Dewi & Chen 2019)—based on Sentinel-2 data. For example, Segal-Rozenhaimer et al. (2020) applied CNN for land cover classification and obtained 91% classification accuracy. Researchers conducted land cover classifications in Victoria, Australia, using three widely used machine learning approaches (RF, Recurrent Neural Network (RNN) and temporal Convolutional Neural Networks (TempCNN)) based on Sentinel-2 images and achieved high overall accuracies of 94.0%, 90.8% and 94.5%, respectively (Charlotte, Geoffrey & Francois 2019). Although Sentinel-2 imagery-based land cover maps have superior 10 m resolution compared to traditional land cover products, no published studies have used Sentinel-2 imagery-based land cover maps as a base map for mapping grass pollen sources.

Besides geospatial landscape information on allergenic plants, satellite data also contribute to the retrieval of key phenology timing of allergenic vegetation to better inform pollen aerobiology and map pollen sources. Using satellite data time series, previous studies have adopted the onset of flowering as the phenological proxy to map allergenic birch pollen sources (Karlsen et al. 2009; Khwarahm et al. 2016). The underlying logic of using flowering phenophase to interpret pollen seasonal dynamics is the good correlations found between timings of birch male flowering and leaf budburst (1.1-day intervals between each other) (Linkosalo 1999, 2011). Further, the timing of these two phenophases appear to be closely synchronised with pollen release (Newnham, Adams-Groom & Smith 2013). However, this approach is not suitable for mapping grass pollen sources; compared to birch (regarded as the major allergenic pollen source in Europe), the flowering time of

grass is difficult to detect using satellite data due to their tiny flowers and their phenology being ecologically sensitive to meteorological variability (Beaumont et al. 2015; Ma et al. 2015). Additionally, Devadas et al. (2018) reported that Australian grass pollinating periods are less synchronous with satellite greenness measures compared with French sites, partly due to the more heterogeneous landscapes and complex species diversity (e.g., co-existence of exotic and native species; see Watson, Restrepo-Coupe & Huete 2019) in Australian grasslands.

In this chapter, we adopt Sentinel-2 data at 10 m resolution to provide geospatial information of grass distributions and grass phenology information and improve understanding of grass pollen aerobiology. Based on the nonlinear correlations between grass pollen concentrations and grass greenness time series reported in the previous chapter, we mapped grass pollen sources around one pollen trap station using Sentinel-2 data. Combining phenocam in-situ observations of grass greenness and grass pollen concentrations from the in-situ pollen station, the following questions were investigated:

(1) What are the differences in grass fractions extracted from three multiresolution grass maps (DLCD, ALUM and Sentinel-2 imagery-derived grass maps)?
(2) Compared with coarser grass maps, does the Sentinel-2 grass map with 10 m resolution have better ability to filter grass greenness information from heterogeneous landscapes?
(3) How do the grass fractions derived from the Sentinel-2 grass map change across different distances and orientations from the Campbelltown phenocam/pollen trap site?
(4) How do grass greenness dynamics (phenology) vary with grass fraction variations across distances and orientations?
(5) How are variations in grass greenness dynamics related to grass pollen concentrations at the pollen station?
(6) Does knowledge of the spatial distribution of grass fractions better explain grass pollen dynamics?
(7) How does the spatial distribution of grass pollen sources change across different years and grass pollen seasons?

4.2 METHODS

4.2.1 Site description

This study was conducted at three sites near Sydney and Brisbane (Fig. 4.1). The Campbelltown pollen station (34.0666 S, 150.7955 E) located on the TAFE New South Wales campus near Campbelltown City. It is located 53 km south-west of Sydney central business district. According to the 2016 census of population, there were 169,572 people in the Campbelltown suburb and Local Government Area (https://www.abs.gov.au/census). To compare the differences between multiresolution grass maps, we conduct this analysis at two other sites in landscapes characterised as urban-rural mixtures: the Richmond site (33.6183 S, 150.7458 E) and Rocklea phenocam site (27.5358 S, 152.9934 E). The Richmond site is located near the campus of Western Sydney University and located approximately 65 km northwest of Sydney city. The Rocklea phenocam site is located approximately 9 km south of Brisbane, Queensland. Further detail on these sites can be found in Chapter 2, Section 2.2.1.

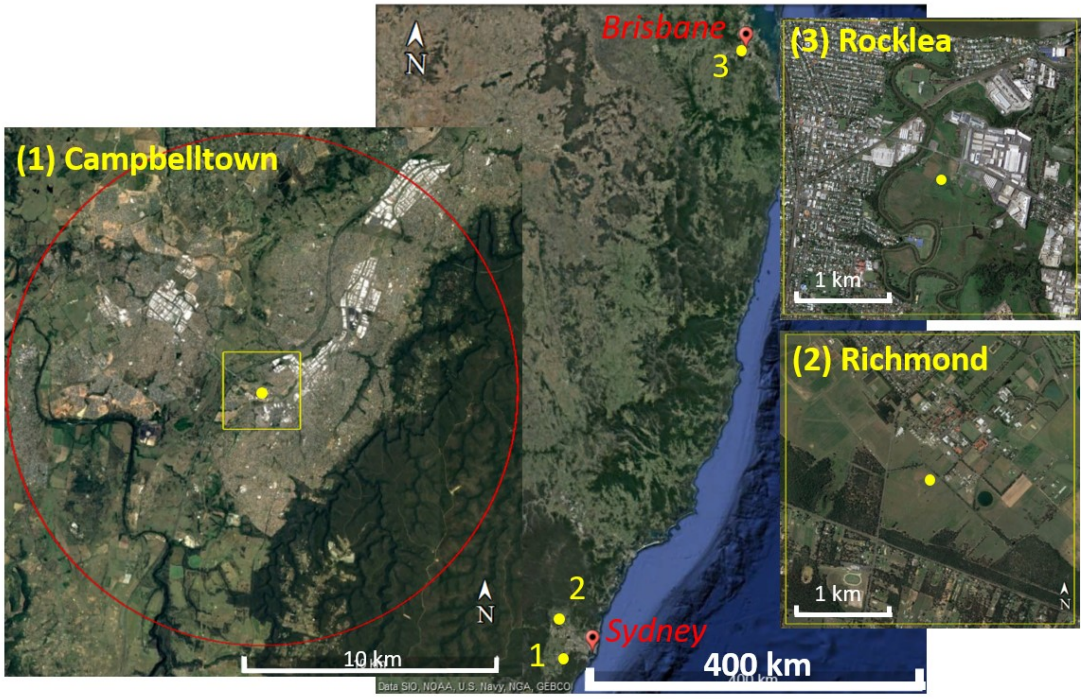

Figure 4.1 Locations of Campbelltown (1), Richmond (2), and Rocklea (3) sites relative to Sydney and Brisbane. Red circular and yellow squares denote regions where conducted analyses in this chapter. The Google Earth Pro provided the base map.

The climate of the Campbelltown site is humid subtropical (Koppen–Geigen classification Cfa) (K̈oppen, Volken & Brönnimann 2011), with warm to hot summers and mild to cool winters. During the study years (2018–2020), the mean annual maximum temperature was 24.8 °C and the mean annual minimum temperature was 10.9 °C (see Table 4.1). During the study years, the monthly mean maximum temperature was 32.1 °C in January and the monthly mean minimum temperature was 4.2 °C in July. The seasonal distribution of temperature is shown in Figure 4.2. During the study years, the area had a mean annual rainfall total of 556.5 mm (see Table 4.1), with mean maximum and minimum monthly rainfall total being 69.9 mm (in December) and 17.9 mm (in April), respectively. The rainfall total is highly variable from year to year, with the highest annual rainfall total being 738.8 mm in 2020 and 401.4 mm in 2019. The seasonal distribution of rainfall is shown in Figure 4.2.

Table 4.1 Mean monthly minimum and maximum temperatures (T) and rainfall taken from Campbelltown (Mount Annan) meteorology station from 2018 to 2020.

	Jan	*Feb*	*Mar*	*Apr*	*May*	*Jun*	*Jul*	*Aug*	*Sep*	*Oct*	*Nov*	*Dec*	*Annual*
Mean max T (°C)	32.1	29.5	27.2	25.8	21.5	18.2	18.9	19.2	22.6	25.2	28.0	29.3	24.8
Mean min T (°C)	18.5	16.7	15.4	12.0	7.0	5.6	4.2	4.3	7.4	11.2	12.9	15.4	10.9
Monthly rainfall (mm)	67.9	34.0	76.8	17.9	22.4	50.3	32.9	37.5	36.5	61.0	60.9	69.9	567.9

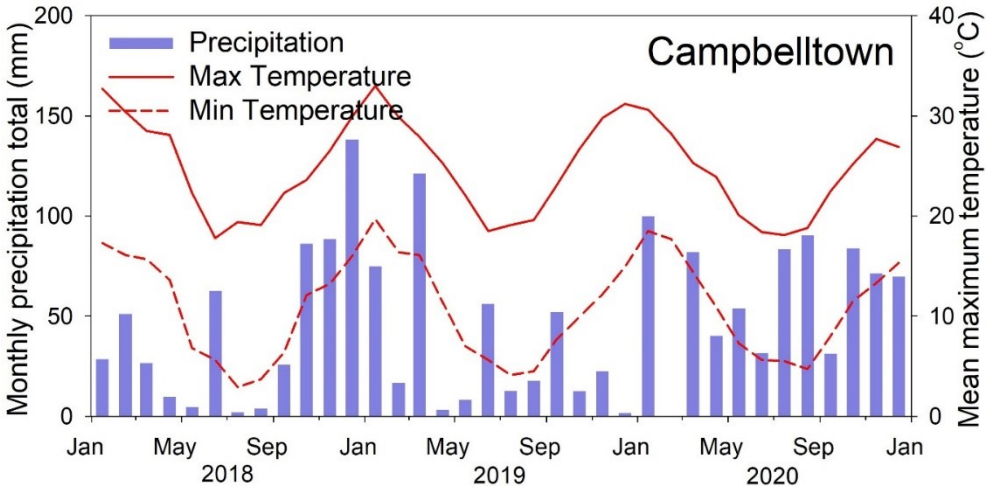

Figure 4.2 Monthly precipitation total and monthly mean maximum and minimum temperature for Campbelltown site from 2018–2020. Source: http://www.bom.gov.au/climate/data/.

4.2.2 Description of multiresolution grass maps

The Dynamic Land Cover Dataset Version 2 (DLCDv2.1) (http://www.ga.gov.au/scientific-topics/earth-obs/accessing-satellite-imagery/landcover) with 250 m spatial resolution was used to extract grass information from the landscape around the grass pollen trap. The latest version (updated until the end of 2015) consists of 14 maps, each based on two years of MODIS (Moderate Resolution Imaging Spectrometer) data. The map used in this study is landcover during January 2014 – December 2015. We generated a grass map—referred as to the DLCD grass map—by compositing six original land cover types related to grass/pasture: *Rain fed pasture*, *Closed Tussock Grassland*, *Open Tussock Grassland*, *Open Hummock Grassland*, *Scattered Shrubs* and *Grass* and *Irrigated pasture*.

The Australian Land Use and Management (ALUM) Classification version 8 (https://www.agriculture.gov.au/abares/aclump/land-use/alum-classification) was used to generate another grass map, referred as to the ALUM grass map. The ALUM Classification system provides a nationally consistent method to collect and present land use information with 50 m resolution. The current version map was developed by the ALUM Classification Technical Working Group in 2016. We composited several original land use classes related to grass/pasture into one type to generate the ALUM grass map: *Native/exotic pasture mosaic*, *Grazing irrigated modified pasture & Grazing modified pastures*, *Pasture legume* and *Pasture legume/grass mixtures*. Note that several classes also include grass, for example, *Recreation and culture*, *Services* and *Public Services* classes usually include public green space and grass lawns to different extents in the urban area. We included the *Recreation and culture* class in the ALUM grass map, as the grass proportion is the highest among these three classes by visual inspection.

To better inform grass cover greenness information from the heterogeneous landscape around the Campbelltown pollen trap station, we generated a grass map with 10 m resolution using CNN, referred to as to the Sentinel-2 grass map. The CNN is a deep learning algorithm for classification that has been widely adopted (Miranda et al. 2019) and increasingly used based on finer resolution Sentinel-2 imagery for land cover classification, including crop (Mazzia, Khaliq & Chiaberge

2020), forest (Miranda et al. 2019) and grassland (Pelletier et al. 2019; Dewi & Chen 2019). We trained the model using 8929 grass samples (i.e. 8929 Sentinel-2 pixels) to generate a 20 × 20 km square grass map. To ensure the timeliness and accuracy of the grass map, all grass samples were selected from Sentinel-2 image of 4-May-2020 (i.e. the greenest image in 2020) by manually checking on Google Earth Pro. The specific details about the process using the CNN model and accuracy are provided in Abdollahi et al. (2021)**.**

4.2.3 Grass greenness and pollen concentration data

The Sentinel-2 EVI image satellite data was used for this study. Details about pre-processing and calculating EVI from Sentinel-2 images are described in Chapter 3, Section 3.2.3.1. To better describe grass cover greenness dynamics from the heterogeneous landscape around the Campbelltown phenocam/pollen trap site, grass cover EVI was extracted from Sentinel-2 EVI images using each grass map with spatial resolutions varied from coarse to finer.

Grass pollen concentration was collected in Campbelltown from January 2018 to June 2020 using Hirst-type volumetric pollen and spore traps (Burkard Scientific Ltd, Uxbridge, UK). Details on this method are provided in Haberle et al. (2014).

4.2.4 Analysis strategies

To explore the capacity of Sentinel-2 grass map with 10 m resolution to filter grass information from heterogeneous landscapes, I compared grass fractions extracted from Sentinel-2 grass map, ALUM, and DLCD, respectively, within 3 × 3 km square area at each site (Fig. 4.1 yellow square in small maps). And then, three grass maps were used to filter the grass EVI from Sentinel-2 landscape EVI images. Using phenocam observation of grass greenness as reference (Green Chromatic Coordinate, GCC), performances of three grass maps were further analysed by comparing correlations between grass EVI and phenocam GCC.

The Sentinel-2 grass map was divided into 40 land plots (5 distances (2, 4, 6, 8, 10 km radii) × 8 orientations) with varied grass fractions within a 20 km buffer around the Campbelltown pollen station (Fig. 4.1. Red circle). Grass EVI were calculated at each land plot. Those grass EVI time series and their relationships between *in-situ* grass pollen concentrations were compared to explore whether grass phenology

and grass pollen – EVI correlations varied across distances and orientations. Furthermore, the role of grass fractions in interpreting grass pollen dynamics was analysed by correlating grass fractions with coefficients of determination between grass pollen and grass EVI time series.

Pixel-wise grass sources maps for each grass pollen season were generated to explore seasonal and inter-annual variations in spatial distributions of grass pollen seasons. First, grass pollen seasons were defined based on peaks timing of grass EVI averaged from the 20 km buffer. Second, grass pixels with 10 m resolution were filtered by the Sentinel-2 grass map from Sentinel-2 landscape images. Third, we explored the relationship between the time series of EVI calculated from each grass pixel and the 5-day mean grass pollen concentrations (i.e. mean value for ± 2 days of the date for corresponding Sentinel-2 EVI) by conducting least-squares polynomial regression analyses to calculate coefficients of determination (R^2). The reason why we adopted polynomial regression is that simple linear regression is not suitable to fit the curvilinear shape between grass pollen concentrations and grass greenness changes, Additionally, although polynomial regression fits a nonlinear model to the data, as a statistical estimation problem it is linear. For this reason, R^2 is a robust statistic for polynomial regression (Fan et al., 1996) and is widely used in previous studies adopted polynomial regression (Oteros et al., 2015; Sadeh et al., 2021). Finally, mapping pixel-wise grass pollen sources for each pollen season using R^2 values obtained in the previous step. Fig. 4.2 shows the flowchart of this study.

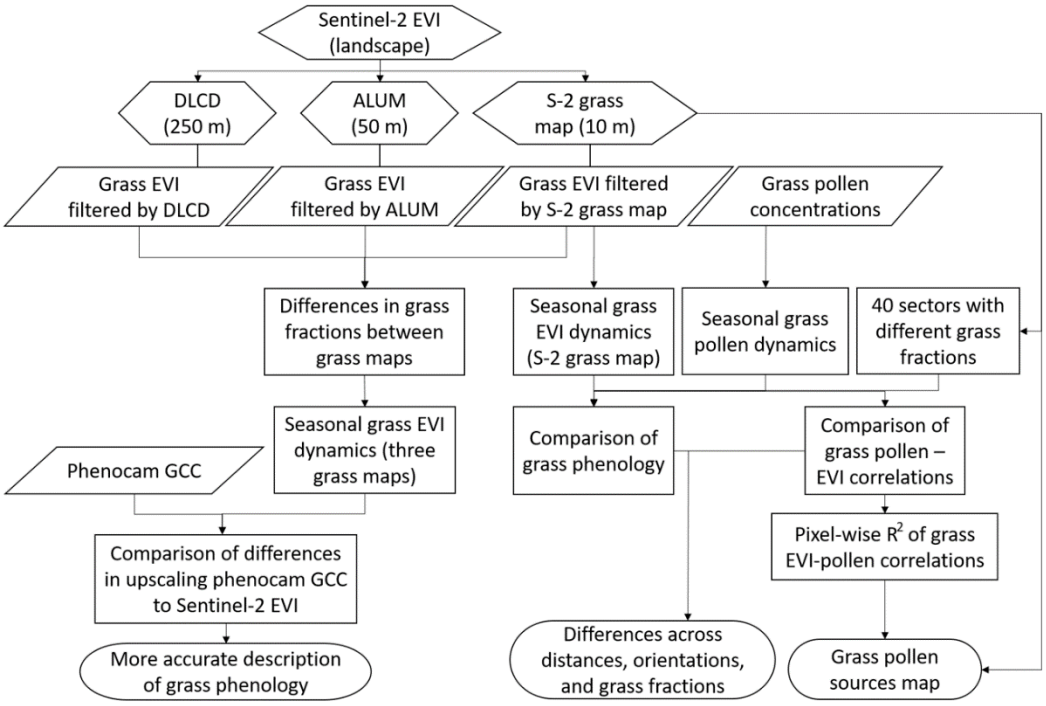

Figure 4.3 The flowchart of this study.

4.3 RESULTS

4.3.1 Comparison of grass spatial distributions among multiresolution grass maps

Figure 4.4 shows landscapes (Google Earth Pro) and grass areas identified by the Sentinel-2 (b, f and j), ALUM (c, g and k) and DLCD (d, h, and l) grass maps around the Campbelltown, Rocklea and Richmond sites.

According to the visual inspection in Figures 4.4 a, e and i, the Richmond site has more grass cover and fewer buildings and roads than the other two sites. For the Campbelltown site, the DLCD (250 m) and ALUM (50 m) incorrectly classified some buildings and roads as grass. For example, the ALUM grass map included a big building chunk located southwest of the pollen trap (the small red points in Figure 4.4 c). Similarly, the DLCD grass map classified those buildings and a lot of roads as grass (see Figure 4.4 d). These two coarse grass maps also missed some grass, such as the grass areas located west of the interchange around the Campbelltown site (see Figures 4.4 c and d). Note that the Sentinel-2 grass map correctly identified those grass areas (see Figure 4.4 a). Similar problems were exhibited in the urban site, Rocklea. Although the ALUM grass map did not include a big chunk of a building as it did in Campbelltown, it classified all trees on the golf course located east of Rocklea pollen trap site as grass (see Figure 4.4 g). The

DLCD missed a large area of grass southwest of the Rocklea pollen trap (see Figure 4.4 h). The problems of coarse grass maps in the relatively rural site (Richmond) were mainly classifying buildings and some bare lands as grass (see Figures 4.4 k and l), but the Sentinel-2 grass map efficiently excluded those bare lands (see Figure 4.4 j).

The proportions of grass areas classified by the different grass maps are summarised in Figure 4.5. The results from statistical analyses are in line with the visual inspection—much more grass areas were identified in Richmond (50.83% from the Sentinel-2 grass map) than in Campbelltown and Rocklea. The Rocklea site exhibited the least grass cover (17.85% from the Sentinel-2 grass map). The amount of identified grass varied greatly among the DLCD, ALUM and Sentinel-2 grass maps, with the least grass recognised by the Sentinel-2 grass map. This result is understandable, given the difference in grass covers between the grass maps. The ALUM and DLCD grass maps incorrectly classified many non-grass areas as grass. Therefore, though ALUM has finer resolution compared to DLCD, it is still not suitable for accurate filtering of grass information from a heterogeneous landscape.

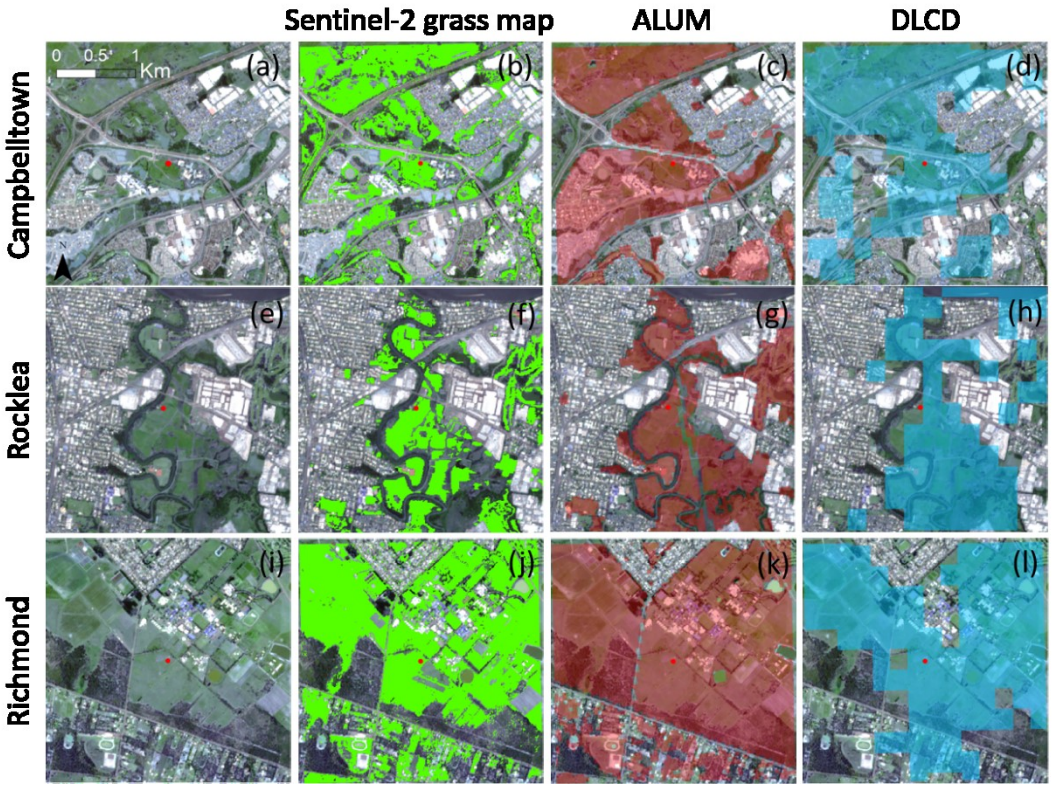

Figure 4.4 Landscapes and grass areas identified by the Sentinel-2, ALUM and DLCD grass maps within the 3 km x 3 km study areas centred on the pollen traps in Campbelltown (a to d), Rocklea (e to h) and Richmond (i to l). The background images of the landscapes were downloaded from Google Earth Pro.

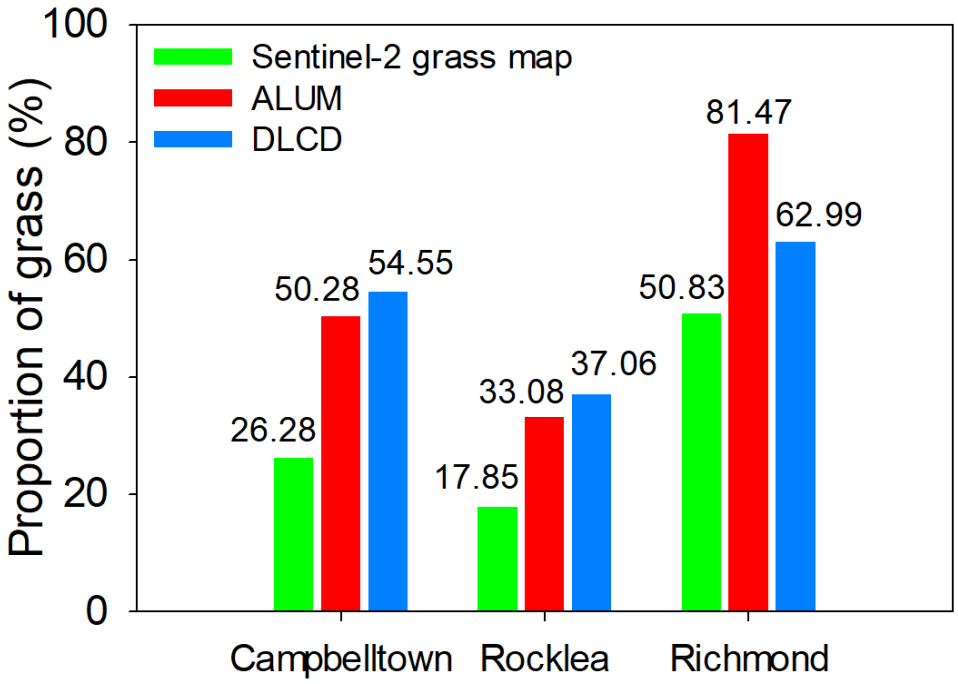

Figure 4.5 Proportion of 3 km x 3 km areas (Campbelltown, Rocklea and Richmond) classified as grass by the Sentinel-2, ALUM and DLCD grass maps. The areas are shown in Figure 4.4.

4.3.2 Comparison of improvement of grass greenness upscaling from phenocam GCC to Sentinel-2 EVI by multiresolution grass maps

Using multiresolution grass maps, we filtered grass information (grass pixels) from the landscape Sentinel-2 EVI images of the 3 km^2 study areas centred on the Campbelltown and Rocklea sites. Phenocams were co-located with pollen traps at these two sites. The time series of phenocam GCC and Sentinel-2 EVI (unfiltered and filtered by grass maps) are shown in Figures 4.6 a and c. The correlations between phenocam GCC and landscape/grass cover Sentinel-2 EVI are shown in Figures 4.6 b and d and Table 4.2.

At the Campbelltown site, all landscape/grass cover EVI time series were consistent with the phenocam GCC temporal profiles, although the EVI exhibited different magnitudes among grass maps (see Figure 4.6 a). At the Rocklea site, the grass EVI

time series reached its second peak earlier than the phenocam GCC (see Figure 4.6 c). The dates of the second peak of grass EVI differed between grass maps. The grass EVI filtered by the Sentinel-2 grass map reached its second peak on 26 April 2019, which is the closest to the second peak date of the phenocam GCC (3 May 2019). In contrast, the grass EVI time series filtered by the ALUM and DLCD grass maps had the same second peak date as the unfiltered EVI (landscape) (6 April 2019). The relatively large time intervals of peaks in the phenocam and Sentinel-2 grass EVI may be due to differences in the phenological dynamics to the grass in the field of view of the phenocam at Rocklea versus the grass around this phenocam site. Regarding differences in magnitudes among grass EVI temporal profiles filtered by multiresolution grass maps, the Sentinel-2 grass map generated the highest EVI values. The unfiltered EVI (landscape) exhibited the lowest EVI values due to the mix-pixel effect reducing the EVI values of landscape Sentinel-2 images. This indicates that the Sentinel-2 grass map and other two coarse grass maps stretched the amplitudes of seasonal grass EVI time series by extracting grass information and then highlighted the seasonal dynamics of grass cover from all heterogeneous landscapes.

We set the correlations between phenocam GCC and 3 x 3 pixel Sentinel-2 EVI at the phenocam footprint (details on determining the phenocam footprint from Sentinel-2 images were provided in Chapter 3, Section 3.2.5) as the reference of the true relationship between grass greenness metrics extracted from the phenocam and Sentinel-2, respectively (dashed lines in Figure 4.6 b and d, and the italic font in Table 4.2). Overall, all correlations between the phenocam GCC and landscape/grass Sentinel-2 EVI in Campbelltown were better than those in Rocklea, with higher R^2 values. This may be attributed to the unconformity of the GCC and EVI at the second peak in Rocklea. All grass cover EVI filtered by grass maps improved the grass greenness upscaling from phenocam to Sentinel-2, with higher R^2 values and slopes, as compared with landscape EVI calculated from 'unfiltered' Sentinel-2 images at both sites. The GCC-grass EVI correlation, filtered by the Sentinel-2 grass map, was the closest to the GCC-EVI correlation at the phenocam footprint scale at both sites (Figures 4.6 b and d). This indicates that the Sentinel-2

grass map exhibited the best performance in upscaling greenness, with the highest R^2 and slope values of all grass maps.

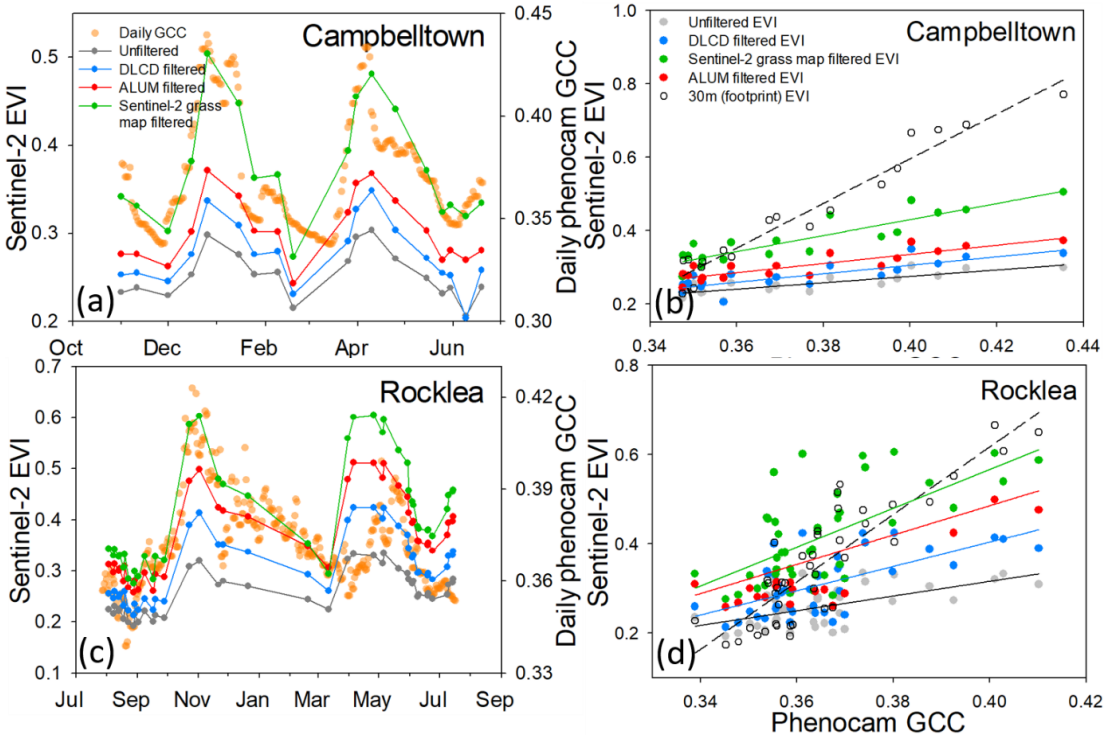

Figure 4.6 Time series of daily the phenocam GCC and Sentinel-2 grass EVI filtered by multiresolution grass maps at Campbelltown and Rocklea (a and c) and the correlations between them (b and d). Analyses conducted at the 3 km x 3 km areas shown in Figure 4.4. The dashed lines in the right panels denote the correlations between Sentinel-2 EVI (3 x 3 pixel) and phenocam GCC.

Table 4.2 Coefficient of determination (R^2) and slopes (a) of linear regression between phenocam GCC and whole landscape Sentinel-2 EVI (i.e., unfiltered EVI) and grass cover Sentinel-2 EVI filtered by the Sentinel-2, ALUM and DLCD grass maps.

	Footprint		*S-2 grass map*		*ALUM*		*DLCD*		*Unfiltered*	
	R^2	*a*	R^2	*a*	R^2	*a*	R^2	*a*	R^2	*a*
Campbelltown	*0.95*	*6.08*	**0.80**	**2.18**	0.76	1.25	0.67	1.16	0.70	0.87
Rocklea	*0.75*	*7.55*	**0.41**	**4.36**	0.40	3.28	0.40	2.72	0.34	1.64

Note: These coefficients correspond to Figures 4.6 b and d. Bold font shows the highest correlation among the three grass maps. All correlations are significant at the $p<0.0001$ level.

To further compare the performances in filtering grass greenness information from landscapes among multiresolution grass maps, we plotted the histogram of pixel numbers from unfiltered and filtered Sentinel-2 EVI images using grass maps at Campbelltown (Figures 4.7 a–c) and Rocklea (Figures 4.7 d–f) (the 3 km^2 areas shown in Figure 4.4) for their greenest days within growing seasons. The grey bars in Figure 4.7 denote the histogram of pixel numbers of landscape (unfiltered) Sentinel-2 EVI with mean EVI values for 0.30 and 0.32 at Campbelltown and Rocklea, respectively. The green, red and blue bars represent the histograms of pixel numbers of Sentinel-2 grass EVI filtered by the Sentinel-2, ALUM and DLCD grass maps, respectively. The thin and thick red lines denote mean Sentinel-2 grass pixels EVI and mean EVI at the phenocam footprint. Closer thin and thick red lines indicate better performance of that grass map in filtering grass information.

For the DLCD grass map, the mean EVI of grass pixels was only 0.34 at Campbelltown and 0.41 at Rocklea. They deviated far from mean EVI at the phenocam footprint (i.e., reference lines). This indicates that although the DLCD grass map filtered a part of pixels (blue part in Figure 4.7 c) from whole landscape pixels, some were not grass pixels. For example, the anomalous pixels with EVI values around –0.1 in Figure 4.7 f. They likely belonged to water pixels located in the north part of the Rocklea site. Compared to the DLCD grass map, the ALUM grass map showed better performance with higher mean grass EVI values at both sites, especially at the Rocklea site (see Figure 4.7 e). The ALUM grass map also successfully filtered water pixels. However, the ALUM grass map only reduced the number of pixels but did not efficiently filter grass pixels at Campbelltown, considering it had a similar mean grass EVI value to the DLCD (0.37). The Sentinel-2 grass map increased mean grass EVI from 0.34 to 0.50 and 0.41 to 0.60 at Campbelltown and Rocklea, respectively (see Figures 4.7 a and d). Both thin red lines were closer to the reference lines at both sites. All grass pixels filtered by the Sentinel-2 grass map kept higher EVI values at whole landscape pixels. In general, our results indicate that the Sentinel-2 grass map had the best performance in filtering grass information from landscapes compared to the ALUM and DLCD coarse grass maps.

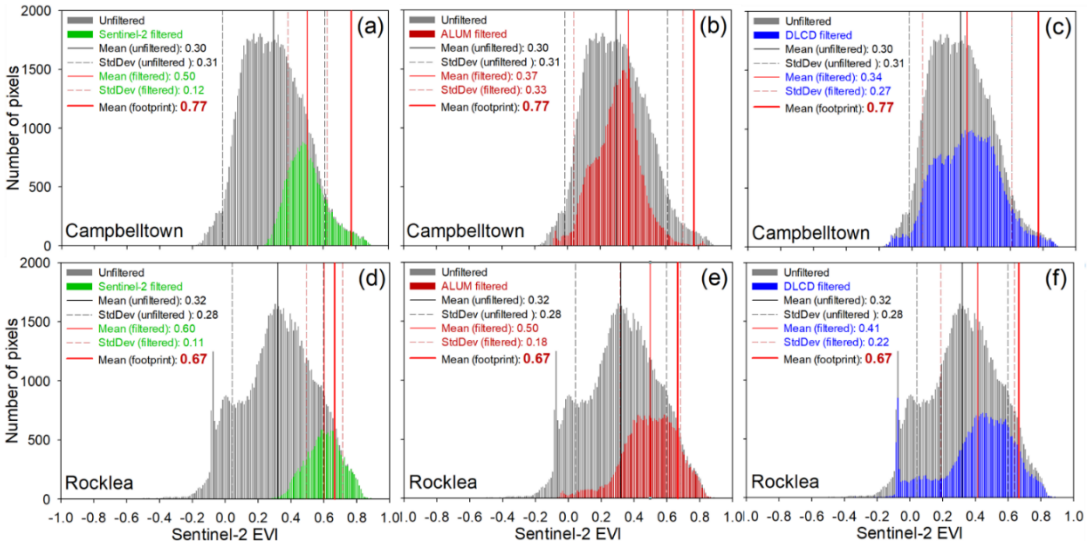

Figure 4.7 Histogram of pixel numbers from unfiltered and filtered Sentinel-2 EVI images (3 km × 3 km areas shown in Figure 4.4) at the greenest day within the growing season for Campbelltown (26 December 2018) and Rocklea (2 November 2018). Red thick solid lines represent the average of Sentinel-2 EVI values extracted from the phenocam footprint (3 x 3 pixels), set as the reference value for real grass greenness at each site.

4.3.3 Seasonal grass dynamics and relationships with grass pollen concentrations around pollen trap station: Case study in Campbelltown

4.3.3.1 Variations of grass fraction at different orientations with extended distances

Based on our results from the above comparisons between multiresolution grass maps, we only used the Sentinel-2 grass map with 10 m resolution for the next analyses due to its superior performance in filtering grass information from heterogeneous landscapes. We selected the Campbelltown site to conduct analyses as the landscape around this pollen station is characterised as a rural-urban mixture. We extracted grass pixels from the area within a 10 km radius of the Campbelltown pollen trap station. Figure 4.8 shows the grass spatial distribution, based on Sentinel-2 grass map, around Campbelltown (the left panel) and the grass fractions of each circular study area (2 km, 4 km, 6 km, 8 km and 10 km radius).

In general, grasses around the Campbelltown site were mainly concentrated at the NE1 (northeast 1, 0°–45°), SW1 (southwest 1, 180°–225°), SW2 (southwest 2, 225°–270°), NW1 (northwest 1, 270°–315°) and NW2 (northwest 2, 315°–365°) orientations (Figure 4.8, right panel). Grass fractions at different orientations were

quite varied (Figure 4.8, left panel). The changes in grass fractions were greatest in NW2 and smallest in NE2 (northeast 2, 45°–90°). The grass fraction changed from 68.39% (within 2 km radius) to 32.82% (within 10 km radius) at NW2 orientation. This indicates that grasses were distributed closer to the pollen trap in this direction. However, grasses were uniformly distributed in NE2 orientation, with grass fractions only changing from 10.64% (2 km radius) to 10.28% (10 km radius). The SE1 (southeast 1, 90°–135°) direction had the least grass fraction of all orientations (3.88% within 10 km radius). Most grasses were concentrated in the SW1 orientation (50.98% within 10 km).

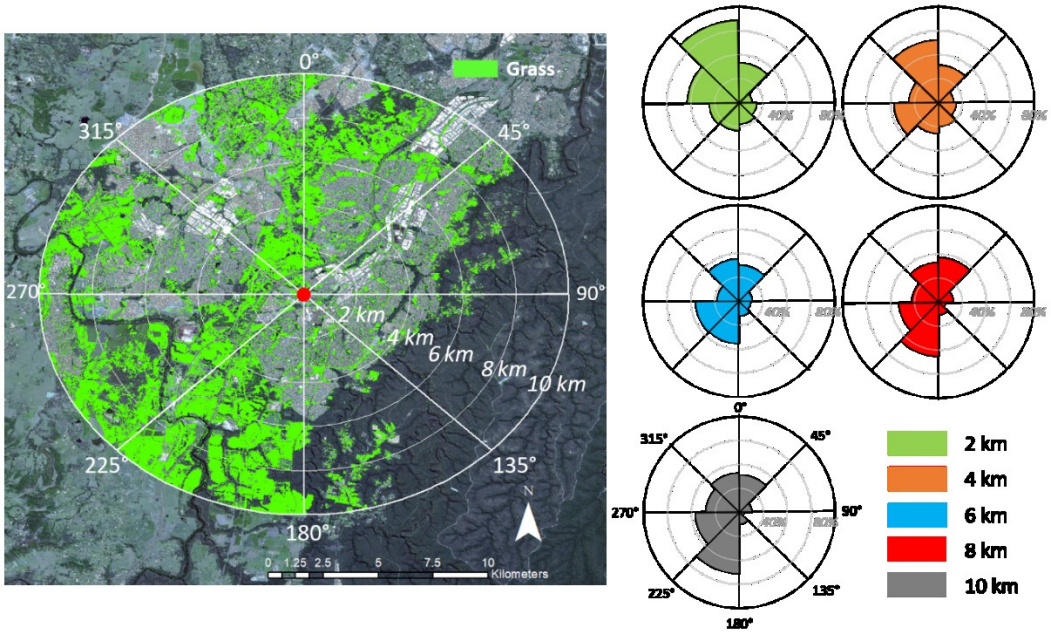

Figure 4.8 Spatial distribution of grass fraction within a 10 km radius of the Campbelltown pollen trap (left panel) and grass proportions at different orientations (right panel). The area was divided into 40 sectors with varied distances and orientations. Light green in the left panel shows grass as identified by the Sentinel-2 grass map. Different colours in the right panel denote different areas within 2 km, 4 km, 6 km, 8 km and 10 km radius from the centre. Grey circles in each radar figure are the scale of grass fraction (0–80%).

4.3.3.2 Variations of grass EVI seasonal dynamics across orientations and distances with varied grass fractions

To explore whether the grass seasonal dynamics in terms of phenology timing and magnitude varied across orientations and distances, we compared grass EVI time

series among the 40 land plots within the 20 km radius area around the Campbelltown site from January 2018 to June 2020 (see Appendix X, Figure A.4.1). Figure 4.9 shows the time series of in-situ grass pollen concentrations and grass EVI extracted from different distances (0–2 km, 2–4 km, 4–6 km, 6–8 km and 8–10 km) at three orientations (NW2, SW1 and NE2). The grass fractions of each land plot are included in Figure 4.9. NW2 (Figure 4.9 a) and SW1 (Figure 4.9 b) were characterised as roughly decreased and increased trends for grass fractions from inner to outer land plot s, respectively. The grass fractions in the NE2 direction showed moderate variations and lower values compared to other orientations. Though all grass EVI profiles exhibited similar phenological dynamics with the same major grass greenness peaks (e.g., peaks occurred in February and October 2018, January and May 2019, and February to May 2020), the specific timing of EVI peaks and magnitudes varied among land plots with different grass fractions.

For the NW2 orientation (Figure 4.9 a), eight grass EVI peaks were identified throughout the entire growing season (from 2018–2020). The areas within 0–2 km (green line and bar) and 4–6 km (black line and bar) had the most and least grass fractions, respectively. Areas with higher grass fractions did not always have higher grass EVI values. For example, although areas within 0–2 km and 2–4 km had relatively higher grass fractions compared to other land plots, their grass EVI values were lower than those extracted from the 6–8 km and 8–10 km areas from January to June 2018. For other grass pollen seasons in 2019 and 2020, however, areas with higher grass fractions had higher grass EVI values (e.g., January and May peaks in 2019, and October and February peaks in 2020). Besides differences in grass EVI magnitude, the phenology of each grass plot showed differences in some grass pollen seasons. Though all grass EVI values in five grass plots reached their maximum values around October 2019, in which a corresponding grass pollen peak occurred, the date of the grass EVI peak of the 6–8 km area (red line) lagged behind the other EVI peaks by 15 days (7 and 22 October, respectively). Additionally, grass EVI values reached their peaks on three different days for the long grass pollen season during February to May 2020 (19 February 2020 for 0–2 km and 2–5 km, 19 March 2020 for 8–10 km, and 14 April 2020 for 4–6 km and 6–8 km).

For the SW1 orientation (Figure 4.9 b), patterns of grass EVI dynamics extracted from different grass plots behaved similarly to those in NW2. In the grass pollen season in February 2018, grass plots with lower grass fractions showed higher grass EVI values (similar to that observed in NW2) and dates of grass EVI peaks were different within the pollen season period. Though grass fraction was slightly lower in the 6–8 km area than in the 8–10 km area, the grass EVI values of the 6–8 km area were higher than that of the 8–10 km area in the October 2018, January 2019 and April 2020 pollen seasons (red line in Figure 4.9 b). Similar to NW2, grass EVI profiles from different grass plots showed different dates of EVI peaks in the October 2019 and April 2020 pollen seasons. For peaks around October 2019, however, the grass EVI peak date of the 6–8 km and 8–10 km areas was 27 September (10 days earlier than the peak in the 0–2 km area in NW2; Figure 4.9 a, green line). For grass peaks around April 2020, EVI profiles from the 0–2 km and 2–4 km areas reached their peaks on 19 April 2020 in SW1 (Figure 4.9 b, green and yellow lines). This lagged behind their peaks in NW2 by one month.

For the NE2 orientation (Figure 4.9 c), the magnitude of grass EVI profiles did not change as strongly as the other two directions due to grass fractions varying moderately among land plots in this orientation (bar plot in Figure 4.9 c). Interestingly, grass EVI values from the 8–10 km area were higher than other EVI profiles throughout almost the entire growing season, even though other grass plots had higher grass fractions. Similar to NW2 and SW1, grass EVI profiles reached their peaks on different dates and plateaued from February to May 2020.

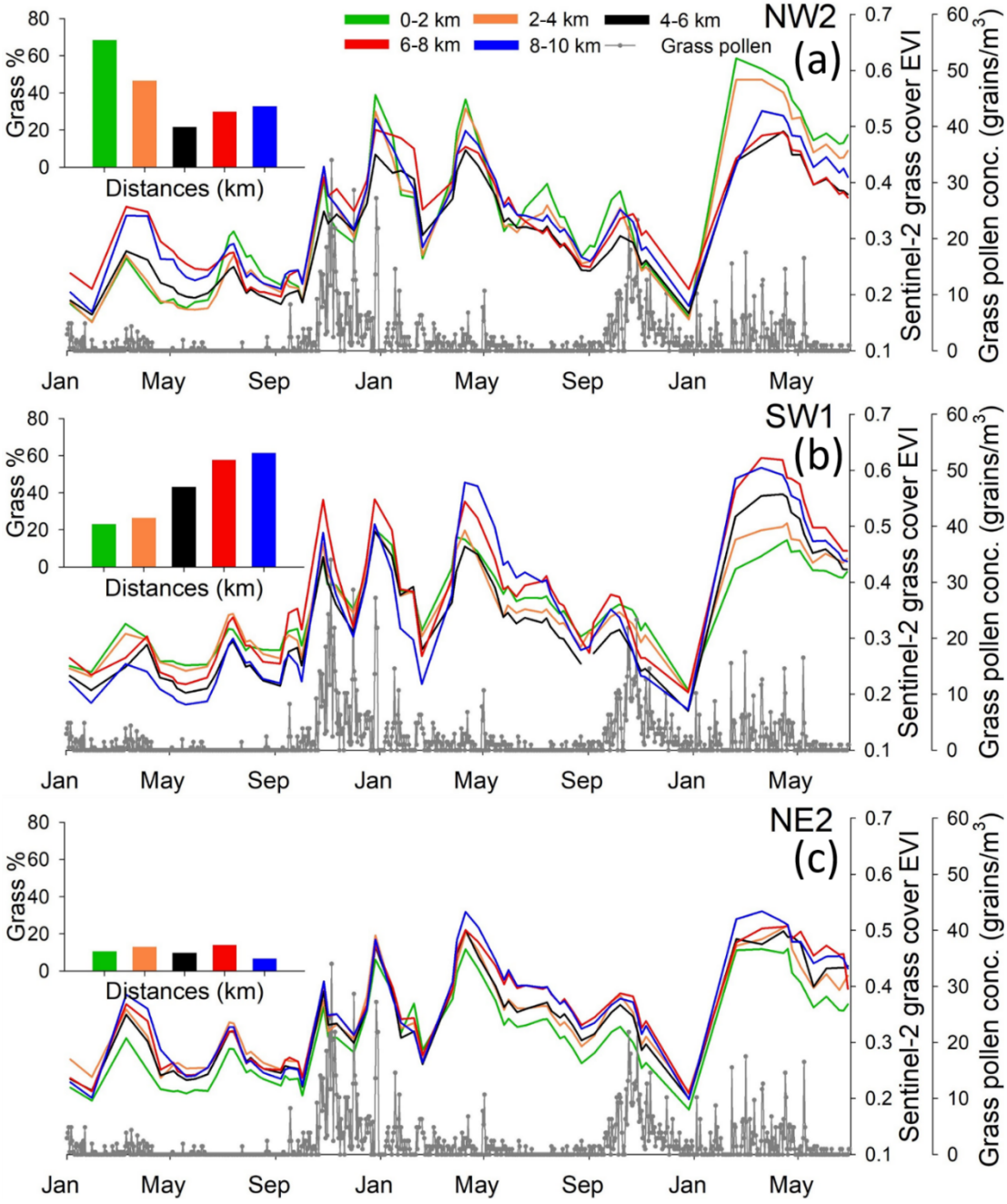

Figure 4.9 Time series plots of grass pollen concentrations and Sentinel-2 grass EVI extracted from (a) NW2 (northwest 2, 315°–365°), (b) SW1 (southwest 1, 180°–225°) and (c) NE2 (northeast 2, 45°–90°) orientations across increased distances for 2018–2020 at the Campbelltown site.

In general, the major differences between grass EVI profiles extracted from each land plot with varied grass fractions related to magnitudes of grass EVI and phenology (i.e., grass peak dates) for different grass pollen seasons. Compared with grass pollen seasons in 2019 and 2020, grass pollen concentrations in 2018 pollen

seasons were dramatically lower. The differences in grass greenness between land plots with higher grass fractions and plots with lower grass fractions can partly explain this finding; areas with much more grass may not release much grass pollen due to being yellower than normal. Therefore, grass pollens mainly came from areas with lower grass fractions and maintained lower pollen concentrations during the pollen season in 2018. In the grass pollen seasons in 2019 and 2020, the grass greenness of areas with higher grass fractions became higher than areas with lower grass fractions. All grasses in the 2019 and 2020 pollen seasons were greener than in February 2018, and grass pollens came from all land plots, especially areas with higher grass fractions. In particular, the grass EVI profiles showed a plateau with higher values and several different peak dates from February to May 2020. This partly explains why this grass pollen season lasted longer, as a longer period of green grasses indicates a larger possibility of releasing grass pollen.

4.3.3.3 Variations of correlations between grass EVI and grass pollen concentrations across orientations with increased distances

According to the analyses in the previous section, grass EVI seasonal dynamics varied with extended distances at different orientations. In this section, we explore changes in correlations between grass pollen concentrations and grass EVI dynamics across orientations and distances around the Campbelltown site. Correlations between grass pollen concentrations and grass EVI in circular areas with increased distances centred on the Campbelltown pollen station are shown in Figure 4.10. The associated coefficient of determination values are shown in Figure 4.11. All analyses in this section were conducted in February to June of their respective study year (2018, 2019 or 2020) to avoid losing inter-annual specific differences due to mixing different years into one research period.

Grass pollen concentrations correlated well with grass EVI dynamics extracted from circular areas with varied distances in 2018 (Figures 4.10 a–e) and 2020 (Figures 4.10 k–o), with R^2 ranging from 0.60 to 0.70. However, grass pollen concentrations did not correlate with greenness dynamics of grasses around the Campbelltown pollen trap station in 2019 (Figures 4.10 f–j). Grass pollen concentrations observed from the in-situ pollen trap showed positive correlations with grass greenness dynamics, which indicates grass pollen concentrations

increased as grass greenness increased. However, the relationship exhibited a nonlinear form. This might be attributed to the peaks of grass pollen concentrations always lagging behind the peaks of grass greenness. For example, the grass EVI peak that occurred around October 2020 triggered the grass pollen peak around November 2020 (Figure 4.9). For the grass pollen – EVI correlations in 2018, the R^2 values increased from 0.60 to 0.70 with the extended research areas. The increasing trend of R^2 values might be due to more grasses being included in study areas as distances increased; therefore, correlations between grass greenness and grass pollen concentrations became stronger as study areas increased in size. In contrast, R^2 values experienced a decreasing trend as study areas extended in 2020. This may indicate that grass pollens came from areas closer to the pollen trap station. More grasses not associated with grass pollen dynamics may have been included in larger study areas, weakening grass greenness – pollen correlations. In general, correlations between grass pollen concentrations and grass EVI varied across distances and years.

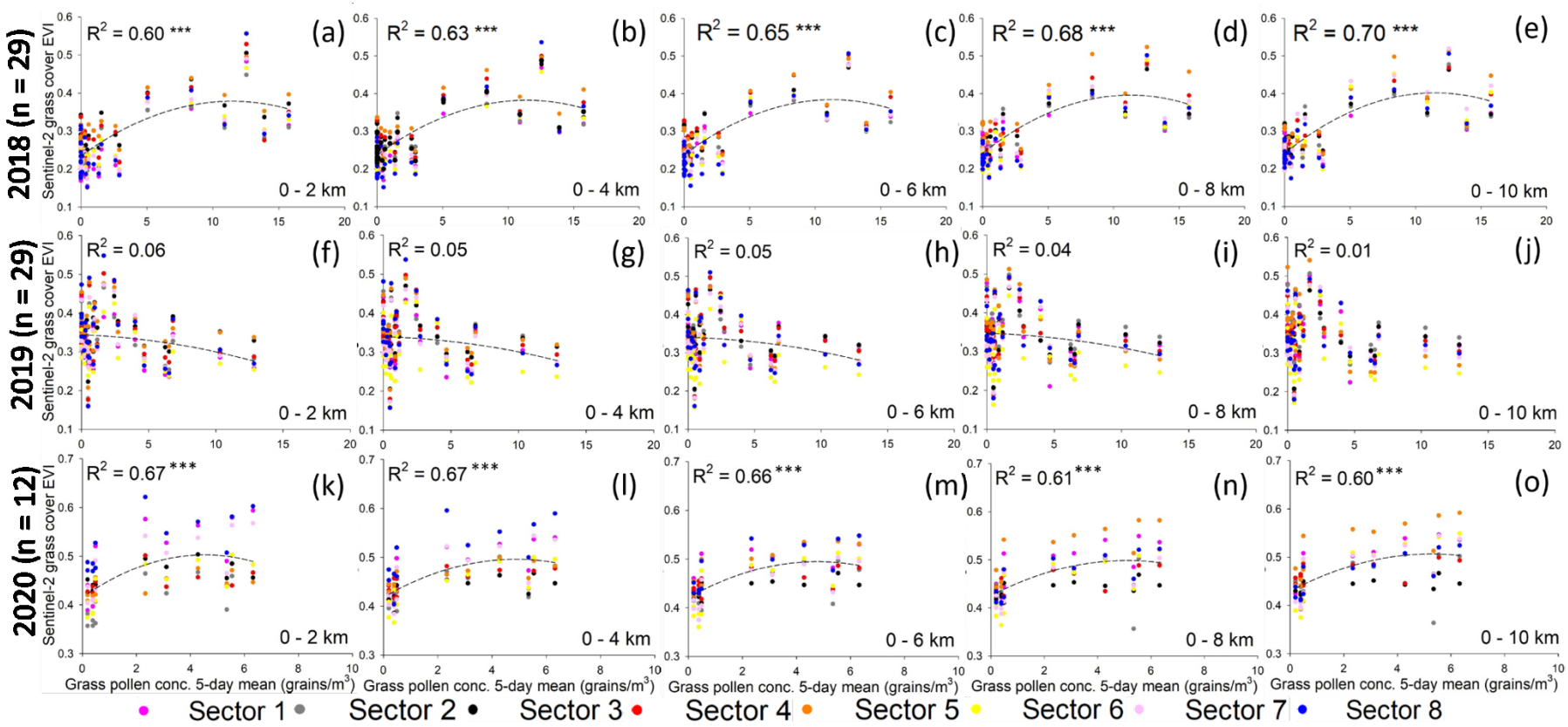

Figure 4.10 Correlations between five-day mean grass pollen concentrations and Sentinel-2 grass EVI for each sector across increased distances (from 2 km to 10 km radius) for February to June 2018, 2019 and 2020 at Campbelltown. n = the number of available images in that year. Sectors 1–8 denote NE1, NE2, SE1, SE2, SW1, SW2, NW1 and NW2, respectively. The five-day mean grass pollen data is the mean value for ±two days from the date for the corresponding Sentinel-2 EVI. Note that the coefficient of determination values (R^2) and regression lines were calculated using mean grass EVI values within the whole circle, rather than every sector in each circle. *** denotes correlation significant at $p = 0.0001$. The R^2 values for each sector are summarised in Figure 4.11.

To analyse differences in grass pollen – EVI correlations at different orientations and further explore why their correlations exhibited opposite trends with increased distances in 2018 versus 2020 (February to June) (as seen in Figure 4.10), we compared correlations between grass pollen and grass greenness for eight different directions in 2018 and 2020 by plotting a heat map of coefficient of determination values (see Figure 4.11). Grass pollen – EVI correlations at varying distances and orientations in 2020 were generally stronger than those in 2018. Of course, a potential reason for this is that the study period included 12 months of 2018 but only five months of 2020. Additionally, correlations varied among orientations, with stronger relationships observed for the SW1, SW2, NW1 and NW2 directions for both 2018 and 2020.

In 2018 (see Figure 4.11 left panel), areas in NE1, NE2 and SE1 had relatively lower R^2 values compared to other orientations. The 0–2 km area in SE2 and 0–10 km area in SW2 exhibited the lowest and highest R^2 values, respectively, among all distances and directions. Within the 0–2 km radius, grass greenness dynamics were more associated with grass pollen dynamics in areas in the SW1, SW2 and NW1 directions. Grass pollen concentrations showed weaker correlations with grass greenness in the SE2 and NW2 directions, though these increased as research areas extended. This indicates that greenness of grasses, clustered in closer areas, was less associated with grass pollen dynamics, and grass pollens might come from grasses beyond the 2 km radius in these two directions. A similar pattern was also found for the SW2 and NW1 orientations and partly explains why grass EVI from increased research areas (i.e., larger radius) exhibited stronger correlations with grass pollen in 2018 (see Figures 4.10 a–e).

In 2020 (see Figure 4.11 right panel), patterns of variations in R^2 values with increasing study distances were different (even opposite) to the 2018 patterns for most orientations. Of the eight orientations, only SW1 and NW2 exhibited increased R^2 values as distances increased. The grass pollen – EVI correlations tended to weaken with increasing distances in the other six orientations, which indicates that grass pollen dynamics in 2020 was more associated with grasses located in areas closer to the Campbelltown pollen trap station. This trend was extremely obvious in the NE2, SE1 and SE2 directions compared with 2018. Grass

pollen – EVI correlations in more distant areas tended to weaken in 2018 (see Figures 4.10 k–o).

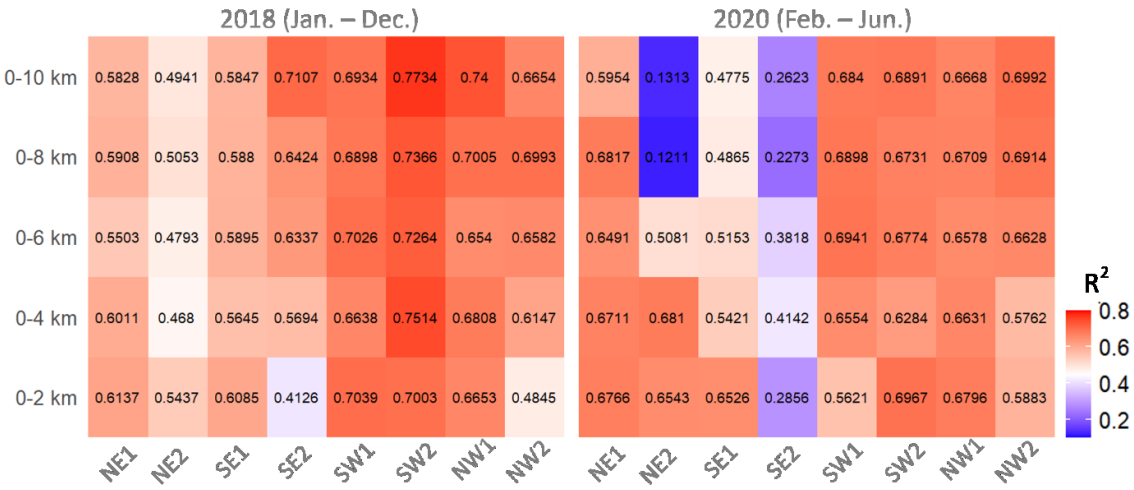

Figure 4.11 Heat map of coefficient of determination values (R^2) for correlations between five-day mean grass pollen concentrations and grass cover EVI for every sector (Campbelltown site) for 2018 and 2020. These R^2 values correspond to the cross plots in Figure 4.10.

4.3.3.4 Variations of correlations between grass EVI and grass pollen concentrations across distances and orientations with varied grass fractions

According to the analyses in Section 4.3.3.3, grass greenness dynamics was more associated with grass pollen concentrations in larger outer areas than in smaller closer areas around the Campbelltown pollen trap sites in some directions for 2018, with an opposite pattern in 2020. However, we cannot firmly conclude that grasses in farther regions were more related to grass pollen dynamics due to study areas overlapping with increasing distances. Further, land plot area (i.e., study areas) tended to be larger as distances increased. For example, the area of land plots in the 8–10 km band was greater than the area of those plots within the 0–2 km band. Therefore, the question arises whether stronger grass pollen – EVI correlations in larger outer study regions were due to the greater amount of grass in these areas, rather than the grass phenological factor? In other words, did land plots with higher grass fractions tend to have a stronger ability to explain grass pollen dynamics? To further analyse differences in grass pollen – EVI correlations across distances and orientations that had varying amounts of grasses, we conducted correlation analyses

for 40 sectors (eight orientations × five distance intervals) (to eliminate the overlapped area effect) and compared their R^2 values with grass fractions (to eliminate the differences in areas of land plots) in each sector.

In general, variation patterns in R^2 values across orientations and distances (sectors in annuli) (Figure 4.12) were similar to the patterns shown in Figure 4.11 (sectors in circles). This firmly indicates that stronger correlations between grass pollen and grass greenness in larger land plots (e.g., areas in the 8–10 km radius in SW2; see Figure 4.11) were due to the greenness of grass in farther areas being better related to grass pollen dynamics than that in closer areas (see Figure 4.12 a). Similarly, the obvious decreasing trend in R^2 values with increasing distances in the SE1 orientation in 2020 (see Figure 4.11) was due to farther grasses showing weaker correlations with grass pollen compared to grasses in closer areas in this direction (see Figure 4. 12 c). Figure 4.12 b shows the R^2 values of grass pollen – EVI correlations for each sector in 2019. As shown in Figures 4.10 f–j, grass greenness dynamics was not associated with grass pollen concentrations in all sectors in 2019. Therefore, we can confidently state that grasses closely related to grass pollen dynamics were distributed across different orientations and distances, and that their patterns of spatial distribution varied across years.

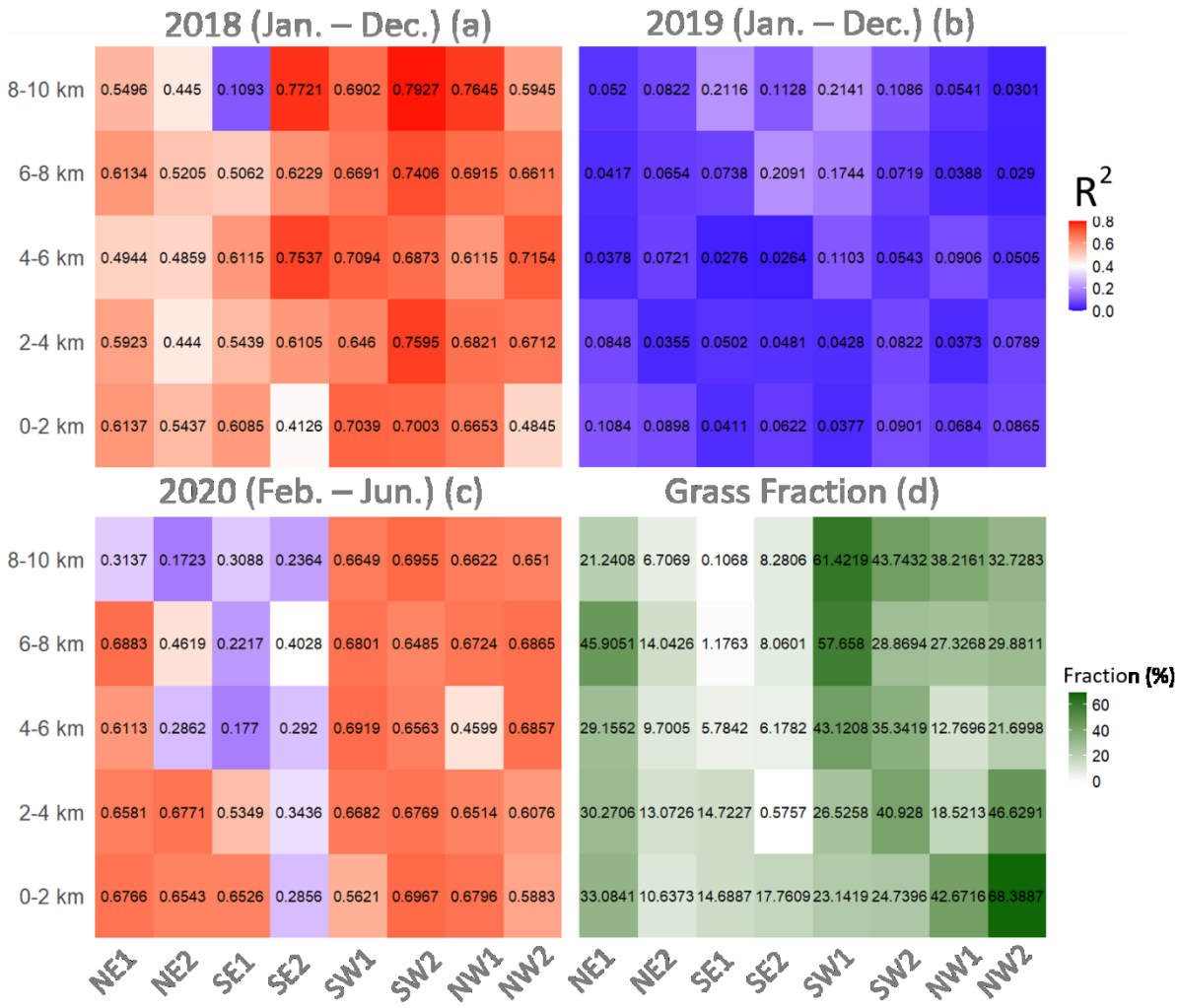

Figure 4.12 Heat map of coefficient of determination values (R^2) for correlations between five-day mean grass pollen concentrations and grass EVI from every sector in each year for (a) 2018, (b) 2019 and (c) 2020 (five months), and (d) the grass fraction at the Campbelltown site.

Additionally, we showed the grass fractions of each land plot (Figure 4.12 d). In general, grass fractions varied greatly across orientations and distances. Land plots in the NE2, SE1, and SE2 directions had relatively low grass fractions compared to other orientations, with higher grass fractions only concentrated in areas closer to the Campbelltown pollen trap station. In the SW1 direction, grass fractions in each land plot increased with increasing distances, which indicates grass was mainly located in farther land plots for this orientation. In contrast, grass fractions in each land plot decreased as distance increased in NW1 and NW2. Grass fraction appeared to be unrelated to distance in the NE1 and SW2 orientations.

In general, the distribution patterns of land plots with higher grass fractions were similar to the R^2 values. For example, higher grass fractions in the land plots within 8–10 km in the SW1, SW2 and NW1 directions corresponded to stronger grass pollen – EVI correlations in 2018 and 2020. In contrast, the land plot within the 8–10 km area in the SE1 direction had the lowest grass fraction and the lowest R^2 value in all years. However, the grass fraction of the land plot within 8–10 km in the SE2 orientation was relatively low (only 8.28%), but the R^2 values derived from grass pollen – EVI correlations in this land plot were 0.77 and 0.24 in 2018 and 2020, respectively. Therefore, to further explore whether land plots with higher grass fractions exhibited a stronger ability to interpret grass pollen dynamics, we correlated R^2 values derived from grass pollen – EVI correlations with grass fractions for 2018 and 2020 (see Figure 4.13).

The coefficient of determination derived from correlations between grass pollen and grass EVI positively correlated with grass fractions in 2018 (see Figure 4.13 a) and 2020 (see Figure 4.13 b) with different significance levels. In 2018, grass fraction only showed a weak correlation with the coefficient of determination derived from grass pollen – EVI correlations ($R^2 = 0.15$). This indicates that more grass did not equate to better ability to interpret grass pollen dynamics in 2018. In contrast, the grass fraction showed significantly positive correlations with R^2 values derived from grass pollen – EVI correlations in 2020, which indicates that variations in grass fractions explained the grass pollen – EVI correlation changes across orientations and distances to some extent. There is a bunch of points kept relatively vertical form in Figure 4.13 b might be because the relationships between grass pollen concentrations and grass phenology remained unchanged despite the grass fraction in some land plots increasing. It indirectly proved that the grass fraction is not the determining factor for understanding grass pollen dynamics, and grass phenological variations played a combined role with grass fraction in interpreting grass pollen dynamics.

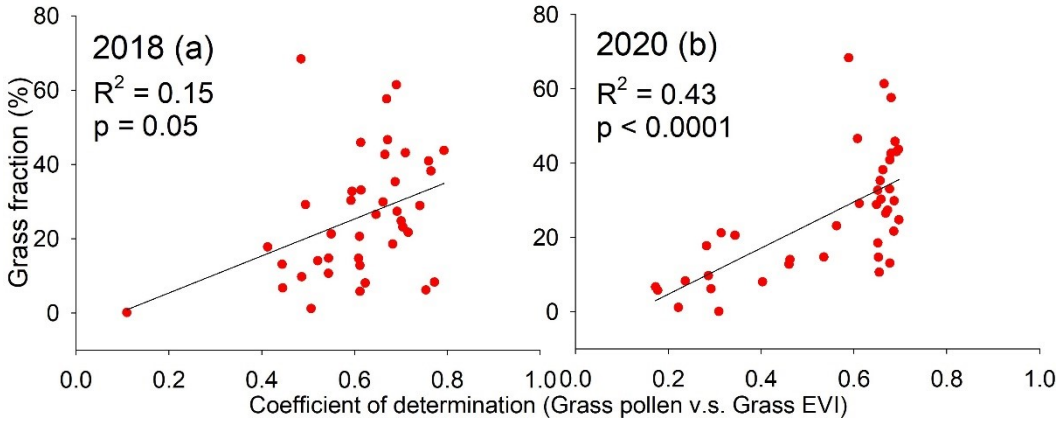

Figure 4.13 Correlations between coefficients of determination (R^2) derived from grass pollen – EVI correlations and grass fractions for each land plot around the Campbelltown site for (a) 2018 and (b) 2020 (five months).

4.3.4 Inter-annual and inter-seasonal variations in spatial distributions of grass pollen sources

Figure 4.14 shows the variations in pixel-wise spatial distributions of grass pollen sources around the Campbelltown pollen station across pollen seasons and years. Given that there were multiple pollen seasons during one Julian year, we divided each year into several grass pollen seasons based on the magnitude of grass pollen concentrations. There were two pollen seasons in 2018 (30 January – 20 May 2018 and 7 September – 1 December 2018), three in 2019 (1 December 2018 – 19 February 2019, 26 March – 9 July 2019 and 23 August – 26 December 2019) and one in 2020 (19 February – 28 June 2020). Grass pollen seasons are highlighted by different colour in the time series of grass EVI and denoted by S1 to S6 in Figure 4.14. The circular plots in Figure 4.14 show the spatial distributions of grass pollen sources for each season and Julian year.

The results of the above analyses show that pixel-wise correlations between grass pollen concentrations and grass EVI time series were stronger in 2018 than in 2019 and 2020, with much more grass pixels with high R^2 values in the research area in 2018. Almost all grass pixels showed low R^2 values in 2019. The magnitudes of R^2 values differed between 2018 and 2020, though the spatial distributions of grass pollen sources were similar (in NE1, SW1, SW2, NW1 and NW2). There were two grass areas located in the 8–10 km area in the SW1 orientation that showed weak correlations (cold colours) in 2018 but relatively strong correlations (warm colours)

in 2020. This suggests the spatial distributions of grass pollen sources varied across years.

For two grass pollen seasons (S1 and S2) in 2018, distributions of grass pollen sources clearly varied in terms of orientations. Grass pollen sources were mainly concentrated in the NE1, NE2, SE1, SW1 and NW2 directions in S1. However, almost all grasses surrounding the Campbelltown pollen station were pollen sources in S2. This indicates that the grass species located in the SW2, NW1 and SE2 directions might differ from the species in the other five directions, which had different pollination periods. For example, the greenness of grass located in the 8–10 km area in the SW1 direction showed strong correlations with grass pollen in S1 but weak correlations in S2. The grass plots (0–2 km) in the NW2 direction showed the same pattern.

Although we did not identify grass pollen sources on a long-term temporal study scale (the entire year) in 2019, some grass pixels exhibiting strong grass pollen – EVI correlations were found when shifting to season scale. This indicates that grass pollen sources varied across distances and orientations among pollen seasons within one year. Another interesting finding is that the distributions and amounts of grass pollen sources were dramatically different between S2 and S5, though both of them were the autumn to summer pollen season. Compared with S2 (2018), grass pollen in S5 came from a smaller number of pollen sources located in farther areas. Additionally, according to grass EVI and pollen profiles, grasses turned very green around January 2019 (corresponded to S3) and a sharp increase in grass pollen concentrations occurred at the same time. However, no obvious grass pollen sources were found within the 10 km radius in S3. It may be that grass pollen came from sources outside the 10 km radius in S3. Overall, the spatial distribution and amount of grass pollen sources varied across each pollen season.

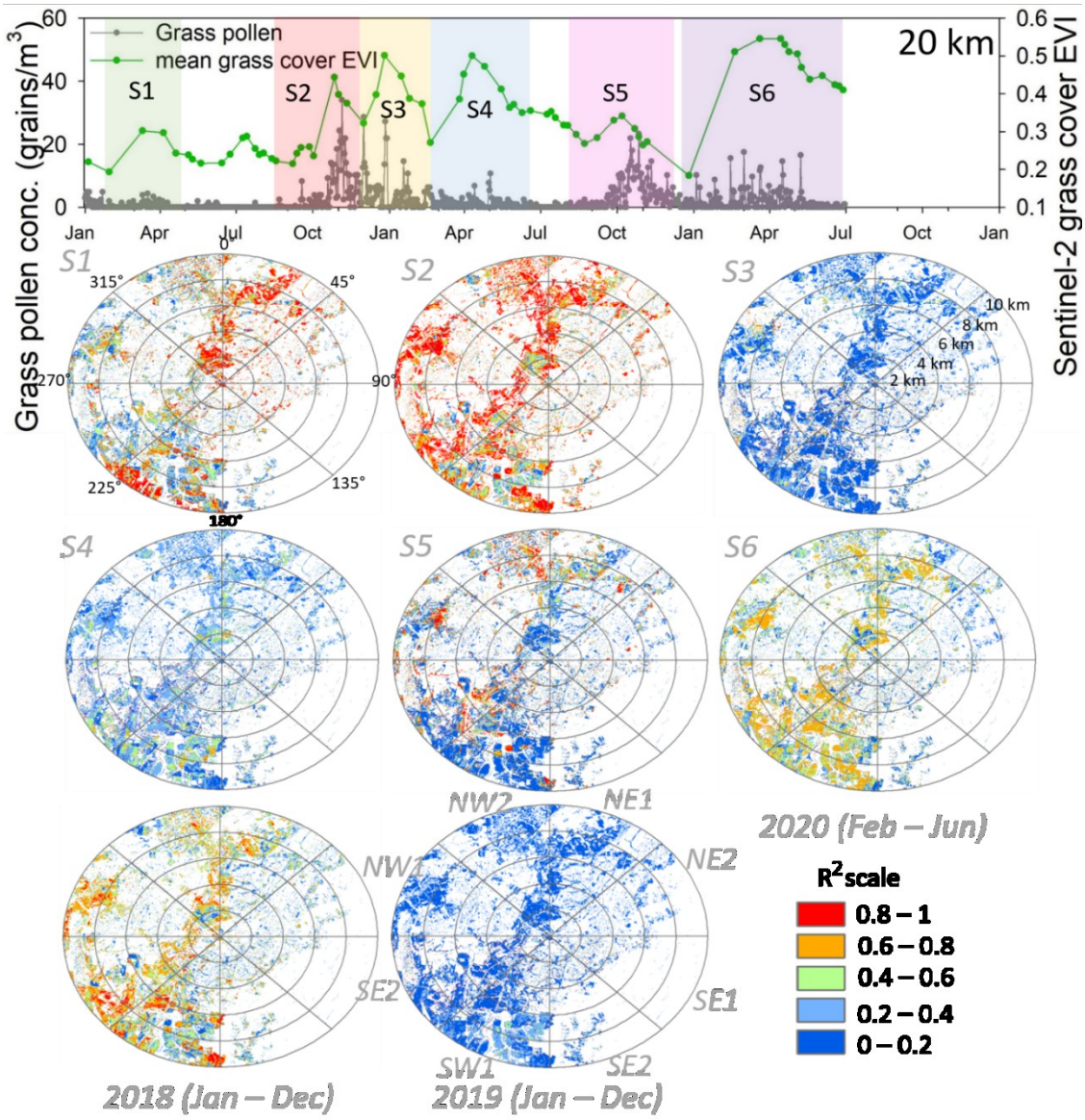

Figure 4.14 Pixel-wise spatial distribution of coefficient of determination (R^2) between five-day mean grass pollen concentrations and grass EVI derived from Sentinel-2 data for each grass pollen season and Julian year (2018–2020). S1 to S6 denote grass pollen seasons 1 to 6, respectively, highlighted by different colours in the top plot. White parts represent non-grass classes according to the Sentinel-2 grass map.

4.4 DISCUSSION

4.4.1 Differences in grass fractions derived from multi-resolution grass maps

Plant species used for ornamental and recreational purposes in urban landscapes (i.e. parks, gardens, tree-alignments or open green spaces in a broad sense) are the most common cause of pollen allergies among the local population (Granada, Spain) (Cariñanos, Casares-Porcel & Quesada-Rubio 2014). However, how to accurately describe grass greenness dynamics in urban is remain unsolved due to land cover products usually have coarse resolutions (> 10 m), which are widely used to filter grass information from landscapes. Using a commercial satellite image - Quickbird (DigitalGlobal Corporate, 2010) with 0.6 m ground resolution, Skjøth et al., (2013) generated an image showing the potential grass pollen source areas in the urban area. Though high-resolution images captured by commercial satellite or unmanned aerial vehicles (UAVs) (Guo et al. 2018) provide a chance to efficiently identify the distribution of grass in urban areas, they are not suitable for applications at national or continental scales.

In this study, by comparing with widely used land cover products in Australia (i.e. DLCD, 250 m; ALUM, 50 m), we proved the promising potential of Sentinel-2 image-derived grass map with 10 m resolution in describing urban grass greenness. According to Fig. 4.4 and 4.5, both DLCD and ALUM products recognized non-grass features as grass due to their coarse resolutions and specific usages. Unlike DLCD (i.e. land cover products), ALUM was designed to provide land use information. Land cover data documents how much of a region is covered by forests, wetlands, agriculture, grassland, and other land and water types. They are usually generated by satellite images. In contrast, land use map shows how people use the landscape – whether for development, conservation, or mixed uses. Therefore, though some classes of ALUM indeed include grass cover, e.g. parks, golf course, and lawns, they did not be included in “grass cover” classes in my study, because those regions included too many buildings or non-grass classes rather pure grass cover. On the other hand, to improve the accuracy of the ALUM grass map, we integrated urban ‘green space’ into it. However, non-grass features will inevitably be included in the grass map, for example, trees surrounding the golf course, or buildings nearby the recreation lawns. That is why though the ALUM

grass map features 50 m resolution, its performance is similar to the DLCD grass map (250 m). The differences in capturing grass greenness between Sentinel-2 grass map, ALUM and DLCD were shown in Fig. 4.6. and 4.7. As compared with coarse grass maps, the Sentinel-2 grass map can efficiently measure and track grass greenness dynamics, even in heterogeneous urban landscapes, due to it successfully excluded non-grass features (Fig. 4.7).

4.4.2 Variations in grass phenology and relationships with grass pollen concentrations across distances and orientations

According to our results (Fig. 4.8 to 4.13, and Appendix Fig. 4.A1 and A2), grass fractions varied across distances and orientations around the pollen trap station. Meanwhile, grass phenology, which derived from Sentinel-2 grass images, and relationships between grass pollen concentrations were varied in different degrees with distances and orientations changes.

Though grass fractions were varied at different land plots around the Campbelltown site, their grass phenology exhibited similar temporal trends from January 2018 to June 2020, with slight shifts in greenness peak timing between different land plots (Fig. 4.9). In contrast, the magnitude of grass greenness around peak timings varied obviously and it was associated with grass fractions, i.e. higher grass fractions, higher magnitudes of grass greenness. However, grass phenology derived from different land plots around March 2018 exhibited the opposite 'fraction - magnitude' pattern compared with other grass greenness peaks. It might be attributed to the differences in responding to precipitation between C_3 (cool season) and C_4 (warm season) species. The summer-autumn months (from January to May) in 2018 were dryer than 2019 and 2020, with monthly precipitation totals of 121.2 mm, 225 mm, and 276.6 mm for 2018, 2019 and 2020, respectively (Fig. 4.2). According to previous studies, aridity does seem to help C_4 vegetation to persist at temperatures that would otherwise have led to C_3 dominance (Sage et al. 1999; Cabido et al. 2008). Therefore, the aridity suppressed the growth of C_3 vegetation, which is located at land plots with high grass fractions (Fig. 4.9), and then reduced the magnitude of their greenness in summer-autumn months, 2018. As precipitation increased in 2019 and 2020, C_3 species became to be dominated again, and thus their magnitude of greenness increased.

Although the grass phenology did not vary obviously across distances and orientations, relationships between grass phenology and grass pollen concentrations varied a lot at different years (Fig. 4.10 to 4.12). The grass greenness dynamics around pollen station associated well with *in-situ* trapped grass pollen concentrations in 2018 and 2020, but not 2019. Furthermore, grass greenness extracted from several farther land plots showed higher correlations with grass pollen as compared with closer grass plots in 2018 (e.g. Fig. 4.12 a). In contrast, grass pollen – EVI correlations exhibited a relatively consistent pattern with distances increased in 2020 (e.g. Fig. 4.12 c).

I tried to explain whether varied grass fractions in different land plots are the key reason that caused the variations in grass pollen – EVI correlations across distances and orientations (Fig. 4.13). In general, land plots with more grass (higher grass fractions) are thought to have greater possibilities to release grass pollen and therefore their grass greenness possesses stronger performance to interpret grass pollen dynamics. However, the grass fraction seems to act as a secondary control in my results. For example, in 2020, correlations between grass greenness and pollen concentrations did not continue to increase when the grass fraction reached a certain level (Fig. 4.13 b). And in 2018, the year where grass greenness showed strong correlations with pollen, even grass greenness derived from land plots with small grass fractions (i.e. less grass) could better interpret pollen dynamics than land plots with more grass (Fig. 4.13 a).

4.4.3 Seasonal variations in spatial distributions of grass pollen sources

To improve the advances in pollen forecast systems, mapping grass pollen emission sources is critical, particularly in diverse landscapes where mixtures of species composition are not well represented in existing coarse land cover products. In this study, the promising performance of Sentinel-2 data had been proved for improving the description of grass greenness from space and for mapping grass pollen sources with finer spatial resolution. It provides firm data support to better inform grass pollen aerobiology in urban areas, especially considering the growing allergenicity related to urban green spaces that had been reported in previous studies (Cariñanos et al. 2002; De Linares et al. 2010).

I mapped grass pollen sources based on grass pollen – EVI correlations using Sentinel-2 grass map for a 20 × 20 km circular area centred at Campbelltown pollen station. The grass surrounding the pollen station exhibited six greenness peaks from January 2018 to June 2020, which corresponded to grass pollen activities (Fig. 4.14). This is due to grass cover in Sydney region consist of native/ exotic species, and the co-existence of mixed C_3 (cool-season grasses)/C_4 (subtropical or summer-flowering grasses) species (Davies et al. 2015). These functionally diverse grasses, which with contrasting growth requirements, contributed to multiple peaks of grass greenness and pollen (Medek et al. 2016).According to grass pollen sources maps (Fig. 4.14), the deviation in spatial distributions and amounts of pollen sources were evident across pollen seasons.

Although S1, S4, and S6 (Fig. 4.14), were summer-autumn pollen seasons associated with C_4 grasses (highlighted by red color in Fig. 4.15), their grass pollen sources were different in terms of spatial distribution and amounts. As discussed above (section 4.4.2), C_4 grasses exhibited only minor senescence during S1 when low rainfall promoted browning in C_3 grasslands (Watson, Restrepo-Coupe & Huete 2019). Therefore, only C_4 – dominated grasslands around pollen station (i.e. NW2, within 4 km; NE1, NE2, and SW1) contributed pollens in S1 (Fig. 4.14). In contrast, besides those four orientations, SE2 and NW1 also contributed pollens to S6. It can be attributed to high rainfall during S6 might favour the growth for both C_3 and C_4, and thus grass greenness in S6 were dramatically high (Fig. 4.15). Additionally, to compensate for growth disadvantages in competing for growth resources and space with C_4 grasses, C_3 grasses may flower earlier and reproduce longer. Therefore, the possibility of both C_4 and C_3-dominated grasslands contributing pollens to S6 and forming a long pollen season was not be excluded. Furthermore, to better interpret the combined or individual impact of grass species on grass pollen concentration dynamics, categories of grass classified by temporal sequences of grass greening and grass flowering of specific grass species (e.g., species flowering prior/after to vegetative green peak) is worth to study in the future. Although grass exhibited a greenness peak around April 2019 (i.e. S4), only small amounts of grass were associated with pollen activities at S4 as compared with S1 and S6 (Fig. 4.14). It might be due to the fact that although the grass turned

green but did not release grass pollens and, therefore, the amount of grass pollen concentrations trapped by pollen station was small at S4. Another assumption is grass released pollen but they were not captured by pollen trap due to meteorological variables – for example, increased relative humidity that usually hindered airborne pollen transport (Rojo et al. 2015), especially considering a heavy rainfall occurred at the start of S4 (Fig. 4.15).

The spring pollen season S2 and S5 were associated with cool-season C_3 grasses (highlighted by blue color in Fig. 4.15). The C_3 species generally reached greenness peak in late October to early November in Australia, but high rainfall has been demonstrated to drive a C_3 green peak occurred in January in a previous study (Watson, Restrepo-Coupe & Huete 2019). It keeps in line with my results – there was a January (2019) greenness peak after a heavy rainfall occurred around December 2018. Therefore, the S3 was identified as pollen season that was associated with C_3 grasses and highlighted by green in Fig. 4.15. Given greenness peak in S3 was an anomalous peak driven by rainfall, it might do not have the pollination ability. And thus, grass pollen concentrations decreased alongside grass greenness increased and only small amounts of grass were associated with pollen dynamics in S3 (Fig. 4.15). As for other two spring seasons, fewer pollen sources and lower grass greenness for S5 can be partly attributed to lower precipitation as compared with S2 (Fig. 4.15). Overall, variations in grass pollen sources distribution among seasons were driven by not only grass phenology, but also other explanatory variables (e.g. precipitation, relative humidity, temperature, and wind). The effect of meteorological variables on pollen emission and dispersal should be taken into account in informing the aerobiology of grass pollen using satellite-based remote sensing.

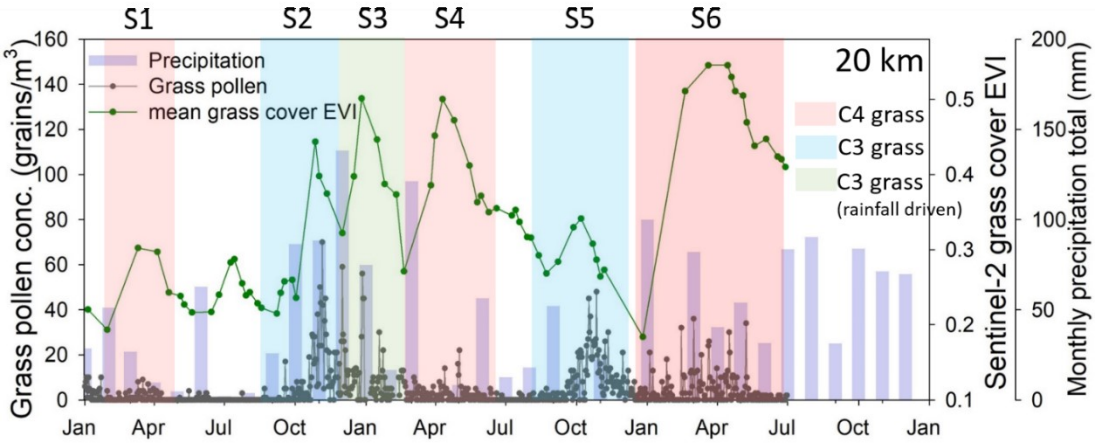

Figure 4.15 Time series plots of monthly precipitation total and mean grass Sentinel-2 EVI averaged from the 20 × 20 km circular area around Campbelltown site from 2018 to 2020. Summer-autumn pollen seasons associated with C_4 grasses are highlighted by red colors. Blue and green colors highlight spring pollen seasons associated with C_3 grasses.

For further provide some clues to interpret seasonal dynamics of grass pollen concentrations across all grass pollen seasons, we plotted the wind speeds and directions roses (Figure 4.16). Due to grass pollen seasons could be roughly divided into two types, i.e., S1, S4, and S6 – the pollen peak appeared around April; and S2 and S5 – the pollen peak appeared around October (Figure 4.15), we analyses the wind speeds and prevailing wind directions for time period from the middle of March to the middle of April (hereafter: Mar-Apr wind) and from the middle of October to the middle of November (hereafter: Oct-Nov wind).

As compared with April pollen peaks (i.e., S1, S4, and S6), grass pollen concentrations are usually higher than November pollen peaks (i.e., S2 and S5). It is partly contributed to wind were faster in Oct-Nov wind and showed much more diverse directions than Mar-Apr wind (Figure. 4.16). For example, the prevailing wind only blew from the SSW at 9:00 am for Mar-Apr wind (Figure 4.16 a). However, besides SSW direction, almost 20% of wind blew from the north at 9:00 am for Oct-Nov wind (Figure 4.17 c). Additionally, the wind that was larger than 20 km/h was only found at Oct-Nov wind rose (Figure 4.17 d).

Regarding the inter-annual differences in terms of pollen concentrations among the same pollen seasons, the wind speeds and directions also provided some insights by

combining grass pollen sources map. According to Figure 4.14, there were much more grass plots located at SW1 and SW2 directions (i.e., the prevailing wind direction, SSW, in Mar-Apr wind rose, Figure 4.16 a) were recognized as pollen sources in S6 compared with S1 and S4. Therefore, the prevailing wind carries pollens in SSW directions to pollen trap and consequently the pollen concentrations increased in S6. Furthermore, though there were fewer grass pollen sources in S5 as compared with S2, diverse wind directions and faster wind speeds in Oct-Nov wind could be used to explain the similar amount of grass pollen concentrations in S2 and S5. In other words, grass pollens collected by the trap in S5 might come from pollen sources beyond our research regions, which were carried by stronger winds from diverse directions.

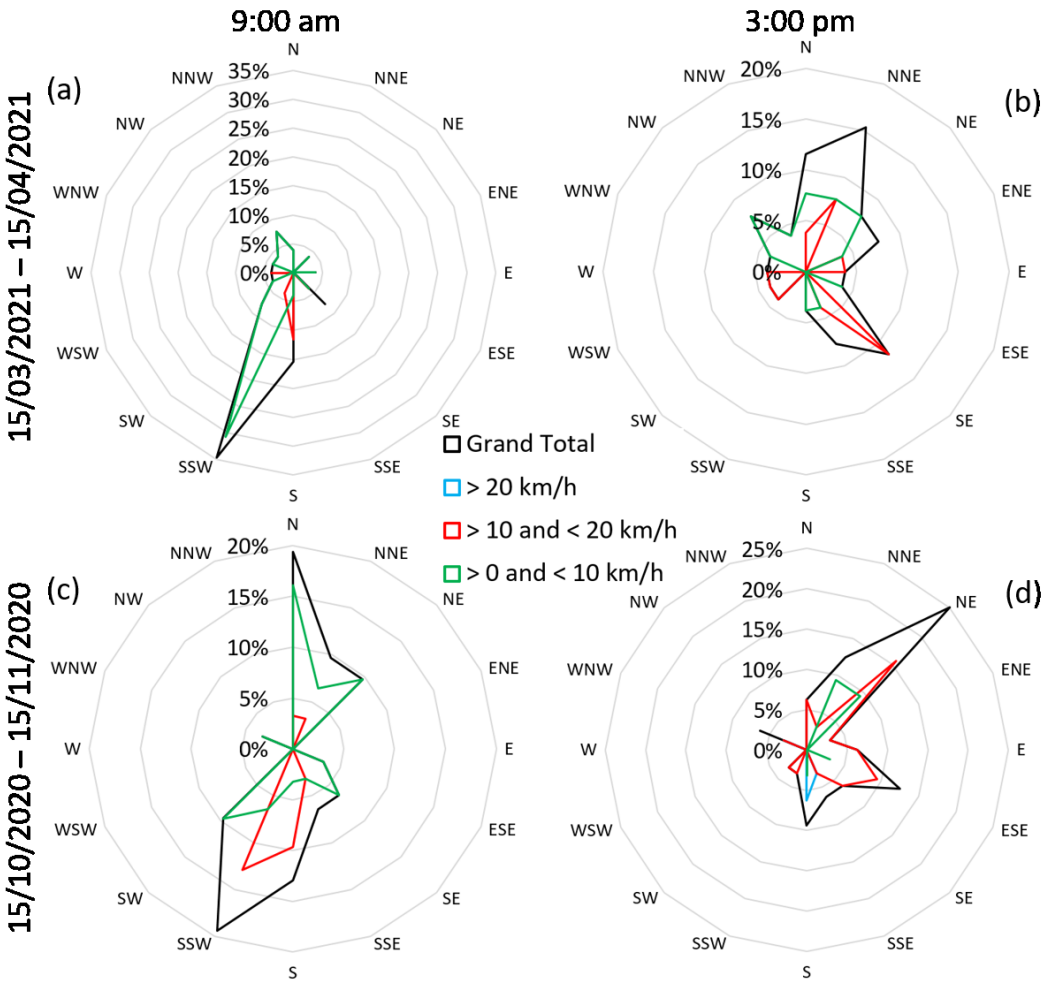

Figure 4.16 The wind speed and direction rose at Campbelltown for 15/03/2021 – 15/04/2021 and 15/10/2020 – 15/11/2020. Wind directions are divided into sixteen compass directions. The circles around the image represent the various percentages

of occurrence of the winds (e.g., if the line to the south just reaches the 20% ring it means a frequency of 20% blowing from that direction). Wind speeds are grouped into three compass speeds. The black lines denote the grand total of all wind speeds. The left panels (a and c) and right panels (b and d) is wind rose for 9:00 am and 3 pm, respectively.

4.5 CONCLUSION

In this study, we explored the potential of Sentinel-2 data with 10 m resolutions for improving filter grass information from heterogeneous landscapes and for mapping grass pollen sources. Despite the complex landscape conditions, this study has shown that the Sentinel-2 grass map can function effectively in monitoring and tracing grass greenness dynamics, and thus improve our understanding on the aerobiology of grass pollen. The Sentinel-2 data contributed both to the timing of grass phenology growth periods and important geospatial landscape information on local and regional grass pollen emission sources. Results from this study are promising because they offer a new avenue to use Sentinel-2 data with a 10 m resolution globally for mapping grass pollen sources and their seasonal dynamics at a large scale. The results and discussions have identified four key conclusions:

(1) Compared with ALUM and DLCD grass maps, the Sentinel-2 grass map (10 m) could effectively exclude non-grass features, which were recognized as grass class by the two coarser grass maps, and grass greenness information filtered by the Sentinel-2 grass map was better correlated with phenocam observation of grass at *in-situ* scale. Therefore, the Sentinel-2 grass map has the improved ability to filter grass greenness information from heterogeneous landscapes.

(2) Grass greenness dynamics (phenology) derived from the Sentinel-2 grass map and their relationships with grass pollen concentrations varied across different distances and orientations, with significant inter-annual variability.

(3) Although the grass fraction derived from the Sentinel-2 grass map changed across different distances and orientations, it was a secondary factor to affect the relationships between grass greenness dynamics and grass pollen concentrations.

(4) Seasonal and inter-annual variability of grass pollen sources in terms of spatial distributions and amounts were high for the Campbelltown pollen station. To

accurately interpret these variations, meteorological factors and influences on the phenology of C_3/C_4 grassland functional types and pollen emission/ transport need further attention.

4.6 REFERENCES

Abolfazl Abdollahi, Yuxia Liu, Biswajeet Pradhan, Alfredo Huete, Abhirup Dikshit, Ngoc Nguyen Tran, 2021, Short-Time-Series Grass Mapping Using Sentinel-2 Imagery and Deep Learning-based Architecture, Sensors (submitted).

Beaumont, L.J., Hartenthaler, T., Keatley, M.R. & Chambers, L.E. 2015, 'Shifting time: Recent changes to the phenology of Australian species', *Climate Research*, vol. 63, no. 3, pp. 203–14.

Cabido, M., Pons, E., Cantero, J.J., Lewis, J.P. & Anton, A. 2008, 'Photosynthetic pathway variation among C4 grasses along a precipitation gradient in Argentina', *Journal of Biogeography*, vol. 35, no. 1, pp. 131–40, viewed 16 July 2021, <https://onlinelibrary.wiley.com/doi/full/10.1111/j.1365-2699.2007.01760.x>.

Cariñanos, P., Casares-Porcel, M. & Quesada-Rubio, J.M. 2014, 'Estimating the allergenic potential of urban green spaces: A case-study in Granada, Spain', *Landscape and Urban Planning*, vol. 123, pp. 134–44.

Cariñanos, P., Sánchez-Mesa, J.A., Prieto-Baena, J.C., Lopez, A., Guerra, F., Moreno, C., Domínguez, E. & Galan, C. 2002, 'Pollen allergy related to the area of residence in the city of Córdoba, south-west Spain', *Journal of Environmental Monitoring*, vol. 4, no. 5, pp. 734–8.

Charlotte Pelletier, Geoffrey I. Webb, F.P. 2019, Deep learning for the classification of Sentinel-2 image time series, pp. 461–4.

Chen, Jun, Chen, Jin, Liao, A., Cao, X., Chen, L., Chen, X., He, C., Han, G., Peng, S., Lu, M., Zhang, W., Tong, X. & Mills, J. 2015, 'Global land cover mapping at 30 m resolution: A POK-based operational approach', *ISPRS Journal of Photogrammetry and Remote Sensing*, vol. 103, pp. 7–27.

Clark, M.L. 2017, 'Comparison of simulated hyperspectral HyspIRI and multispectral Landsat 8 and Sentinel-2 imagery for multi-seasonal, regional land-cover mapping', *Remote Sensing of Environment*, vol. 200, pp. 311–25.

Davies, J.M., Beggs, P.J., Medek, D.E., Newnham, R.M., Erbas, B., Thibaudon, M., Katelaris, C.H., Haberle, S.G., Newbigin, E.J. & Huete, A.R. 2015, 'Trans-disciplinary research in synthesis of grass pollen aerobiology and its importance for respiratory health in Australasia', *Science of the Total Environment*, vol. 534, pp. 85–96.

Denize, J., Hubert-Moy, L., Corgne, S., Betbeder, J. & Pottier, E. 2018, 'Identification of winter land use in temperate agricultural landscapes based on Sentinel-1 and 2 times-series.', *International Geoscience and Remote Sensing Symposium (IGARSS)*, vol. 2018- July, pp. 8271–4.

Descals, A., Verger, A., Yin, G. & Peñuelas, J. 2020, 'Improved estimates of arctic land surface phenology using sentinel-2 time series', *Remote Sensing*, vol. 12, no. 22, pp. 1–13.

Devadas, R., Huete, A.R., Vicendese, D., Erbas, B., Beggs, P.J., Medek, D., Haberle, S.G., Newnham, R.M., Johnston, F.H., Jaggard, A.K., Campbell, B., Burton, P.K., Katelaris, C.H., Newbigin, E., Thibaudon, M. & Davies, J.M. 2018, 'Dynamic ecological observations from satellites inform aerobiology of allergenic grass pollen', *Science of the Total Environment*, vol. 633, pp. 441–51, viewed 15 May 2019, <https://doi.org/10.1016/j.scitotenv.2018.03.191>.

Dewi, C. & Chen, R. 2019, Intelligent information and database systems: Recent developments, Intelligent Information and Database Systems: Recent Developments, vol. 830, Springer International Publishing.

Emmerson, K.M., Silver, J.D., Newbigin, E., Lampugnani, E.R., Suphioglu, C., Wain, A. & Ebert, E. 2019, 'Development and evaluation of pollen source methodologies for the Victorian Grass Pollen Emissions Module VGPEM1.0', *Geoscientific Model Development*, vol. 12, no. 6, pp. 2195–214.

Fragoso-Campón, L., Quirós, E., Mora, J., Gutiérrez, J.A. & Durán-Barroso, P. 2018, 'Accuracy Enhancement for Land Cover Classification Using LiDAR and Multitemporal Sentinel 2 Images in a Forested Watershed', *Proceedings 2018, Vol. 2, Page 1280*, vol. 2, no. 20, p. 1280, viewed 14 July 2021, <https://www.mdpi.com/2504-3900/2/20/1280>.

Gómez-Giráldez, P.J., Pérez-Palazón, M.J., Polo, M.J. & González-Dugo, M.P. 2020, 'Monitoring grass phenology and hydrological dynamics of an oak-grass savanna ecosystem using sentinel-2 and terrestrial photography', *Remote Sensing*, vol. 12, no. 4.

Guo, W., Zheng, B., Potgieter, A.B., Diot, J., Watanabe, K., Noshita, K., Jordan, D.R., Wang, X., Watson, J., Ninomiya, S. & Chapman, S.C. 2018, 'Aerial imagery analysis – Quantifying appearance and number of sorghum heads for applications in breeding and agronomy', *Frontiers in Plant Science*, vol. 871, no. October, pp. 1–9.

Haberle, S.G., Bowman, D.M.J.S., Newnham, R.M., Johnston, F.H., Beggs, P.J., Buters, J., Campbell, B., Erbas, B., Godwin, I., Green, B.J., Huete, A., Jaggard, A.K., Medek, D., Murray, F., Newbigin, E., Thibaudon, M., Vicendese, D., Williamson, G.J. & Davies, J.M. 2014, 'The macroecology of airborne pollen in Australian and New Zealand urban areas', *PLoS ONE*, vol. 9, no. 5.

Karlsen, S.R., Ramfjord, H., Høgda, K.A., Johansen, B., Danks, F.S. & Brobakk, T.E. 2009, 'A satellite-based map of onset of birch (Betula) flowering in Norway', *Aerobiologia*, vol. 25, no. 1, pp. 15–25, viewed 9 June 2021, <https://link.springer.com/article/10.1007/s10453-008-9105-3>.

Khwarahm, N.R., Dash, J., Skjøth , C.A., Newnham, R.M., Adams-Groom, B., Head, K., Caulton, E. & Atkinson, P.M. 2016, 'Mapping the birch and grass pollen seasons in the UK using satellite sensor time-series', *Science of the Total Environment*, vol. 578.

K̈oppen, W., Volken, E. & Brönnimann, S. 2011, 'The thermal zones of the Earth according to the duration of hot, moderate and cold periods and to the impact of heat on the organic world', *Meteorologische Zeitschrift*, vol. 20, no. 3, pp. 351–60.

Längkvist, M., Kiselev, A., Alirezaie, M. & Loutfi, A. 2016, 'Classification and segmentation of satellite orthoimagery using convolutional neural networks', *Remote Sensing*, vol. 8, no. 4.

De Linares, C., Díaz De La Guardia, C., Nieto Lugilde, D. & Alba, F. 2010, 'Airborne study of grass allergen (Lol p 1) in different-sized particles', *International Archives of Allergy and Immunology*, vol. 152, no. 1, pp. 49–57.

Linkosalo, T. 1999, 'Regularities and patterns in the spring phenology of some Boreal trees', *Silva Fennica*, vol. 33, no. 4, pp. 237–45.

Linkosalo, T. 2011, 'Mutual regularity of spring phenology of some boreal tree species: predicting with other species and phenological models', *https://doi.org/10.1139/x99-243*, vol. 30, no. 5, pp. 667–73, viewed 14 July 2021, <https://cdnsciencepub.com/doi/abs/10.1139/x99-243>.

Ma, X., Huete, A., Moran, S., Ponce-Campos, G. & Eamus, D. 2015, 'Abrupt shifts in phenology and vegetation productivity under climate extremes', *Journal of Geophysical Research: Biogeosciences*, vol. 120, no. 10, pp. 2036–52.

Mazzia, V., Khaliq, A. & Chiaberge, M. 2020, 'Improvement in land cover and crop classification based on temporal features learning from Sentinel-2 data using recurrent-Convolutional Neural Network (R-CNN)', *Applied Sciences (Switzerland)*, vol. 10, no. 1, pp. 1–23.

McInnes, R.N., Hemming, D., Burgess, P., Lyndsay, D., Osborne, N.J., Skjøth, C.A., Thomas, S. & Vardoulakis, S. 2017, 'Mapping allergenic pollen vegetation in UK to study environmental exposure and human health', *Science of The Total Environment*, vol. 599–600, pp. 483–99, viewed 9 May 2019, <https://www.sciencedirect.com/science/article/pii/S0048969717309749?via%3Dihub>.

Medek, D.E., Beggs, P.J., Erbas, B., Jaggard, A.K., Campbell, B.C., Vicendese, D., Johnston, F.H., Godwin, I., Huete, A.R., Green, B.J., Burton, P.K., Bowman, D.M.J.S., Newnham, R.M., Katelaris, C.H., Haberle, S.G., Newbigin, E. & Davies, J.M. 2016, 'Regional and seasonal variation in airborne grass pollen levels between cities of Australia and New Zealand', *Aerobiologia*, vol. 32, no. 2, pp. 289–302.

Miranda, E., Mutiara, A.B., Ernastuti & Wibowo, W.C. 2019, 'Forest classification method based on convolutional neural networks and sentinel-2 satellite

imagery', *International Journal of Fuzzy Logic and Intelligent Systems*, vol. 19, no. 4, pp. 272–82.

Newnham, R., Adams-Groom, B. & Smith, M. 2013, 'Pollen season and climate: is the timing of birch pollen release in the UK approaching its limit?', *International journal of biometeorology*, vol. 57, no. 3, pp. 391–400, viewed 14 July 2021, <https://pubmed.ncbi.nlm.nih.gov/22710742/>.

Newson RB, van Ree R, Forsberg B, Janson C, Lötvall J, Dahlén SE, Toskala EM, Baelum J, Brożek GM, Kasper L, Kowalski ML, Howarth PH, Fokkens WJ, Bachert C, Keil T, Krämer U, Bislimovska J, Gjomarkaj M, Loureiro C, Burney PG, Jarvis D. 2014, 'Geographical variation in the prevalence of sensitization to common aeroallergens in adults: the GA(2) LEN survey', *Allergy*, vol. 69, no. 5, pp. 643-51. <https://doi: 10.1111/all.12397>. Nguyen, H.T.T., Doan, T.M., Tomppo, E. & McRoberts, R.E. 2020, 'Land Use/Land Cover Mapping Using Multitemporal Sentinel-2 Imagery and Four Classification Methods—A Case Study from Dak Nong, Vietnam', *Remote Sensing 2020, Vol. 12, Page 1367*, vol. 12, no. 9, p. 1367, viewed 14 July 2021, <https://www.mdpi.com/2072-4292/12/9/1367/htm>.

Phiri, D., Simwanda, M., Salekin, S., Nyirenda, V.R., Murayama, Y. & Ranagalage, M. 2020, 'Sentinel-2 Data for Land Cover/Use Mapping: A Review', *Remote Sensing 2020, Vol. 12, Page 2291*, vol. 12, no. 14, p. 2291, viewed 13 July 2021, <https://www.mdpi.com/2072-4292/12/14/2291/htm>.

Qiu, C., Schmitt, M., Geiß, C., Chen, T.H.K. & Zhu, X.X. 2020, 'A framework for large-scale mapping of human settlement extent from Sentinel-2 images via fully convolutional neural networks', *ISPRS Journal of Photogrammetry and Remote Sensing*, vol. 163, no. September 2019, pp. 152–70.

Rapinel, S., Mony, C., Lecoq, L., Clément, B., Thomas, A. & Hubert-Moy, L. 2019, *Evaluation of Sentinel-2 time-series for mapping floodplain grassland plant communities*, viewed 30 May 2019, <https://doi.org/10.1016/j.rse.2019.01.018>.

Rojo, J., Rapp, A., Lara, B., Fernández-González, F. & Pérez-Badia, R. 2015, 'Effect of land uses and wind direction on the contribution of local sources to airborne pollen', *Science of The Total Environment*, vol. 538, pp. 672–82.

Segal-Rozenhaimer, M., Li, A., Das, K. & Chirayath, V. 2020, 'Cloud detection algorithm for multi-modal satellite imagery using convolutional neural-networks (CNN)', *Remote Sensing of Environment*, vol. 237, p. 111446.

Skjøth, C.A., Ørby, P. V., Becker, T., Geels, C., Schlünssen, V., Sigsgaard, T., Bønløkke, J.H., Sommer, J., Søgaard, P. & Hertel, O. 2013, 'Identifying urban sources as cause of elevated grass pollen concentrations using GIS and remote sensing', *Biogeosciences*, vol. 10, no. 1, pp. 541–54.

Verstraeten, W.W., Kouznetsov, R., Hoebeke, L., Bruffaerts, N., Sofiev, M. & Delcloo, A.W. 2021, 'Modelling grass pollen levels in Belgium', *Science of The Total Environment*, vol. 753, p. 141903.

Vrieling, A., Meroni, M., Darvishzadeh, R., Skidmore, A.K., Wang, T., Zurita-Milla, R., Oosterbeek, K., O'Connor, B. & Paganini, M. 2018, 'Vegetation phenology from Sentinel-2 and field cameras for a Dutch barrier island', *Remote Sensing of Environment*, vol. 215, pp. 517–29.

Watson, C.J., Restrepo-Coupe, N. & Huete, A.R. 2019, 'Multi-Scale Phenology of Temperate Grasslands: Improving Monitoring and Management With Near-Surface Phenocams', *Frontiers in Environmental Science*, vol. 7, p. 14, viewed 13 May 2019, <https://www.frontiersin.org/article/10.3389/fenvs.2019.00014/full>.

Zink, K., Pauling, A., Rotach, M.W., Vogel, H., Kaufmann, P. & Clot, B. 2013, 'EMPOL 1.0: A new parameterization of pollen emission in numerical weather prediction models', *Geoscientific Model Development*, vol. 6, no. 6, pp. 1961–75.

4.7 APPENDIX

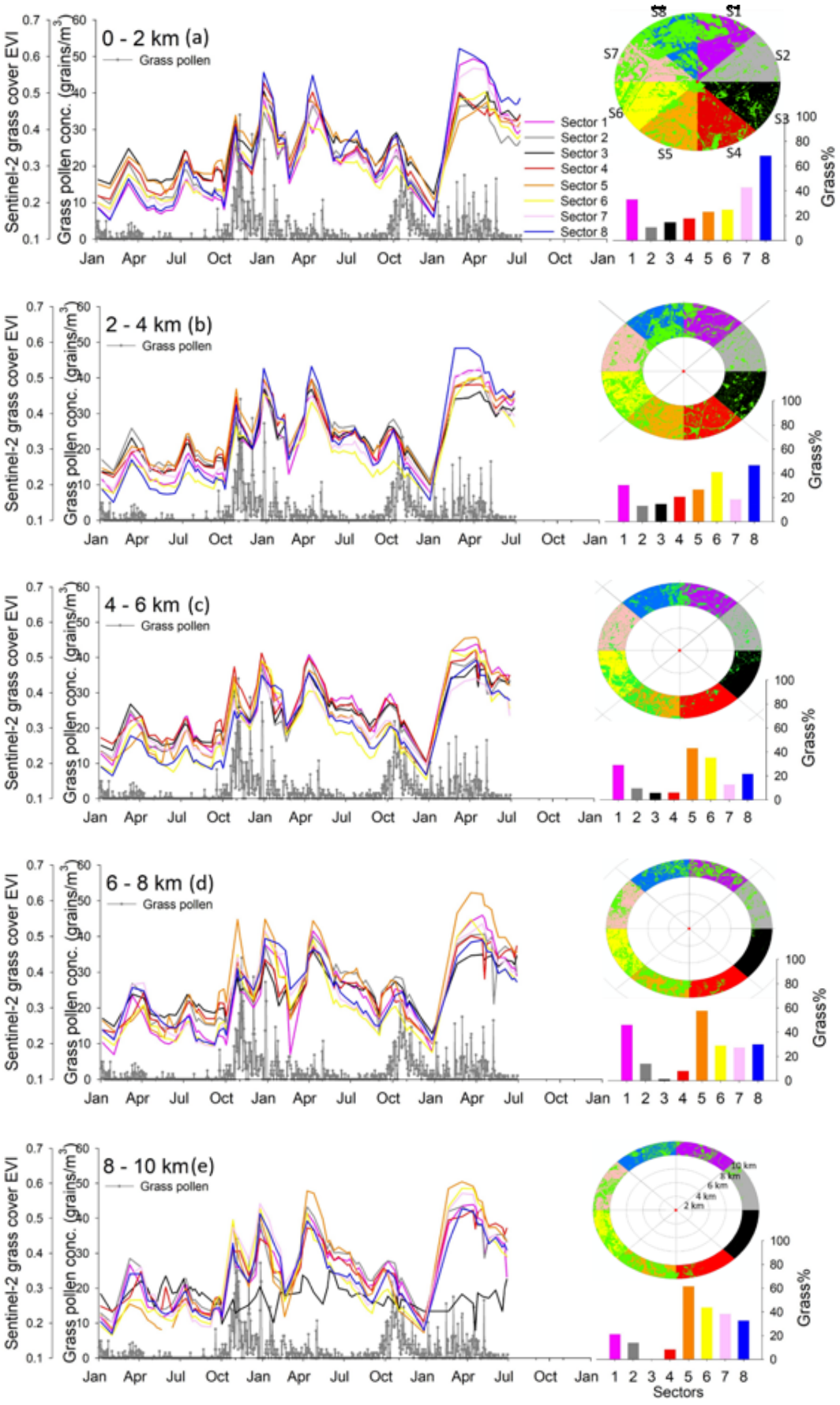
0 - 2 km (a)
2 - 4 km (b)
4 - 6 km (c)
6 - 8 km (d)
8 - 10 km(e)
Grass pollen
Sentinel-2 grass cover EVI
Grass pollen conc. (grains/m3)
Grass%
Sector 1
Sector 2
Sector 3
Sector 4
Sector 5
Sector 6
Sector 7
Sector 8
S1
S2
S3
S4
S5
S6
S7
S8
Jan Apr Jul Oct Jan Apr Jul Oct Jan Apr Jul Oct Jan 1 2 3 4 5 6 7 8
Sectors

Figure 4.A1. Time series plots of grass pollen concentrations and Sentinel-2 grass EVI extracted from different sectors in each annulus, which showed in top-right panels, for 2018 Jan to 2020 Jun at Campbelltown site. The bottom-right panels show grass proportions in sectors within each annulus. Sector 1 to 8 respectively corresponded to areas of 0° - 45° to 315° - 365° in Fig. 4.8.

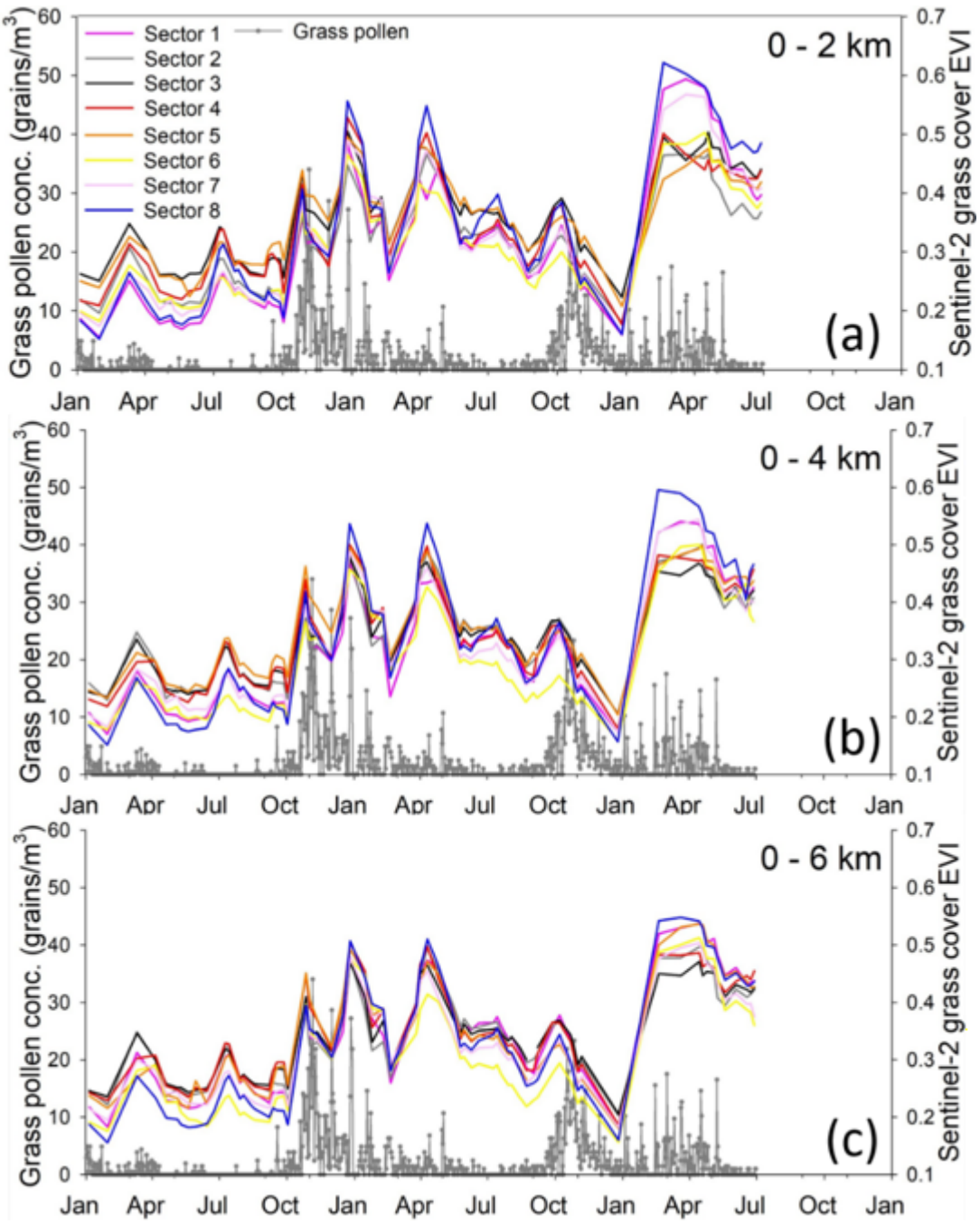

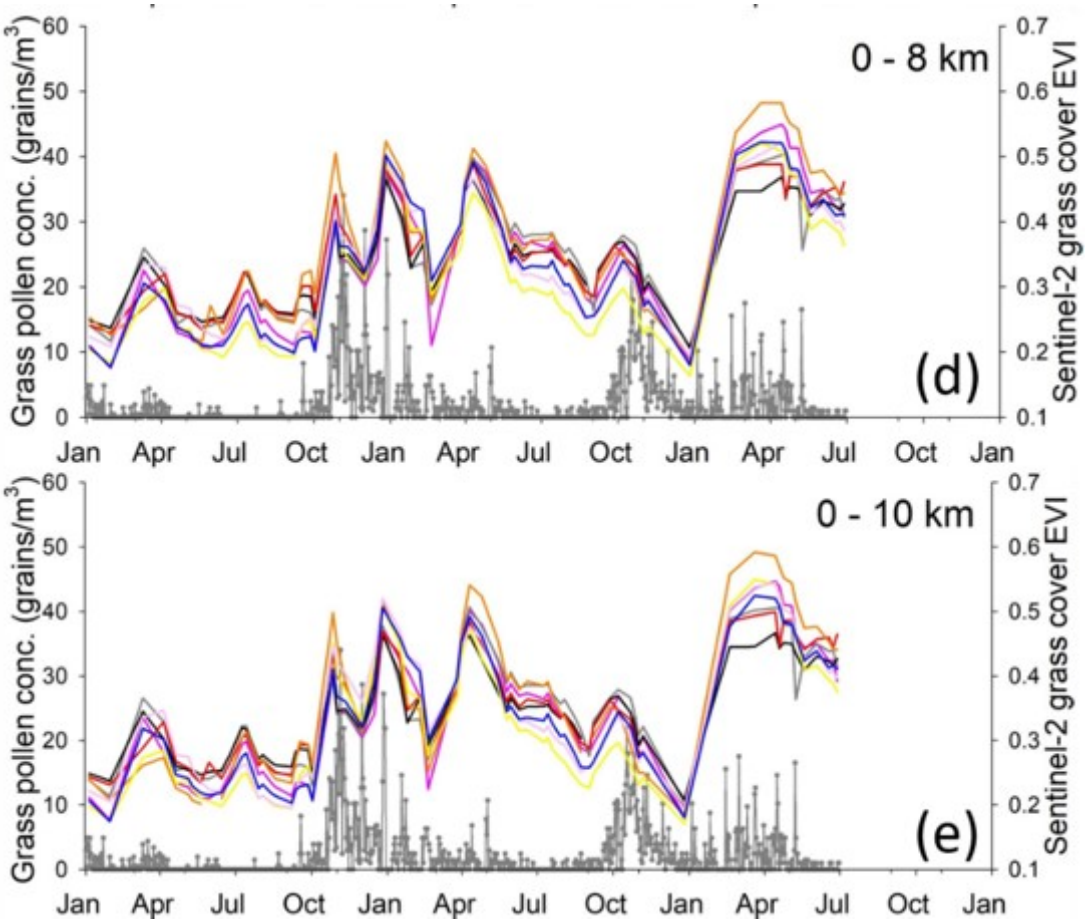

Figure 4.A2. Time series plots of grass pollen concentrations and Sentinel-2 grass EVI extracted from different orientations across extended distances for 2018 Jan to 2020 Jun at Campbelltown site. Sector 1 to 8 respectively corresponded to areas of 0° - 45° to 315° - 365° in Fig. 4.8.

CHAPTER 5

Chapter 5 Conclusion

As a natural ecosystem dominated by grasses and other herbaceous species, grassland/ pasture and its phenological studies have attracted increased attention due to their important roles in public health around the world. Allergenic grass pollen is widely regarded as the major source of clinically relevant outdoor aeroallergens, e.g. seasonal hay fever and asthma, affecting a worldwide population. Furthermore, the public is experiencing an increasing exposure to aeroallergens with higher frequency of high pollen concentrations days under the current climate change background (Davies et al. 2020, Ziska et al. 2011, Beggs et al. 2015). In contrast to the well-studied aerobiology of allergenic grass pollen in the Northern Hemisphere, although the prevalence and morbidity of allergic diseases in Australasia are among the highest globally, the precise ecological information on grassland/ pasture including phenology status and spatial distribution of pollen sources is not well understood yet. Also, the knowledge gap in how these ecological factors impact grass pollen seasonal dynamics restricts the development of accurate pollen forecasts as guidance for the management of public health.

Satellite remote sensing offers a promising method to detect ecologically relevant landscape variables via providing timely and repetitive updates of vegetation phenological dynamics and land cover conditions at regional scale. Meanwhile, as an alternative approach to labour-intensive field surveys, near-surface remote sensing (phenocams) can provide diurnal and long-term vegetation greenness observation at the *in-situ* scale.

Through integrating satellite data and phenocams imagery with grass pollen concentrations, the primary goal of this thesis is to address critical knowledge gaps in our understanding of the ecological drivers of grass pollen aerobiology. To achieve this goal, at the south-eastern Australia grassland/ pasture ecosystem, I first used a set of phenocams to investigate the diurnal and seasonal pasture greenness variations. It provides the reliable surface ground truth observation of grassland/ pasture phenological dynamics. Next, to better understand the regional grassland/ pasture phenology and its impacts on grass pollen seasons, I investigated the possibility and limitations of upscaling greenness observations from phenocam to multi-sensor satellites (i.e. Sentinel-2 MIS, MODIS, and Himawari-8 AHI). And then, I explored relationships between seasonal grass pollen dynamics and grass

greenness derived from multi-sources remote sensing in peak timing and amplitude scopes. Furthermore, I compared a finer-resolution grass map generated by Sentinel-2 data with developed but coarse land cover/use products in terms of characterizing grass distributions and filtering grass greenness information from landscape scales. Finally, based on correlations between grass greenness and total pollen concentrations, a grass pollen sources map, with 10 m resolution, was generated to reveal the spatial distribution of grass pollen sources for each pollen season.

The results showed that diurnal grass greenness (GCC) observed by phenocam characterized a concave pattern with smaller solar angles tended to larger GCC values, which is opposite with diurnal greenness index from forest canopy. Therefore, I proposed a diurnal-to-daily compositing approach based on the minimum solar angle over a day to achieve grass GCC seasonal profiles. As compared to the compositing approach proposed by forest canopy, our method tended to composite GCC obtained from optimal illumination images (noon time or clear sky condition) as daily value. Therefore, I recommend using this method to composite phenocam GCC in grassland/ pasture ecosystem. Near-surface remote sensing technology has long been used to track environmental change occurring on decadal time scales. As compared with the forest ecosystem. However, the phenology research of grassland using phenocam should put more effort, especially considering the potential applications for monitoring grass flowering using phenocam, which is impossible for satellites from space. It is also an important direction for our further study. As the phenocam network continues to grow, my results highlighted that image processing and analyses should be treated differently when using phenocams in grassland and forest ecosystem. And it lays a foundation for the further use of phenocam to reveal grassland phenology and possible to detect grass flowering.

Regarding the upscaling grass greenness observations from *in-situ* phenocam to regional multi-sensor satellites, my results indicated the Sentinel-2 data with finer spatial resolution can efficiently achieve grass greenness dynamics at phenocam footprint. Although coarse resolution satellites - MODIS (250 m) and Himawari-8 AHI (1 km) - also can monitor the grass dynamics at regional scale, their abilities were subjected to complex landscapes. In general, grass greenness dynamics as

measured by phenocam and satellites were associated with grass pollen concentrations, but their interrelationships were highly site-dependent. The Sentinel-2 observation with finer spatial resolution indeed benefited to observe grass greenness as compared with coarse resolution satellites, especially considering the spatial heterogeneity in Australian grassland. However, for the grass pollen aerobiology research, the choice of temporal resolution scales of satellite observation should depend on the application scenarios.

The Sentinel-2 grass map with 10 m resolution has the potential as a land cover filter to improve greenness upscaling from phenocam to satellites. Also, compared to currently mature land cover/use products, it can more precisely recognize the grass from complex landscapes and furtherly support filter grass information from satellite images. Although grass phenology and relationships between grass pollen concentrations varied across different distances and orientations centred at pollen sampler, grass fractions only play a secondary role in affecting the interrelationships between grass pollen and greenness dynamics. Strong seasonal and inter-annual variability of grass pollen sources in terms of spatial distributions and amount attested to the complexity of understanding on aerobiology of grass pollen in Australia. However, this thesis highlights the promising ability of near-surface and finer resolution satellite (i.e. Sentinel-2) to offer a new avenue for tracing grass phenology and mapping pollen sources at a large scale.

According to my knowledge, my study is the first time to adopt Sentinel-2 data for exploring grass phenology – grass pollen relationships and mapping grass pollen sources at 10 m resolution. Results from this thesis are promising because they offer a new avenue to use Sentinel-2 data with a finer spatial resolution globally for mapping grass pollen seasons and their dynamics at a large scale. The good agreement between grass greenness amplitude and grass pollen concentrations (rather than grass flowering humanly observed by dispersed *in-situ* stations) are potential of great use in future grass pollen-induced public health assessment using remote sensing technology. Meanwhile, grass pollen source maps with finer resolution can be used for assessing the risk of respiratory allergies, especially in urban areas with complex landscapes. My thesis demonstrated the promising application of near-surface and satellite-based remote sensing in informing grassland phenology and aerobiology of grass pollen in Australia.

REFERENCES

Beggs PJ, Katelaris CH, Medek D, Johnston FH, Burton PK, Campbell B, Jaggard AK, Vicendese D, Bowman DM, Godwin I, Huete AR, Erbas B, Green BJ, Newnham RM, Newbigin E, Haberle SG, Davies JM. Differences in grass pollen allergen exposure across Australia. *Aust N Z J Public Health*. 2015 Feb;39(1):51-5.

Davies JM, Berman D, Beggs PJ, Ramón GD, Peter J, Katelaris CH, Ziska LH. Global Climate Change and Pollen Aeroallergens: A Southern Hemisphere Perspective. *Immunol Allergy Clin North Am*. 2021 Feb;41(1):1-16.

Ziska L, Knowlton K, Rogers C, Dalan D, Tierney N, Elder MA, Filley W, Shropshire J, Ford LB, Hedberg C, Fleetwood P, Hovanky KT, Kavanaugh T, Fulford G, Vrtis RF, Patz JA, Portnoy J, Coates F, Bielory L, Frenz D. Recent warming by latitude associated with increased length of ragweed pollen season in central North America. *Proc Natl Acad Sci U S A*. 2011 Mar 8;108(10):4248-51.